Developing electron spin resonance spectroscopy for pL samples using superconducting circuits

Arne Bahr

▶ **To cite this version:**

Arne Bahr. Developing electron spin resonance spectroscopy for pL samples using superconducting circuits. Quantum Physics [quant-ph]. Ecole normale supérieure de lyon - ENS LYON, 2023. English. NNT : 2023ENSL0062 . tel-04352331

HAL Id: tel-04352331

https://theses.hal.science/tel-04352331

Submitted on 19 Dec 2023

HAL is a multi-disciplinary open access archive for the deposit and dissemination of scientific research documents, whether they are published or not. The documents may come from teaching and research institutions in France or abroad, or from public or private research centers.

L'archive ouverte pluridisciplinaire **HAL**, est destinée au dépôt et à la diffusion de documents scientifiques de niveau recherche, publiés ou non, émanant des établissements d'enseignement et de recherche français ou étrangers, des laboratoires publics ou privés.

THESE

en vue de l'obtention du grade de Docteur, délivré par

l'ECOLE NORMALE SUPERIEURE DE LYON

Ecole Doctorale N° 52
Ecole Doctorale de Physique et Astrophysique

Discipline : Physique

Soutenue publiquement le 28/09/2023, par :

Arne Alexander BAHR

Developing electron spin resonance spectroscopy for pL samples using superconducting circuits

Développement de la spectroscopie par résonance de spin électronique pour les échantillons picolitre à l'aide de circuits supraconducteurs

---

Devant le jury composé de :

BERTAINA,	Sylvain	Chargé de recherche	IM2NP	Rapporteur
CARPENTIER,	David	Directeur de recherche	ENS de Lyon	Examinateur
DE GRAAF,	Sebastian	Chercheur senior	NPL	Rapporteur
GUERON,	Sophie	Directrice de recherche	LPS	Examinatrice
BIENFAIT,	Audrey	Chargée de recherche	ENS de Lyon	Examinatrice
HUARD,	Benjamin	Professeur des universités	ENS de Lyon	Directeur de thèse

DEVELOPING ELECTRON SPIN RESONANCE SPECTROSCOPY FOR PICOLITRE SAMPLES USING SUPERCONDUCTING CIRCUITS

ARNE ALEXANDER BAHR

Supervised by Audrey Bienfait and Benjamin Huard
École Normale Supérieure de Lyon

28th September 2023

ABSTRACT

Electron spin resonance (ESR) is a powerful spectroscopy method which allows identifying and characterizing paramagnetic species. It usually relies on detecting microwave radiation absorbed or emitted by the spins into a microwave resonator tuned to their Larmor precession frequency. Because of the weak spin-microwave coupling, conventional ESR spectroscopy has a low sensitivity. Recent experiments have demonstrated that superconducting quantum circuits have the potential to enhance the spin detection sensitivity to single spin detection; by namely using high-quality factor small mode volume resonator. However, these demonstrations have been realized in very restrictive conditions, using well-known spin systems. To probe samples coming from chemistry or biology, quantum-circuit enabled spectrometers have to be adapted to be robust to losses. They have typically two origins: the dielectric losses introduced by the samples, mostly aqueous, and losses coming from the strong magnetic field required to tune the electronic spins to the resonator frequency. This PhD work centred on implementing a resonator that would achieve the same ESR sensitivity while being robust to dielectric losses and strong magnetic fields. Using NbTiN films deposited on sapphire, microwave resonators were shown to have quality factors above $Q = 10^5$ in magnetic field, even when samples with dielectric losses above $\tan(\delta) > 0.05$ were introduced. A study of the resonator intrinsic losses showed marked drops at multiple specific magnetic fields: a signature of coupling to spurious systems. Over the course of the PhD, nano-fabrication techniques for mitigating these contaminants were developed, such as hard mask etching and annealing, to remove all but one of these contaminants. Finally, tests of the spectrometer on a benchmark species (BDPA, α,γ-Bisdiphenylene-β-phenylallyl, a known ESR marker) were realized.

RÉSUMÉ

La résonance de spin électronique (RSE) est une méthode de spectroscopie qui permet d'identifier et de caractériser les espèces paramagnétiques. Elle repose généralement sur la détection du rayonnement micro-onde absorbé ou émis par des spins insérés dans un résonateur micro-ondes accordé à leur fréquence de précession de Larmor. En raison du faible couplage entre le spin et le champ micro-onde, la spectroscopie RSE conventionnelle a une faible sensibilité. Des expériences récentes ont démontré que les circuits quantiques supraconducteurs ont le potentiel d'améliorer la sensibilité de la détection des spins jusqu'à la détection d'un seul spin, notamment en utilisant un résonateur à petit volume de mode et à facteur de qualité élevé. Cependant, ces démonstrations ont été réalisées dans des conditions très restrictives, en utilisant des systèmes de spin cristallins bien connus. Pour sonder des échantillons chimiques ou biologiques, les spectromètres à circuits quantiques doivent être adaptés pour être robustes aux pertes. Celles-ci ont typiquement deux origines : les pertes diélectriques introduites par les échantillons, le plus souvent aqueux, et les pertes provenant du champ magnétique statique nécessaire pour accorder les spins électroniques à la fréquence du résonateur. Ce doctorat s'est focalisé sur la mise en œuvre d'un résonateur qui atteindrait une sensibilité RSE proche de l'état de l'art tout en étant robuste aux pertes diélectriques et aux champs magnétiques intenses. En utilisant des films de NbTiN déposés sur du saphir, il est démontré que les résonateurs micro-ondes ont des facteurs de qualité supérieurs à $Q = 10^5$ dans le champ magnétique, même lorsque des échantillons avec des pertes diélectriques supérieures à $\tan(\delta) > 0.05$ sont introduits. Les pertes intrinsèques du résonateur s'avèrent néanmoins dépendre du champ magnétique, avec notamment des raies apparaissant à des champs magnétiques spécifiques démontrant un couplage à des systèmes de spins parasites. Au cours de la thèse, des techniques de nanofabrication atténuant la contribution de ces contaminants ont été mises au point, telles que la gravure par masque dur et le recuit post-fabrication, menant à l'élimination de toutes les raies sauf une. Enfin, le spectromètre a été testé sur une espèce de référence, le BDPA (α,γ-Bisdiphenylene-β-phenylallyl), un marqueur RSE fréquemment utilisé.

ACKNOWLEDGMENTS

The last three years have been an amazing adventure for me. I would like to thank everyone who has accompanied me throughout this time. Special thanks goes to Audrey Bienfait who not only made the whole project possible, but also has been a source of great support, guidance, and motivation. Additionally, I would like to thank her for the immense support while writing my thesis paper. Even more so, does she deserve all my respect spending way too much time in the lab before she got her first child. I would like to thank Benjamin Huard not only for the help during the time Audrey was not available, but also for his kindness, overall joyfulness, and contagious joy at physics. It has been genuinely a pleasure to be part of this group.

Joyfulness, kindness and enthusiasm for physics are the keywords I would use to describe the Quantum Circuits group. The group changed a lot since I first arrived during Covid times and it is due to Alexis, Réouven, Antoine, Jeremy, Rémy and Daniel that the on-boarding was great a experience, that from the very first day the working atmosphere was welcoming and always friendly, and that there was always time to discuss, crack a joke or hang out for a drink.

I would especially like to thank Alexis who helped me with all the bureaucracy hurdles I had to face outside the lab without speaking French. Furthermore, I would like to thank him for all the great discussions and the honest personal advice.

I will never forget "The Basement" with its lovely view, special equipment and inhabitants, whether that may be in the actual basement or on the first floor. A special place in my heart is now reserved for our forever super mega intern Hector and the lovely Tigrou (Tony) with his small spoon. I will remember the pleasure of sharing the daily life with the two of you.

Especially with the arrival of Matteo, I had the pleasure of seeing the nanoESR project grow and develop. It is a nice feeling seeing a once empty place in a shared fridge becoming a full-fledged dedicated new fridge.

I would also like to thank my long time flat mates Fanny, Simon, Gustave, Marie, and Julian for the great time together, although I am still not believing that Studio Ghibli movies are the all time pinnacle of movies. Living with you guys has been more than sharing a flat. Mahieddine and Jens, for the speleo-counterbalance to studying and integration into the French underground life, I blame you for the focus my French vocabulary has on mud. I would like to thank my parents and my brother for always being there and looking out for me. Furthermore, I would like to thank Lilo for encouraging me to go on this adventure against her own interests as well as supporting me, disregarding all changes. And lastly, I would like to thank Tia and Leo for their support on the last stretch.

CONTENTS

1 INTRODUCTION

La découverte de la résonance de spin électronique (RPE) par Evgeny Zavoisky en 1944 [1] ainsi que les travaux de Rabi [2], Bloch [3], Purcel [4] et bien d'autres ont permis de sonder la matière d'une nouvelle manière en étudiant les spins qui s'y trouvent. La résonance paramagnétique électronique (RPE) et la spectroscopie de résonance magnétique nucléaire sont aujourd'hui des outils d'analyse largement utilisés dans divers domaines de recherche. Cela va des études des interactions au sein d'un système de spin, à l'analyse structurelle des molécules en chimie [5] et en biologie [6], jusqu'aux applications en pharmacie [7]. Bien que la spectroscopie RPE se soit imposée comme un outil de spectroscopie standard,une de ses limites est sa faible sensibilité. Pour la spectroscopie RPE par détection inductive, la principale limite provient de la faible interaction entre le spin et le champ micro-onde. Néanmoins, il existe un besoin de sonder des échantillons de volume limité : Un bon exemple est l'analyse structurelle en biologie à l'aide de spins marqueurs insérés sur certains sites [6, 8, 9]. Dans ce cas, des monocristaux de protéines, d'une taille allant de 0.2 µm to 300 µm sont utilisés [10], cependant, ces échantillons ne sont actuellement pas mesurables compte tenu des sensibilités RPE actuelles [11].

Étant donné qu'il existe un besoin important pour détecter ces échantillons à volume limité, de nombreux outils complémentaires ont été développés pour la spectroscopie RPE en plus de la détection inductive. Par exemple, la résonance magnétique par détection optique [23, 24] et la résonance magnétique par détection électrique ont atteint une sensibilité au niveau du spin unique [25, 26]. Ces deux techniques nécessitent toutefois l'existence d'un mécanisme de conversion entre le degré de liberté du spin et un photon optique ou un porteur de charge et ne sont donc applicables qu'à des systèmes spécifiques. Des dispositifs de balayage ont également été mis au point [27, 28, 29, 30], à savoir la microscopie à effet tunnel (STM-RPE), qui combine la haute résolution spatiale d'un STM avec des capacités de détection de spin RPE, la microscopie à force de résonance magnétique qui détecte la force exercée par les spins sur une pointe magnétique ; et la détection indirecte via la microscopie utilisant un centre azote-lacune du diamant. Ces dispositifs de balayage ont une faible portée (< 50 nm) et n'offrent qu'un accès limité aux interactions spin-spin par rapport à la spectroscopie inductive. Cette limite est principalement due à la faible résolution spectrale du capteur. Par conséquent, l'amélioration de la spectroscopie RPE à détection inductive pour atteindre une plus grande sensibilité reste une direction de recherche importante pour l'étude des échantillons de peitis volumes.

Récemment, le domaine de l'électrodynamique quantique des circuits (CQED) a démontré que les circuits supraconducteurs pouvaient stocker, manipuler et mesurer des états quantiques, offrant ainsi une plateforme prometteuse pour l'informatique quantique. La CQED travaille principalement avec des atomes artificiels ou des systèmes à deux niveaux créés à l'aide d'éléments non linéaires, tels que des jonctions Josephson

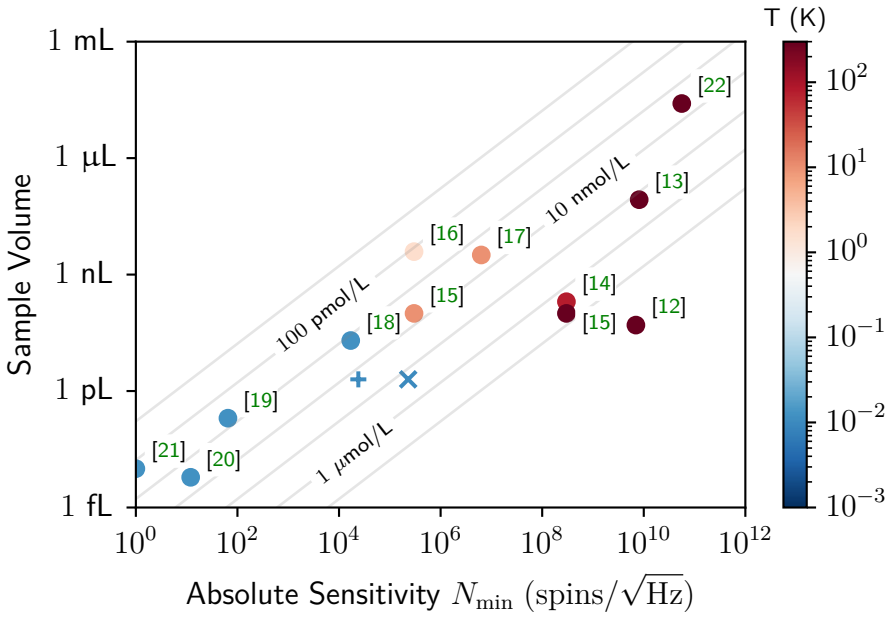

Figure 1.1: Volume de l'échantillon, défini par le volume actif du champ magnétique, en fonction du nombre minimal de spins nécessaire pour une détection avec un RSB de un, pour diverses valeurs trouvées dans la littérature. Toutes les expériences citées fonctionnent dans la gamme de fréquences de 7 GHz à 9 GHz, à l'exception de [17] à 36 GHz et de [15] à 16 GHz. [22] est un spectromètre RPE commercial. La croix correspond à la sensibilité RPE à ondes continues mesurée de 2.3×10^{5} spins/$\sqrt{\mathrm{Hz}}$ en utilisant un échantillon BDPA et le plus à la sensibilité RPE à ondes continues extrapolée à la sensibilité RPE à impulsions de 2.4×10^{4} spins/$\sqrt{\mathrm{Hz}}$.

intégrées à des résonateurs supraconducteurs à facteur de qualité élevé ($Q \approx 10^{5}$). Un certain nombre de technologies et de capacités ont été développées pour manipuler et détecter les champs micro-ondes au niveau du photon unique dans ce domaine de recherche. Les amplificateurs quantiques limités, capables d'amplifier les signaux tout en n'ajoutant que le bruit minimal autorisé par la mécanique quantique, sont les plus pertinents pour le domaine de la spectroscopie RPE. Dans le domaine de la CQED, une classe de systèmes hybrides est apparue, utilisant des spins physiques comme éléments du circuit. Jusqu'à présent, des spins à longue durée de vie intégrés dans des échantillons cristallins, tels que des donneurs de silicium, des ions de terres rares ou des spins dans le diamant ont souvent été utilisés. Ces spins peuvent se coupler par induction à un résonateur et être utilisés pour stocker un bit d'information. La manipulation de ces spins est analogue à conduire une expérience de RPE en utilisant des circuits supraconducteurs et des avancées récentes ont montré des sensibilités élevées, atteignant la détection d'un seul spin avec un volume de sonde de ≈ 5 fl [20, 18, 21]. Ces sensibilités ont été rendues possibles par les facteurs de qualité élevés que l'on peut atteindre dans les circuits supraconducteurs, associés à une polarisation complète des spins en raison des températures de l'ordre du millikelvin, ainsi que par l'amplification du signal à très faible bruit mentionnée plus haut. La figure 1.1 présente une petite sélection de la sensibilité de différentes expériences utilisant la RPE détectée par induction. Jusqu'à présent, ces expériences ont été réalisées sur des échantillons

cristallins, ce qui ne représente qu'une petite partie des échantillons pour lesquels une RPE de grande sensibilité est nécessaire.

L'objectif de ce travail de doctorat est de transposer ces expériences de circuits quantiques à des échantillons de l'ordre du picolitre, avec des temps de cohérence éventuellement courts. Il faut pour cela créer des résonateurs à faibles pertes capables de sonder des échantillons de la taille du micron, qui peuvent présenter des pertes diélectriques aux fréquences micro-ondes, développer des techniques d'insertion pour placer l'échantillon de spin dans la zone active, et enfin étalonner le spectromètre en utilisant le α,γ-Bisdiphenylene-β-phenylallyl (BDPA), une espèce connue pour sa caractérisation par RPE.

Pour une RPE à grande sensibilité, il est essentiel de disposer de résonateurs à facteur de qualité élevé. Ceux-ci peuvent être obtenus à des températures modérément élevées (supérieures à 10 K) soit en utilisant des résonateurs diélectriques [31], soit en focalisant le volume du mode à l'aide de micro-résonateurs [13], de structures en forme d'arc [32], de résonateurs en boucle [33, 34], ou de résonateurs anapolaires [35]. Ces systèmes fonctionnent tous à des températures généralement supérieures à 10 K et atteignent des sensibilités de concentration aussi faibles que nmol/L et un nombre minimal de spins détectables de 1×10^7 spins/$\sqrt{\text{Hz}}$. Dans les expériences CQED, ces hauts facteurs de qualité sont obtenus en utilisant des résonateurs planaires fabriqués à partir de films minces supraconducteurs déposés sur des substrats à faibles pertes tels que le silicium et le saphir. L'introduction d'un échantillon présentant des pertes diélectriques potentiellement importantes peut réduire considérablement le facteur de qualité. Nous devons donc concevoir le résonateur de manière à supprimer le couplage à ces canaux de pertes. En outre, nous devrons choisir un supraconducteur dont le champ critique est suffisamment élevé pour résister aux champs magnétiques de l'ordre de 0.25 T to 0.5 T afin de sonder un spin 1/2, tout en préservant le facteur de qualité du résonateur.

Cependant, le fait de disposer d'un tel résonateur avec un volume de détection de l'ordre du micron ne suffit pas pour mesurer un échantillon réel. Cet échantillon doit encore être inséré dans cette zone. Ces échantillons peuvent être cristallins ou se présenter sous forme de solution et nous avons besoin d'un moyen fiable de les déposer.

Un spectromètre RPE conventionnel permet de changer d'échantillon en quelques minutes, ce qui est une nécessité dans les expériences où un paramètre est modifié et où de nombreux échantillons doivent être caractérisés. Ce cycle rapide est impossible avec l'utilisation de cryostats à dilution nécessaires pour les températures de l'ordre du milli kelvin. Un moyen de compenser cette limitation serait de mesurer plusieurs échantillons au cours d'un seul refroidissement.

Enfin, nous devons garder à l'esprit que les expériences de démonstration de principe ont été réalisées avec des systèmes de spin bien choisis ayant de longs temps de cohérence $> 100\,\mu$s. Il n'en va pas de même pour les espèces de spin dans les substances organiques, qui présentent souvent des temps de cohérence courts. Pour mesurer ces espèces, il faut soit choisir un résonateur avec un facteur de qualité modéré, soit utiliser des impulsions micro-ondes courtes [20]. Comme la première solution va à l'encontre de la haute sensibilité visée, l'utilisation d'impulsions courtes semble préférable.

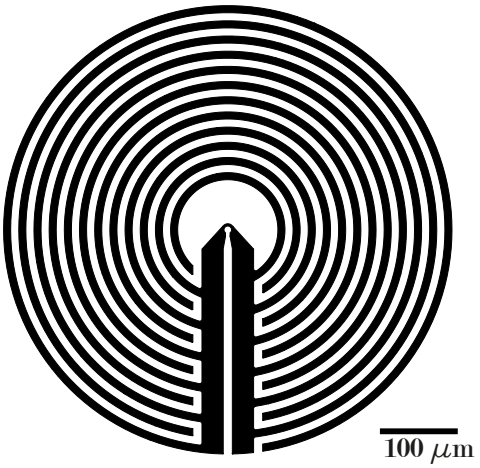

Figure 1.2: Géométrie du résonateur. La boucle inductive au centre a un rayon de 5 µm, la zone à l'intérieur de cette boucle est l'espace où est inséré l'échantillon.

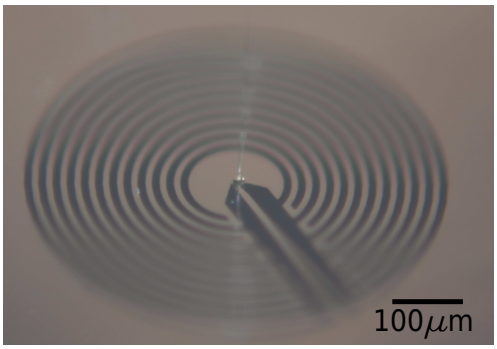

Figure 1.3: Goutte de 7.6 pl de BDPA mélangé à du PMMA placé sur le résonateur illustré à la figure 1.2.

CONCEPTION DU RÉSONATEUR ET PERTES DANS LE CHAMP MAGNÉTIQUE

À partir du chapitre 3, nous présentons la conception de notre résonateur, qui est en théorie bien adapté aux échantillons présentant des pertes, car sa géométrie circulaire permet d'annuler le champ électrique au centre de l'échantillon (voir la figure 1.2). En faisant varier le diamètre de la boucle intérieure et le condensateur circulaire, nous visons différentes sensibilités allant de $300, \text{spins}/\sqrt{\text{Hz}}$ à $10^3\,\text{spins}/\sqrt{\text{Hz}}$. Nous plaçons huit de ces résonateurs sur un puce, ce qui permet de mesurer plusieurs échantillons en un seul refroidissement. Ces puces ont été fabriqués en NbTiN sur saphir et nous avons pu obtenir des facteurs de qualité de l'ordre de 1×10^5 to 1×10^6. La mesure de ces résonateurs sans échantillon de spin sous champ magnétique a révélé un total de six raies d'absorption différentes et deux plateaux abaissant le facteur de qualité des résonateurs de manière drastique, empêchant effectivement les mesures RPE sur les échantillons (voir Figure 1.4).

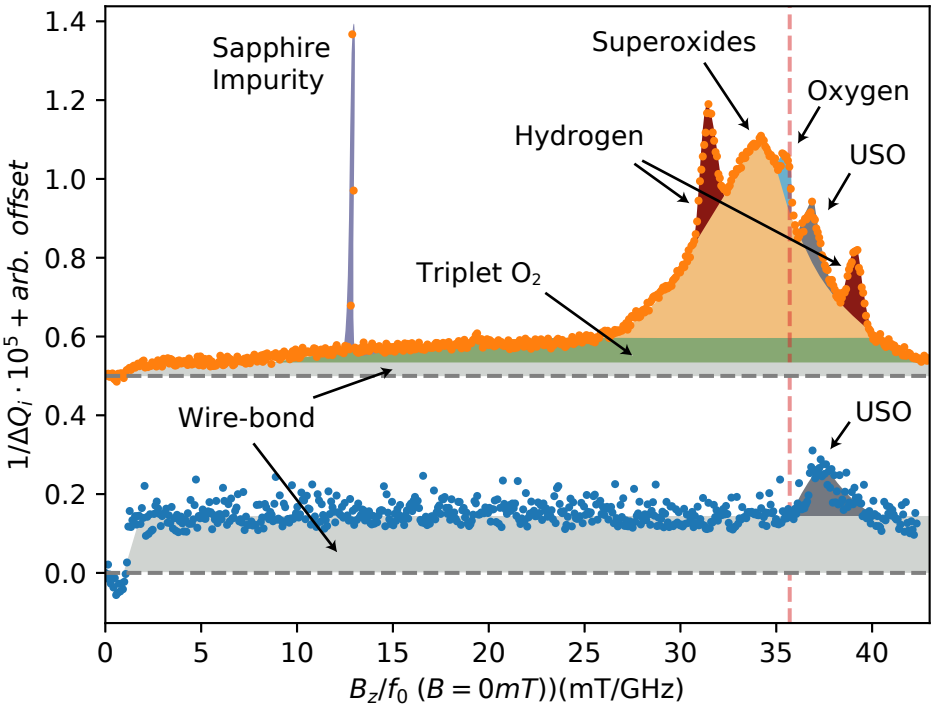

Figure 1.4: Contribution aux pertes intrinsèques en fonction du champ magnétique $1/Q_\mathrm{i}(B) - 1/Q_\mathrm{i}(B = 0\,\mathrm{mT})$ du premier dispositif (en haut) et du dernier dispositif (en bas) avec toutes les améliorations apportées au processus de fabrication.

Ces raies d'absorption sont analysées au chapitre 5. Nous pouvons identifier les pertes dues à l'hydrogène physisorbé [36], au triplet O_2 et aux superoxydes [37]. L'impureté du saphir a déjà été observée [38] mais son origine exacte n'est pas claire. En adaptant notre processus de fabrication en passant d'un masque de résine optique à un masque d'aluminium, en incluant une étape de recuit et en changeant de type de saphir, nous avons pu atténuer la plupart des pertes. Il reste une raie d'absorption surnommée USO (unidentified spin object : objet spin non identifié) dont nous avons essayé de trouver l'origine en étudiant une éventuelle dépendence entre l'intensité des pertes et la géométrie du résonateur. Nous avons remarqué une dépendance à la température de recuit, ce qui nous a conduit, avec l'étude précédente, à suspecter la présence de nitrites dans le NbTiN. Enfin, nous notons une petite contribution probablement due aux pertes électriques introduites par les fils de micro-soudures au-dessus de 10 mK, après quoi l'aluminium devient normal.

BDPA : MESURES EN RÉGIME CONTINU ET PULSÉ.

Nous nous tournons ensuite vers l'étude d'un échantillon de spin : le BDPA, une espèce de caractérisation couramment utilisée en spectroscopie RPE. Dans le chapitre 3, nous décrivons notre solution maison pour placer le BDPA mélangé au PMMA A2 (une réserve courante dans la microfabrication qui est silencieuse en RPE) dans des gouttes avec des volumes de l'ordre de 10 pL. Un tel échantillon est illustré à la figure 1.8.

Nous avons essayé de mesurer des concentrations de spin allant de 10^{12} spins/mL à $6 \cdot 10^{17}$ spins/mL, qui sont toutes censées être des concentrations mesurables.

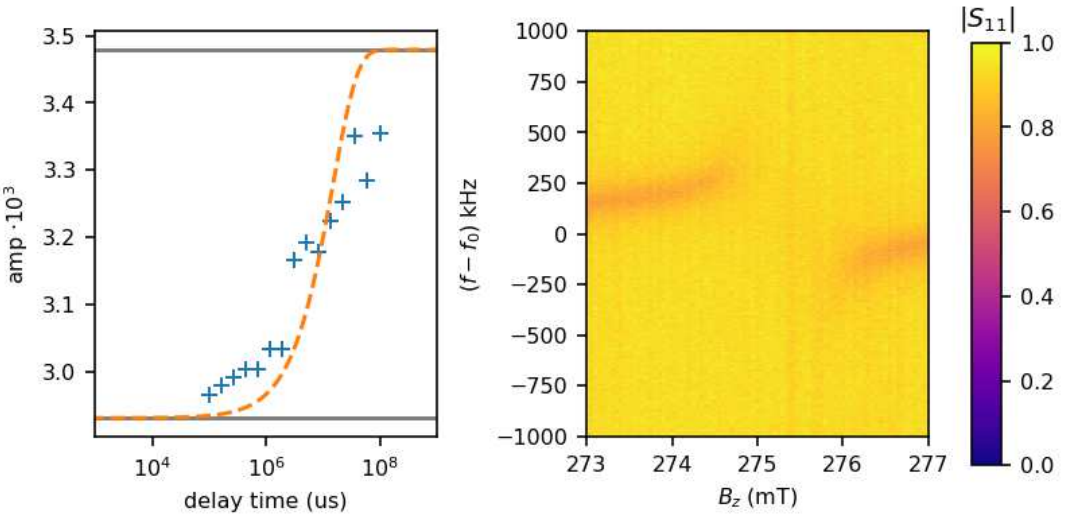

Figure 1.5: Mesure de la récupération de la saturation de T_1 et du franchissement évité du niveau de la BDPA mesurée. $f_0 = 7.704\,25\,\text{GHz}$.

Motivés par les tests initiaux avec des concentrations élevées de BDPA, nous avons entrepris au chapitre 6 d'effectuer des mesures RPE pulsées sur des concentrations de spin faibles, mais détectables. Cela n'a cependant pas donné de résultats et nous avons par la suite augmenté la concentration. Ces mesures nous ont permis de mesurer une raie RPE d'une largeur inhomogène $\Gamma_t/(2\pi) = 12.5\,\text{MHz}$. En raison du temps de cohérence court et des problèmes liés à l'amplificateur limité quantiquement utilisé, nous n'avons pas pu appliquer des impulsions courtes d'une puissance suffisante pour observer un écho de spin. Néanmoins, nous avons effectué une mesure de saturation-relaxation pour extraire un temps de relaxation $T_1 = 15\,\text{s}$. En utilisant la saturation de la raie en fonction de la puissance du ton de sonde, nous pouvons alors déduire un temps de cohérence $T_2 = 180\,\text{ns}$. Nous concluons les efforts de détection des spins par une caractérisation de la sensibilité du spectromètre RPE à onde continue de $N_{min} = 2,3 \times 10^5 spins/\sqrt{Hz}$.

The discovery of electron spin resonance (ESR) by Yevgeny Zavoisky in 1944 [1] together with the works of Rabi [2], Bloch [3], Purcel [4] and many others has opened up a window into matter by studying the spins therein. Electron paramagnetic resonance (EPR) and nuclear magnetic resonance spectroscopy are nowadays broadly used analysis tools throughout various fields of research. This ranges from studies of the interaction within a spin system and its properties, over structural analysis of molecules in chemistry [5] and biology [6] all the way to applications in pharmacy [7]. Although EPR spectroscopy has established itself as a standard spectroscopy tool it is also known for its inherent low sensitivity. For inductively-detected EPR spectroscopy, the main limitation comes from the weak microwave-spin interaction. Nevertheless, there exists a need for probing limited volume samples: A good example is structural analysis in biology using spin labelled sites [6, 8, 9]. Here volume-limited protein single crystals ranging in size from 0.2 µm to 300 µm [10] are of interest. However, these samples are currently not measurable considering the current EPR sensitivities [11].

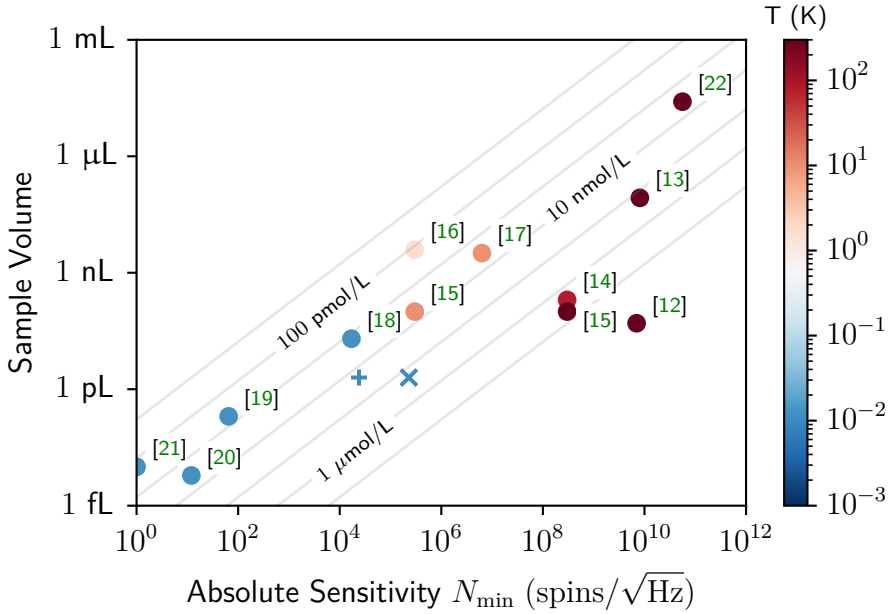

Figure 1.6: Sample volume, defined by the magnetic-field active volume, versus the minimal number of spins needed for a detection with a SNR of one, for various values found in literature. All cited experiments work in the frequency range of 7 GHz to 9 GHz except for [17] at 36 GHz and [15] at 16 GHz. [22] is a commercial EPR spectrometer. The cross is the measured continuous-wave EPR sensitivity of 2.3×10^5 spins/$\sqrt{\mathrm{Hz}}$ using a BDPA sample and the plus the from the continuous-wave sensitivity extrapolated pulsed EPR sensitivity of 2.4×10^4 spins/$\sqrt{\mathrm{Hz}}$.

Because a strong need exists for detecting these volume-limited samples, many complementary tools were developed for EPR spectroscopy besides inductive detection.

For example, optically-detected magnetic resonance [23, 24] and electrically detected magnetic resonance have reached single-spin sensitivity [25, 26]. Both techniques, however, require the existence of a conversion mechanism between the spin degree of freedom and an optical photon or a charge carrier and are thus only applicable to specific products. Scanning setups have also been developed [27, 28, 29, 30], namely scanning tunnelling microscopy (STM) EPR, which combines the high spatial resolution of a STM with EPR spin detection capabilities, magnetic resonance force microscopy which detects the force exerted by the spins on a magnetic tip; and indirect detection via nitrogen-vacancy defects in diamond microscopy. These scanning setups have a small probing range ($<$ 10 nm to 50 nm) and offer only limited access to spin-spin interactions when compared to inductive spectroscopy. This limitation primarily stems from the sensor's poor spectral resolution. Therefore, advancing inductively-detected EPR spectroscopy to achieve higher sensitivity remains an important research direction for investigating volume-limited samples.

In recent history the field of circuit quantum electro dynamics (CQED) has demonstrated that superconducting circuits could host, manipulate and probe quantum-states, providing a promising platform for quantum computing. CQED is working mainly with artificial atoms or two level systems created using non-linear elements such as Josephson junctions embedded with high quality factor superconducting resonators. A number of technologies and capabilities have been developed for manipulating and detecting microwave fields at the single photon level within this research field. Most relevant for the field of EPR spectroscopy are quantum limited amplifiers capable of amplifying signals all the while adding only the quantum mechanically minimal allowed noise. Within the field of CQED a class of hybrid systems has emerged using physical spins as part of the circuit. So far, mostly long-lived spins embedded in crystalline samples have been used, such as silicon donors, rare-earth ions, or spins in diamond. These spins can couple inductively to a resonator and can be used to encode information. The manipulation of these spins is essentially describing an EPR experiment in the context of superconducting circuits. Recent advances have shown high sensitivities, reaching single spin detection with a probe volume of $\approx$ 5 fl [20, 18, 21]. These sensitivities were made possible by the high quality factors reachable in superconducting circuits paired with full spin polarization due to the millikelvin temperatures as well as the mentioned ultra low noise signal amplification. A small selection of the sensitivity of different experiments using inductively detected EPR is shown in Figure 1.6. So far these experiments were realized on pristine samples, which only encompass a narrow section of samples for which high sensitivity volume-limited EPR is needed. The goal of this PhD work was thus to transpose these quantum circuits experiments for pL samples, with possibly short coherence times. It requires creating low-loss resonators able to probe micron-size samples which are possibly lossy at microwave frequencies, developing insertion techniques to place the spin sample into the active area, and finally benchmark the spectrometer using α,γ-Bisdiphenylene-β-phenylallyl (BDPA) a known EPR characterization species.

For high-sensitivity EPR, high quality factor resonators are crucial. These can be achieved at moderately high temperatures (above 10 K) either by using dielectric resonators [31], or by focusing the mode-volume using micro-resonators [13], bow-like

structures [32], loop-gap [33, 34], or anapole resonators [35]. These systems all operate at temperatures typically above 10 K and achieve concentration sensitivities as low as nmol/L and a minimal number of detectable spins of 1×10^7 spins/$\sqrt{\text{Hz}}$. In CQED experiments, these high-quality factors are achieving by patterning planar resonators in superconducting thin films deposited on low-loss substrates such as silicon and sapphire. Introducing a sample with potentially large dielectric losses can severely lower the quality factor. We therefore need to engineer the resonator in such a way that coupling to these loss channels is suppressed. Furthermore, we will need to choose a superconductor with a critical field high enough to withstand the magnetic fields in the range of 0.25 T to 0.5 T to probe a spin 1/2, all the while maintaining its quality factor.

However, having such a resonator with a micron-scale area for the sample and being able to probe it is not enough to measure an actual sample. This sample still needs to be inserted into said area. These samples can be crystalline or come in a solution, and we need a reliable way of depositing them. A conventional EPR spectrometer allows

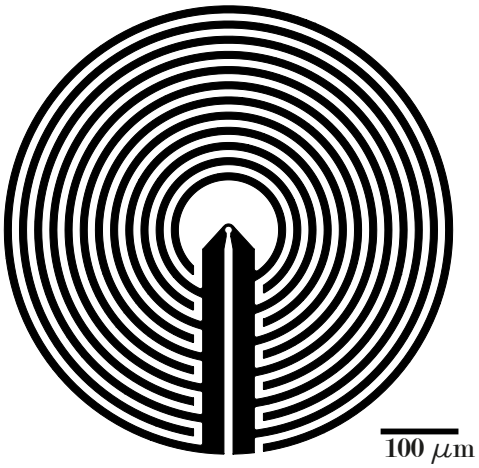

Figure 1.7: Resonator design. The inductive loop in the centre has a radius of 5 µm, the area within this loop is the designated sample space.

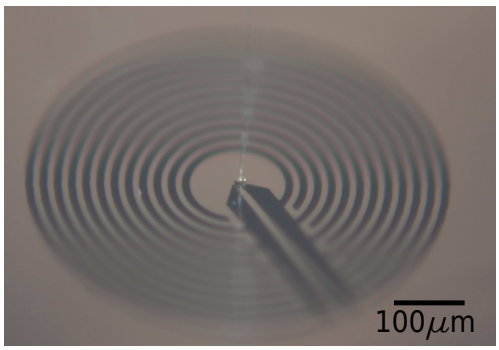

Figure 1.8: Drop of 7.6 pL of BDPA mixed with PMMA placed on the resonator shown in Figure 1.7.

for sample changes within minutes, which is a necessity in experiments in which a parameter is varied, and many samples need to be characterized. This fast cycling is impossible with the use of dilution cryostats needed for the milli kelvin temperatures. A way to compensate for this shortcoming would be a way to measure multiple samples within a single-cool-down.

Lastly, we need to keep in mind that the proof-of-principle experiments in CQED were performed with well chosen spin systems having long coherence times > 100 µs. The same cannot be said about the spin species in organics, which often display short coherence times. To measure these species, one either needs to choose a resonator with moderate quality factor or use short microwave pulses [20]. As the former is working against the targeted high sensitivity it is not suitable, which leaves us with the approach of using short microwave pulses.

1.1 RESONATOR DESIGN AND LOSSES IN MAGNETIC FIELD

Starting in Chapter 3 we introduce our resonator design, which is in theory well suited for lossy samples due to its circular geometry averaging out the electric field at the sample site in the centre (see Figure 1.7). Varying the inner loop diameter and the circular capacitor we target different sensitivities from 300 spins/$\sqrt{\text{Hz}}$ to 10^3 spins/$\sqrt{\text{Hz}}$. We place eight of these resonators on a device, enabling the measurement of multiple samples in one cool-down. These devices were fabricated in NbTiN on sapphire, and we were able to achieve quality factors in the range of 1×10^5 to 1×10^6. Measuring these resonators without a spin sample under magnetic field revealed a total of six different absorption lines and two offsets lowering the resonators quality factor drastically, effectively preventing EPR measurements on samples (see Figure 1.9).

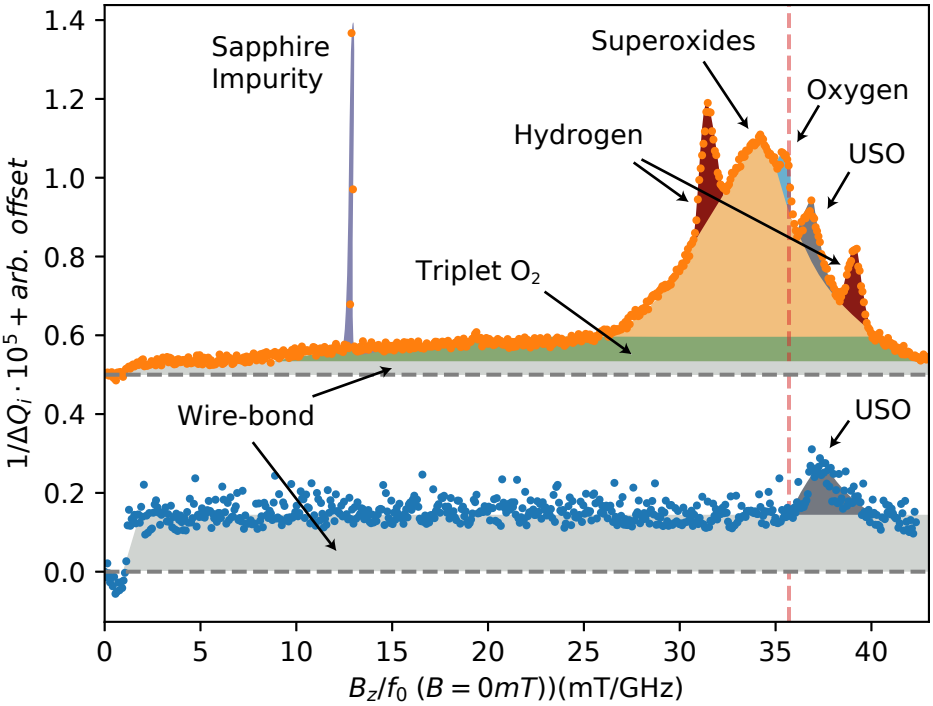

Figure 1.9: Magnetic field depended contribution to the intrinsic losses $1/Q_\text{i}(B) - 1/Q_\text{i}(B = 0\,\text{mT})$ of the first (aged) device (top) and the last device (bottom) with all improvements to the fabrication process.

These features are then discussed in Chapter 5. We can identify losses due to physisorbed hydrogen [36], triplet O_2 and superoxides [37]. The sapphire impurity has been observed before [38] but the exact origin is unclear. Adapting our fabrication process by switching from an optical resist mask to an aluminium mask, including an annealing step and changing the sapphire substrate, we were able to mitigate most losses. Remaining is a feature nicknamed USO (unidentified spin object) for which we tried to find the origin by investigating the participation ratio and the feature intensity. We noticed a dependence on the annealing temperature leading us, together with the participation ratio study, to suspect nitrites in the NbTiN. Lastly, we note a small

contribution likely due to the electric losses introduced by the wire bonds above 10 mK after which the aluminium turns normal.

1.2 CWEPR MEASUREMENTS OF BDPA

We then turn towards studying an actual spin sample: BDPA a commonly used characterization species in EPR spectroscopy. In Chapter 3 we describe our homebuilt solution to place BDPA mixed with PMMA A2 (a common resist in microfabrication which is EPR silent) in drops with volumes in the order of 10 pL. Such a sample is shown in Figure 1.8. We attempted to measure spin concentrations ranging from 10^{12} spins/mL to $6 \cdot 10^{17}$ spins/mL, which all are predicted to be measurable concentrations.

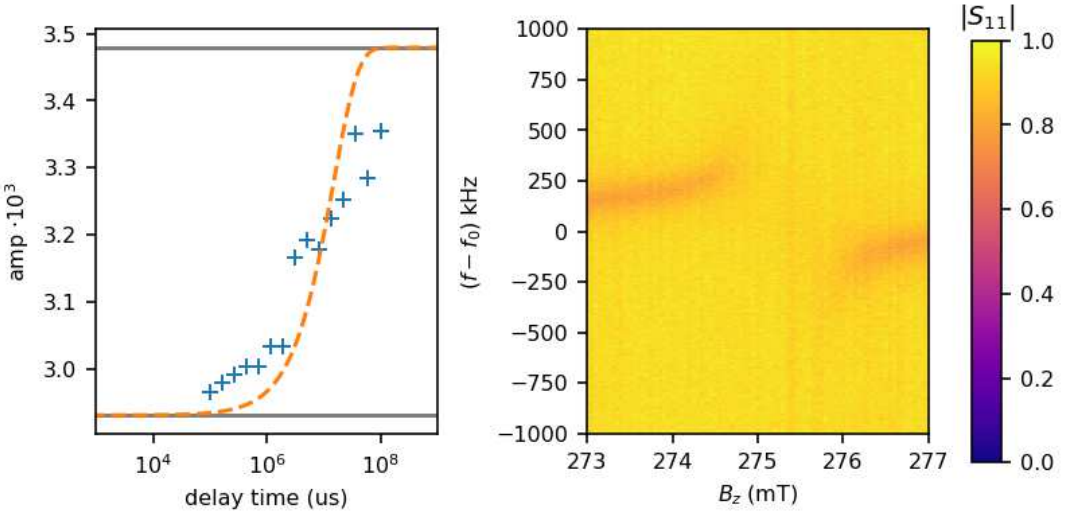

Figure 1.10: T_1 saturation recovery measurement and the avoided level crossing of the measured BDPA. $f_0 = 7.704\,25$ GHz.

Motivated by initial tests with BDPA high concentrations, we set out in Chapter 6 to perform pulsed EPR measurements on low, but detectable spin concentrations. This was however fruitless, and we subsequently increased the concentration. Finding again a continuous wave EPR signal at high concentrations revealed a rather broad EPR line with $\Gamma_t/(2\pi) = 12.5$ MHz. Due to the short coherence time and problems related to the used quantum-limited amplifier, we could not apply short pulses of sufficient power to observe a spin-echo. Nevertheless, we performed a T_1 saturation recovery measurement to extract $T_1 = 15$ s. Using the saturation power dependence of the absorption line we can then deduce a $T_2 = 180$ ns. We conclude the efforts of detecting spins with a characterization of the continuous wave EPR spectrometer sensitivity of $N_{min} = 2.3 \times 10^5 spins/\sqrt{Hz}$.

2

BACKGROUND

In this work, we are aiming to apply the tools and techniques of superconducting quantum circuits to the spectroscopy of electron paramagnetic resonance. We will thus introduce a quantum-mechanical description of these circuits, and discuss two of their key elements: harmonic oscillators and linear amplifiers, as well as briefly outline a few properties of superconducting films as pertinent for the implementation of these planar circuits. We will then introduce the coupling of these circuits to an ensemble of spins in the framework of EPR experiments, and express the parameters setting the sensitivity of continuous-wave or pulsed EPR measurements, in particular in the limit targeted during the thesis: lossy and short-lived spin species. [39, 40, 41, 42, 43]

Typically, microwave oscillators operated in the quantum regime are either implemented by superconducting bulk cavity or by planar structures made from thin film superconductors. They generally operate in the range of 2 GHz to 12 GHz. Independently of their physical implementation that will be described in the next chapter, these oscillators can be described as a resonant circuit. They thus can always be recast as a simple LC oscillator comprising an inductance L in parallel to a capacitor C such as depicted in Figure 2.2, [44, 45]. We will now give their quantum mechanical description, focusing in particular on the magnetic field produced by the inductance which is key to express their coupling to spins [46, 47].

2.0.1 *LC resonator*

The Hamiltonian of the resonator can be expressed using the operators describing the charge in the capacitor $\hat{Q}$ and the flux in the inductor $\hat{\phi}$ [45]:

$$\hat{H}_\mathrm{r} = \frac{\hat{Q}^2}{2C} + \frac{\hat{\phi}^2}{2L}. \tag{2.1}$$

These operators are related by the commutation relation $\left[\hat{\phi}, \hat{Q}\right] = i\hbar$. The characteristic impedance of the resonator is $Z = \sqrt{L/C}$ and its resonance frequency is $\omega_0 = 1/\sqrt{LC}$. The usual ladder operators $\hat{a}$ and $\hat{a}^\dagger$ obeying the usual commutation relation $\left[\hat{a}, \hat{a}^\dagger\right]$ are related to the charge and flux operators:

$$a^\dagger = \frac{1}{\sqrt{2\hbar Z}} \left(\hat{\phi} - iZ\hat{Q}\right), \tag{2.2}$$

$$\tag{2.3}$$

and can be used to rewrite the Hamiltonian into the usual form of a harmonic oscillator

$$\hat{H}_\mathrm{r} = \hbar\omega_0(\hat{a}^\dagger\hat{a} + 1/2). \tag{2.4}$$

This Hamiltonian is diagonal in the Fock basis, where an eigenvalue $E_n = \hbar\left(n + \frac{1}{2}\right)$ and its associated Fock state $|n\rangle$ corresponds to exactly n photons stored in the resonator [48].

2.0.2 *Current rms in ground state*

Later on, we will be interested in the vacuum fluctuations of the magnetic field generated by the inductance, as they determine the coupling strength between the spins and the resonator. The voltage across the resonator and the current flowing in the inductor can be expressed as [49]:

$$\hat{V} = i\sqrt{\frac{\hbar Z\omega_0^2}{2}}(\hat{a}^\dagger - \hat{a}), \tag{2.5}$$

$$\hat{I} = \sqrt{\frac{\hbar\omega_0^2}{2Z}}(\hat{a}^\dagger + \hat{a}). \tag{2.6}$$

The vacuum fluctuations of the current and voltage are thus:

$$\delta V^2 = \langle 0|\hat{V}^2|0\rangle = \frac{\hbar Z\omega_0^2}{2}, \tag{2.7}$$

$$\delta I^2 = \langle 0|\hat{I}^2|0\rangle = \frac{\hbar\omega_0^2}{2Z}. \tag{2.8}$$

The magnetic field at position $\vec{r}$ generated by the inductor is $\vec{B} = \delta\vec{B}(\vec{r})(\hat{a}^\dagger + \hat{a})$, where $\delta\vec{B}$ are the root-mean-square vacuum fluctuations of the magnetic field. They can be calculated using the Biot-Savart law and considering a current of amplitude δI flowing through the inductor. Similarly, the electric field can be calculated using $\vec{E} = \delta\vec{E}(\vec{r})(\hat{a}^\dagger - \hat{a})$.

2.0.3 *Driving and measuring a quantum mechanical oscillator*

To describe the measurement of such an oscillator, we imagine n ports, each coupled to the resonator with a strength $\kappa_{\mathrm{p},j}$. For each of these ports, we can define an incoming and outgoing bosonic fields $\hat{a}_{\mathrm{in},j}$ and $\hat{a}_{\mathrm{out},j}$.

The evolution of the intra-resonator field $\hat{a}$ is then described by the following master equation in the Heisenberg picture [48]:

$$\frac{\partial\hat{a}}{\partial t}(t) = \frac{i}{\hbar}\left[\hat{H}_{\mathrm{r}}, \hat{a}(t)\right] - \frac{\kappa_{\mathrm{t}}}{2}\hat{a}(t) - \sum_{j=1}^{n}\sqrt{\kappa_{p,j}}\hat{a}_{\mathrm{in},j}(t), \tag{2.9}$$

where κ_{t} is the total energy loss rate of the resonator and has two contributions: the loss of energy through each port $\kappa_{\mathrm{c}} = \sum_{j=1}^{n}\kappa_{p,j}$ and the loss of energy through dissipation into Markovian baths outside the scope of the measurement apparatus, such that $\kappa_{\mathrm{t}} = \kappa_{\mathrm{c}} + \kappa_{\mathrm{int}}$. The master equation is accompanied by a continuity equation at each port:

$$\hat{a}_{\mathrm{in},j} = \hat{a}_{\mathrm{out},j} + \sqrt{\kappa_{\mathrm{p},j}}\hat{a}(t). \tag{2.10}$$

When measuring the resonators, we apply a classical microwave drive field on a single port. The corresponding input field $\hat{a}_{\mathrm{in},i}$ is then given by a coherent drive $\alpha_{\mathrm{in},i}(t)e^{i\omega t}$, of amplitude $\alpha_{\mathrm{in},i}$ and frequency ω [19, 48]. Using the master equation to express the mean intra-resonator field $\alpha(t) = \langle \hat{a}(t) \rangle$, one finds

$$\frac{\partial \alpha}{\partial t}(t) = i\omega_0 \alpha(t) + \frac{\kappa_\mathrm{t}}{2}\alpha(t) - \sqrt{\kappa_{\mathrm{p},i}}\alpha_{\mathrm{in},i}(t). \tag{2.11}$$

Using a Fourier transform, we obtain $\alpha(\omega)$:

$$\alpha(\omega) = \frac{2\sqrt{\kappa_{\mathrm{p},i}}}{\kappa_\mathrm{t} - 2i(\omega - \omega_0)}\alpha_{\mathrm{in},i}(\omega). \tag{2.12}$$

In this thesis, we have mainly used one and two port measurements using respectively a reflection and hanger geometry, shown in Figure 2.2. The transmission or reflection of an incident drive through these geometries can be described using a scattering matrix (often called S-matrix) linking the incoming and outgoing coherent field at each port of the device [46, 48, 44]:

$$\alpha_{\mathrm{out},j} = \sum_i S_{ji}\alpha_{\mathrm{in},i}. \tag{2.13}$$

These parameters can be experimentally obtained using a vector network analyser (VNA), since the incoming field at port i can be defined as $\alpha_{\mathrm{in},i} = (V_i + Z_c I_i)$ and the outgoing field at port i as $\alpha_{\mathrm{out},i} = (V_i - Z_c I_i)$, where V_i and I_i are the complex voltage and current amplitudes at port i when connected to a wave guide of impedance Z_c.

HANGER GEOMETRY In this geometry, the resonator is connected through a single element (for us a simple capacitor as depicted in Figure 2.3) to two transmission lines going to distinct ports 1 and 2. The symmetry in this probing geometry results in identical coupling of the resonator to each port: $\kappa_{p,1} = \kappa_{p,2} = \kappa_\mathrm{c}/2$. Using equations 2.10 and 2.12, the transmission through this device is thus [46, 47]:

$$S_{21}^{\mathrm{hanger}} = \left.\frac{\alpha_{out,2}}{\alpha_{in,1}}\right|_{\alpha_{in,2}=0} = 1 - \frac{\kappa_\mathrm{c}}{\kappa_\mathrm{c} + \kappa_\mathrm{int} - 2i\,(\omega - \omega_0)}. \tag{2.14}$$

REFLECTION GEOMETRY In this geometry, the resonator is connected to a single port $\kappa_{p,1} = \kappa_\mathrm{c}$ using a coupling element (here a capacitor). The reflection coefficient is then given by [46, 47]:

$$S_{11}^{\mathrm{refl}} = \frac{\alpha_\mathrm{out}}{\alpha_\mathrm{in}} = 1 - \frac{2\kappa_\mathrm{c}}{\kappa_\mathrm{t} - 2i\,(\omega - \omega_0)}. \tag{2.15}$$

INTRA-RESONATOR PHOTON NUMBER The input power of the drive applied to port i of the resonator is given by $P_{in} = \hbar\omega|\hat{a}_{\mathrm{in},i}|^2$, where $|a_{\mathrm{in},i}|^2$ describe a photon flux. The intra-resonator photon number at resonance $\bar{n}^{\mathrm{hanger}} = |\alpha|^2$ for each geometry is thus:

$$\bar{n}^{\mathrm{hanger}} = \frac{2\kappa_\mathrm{c}}{\hbar\omega_0\kappa_\mathrm{t}^2}P_\mathrm{in}, \tag{2.16}$$

and

$$\bar{n}^{\mathrm{refl}} = \frac{4\kappa_\mathrm{c}}{\hbar\omega_0\kappa_\mathrm{t}^2}P_\mathrm{in}. \tag{2.17}$$

2.0.3.1 *Coupling regimes*

In both hanger and reflection geometry, one expects to obtain a full transmission / reflection away from resonance. At resonance, however, the behaviour is governed by the ratio between coupling and intrinsic losses. We can distinguish three different regimes of coupling, illustrated in Figure 2.1 and described in the table below [50, 48, 51].

Table 2.1: Overview of the S-parameters behaviour for the reflection and hanger geometry at resonance.

	over coupled: $\kappa_c \gg \kappa_i \rightarrow \kappa_t \approx \kappa_c$	critically coupled: $\kappa_c \approx \kappa_i \rightarrow \kappa_t \approx \kappa_c/2$	under coupled: $\kappa_c \ll \kappa_i$
Reflection	$\lvert S_{11}\rvert \rightarrow 1$ and 2π phase shift	$\lvert S_{11}\rvert \rightarrow 0$, π phase shift	minimal response of $\lvert S_{11}\rvert$ and $\arg S_{11}$
Hanger	$\lvert S_{21}\rvert \rightarrow 0$, π phase shift	$\lvert S_{21}\rvert \rightarrow 0.5$, reduced phase shift	($\lvert S_{21}\rvert$, $\arg S_{21}$), width governed by κ_i

2.0.3.2 *Linking coupling and intrinsic rates to physical quantities*

It is interesting to relate this quantum-mechanical description of the resonator to the physical quantities describing the LC circuit and its environment. We consider the circuit shown in Figure 2.2, where the resonator is linked to one or two transmission lines of impedance Z_0 using a coupling capacitor C_c. We have also introduced a resistor R representing any resonator internal losses. The impedance of the circuit taken between point A in Figure 2.2 and the ground, considering each transmission line is terminated by a matched load, is [44]:

$$Z_t^{-1} = R^{-1} + iC\omega + (iL\omega)^{-1} + \left(Z_c + \frac{1}{iC_c\omega}\right)^{-1} \tag{2.18}$$

$$= R^{-1} + \underbrace{\frac{Z_c C_c^2 \omega^2}{1 + (Z_c C_c \omega)^2}}_{= R_{ext}^{-1}} + \underbrace{i\left(\omega\left[C + \frac{C_c}{1 + (Z_c C_c \omega)^2}\right] - (L\omega)^{-1}\right)}_{= Z'^{-1}_{reso}}. \tag{2.19}$$

For a reflection measurement, $Z_c = Z_0$ as only a single line is connected, whereas $Z_c = Z_0/2$ for the hanger geometry. In the approximation of small coupling such that $Z_c C_c \omega << 1$, the resonator resonance frequency is shifted to $\omega_0 = 1/\sqrt{L(C + C_c)}$ and its characteristic impedance to $Z = \sqrt{L/(C + C_c)}$. We find that in addition to the internal resistance of the LCR-resonator we can identify an additional resistance R_{ext} arising from the coupling to the transmission line(s) [46, 52].

Any LCR-resonator can furthermore be characterized by its quality factor Q, which can be either understood as the ratio between the stored energy and the energy loss per period or as the ratio of the resonator eigenfrequency and its bandwidth. For a parallel LCR-resonator, the quality factor is given by $Q = (R + R_{ext})\sqrt{C/L}$ and can be related to the total energy damping rate or coupling $Q_t = \omega_0/\kappa_t$. Here, we can also separate into an internal quality factor $Q_i = R \cdot \sqrt{(C + C_c)/L}$ and a coupling quality factor $Q_c = R_{ext} \cdot \sqrt{(C + C_c)/L}$.

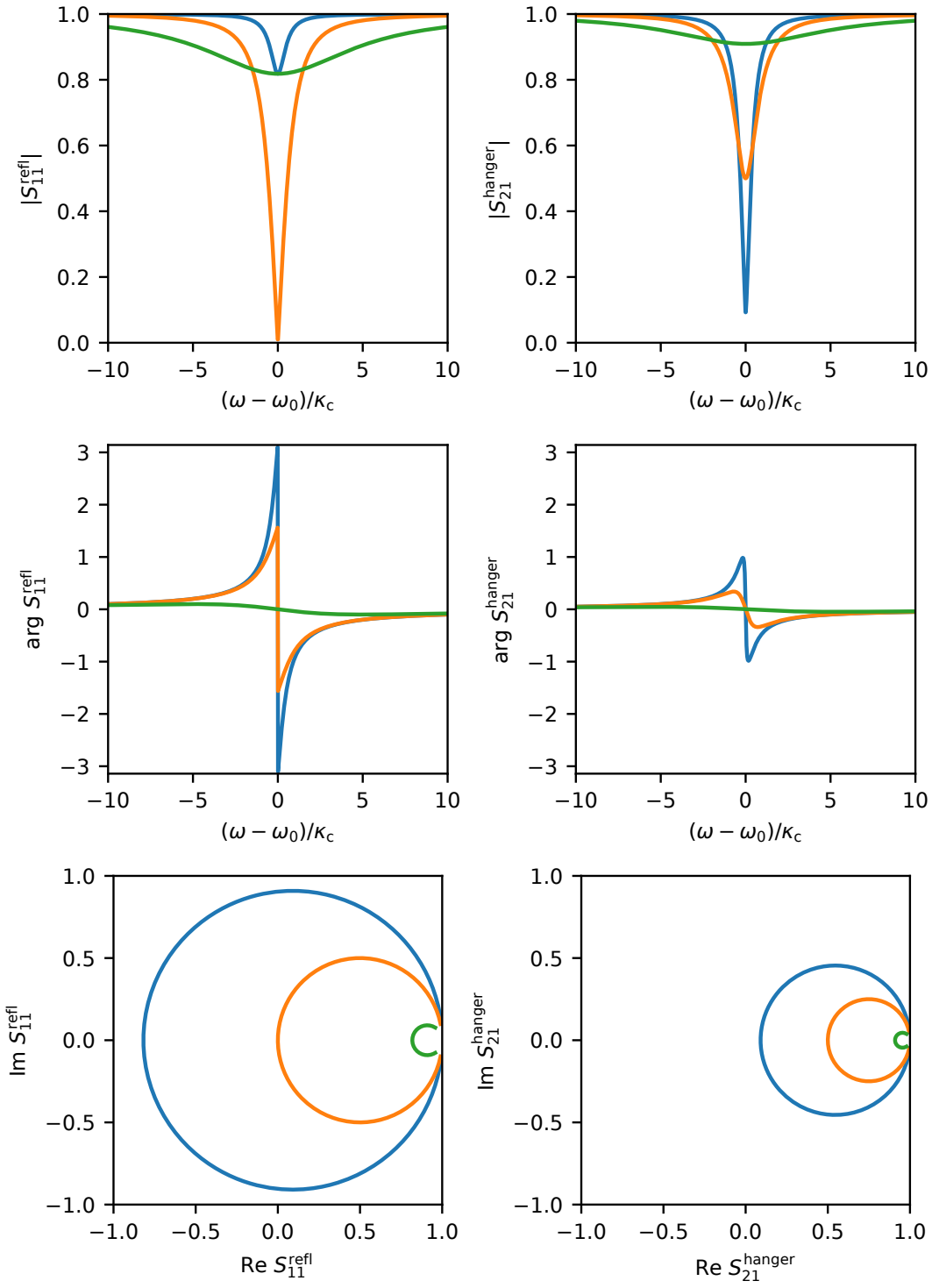

Figure 2.1: Absolute and phase for the S-parameters of a resonator measured in reflection (left) and hanger geometry (right) for the different coupling regimes (blue: over coupled, $\kappa_i = 0.1\kappa_c$; orange: critical coupled, $\kappa_i = \kappa_c$; green: under coupled, $\kappa_i = 10\kappa_c$)

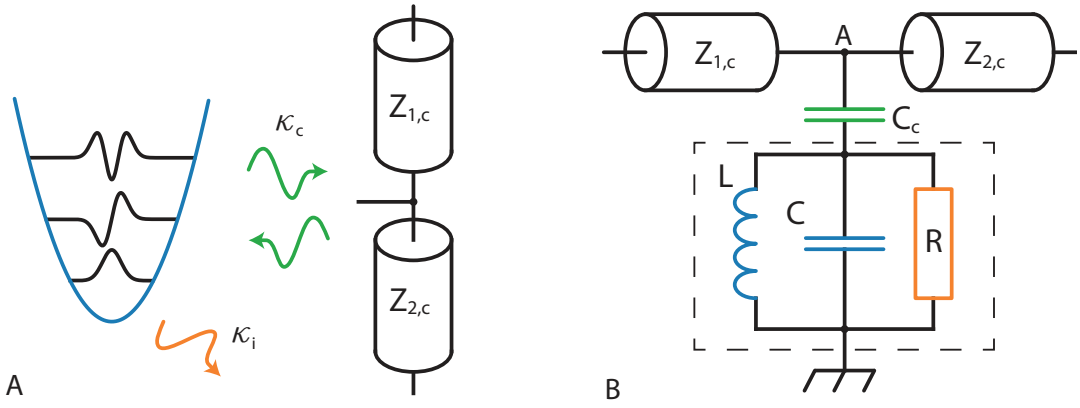

Figure 2.2: A: Schematic representation of a harmonic oscillator coupled to a transmission line. B: The LCR-resonator (dashed box) consisting of L, C and R is coupled to a transmission line having an impedance $Z_{1,c} = Z_{2,c}$ via C_c. The depicted circuit is adequate for a hanger transmission measurement. For a reflection measurement, the impedance $Z_{2,c}$ does not exist. [46, 50].

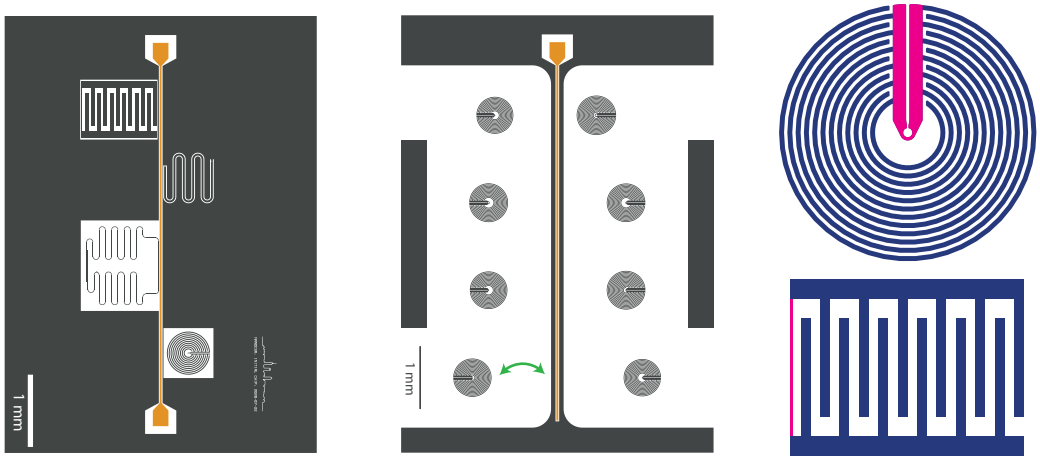

Figure 2.3: Left: The initial device (see Chapter 3) which consists of four resonators coupled capacitively to the transmission line (orange) measured in hanger geometry. The in/output are at the top/bottom. Middle: BDPA device (see Chapter 3) measures eight resonators in reflection. The strength of the coupling is adjusted by the distance (green) to the transmission line. Right: Two different resonator designs (top: circle resonator used in this thesis, bottom: interdigitated resonator) with the capacitative part (blue) and the inductive part (pink).

2.1 SUPERCONDUCTING RESONATORS

We are using superconducting thin films to realize the resonator circuit for the EPR experiments. Such experiments require a magnetic field which is going to affect not only the spin ensemble but also the superconducting microwave circuit. One of the most noticeable effects in our measurements is a shift of the resonator frequency with the magnetic field due to its kinetic inductance.

To understand the concept of kinetic inductance, it is sufficient to express the conductivity using the Drude model [53]. Within this framework, the conductivity is modelled as a gas of charge carriers with the density n, their charge e, mass m, and a mean time τ between scattering events. The conductivity is a complex and frequency dependent quantity $\sigma(\omega) = \sigma_1 - i\sigma_2$ and given by $\sigma = \frac{ne^2\tau}{m(1+i\omega\tau)}$. Separating this into the imaginary and real part gives

$$\sigma = \frac{ne^2\tau}{m(1+\omega^2\tau^2)} - i\frac{ne^2\omega\tau^2}{m(1+i\omega^2\tau^2)}. \tag{2.20}$$

For normal metals one finds that $\omega\tau$ is negligible for frequencies below 100 GHz and the conductance is the DC conductance $\sigma_{\mathrm{DC}} = \frac{ne^2\tau}{m}$ [53]. In the case of a superconductor $\tau \to \infty$ and thus the imaginary part cannot be neglected. The charge carriers are Cooper pairs: the mass of the charge carriers is $2m_{\mathrm{e}}$, the charge $2e$, and n_{s} is the density of the Cooper pairs or superconducting fluid. The imaginary part of the conductivity becomes $\sigma_2 = \frac{2n_{\mathrm{s}}e^2}{m_{\mathrm{e}}\omega}$.

To get a physical meaning of this non-vanishing imaginary conductance, one can first write the current density J_{s} in a superconducting volume of length l and of cross-section A as a response to an ac electrical field $E = E_0\cos(\omega(t))J_{\mathrm{s}}(\omega) = \sigma E = -i\sigma_2 E(\omega)$. If one reverts this expression into the time domain, it yields the first London equation:

$$\frac{\mathrm{d}}{\mathrm{d}t}J_{\mathrm{s}} = 2n_{\mathrm{s}}e^2/m_{\mathrm{e}}\omega E, \tag{2.21}$$

which can also be expressed using the London penetration depth

$$\lambda_{\mathrm{l}} = \sqrt{\frac{m_{\mathrm{e}}}{\mu_0 n_{\mathrm{s}}e^2}}. \tag{2.22}$$

so that $\mu_0\lambda_{\mathrm{l}}^2 dJ_{\mathrm{s}}/dt = E$. It thus becomes clear that this effect gives rise to an effective inductive behaviour in a superconducting strip.

To derive this inductance coming from the non-negligible kinetic energy of the Cooper pairs in the strip, we express the kinetic energy stored in the strip due to the movement of the Cooper pairs as:

$$E_{\mathrm{kin}} = \frac{1}{2}(n_{\mathrm{s}}lA)(2m_{\mathrm{e}})v_{\mathrm{s}}^2, \tag{2.23}$$

where v_{s} is the velocity of the Cooper pairs in the strip. The super-current density is also related to the movement of charge carriers by $J_{\mathrm{s}} = -2n_{\mathrm{s}}ev_{\mathrm{s}}$. For a thin film ($t << \lambda_l$), the current flows on the entire cross-section so that $I = 2An_{\mathrm{s}}ev_{\mathrm{s}}$ and thus [54]:

$$E_{\mathrm{kin}} = \frac{1}{2}\frac{lm_{\mathrm{e}}}{2An_{\mathrm{s}}e^2}I^2, \tag{2.24}$$

where we can identify the kinetic inductance

$$L_{\mathrm{kin}} = \frac{l m_{\mathrm{e}}}{2 A n_{\mathrm{s}} e^2} = \mu_0 \lambda^2 \frac{l}{A}. \tag{2.25}$$

Once an external magnetic field B is applied, the density of the superconducting fluid decreases and therefore the penetration depth increases as [55, 56]:

$$\lambda_{\mathrm{eff}}^{-1} = \lambda^{-1}(T) \left(1 - \alpha(T) \left(\frac{B}{B_{\mathrm{c}}(T)} \right)^2 \right). \tag{2.26}$$

Here α is a positive and temperature dependent constant and B_{c} the critical magnetic field. We can therefore see that the kinetic inductance of the superconductor is increasing quadratically with the applied field. Recalling the eigenfrequency of the resonator $\omega_0 = 1/\sqrt{LC}$ we expect a quadratic shift to lower frequencies when applying a magnetic field. Within Bardeen-Cooper-Schrieffer (BSC)-theory, the penetration depth in thin films can be related to the room-temperature film resistance

$$\lambda(T = 0) = \sqrt{\frac{\hbar \rho}{\mu_0 \pi \Delta}}, \tag{2.27}$$

where Δ is the energy gap [57]. The BCS-theory relates the energy gap at zero temperature to the critical temperature T_{c} of the material [57]:

$$\Delta(T = 0) = 1.76 k_{\mathrm{B}} T_{\mathrm{c}}. \tag{2.28}$$

Assuming the superconducting film behaves perfectly as predicted by the BCS theory, one can thus relate the critical temperature and the kinetic inductance.

The effect of an applied magnetic field on a superconducting film is dependent on whether the field is applied parallel to the film [57]. We thus expect the frequency of our resonator to vary as:

$$\frac{\omega}{\omega_0} = 1 - k_{\perp} B_{\perp}^2 - k_{\parallel} B_{\parallel}^2, \text{ with } k_{\perp} \gg k_{\parallel}. \tag{2.29}$$

2.2 QUANTUM-LIMITED LINEAR AMPLIFIER

The environment and the quantum regime in which the experiments take place naturally have a noise level which is lower than a room temperature detection apparatus. Thus, one needs to amplify the signal so that it can be detected at room temperature. However, every amplification step introduces some noise. In the following we will briefly discuss the amplifier noise limit imposed by quantum mechanics and the Josephson travelling wave parametric amplifier (JTWPA) we have used which enables detection close to this regime.

A transmission line can be seen as a continuum of bosonic travelling modes covering the entire spectrum [58]. A mode $\hat{a}$ has for quadrature operators:

$$\hat{I} = (\hat{a} + i\hat{a}^\dagger)/2, \tag{2.30}$$

$$\hat{Q} = (\hat{a} - i\hat{a}^\dagger)/(2i). \tag{2.31}$$

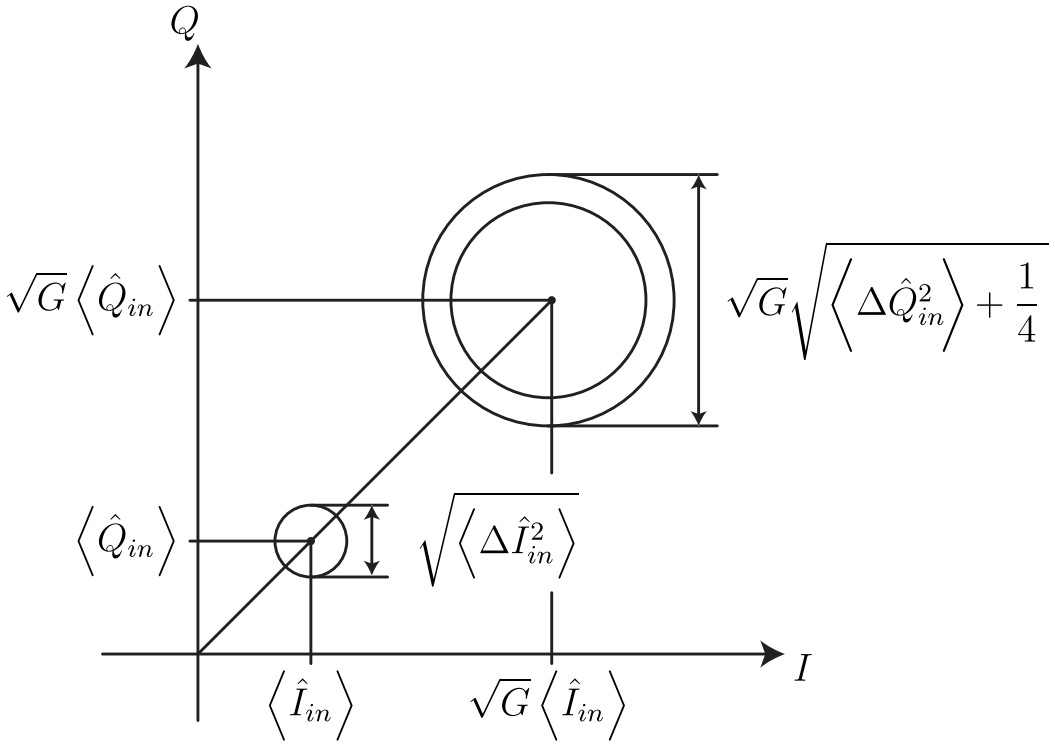

Figure 2.4: Phase preserving amplification

These quadratures can be measured using homodyne detection. The operators $\hat{I}$ and $\hat{Q}$ obey the commutation relation $\left[\hat{I}, \hat{Q}\right] = i/2$ and the Heisenberg uncertainty relation $\left\langle \Delta\hat{Q}^2 \right\rangle \left\langle \Delta\hat{I}^2 \right\rangle \geq 1/16$. When a mode is in its vacuum state, the variance of the quadratures are:

$$\left\langle \Delta\hat{Q}^2 \right\rangle = \left\langle \Delta\hat{I}^2 \right\rangle = 1/4, \tag{2.32}$$

and typically set what is called the standard quantum limit. These relations set a lower limit on the signal-to-noise ratio of an experiment using homodyne detection, and is important for the later understanding of the noise added by an amplifier. We can further describe a vacuum thermal state with

$$\left\langle \hat{Q} \right\rangle = \left\langle \hat{I} \right\rangle = 0, \tag{2.33}$$

$$\left\langle \Delta\hat{Q}^2 \right\rangle = \left\langle \Delta\hat{I}^2 \right\rangle = \frac{1}{4} + \frac{n_{\text{th}}}{2}, \tag{2.34}$$

with the average number of thermal photons $n_{\text{th}} = \frac{1}{\exp[(\hbar\omega)/(k_{\text{B}}T)]-1}$ is given by the temperature T of the microwave field following Boltzmann statistics [58]. We are going to work at $\approx 7\,\text{GHz}$ and $10\,\text{mK}$. These operating conditions give $n_{\text{th}} = 0.001$ and therefore place us in the quantum regime with little thermal excitation.

2.2.1 *Phase preserving amplification*

In general, one can distinguish between phase preserving and phase sensitive amplification. The former amplifying both quadratures equally, while the later ”discards”

information on one in favour of a noiseless amplification on the other. The amplifier used during this thesis is a phase preserving amplifier [58]. Naively, one could try to relate the in- and output fields by $\hat{Q}_{\text{out}} = \sqrt{G}\hat{Q}_{\text{in}}$ and $\hat{I}_{\text{out}} = \sqrt{G}\hat{I}_{\text{in}}$. This however only fulfils the commutation relation for the in- and output fields if the gain G is one [59, 58]. This problem can be circumvented by introducing an idler mode $\hat{b}$. We require that $\left[\hat{b}_{in}, \hat{b}_{in}^{\dagger}\right] = 1$, $\left[\hat{b}_{in}, \hat{a}_{in}^{\dagger}\right] = 0$, and $\left\langle \hat{b}_{\text{in}} \right\rangle = 0$. With this, the output field is $\hat{a}_{out} = \sqrt{G}\hat{a}_{in} + \sqrt{G-1}\hat{b}_{in}^{\dagger}$ and we find for the amplified signal [58]:

$$\left\langle \hat{Q}_{\text{out}} \right\rangle = \sqrt{G}\left\langle \hat{Q}_{\text{in}} \right\rangle \text{ and } \left\langle \hat{I}_{\text{out}} \right\rangle = \sqrt{G}\left\langle \hat{I}_{\text{in}} \right\rangle. \tag{2.35}$$

Using this description for amplification, let us look at the noise added by the amplification process [58]

$$\left\langle \Delta\hat{Q}_{\text{out}}^2 \right\rangle + \left\langle \Delta\hat{I}_{\text{out}}^2 \right\rangle = \underbrace{G\left[\left\langle \Delta\hat{Q}_{\text{in}}^2 \right\rangle + \left\langle \Delta\hat{I}_{\text{in}}^2 \right\rangle\right]}_{\text{input noise}} + \underbrace{(G-1)\left[\left\langle \Delta\hat{Q}_{b}^2 \right\rangle + \left\langle \Delta\hat{I}_{b}^2 \right\rangle\right]}_{\text{added noise}}. \tag{2.36}$$

In addition to the thermal noise which is already present on the input side, there is a second contribution due to the idler mode $\left\langle \Delta\hat{Q}_{b}^2 \right\rangle + \left\langle \Delta\hat{I}_{b}^2 \right\rangle$. Assuming that the added noise is equal on both quadratures $\left\langle \Delta\hat{I}_{b}^2 \right\rangle = \left\langle \Delta\hat{Q}_{b}^2 \right\rangle$ the Heisenberg uncertainty yields $\left\langle \hat{I}_{b}^2 \right\rangle \geq 1/4$, so that at high gain $G >> 1$, the above equation becomes

$$\left\langle \Delta\hat{I}_{\text{out}}^2 \right\rangle + \left\langle \Delta\hat{Q}_{\text{out}}^2 \right\rangle \geq G\left[\left\langle \Delta\hat{Q}_{\text{in}}^2 \right\rangle + \left\langle \Delta\hat{I}_{\text{in}}^2 \right\rangle + \frac{1}{2}\right]. \tag{2.37}$$

Therefore, we conclude that in the best-case scenario, the phase-preserving amplifier adds 1/4 of a noise photon for each quadrature of the signal upon its amplification, as predicted by Caves [60]. Fulfilling the above inequality is called operating at the quantum-limit.

In addition to the typical metrics used for an amplifier (gain, bandwidth, saturation power, ect.), an amplifier operating near the quantum limit is characterized either by the number of noise photons $N_{\text{A}} > 1/2$ it adds to the output (giving $\left\langle \Delta\hat{I}_{b}^2 \right\rangle$), or by its noise temperature $T_{\text{A}} = \hbar\omega N_{\text{A}}/k_{\text{B}}$.

2.2.2 *Quantum efficiency*

We now consider a signal emitted on mode a_{in}, amplified by such an amplifier, and detected via homodyne measurement. We introduce the quantum efficiency, which compares the noise added by the amplification chain to a vacuum input state, to the situation of noiseless amplification:

$$\eta = \frac{1/2}{1/2 + n_{\text{a}}} \tag{2.38}$$

For a phase-preserving amplifier operating at the quantum-limit with microwave fields thermalized perfectly to their ground state, this efficiency reaches a maximum of

50%. The quantum efficiency can be used to express the noise at the output of the amplification chain. Indeed, we find:

$$\left\langle \Delta a_{\text{out}}^2 \right\rangle = \frac{G}{\eta}\left(\frac{1-\eta}{2} + \eta \left\langle a_{\text{in}}^2 \right\rangle\right). \tag{2.39}$$

We finally relate η to the SNR of a measurement. a_{in} is amplified on mode a_{out}, and gives rise to a record $a_{\text{out}}(t)$ after detection and digitization. The integrated signal $\langle a_{\text{out}} \rangle$ can be calculated using $\langle a_{\text{out}} \rangle = \int_t a_{\text{out}}(t) u(t) \mathrm{d}t$, where $u(t)$ is a filter function giving the window of integration and is normalized to $\int |u|^2 = 1$. The SNR of this measurement is thus given by:

$$\text{SNR} = \frac{\sqrt{G}\,\langle a_{\text{in}} \rangle}{\sqrt{\left\langle \Delta a_{\text{out}}^2 \right\rangle}}. \tag{2.40}$$

Assuming a_{in} is a displaced vacuum state (i.e., $\left\langle \Delta a_{\text{in}}^2 \right\rangle = 0$), we can therefore simply express the SNR as

$$\text{SNR} = \sqrt{2\eta}\,\langle a_{\text{in}} \rangle\,. \tag{2.41}$$

2.2.3 *Josephson travelling wave parametric amplifier*

The phase-preserving amplifier we used in this thesis is a Josephson Travelling Wave Parametric Amplifier (JTWPA) developed and supplied by the Lincoln Labs [61, 62]. Parametric amplification is based on driving a non-linear medium using a pump tone at frequency f_{p} to create a mixing process resulting in the amplification of an incoming signal tone at frequency f_{s}. Through the mixing process, a third so-called idler tone f_{i} is generated. One distinguishes between a three wave mixing, where $f_{\text{p}} = f_{\text{s}} + f_{\text{i}}$ and four wave mixing, where $2f_{\text{p}} = f_{\text{s}} + f_{\text{i}}$. This amplification process, if done through a lossless medium, can provide amplification at the quantum-limit such as described above.

Analogue to non-linear crystals in optics, one can engineer non-linear meta-materials to enable the required mixing. In the case of the JTWPA, this is done by creating a transmission line using a series of Josephson junctions to generate the needed non-linearity. It is then necessary to ensure that the wave-vectors of the signal, idler and pump modes are also matched to ensure the amplification process occurs along the entirety of the transmission line. Since a microwave transmission line has a linear dispersion relation at the considered frequency band, this matching occurs naturally at low pump powers: $2k_{\text{p}} - k_{\text{s}} - k_{\text{i}} \approx 0$. However, the non-linearity introduces deviations to the dispersion relation:

$$\Delta k = 2k_{\text{p}} - k_{\text{s}} - k_{\text{i}} - 2k_{\text{p}}\kappa_{\text{nl}}, \tag{2.42}$$

where $2k_{\text{p}}\kappa_{\text{nl}}$ is a power dependent phase shift. To achieve the best possible amplifier gain, one needs to ensure that $\Delta k = 0$. This can be done by engineering the dispersion relation either by means of a spatial impedance modulation or via resonant elements in the transmission line. The latter approach creates a stop-band gap and placing the

pump tone in its vicinity enables an increase in k_p compensating the power dependent term in equation 2.42. The JTWPA used in this thesis uses the above approach. It can provide $\approx 20\,\mathrm{dB}$ of gain on a bandwidth of a few GHz centred on the dispersive bandgap. Its noise temperature is close to the quantum-limit, with 0.6 added noise photons and a quantum efficiency of $\eta = 0.38$ [62].

2.3 SPINS SYSTEMS IN MAGNETIC FIELD

We now turn to the description of a spin ensemble that will interact with the described LC-resonator in the context of EPR experiments.

Ignoring any internal structure, the magnetic moment of an ideal electronic spin is given by $\hat{\boldsymbol{\mu}} = g\frac{\mu_B}{\hbar}\hat{\mathbf{S}}$, where μ_B is the Bohr magneton, $\hat{\mathbf{S}} = \left(\hat{S}_x, \hat{S}_y, \hat{S}_z\right)$ are the spin angular momentum operators, and g is a dimensionless quantity called the g-factor. For a perfect spin-1/2, $g = 2.002318$. The interaction of the spin with a static magnetic field $\mathbf{B}_0$ results in the Zeeman Hamiltonian $\hat{H}_Z = -\hat{\boldsymbol{\mu}} \cdot \mathbf{B}_0$. When considering a spin embedded in a structure, other phenomena contribute to the spin Hamiltonian [63, 64].

G-TENSOR ANISOTROPY When the unpaired electron giving rise to a spin is embedded into a crystal or a molecule, the Zeeman Hamiltonian can be anisotropic due to the symmetry of the host matrix, or due to spin-orbit coupling. It results in a more complex Zeeman Hamiltonian $\hat{H}_s = \frac{\mu_B}{\hbar}\mathbf{B}_0^T \cdot \mathbf{g} \cdot \hat{\mathbf{S}}$, where $\mathbf{g}$ is now a tensor (called the g-tensor) with 6 independent variables. Due to this asymmetry, the spin quantization axis may not be aligned to the magnetic field. The effect of different symmetries in the g-tensor are shown for a powder spectrum in Figure 2.5 [65]. For most complexes, one can, however, eliminate the cross terms in the g-tensor and express the Hamiltonian using an effective g-factor g_eff assuming a magnetic field aligned along the z-axis:

$$\hat{H}_\mathrm{S} = \frac{\mu_B}{\hbar} g_\mathrm{eff} B_\mathrm{z} \hat{S}_\mathrm{z}. \tag{2.43}$$

HYPERFINE COUPLING. A dipole-dipole coupling between the electron and nuclear spin gives rise to a hyperfine interaction

$$\hat{H}_\mathrm{HF} = \hat{\mathbf{I}}\mathbf{A}\hat{\mathbf{S}}, \tag{2.44}$$

where $\mathbf{A}$ describes the anisotropic coupling between the nucleus and the electronic spin. This interaction can lead to zero-field splitting in the energy levels of the spin system [64].

Assuming the spin Hamiltonian is known, it is possible to compute the energy-levels and eigenstates of the spin system. Among these states, it is possible to isolate a two-level system $\{|\uparrow\rangle, |\downarrow\rangle\}$ with transition frequency $\hbar\omega_\mathrm{s}$ [64]. Introducing the Pauli matrices:

$$\hat{\sigma}_x = \begin{pmatrix} 0 & 1 \\ 1 & 0 \end{pmatrix}, \; \hat{\sigma}_y = \begin{pmatrix} 0 & -i \\ i & 0 \end{pmatrix}, \; \hat{\sigma}_z = \begin{pmatrix} 1 & 0 \\ 0 & -1 \end{pmatrix} \tag{2.45}$$

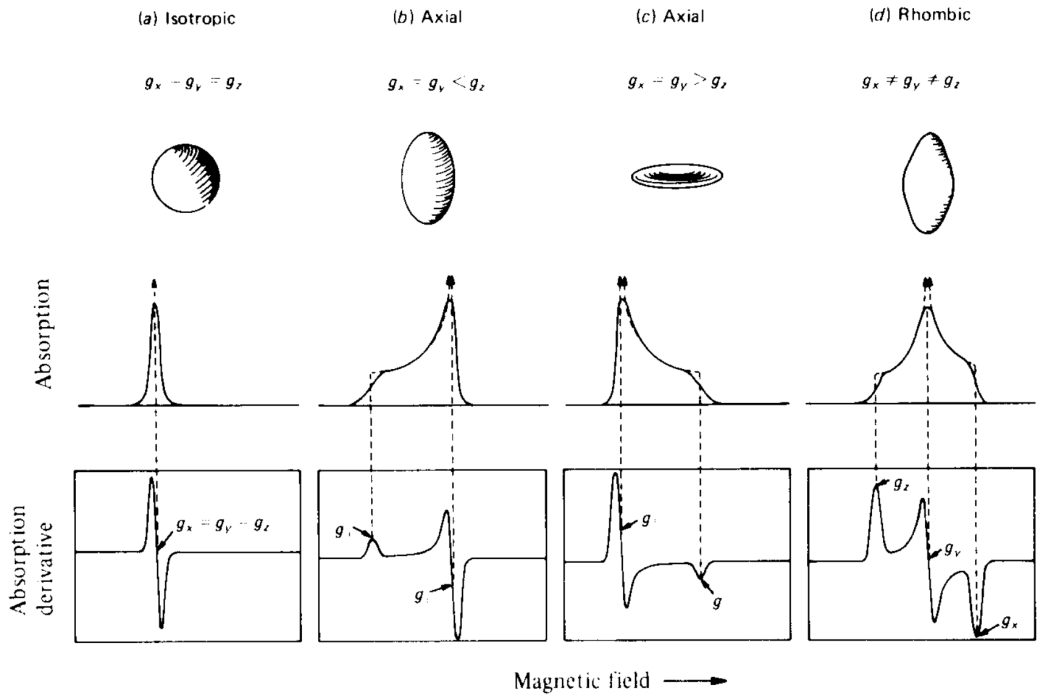

Figure 2.5: Continuous wave EPR absorption spectra for different g-tensor symmetries on powder samples. For a powder sample, the spectrum is the average of all orientations. Figure taken from [65].

we can express $\hat{S} = \hbar/2\,(\hat{\sigma_{\mathrm{x}}}, \hat{\sigma_{\mathrm{y}}}, \hat{\sigma_{\mathrm{z}}})$. The spin Hamiltonian in the basis $\langle |\uparrow\rangle, |\downarrow\rangle\rangle$ can thus be simplified to:

$$H_{\mathrm{S}} = \frac{\hbar\omega_{\mathrm{s}}}{2}\sigma_z. \tag{2.46}$$

2.4 SPINS COUPLED TO A RESONATOR

The spin interacts with the resonator through its AC magnetic field $\hat{\mathbf{B}}_1$. Using equation 2.43, we can thus express the interaction Hamiltonian as

$$\hat{H}_{\mathrm{int}} = \frac{\mu_{\mathrm{B}}}{\hbar}\hat{\mathbf{B}}_1 \cdot \mathbf{g} \cdot \hat{\mathbf{S}} = \frac{\mu_B}{\hbar}\delta\mathbf{B}(r) \cdot \mathbf{g} \cdot \hat{\mathbf{S}}\left(\hat{a} + \hat{a}^\dagger\right). \tag{2.47}$$

Restricting the analysis to the two-level system $\{|\uparrow\rangle, |\downarrow\rangle\}$ identified above, the interaction Hamiltonian in the spin-basis takes the form [66]

$$\hat{H}_{\mathrm{int}} = \hbar\left(\hat{a} + \hat{a}^\dagger\right)\left(\alpha_\uparrow |\uparrow\rangle\langle\uparrow| + \alpha_\downarrow |\downarrow\rangle\langle\downarrow| + \hbar g_0\left[\hat{\sigma}_+ + \hat{\sigma}_-\right]\right). \tag{2.48}$$

where $\hat{\sigma}_\pm = \frac{1}{2}\left(\hat{\sigma}_x \pm i\hat{\sigma}_y\right)$ and we define

$$\alpha_\uparrow = \frac{\mu_B}{\hbar}\delta\mathbf{B} \cdot g \cdot \langle\uparrow|\hat{\mathbf{S}}|\uparrow\rangle, \qquad \alpha_\downarrow = \frac{\mu_B}{\hbar}\delta\mathbf{B} \cdot g \cdot \langle\downarrow|\hat{\mathbf{S}}|\downarrow\rangle, \tag{2.49}$$

$$\hbar g_0 = \frac{\mu_B}{\hbar}\delta\mathbf{B} \cdot g \cdot \langle\uparrow|\hat{\mathbf{S}}|\downarrow\rangle, \qquad \hbar g_0^* = \frac{\mu_B}{\hbar}\delta\mathbf{B} \cdot g \cdot \langle\downarrow|\hat{\mathbf{S}}|\uparrow\rangle. \tag{2.50}$$

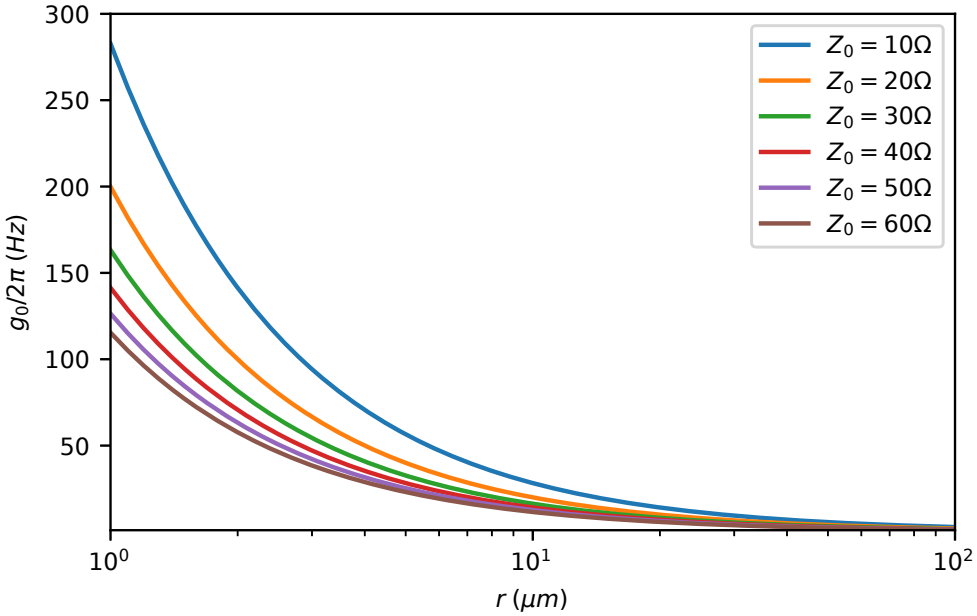

Figure 2.6: Resonator to spin coupling of a spin 1/2 and a resonator frequency of 7 GHz for different spin-wire distances and resonator impedances.

The basis $\{|\uparrow\rangle, |\downarrow\rangle\}$ can be redefined such that $g_0 = g_0^*$ [66]. The interaction Hamiltonian can then be treated as a time-dependent perturbation to the Zeeman and bare resonator Hamiltonian, and fast-rotating terms can be neglected. Performing this so-called rotating wave approximation yields the following interaction Hamiltonian in the Schrödinger picture:

$$\hat{H}_\mathrm{i} = \hbar g_0 \left(\hat{\sigma}_+ \hat{a} + \hat{\sigma}_- \hat{a}^\dagger \right), \tag{2.51}$$

which is the Jaynes-Cummings Hamiltonian [67]. The isolated total system thus has for Hamiltonian:

$$\hat{H}_\mathrm{tot} = \hbar\omega \left(\hat{a}^\dagger \hat{a} + \frac{1}{2} \right) + \frac{\hbar}{2} \omega_\mathrm{s} \hat{\sigma}_\mathrm{z} + \hbar g_0 \left(\hat{\sigma}_+ \hat{a} + \hat{\sigma}_- \hat{a}^\dagger \right). \tag{2.52}$$

We note that the interaction term allows for the swap of an excitation from the spin to the resonator and vice versa. If the system starts with a spin initially in the excited state and the cavity in the vacuum state $|e, 0\rangle$, the spin-resonator system will evolve according to

$$|\Psi(t)\rangle = \cos\left(\frac{\Omega}{2} t\right) |e, 0\rangle - i \sin\left(\frac{\Omega}{2} t\right) |g, 1\rangle, \tag{2.53}$$

describing the coherent exchange of the excitation between the spin and the resonator. This phenomenon is known as Rabi-oscillation, and $\Omega = 2g_0$ is the Rabi frequency. Without damping or coupling to the outside, this oscillation would continue indefinitely.

The spin–resonator coupling g_0 plays, as mentioned before, an important role in the sensitivity of the EPR setup, and we are now in the position to give a first estimate for

it. We are considering the spin 1/2 at a distance r to the inductor, and using equation 2.8, we find:

$$\frac{g_0}{2\pi} = \frac{g\mu_B}{h}\delta B \langle\uparrow|\hat{S}/\hbar|\downarrow\rangle = \frac{g\mu_B}{h}\frac{\mu_0\omega_0}{4\pi r}\sqrt{\frac{\hbar}{2Z_0}}. \tag{2.54}$$

Therefore, for a spin 1/2 with $g = 2$ sitting at a distance of $r \approx 1\,\mu m$ to the inductor of the resonator with an eigenfrequency of $\omega_0/2\pi \approx 7\,GHz$ and an impedance, of $Z_0 \approx 50\,\Omega$ we find $g_0/2\pi \approx 130\,Hz$ or at a distance $r \approx 10\,\mu m$ a coupling of $\approx 13\,Hz$. We further notice that the lower the impedance, the stronger the coupling, as illustrated in Figure 2.6.

2.4.1 *Single spin coupling to a resonator*

2.4.1.1 *Dynamics of the spin-resonator system*

We now want to consider what happens when the resonator is coupled to the environment. For the resonator, this is described by the previously discussed energy damping rate κ_t. In other words, a photon in the resonator has a lifetime of $1/\kappa_t$ during which it may interact with the spin.

The spin, on the other hand, is loosing its coherence at a rate $\Gamma_2 = 1/T_2$, with the two contributions of de-phasing and relaxation $\Gamma_2 = 1/T_\phi + 1/(2T_1)$.

- For $g_0 \gg \kappa_t,\ \Gamma_2$ one can observe Rabi-oscillations as they happen faster than the spin is loosing its coherence or the resonator looses the photon. This is called the strong coupling regime.
- For $g_0 \ll \kappa_t,\ \Gamma_2$ the damping of the resonator and the coherence loss of the spin happen faster than the Rabi-oscillation, which thus cannot be observed in the so-called weak coupling regime.

For resonators at $\omega_0/(2\pi) = 7\,GHz$ with quality factors of the order of 10^5 and the above estimated g_0 we find that $g_0/2\pi \approx 10\,Hz \ll \kappa_t/2\pi \approx 100\,kHz$ and we are thus operating in the weak coupling regime.

2.4.1.2 *Resonator-induced relaxation: Purcell effect*

In the weak coupling regime, the resonator has nonetheless an impact on the spin dynamics: the presence of the resonator leads to an enhancement of the relaxation of the spin by emission of photons into the cavity. This was first described by Purcell, Torrey, and Pound [4] in 1946 and recently shown for a spin donor in bismuth coupled to a superconducting circuit in [52] and [48]. The Purcell rate is given by

$$\Gamma_P(\Delta) = \frac{g_0^2\kappa_t}{\kappa_t^2/4 + \Delta^2}, \tag{2.55}$$

where $\Delta = \omega_0 - \omega_s$ [66]. Spin measurements are mostly performed at resonance, such that $\Gamma_P(0) = 4g_0^2/\kappa_t$. For $g_0/2\pi = 30\,Hz$ and $\kappa_t/(2\pi) = 100\,kHz$, we find $1/\Gamma_P(0) = 4.4\,s$, which makes it relevant for measurements realized at cryogenics temperatures since the spin relaxation rates generally decreases dramatically at low temperatures.

2.4.1.3 *Driven spin-resonator system*

In an EPR experiment, the spins are driven through the resonator. We thus now consider the effect of a drive on the system. Assuming a coherent state is sent on one of the ports coupling to the resonator, the drive Hamiltonian is $H_d = -i\hbar\sqrt{\kappa_\mathrm{p}}(\alpha_\mathrm{in}\hat{a}^\dagger e^{-i\omega_\mathrm{d}} + \alpha_\mathrm{in}^\star \hat{a}^\dagger e^{i\omega_\mathrm{d}})$ where α_in and ω_d are the amplitude and the frequency of the drive [48]. The state of the system at the time t is described by its density matrix $\rho(t)$. Using the Lindblad equation, the evolution of ρ is given by:

$$\dot{\rho} = -\frac{i}{\hbar}[\hat{H}_\mathrm{tot} + \hat{H}_\mathrm{d}, \rho] + \sum_i \mathcal{L}_i[\rho] \tag{2.56}$$

where $\mathcal{L}_i[\rho]$ are superoperators and describe the interaction of the spin-resonator system with the environment, assuming these processes are Markovian [51]. They are defined as $\mathcal{L}_i[\rho] = L_i\rho L_i^\dagger - \frac{1}{2}(L_i^\dagger L_i\rho + \rho L_i^\dagger L_i)$, where L_i are Lindblad jump operator. In the spin-resonator system, four Lindblad jump operators can be introduced [68, 48]:

INTRINSIC NON-RADIATIVE RELAXATION The corresponding jump operators are $L_{\mathrm{NR}\text{-}} = \sqrt{\Gamma_{\mathrm{NR}\text{-}}}\hat{\sigma}_\text{-}$ and $L_{\mathrm{NR}+} = \sqrt{\Gamma_{\mathrm{NR}+}}\hat{\sigma}_+$, where $\Gamma_{\mathrm{NR}\text{-}}$ and $\Gamma_{\mathrm{NR}+}$ are defined so that $\Gamma_{\mathrm{NR},0} = \Gamma_{\mathrm{NR}\text{-}} - \Gamma_{\mathrm{NR}+}$ is the intrinsic non-radiative relaxation at zero temperature. For spins in solids, it is most likely governed through interaction with phonons. The effective temperature of the bath setting the relaxation is considered by including both $L_{\mathrm{NR}\text{-}}$ and $L_{\mathrm{NR}+}$ and is given by $e^{-\hbar\omega_\mathrm{s}/(k_\mathrm{B}T_\mathrm{bath})} = \Gamma_{\mathrm{NR}+}/\Gamma_{\mathrm{NR}\text{-}}$. The effective relaxation considering the finite temperature of the bath is $\Gamma_\mathrm{NR} = \Gamma_{\mathrm{NR}\text{-}} + \Gamma_{\mathrm{NR}+}$.

RADIATIVE RELAXATION The corresponding Purcell jump operators are $L_{P-} = \sqrt{\Gamma_\mathrm{P}(1+n_\mathrm{th})}\hat{\sigma}_\text{-}$ and $L_{1+} = \sqrt{\Gamma_\mathrm{P} n_\mathrm{th}}\hat{\sigma}_+$, where n_th is the thermal occupancy of the resonator and is given by $n_\mathrm{th} = 1/(e^{\hbar\omega_0/(k_\mathrm{B}T)} - 1)$.

DE-PHASING The spin de-phasing is taken into account by introducing $L_{P-} = \sqrt{1/(2T_\phi)}\hat{\sigma}_\mathrm{z}$

2.4.2 *Bloch equations*

We now consider the effect of a coherent drive of amplitude β on the spin-resonator system in the weak coupling regime. In the absence of spins, the resonator field would reach the mean-value of $\alpha = 2\sqrt{\kappa_\mathrm{p}}\alpha_\mathrm{in}/(\kappa_\mathrm{t} - 2i(\omega_\mathrm{d} - \omega_0))$. In presence of spins, the resonator field can therefore be written as $\hat{a} = \alpha + \hat{b}$. Since the coupling is weak, one can proceed to the adiabatic elimination of $\hat{b}$ within the quantum optics framework. This is derived in [49, 48].

The derivation leads to the following master equation in the frame of the drive and effective Hamiltonian for the system reduced to the spin system:

$$\dot{\rho}_\mathrm{s} = -i\left[\hat{H}_\mathrm{eff}, \rho_\mathrm{s}\right] + \sum_i \mathcal{L}_i[\rho_\mathrm{s}], \tag{2.57}$$

$$\hat{H}_\mathrm{eff} \approx \hbar\frac{\Delta_\mathrm{s}}{2}\hat{\sigma}_\mathrm{z} + g_0\left(\alpha\hat{\sigma}_+ + \alpha^*\hat{\sigma}_\text{-}\right). \tag{2.58}$$

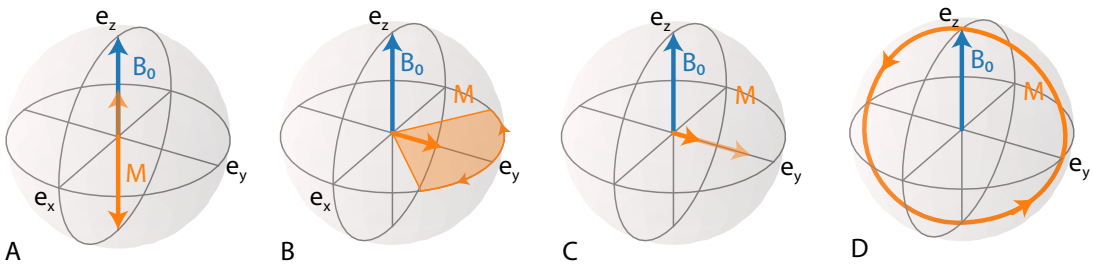

Figure 2.7: A: The time T_1 describes how long it takes for the z-component of the magnetization to relax back after an excitation. B: De-fanning in the xy-plane at the rate Γ_{inh} due to de-phasing. C: The spin de-cohering with the time T_2. D: Continuous drive for $\Delta = 0$ and an initial magnetization in e_z direction.

where $\Delta_s = \omega_s - \omega_d$. We also define $\Delta_0 = \omega_0 - \omega_d$.

Using this derivation enables to recover the semi-classical equations of motion for the spin observables and the resonator field. We define the magnetization vector $\mathbf{M} = (M_x, M_y, M_z)$ where $M_i = \text{Tr}\left(\hat{\rho}_s \hat{\sigma}_i\right) = \langle \hat{\sigma}_i \rangle$:

$$\frac{d}{dt}\mathbf{M} = \begin{pmatrix} -\Gamma_2 & \Delta & -2g_0\text{Im}(\alpha) \\ -\Delta & -\Gamma_2 & -2g_0\text{Re}(\alpha) \\ 2g_0\text{Im}(\alpha) & 2g_0\text{Re}(\alpha) & -\Gamma_1 \end{pmatrix} \cdot \mathbf{M} - \begin{pmatrix} 0 \\ 0 \\ \Gamma_1 \langle \hat{\sigma}_z \rangle_{\text{eq}} \end{pmatrix} \tag{2.59}$$

We recover the so-called Bloch equations [3]. Neglecting all relaxations, one can identify that the application of a drive induces rotation of the spin at frequency $\Omega_R = \sqrt{\Delta^2 + (2g_0\alpha)^2}$. Applying a pulse of amplitude α and duration t_p at resonance create a rotation of angle $2g_0\alpha t_p$ around an axis set by the phase of the drive. Both the longitudinal relaxation $\Gamma_1 = (\Gamma_{NR} + \Gamma_P(1 + 2n_{\text{th}})) = 1/T_1$ and the transversal relaxation $\Gamma_2 = \Gamma_\phi + \Gamma_1/2 = 1/T_2$ are modified by the Purcell rate Γ_P. The term $-\Gamma_1$ is showing that the z-component of the magnetic field is decaying towards the thermal equilibrium $\langle \hat{\sigma}_z \rangle_{\text{eq}}$. The relation between the resonator field and the Bloch equations is given by

$$\langle \hat{a} \rangle = \alpha - \frac{i2g_0}{\kappa_t + 2i\Delta_0} \langle \hat{\sigma}_- \rangle . \tag{2.60}$$

At this point, one can visualize both relaxations on the Bloch-sphere as shown in Figure 2.7.

2.4.3 *From single spin to a spin ensemble*

Up to now we have discussed a single spin which is coupled to a resonator. An EPR experiment, however, involves an ensemble of spins. Assuming all the spins to be identical in frequency, and have identical coupling to the resonators, they can be described using collective spin operators $\hat{\mathcal{S}}_j = \sum_{i=1}^{N} \hat{\sigma}_j^{(i)}$ obtained from the individual

spin Pauli operators $\hat{\sigma}_j^{(i)}$. The spins-resonator system can then be described by the Tavis-Cummings Hamiltonian [69, 70]:

$$\hat{H}/\hbar = \omega_0 \hat{a}^\dagger \hat{a} + \frac{\omega_s}{2}\mathcal{S}_z + \ g_0 \left(\hat{\mathcal{S}}_+ \hat{a} + \hat{\mathcal{S}}_- \hat{a}^\dagger\right). \tag{2.61}$$

However, assuming N absolutely identical spins does not account for the reality of the experiment. First, as all spins have a slightly different environment, they have different resonance frequencies: this effect is called inhomogeneous broadening [64]. Furthermore, their interaction with the resonator depends on the relative strength of the AC magnetic field of the resonator at their position. To consider these spreads in frequencies and in couplings, we will divide the spin ensemble in M families containing N_m spins each. Each family has collective spin operators $\hat{\mathcal{S}}_j^m$, detuning Δ_s^m to the drive frequency, and coupling strength g_0^m. We assume all spin families have the same intrinsic decay rate Γ_{NR} and the same intrinsic de-phasing rate Γ_ϕ. However, each family may be subject to a distinct Purcell rate $\Gamma_{\text{P}}(\Delta_s^m - \Delta_0)$. We make the assumption that no coupling between families exists, and we include a drive applied on to the resonator.

Similarly to equation 2.56, one can write the master equation for considering the resonator and each spin family dynamics in the reference frame of the drive:

$$\dot{\rho} = \left[\hat{H}_{\text{coll}}, \rho\right] + \sum_{m=1}^{M} \hat{L}_j^m \rho, \text{with} \tag{2.62}$$

$$\hat{H}_{\text{coll}}/\hbar = \Delta_0 \hat{a}^\dagger \hat{a} + \sum_{m=1}^{M} \frac{1}{2}\Delta_s^m \hat{\mathcal{S}}_z^m + \sum_{m=1}^{M} g_{\text{m}} \left(\hat{\mathcal{S}}_+^m \hat{a} + \hat{\mathcal{S}}_-^m \hat{a}^\dagger\right) + \hat{H}_{\text{d}} \tag{2.63}$$

From this master equation, the dynamics of the mean-values of the spin collective operators for one family are given by:

$$\dot{S}_{\text{x}}^m = -\Delta_s S_{\text{y}}^m - \Gamma_2 S_{\text{x}}^m - 2g_m S_{\text{z}}^m Y \tag{2.64}$$

$$\dot{S}_{\text{y}}^m = +\Delta_s S_{\text{x}}^m - \Gamma_2 S_{\text{y}}^m - 2g_m S_{\text{z}}^m X \tag{2.65}$$

$$\dot{S}_{\text{z}}^m = 2g_m S_{\text{x}}^m Y + 2g_m S_{\text{y}}^m X - \Gamma_1 (S_{\text{z}}^m - S_{\text{z,eq}}) \tag{2.66}$$

$$\tag{2.67}$$

where for clarity we have simplified the $\left\langle \hat{S}_i^m \right\rangle$ to S_i^m and introduced the quadrature operators for the resonator field: $\hat{X} = (\hat{a} + \hat{a}^\dagger)/2$ and $\hat{Y} = (\hat{a} - \hat{a}^\dagger)/(2i)$. These equations are nothing but the generalization to a spin ensemble of the Bloch equations derived above, with $S_{z,eq}^m$ the equilibrium value of the magnetization for each spin family, equivalently defined by the polarization of the spin ensemble $S_{\text{z,eq}} = -pN_m$. To obtain the above derivation, we have made the approximation that each spin family was in the weak coupling regime so that cross-products such as $\left\langle \hat{S}_{\text{z}}^m \hat{Y} \right\rangle$ are well approximated by $\left\langle \hat{S}_{\text{z}}^m \right\rangle \left\langle \hat{Y} \right\rangle$. This approximation is analogous in this case to performing a Holstein–Primakoff approximation, where the spin collective operators S_- and S_+ are approximated to bosonic operators [71, 72].

The dynamics of the resonator field operator is given by:

$$\dot{a} = -i\Delta_0 a - \frac{\kappa_\mathrm{t}}{2}a - \sqrt{\kappa_\mathrm{p}}\beta - i\sum_{m=1}^{M} g_m S_-^m. \tag{2.68}$$

These equations can be used to simulate the spin dynamics when using typical EPR sequences. In this thesis, these simulations were implemented in Julia and are shown in Chapter 6.

STEADY-STATE REGIME In our attempts to detect short-lived spin species, we have performed continuous-wave EPR experiments. The resonator response is modified in the presence of the spins, and measuring this deviation enables to determine the presence of the spins, their energy relaxation rate, and their inhomogeneous line-width. The deviation can be expressed by calculating the steady-state solution of the expressions above. For the spin-collective ensemble, this results in:

$$S_{\mathrm{x,ss}}^m = \frac{2g_m/\Gamma_2(X + \delta/\Gamma_2 Y)}{1 + (\Delta_s^m/\Gamma_2)^2 + \frac{4g_m^2}{\Gamma_2\Gamma_1}\bar{n}} pN_m \tag{2.69}$$

$$S_{\mathrm{y,ss}}^m = \frac{2g_m/\Gamma_2(Y - \delta/\Gamma_2 X)}{1 + (\Delta_s^m/\Gamma_2)^2 + \frac{4g_m^2}{\Gamma_2\Gamma_1}\bar{n}} pN_m \tag{2.70}$$

$$S_{\mathrm{z,ss}}^m = -\frac{1 + (\Delta_s^m/\Gamma_2)^2}{1 + (\Delta_s^m/\Gamma_2)^2 + \frac{4g_m^2}{\Gamma_2\Gamma_1}\bar{n}} pN_m \tag{2.71}$$

where we recall that $\bar{n}$ is the intra-resonator photon number. One can recognize in these equations the Bloch equations as typically expressed in magnetic resonance by setting $X = 0$ and $\omega_1 = -2g_m Y$, where ω_1 is the drive Rabi frequency. In particular, the term $\frac{4g_m^2}{\Gamma_2\Gamma_1}\bar{n}$ expresses the saturation of the spin ensemble by the drive, which will eventually lead to vanishing magnetization, and thus an absence of interaction of the spins with the resonator.

Using that $\dot{S}_-^m = -(\Gamma_2 + i\Delta_s^m)S_-^m + igS_\mathrm{z}^m a$, we find that the steady-state mean-value for the resonator field is given by:

$$a = -\frac{\sqrt{\kappa_\mathrm{p}}\alpha_\mathrm{in}}{\kappa_\mathrm{t} - 2i(\omega - \omega_0) + \sum_{m=1}^{M}\frac{2g_m^2 pN_m}{\Gamma_2 - i(\omega - \omega_\mathrm{s})}} \tag{2.72}$$

We now introduce the ensemble coupling constant

$$g_\mathrm{ens}^2 = \sum g_m^2 pN_m = \int_g \rho_\mathrm{g}(g)dg g^2, \tag{2.73}$$

which can also be defined using a continuous coupling distribution $\rho_\mathrm{g}(g)$. Assuming the coupling distribution does not correlate with the spin frequency distribution $\rho_\omega(\omega)$, we can express the spin contribution as:

$$F(\omega) = \sum_{m=1}^{M}\frac{2g_m^2 pN_m}{\Gamma_2 - i(\omega - \omega_\mathrm{s})} = \int_g \rho_\mathrm{g}(g)dg \int_\omega \rho_\omega(\omega)d\omega \frac{2g^2}{\Gamma_2 - i(\omega - \omega_\mathrm{s})} \tag{2.74}$$

Assuming the spin inhomogeneous distribution is a Lorentzian of line-width (FWHM) Γ_{inh} and centred on ω_{s}, the spin-frequency distribution is:

$$\rho(\omega) = \frac{\Gamma_{\mathrm{inh}}/2}{\pi} \frac{1}{(\Gamma_{\mathrm{inh}}/2)^2 + (\omega - \omega_{\mathrm{s}})^2} \tag{2.75}$$

so that the spin contribution can be written as [70, 50]

$$F(\omega) = \frac{4g_{\mathrm{ens}}^2}{\underbrace{(2\Gamma_2 + \Gamma_{\mathrm{inh}})}_{=\Gamma_{\mathrm{t}}} - 2i\,(\omega - \omega_{\mathrm{s}})}. \tag{2.76}$$

We see here that it is not possible to distinguish Γ_2 and Γ_{inh} from a measurement of the resonator response. One only has access to the total broadening Γ_{t}. The modified response for the reflection measurement and by analogy also for the hanger geometry are [70, 50]:

$$S_{11}^{\mathrm{refl}} = 1 - \frac{2\kappa_{\mathrm{c}}}{\kappa_{\mathrm{t}} - 2i\,(\omega - \omega_0) + F(\omega)}, \qquad S_{21}^{\mathrm{hanger}} = 1 - \frac{\kappa_{\mathrm{c}}}{\kappa_{\mathrm{t}} - 2i\,(\omega - \omega_0) + F(\omega)}. \tag{2.77}$$

We can look at the denominator of two S-parameters to understand the effect of the spin ensemble on the resonance frequency of the resonator and how it changes the total damping rate. The denominator can be cast into the form

$$D(\omega) = \underbrace{\kappa_{\mathrm{c}} + \kappa_i + \frac{4g_{\mathrm{ens}}^2 \Gamma_{\mathrm{t}}}{\Gamma_{\mathrm{t}}^2 + 4(\omega - \omega_{\mathrm{s}})^2}}_{\tilde{\kappa}_t} - 2i(\omega - \omega_0) + 2i \frac{4g_{\mathrm{ens}}^2}{\Gamma_{\mathrm{t}}^2 + 4\,(\omega - \omega_{\mathrm{s}})^2}\,(\omega - \omega_{\mathrm{s}})\,. \tag{2.78}$$

We can thus identify that the spins contribute to an added dissipation channel in the resonator response, as well as a modification of the resonator frequency. When the spin's Larmor frequency matches the resonator frequency $\omega_0 = \omega_{\mathrm{s}}$, the modified total damping rate $\tilde{\kappa}_t$ is

$$\tilde{\kappa}_t = \kappa_{\mathrm{c}} + \kappa_i + \frac{4g_{\mathrm{ens}}^2}{\Gamma_{\mathrm{t}}} = \kappa_{\mathrm{t}}\,(1 + C)\,, \tag{2.79}$$

where the cooperativity is defined as $C = (4g_{\mathrm{ens}}^2)/(\kappa_{\mathrm{t}}\Gamma_{\mathrm{t}})$ [73, 51].

At $\omega_0 = \omega_{\mathrm{s}}$ the denominator may be rewritten as:

$$D(\omega) = \tilde{\kappa_{\mathrm{t}}} - 2i \frac{4\,(\omega - \omega_0)^2 - (4g_{\mathrm{ens}}^2 - \Gamma_{\mathrm{t}}^2)}{\Gamma_{\mathrm{t}}^2 + 4\,(\omega - \omega_0)^2} (\omega - \omega_0). \tag{2.80}$$

Resonances can be directly identified in the denominator by locating local extrema. When $4g_{\mathrm{ens}}^2 > \Gamma_{\mathrm{t}}$, two resonances can be identified in the denominator: $\omega = \omega_0 \pm \sqrt{4g^2 - \Gamma_{\mathrm{t}}^2}$. This is the signature of an avoided level crossing. When the cooperativity is smaller than 1, however, only a single resonance exists, with a frequency shift given by $\approx \frac{4g_{\mathrm{ens}}^2(\omega_0 - \omega_{\mathrm{s}})}{\Gamma_{\mathrm{t}}^2 + 4(\omega_0 - \omega_{\mathrm{s}})^2}$.

In Figure 2.8 the reflection coefficient, the frequency shift, and the internal damping rate are plotted for different cooperativities.

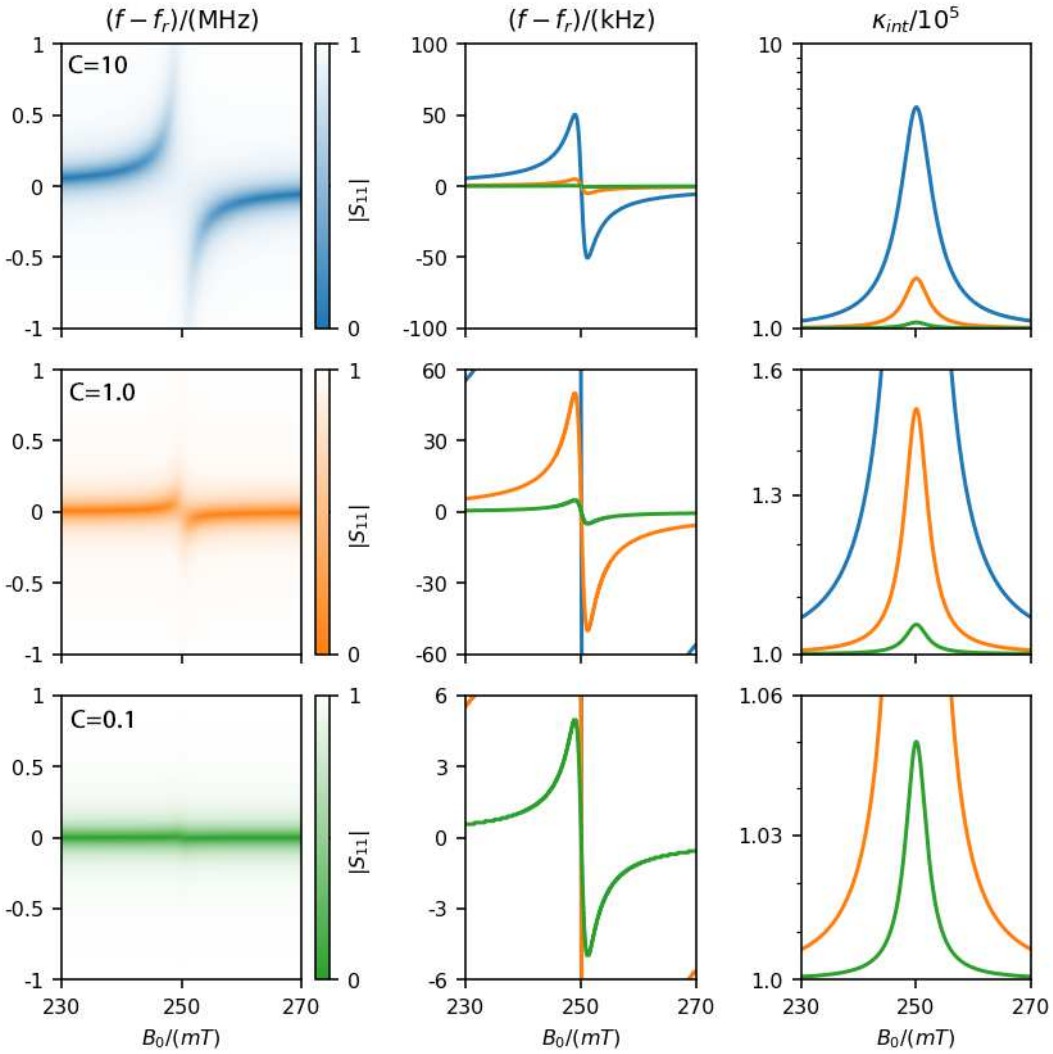

Figure 2.8: The reflection coefficient S_{11} (first column), the tracking of the resonance frequency, and the modified internal damping rate are plotted for a resonator coupled to a spin ensemble. The resonator has a resonance frequency of $f_\mathrm{r} = 7\,\mathrm{GHz}$ and $\kappa_\mathrm{i} = \kappa_\mathrm{c} = 1 \cdot 10^5$ at zero field. For the spin ensemble we assumed a line-width $\Gamma/(2\pi) = 10\,\mathrm{MHz}$ and $g = 2$, its frequency is given by the Zeeman Hamiltonian. The ensemble couplings differ $g_\mathrm{ens}/(2\pi) = 0.89,\ 0.28,\ 0.01\,\mathrm{MHz}$ in accordance to the colour coded cooperativities $C = 10,\ 1,\ 0.1$ (blue, orange, green). The first column shows the absolute of the S_{11} reflection measurement. The second column the frequency shift and the third column the modified internal damping rate.

2.5 ELECTRON SPIN RESONANCE SPECTROSCOPY: SENSITIVITY

Using the formalism introduced above, we now turn to a discussion on what sets the sensitivity of an EPR experiment, aiming more specifically for short-lived non-implanted species. We consider two cases: continuous-wave spectroscopy, where the steady-state absorption of microwave by the spins is detected, and pulsed spectroscopy, where a pulse train engineers the emission of radiation by the spins into the resonator.

2.5.1 *Continuous wave EPR*

In continuous wave EPR (cwEPR), the steady-state response of the resonator is probed as a function of the magnetic field $B_0(t)$. As discussed above, depending on the interplay between the ensemble coupling g_{ens}, the total damping rate κ_{t} and the spin line width Γ_{t}, two distinct behaviours manifest when the spin ensemble comes into resonance, see Figure 2.8). In the high cooperativity regime ($C \gg 1$) one observes an avoided crossing where the resonator frequency matches the spin transition. This avoided level crossing decreases for smaller cooperativities until it disappears for $C \ll 1$. In the low cooperativity regime, only an extra absorption rate remains with a small deviation to the resonator frequency. Finding the centre of the avoided level crossing, or which magnetic field maximises the extra absorption rate, allows to determine when the spin Larmor precession matches the resonator frequency. It is also possible to extract the inhomogeneous line-width of the spin ensemble. Using several resonators at different frequencies allows to reconstruct the frequency-field diagram of the spins, and thus allows to determine the Hamiltonian governing the energy levels of the spin system.

2.5.1.1 *Sensitivity*

We now evaluate the sensitivity of cwEPR spectroscopy using the formalism developed for quantum circuits. We make the assumption that the number of spins to be detected is low enough that we are in the low cooperativity regime, and that we operate with a resonator in reflection (by far the more common in EPR experiments, a schematic of such an experiment is shown in Figure 2.10). A coherent drive of amplitude $|\alpha_{\mathrm{in}}\rangle$ is sent to the resonator with the spins tuned at resonance, resulting in the detection of a homodyne signal $\alpha_{\mathrm{out}}(t)$ leaving the cavity. The steady-state mean-value of this signal is related to the steady-state intra-resonator field amplitude in the presence of the spins with $\alpha_{\mathrm{out}}(t) = \sqrt{\kappa_{\mathrm{c}}}\alpha_{\mathrm{s}}$ where $\alpha_{\mathrm{s}} = 2\sqrt{\kappa_{\mathrm{c}}}\alpha_{\mathrm{in}}/(\kappa_{\mathrm{i}}+\kappa_{\mathrm{c}}+\kappa_{\mathrm{s}})$ and $\kappa_{\mathrm{s}} = 4g_{\mathrm{ens}}^2/\Gamma_{\mathrm{t}} = 4N\bar{g_0}^2\Gamma_{\mathrm{t}}$. In the absence of the spins, it simplifies to $\sqrt{\kappa_{\mathrm{c}}}\alpha_0 = 2\sqrt{\kappa_{\mathrm{c}}}\alpha_{\mathrm{in}}/(\kappa_{\mathrm{i}}+\kappa_{\mathrm{c}})$.

Detecting the spins is thus analogous to distinguishing between two coherent states of mean values α_{s} and α_0 using the averaged homodyne signal extracted at rate κ_{c} from the resonator and recorded within a given measurement time t_m. In other words, it is about distinguishing between two Gaussian distributions, which becomes better resolved with increasing time. The amplitude signal-to-noise ratio of this measurement is given by $\mathrm{SNR} = \sqrt{2\eta\Gamma_{\mathrm{m}}}$ where η is the efficiency of the quantum-limited detection

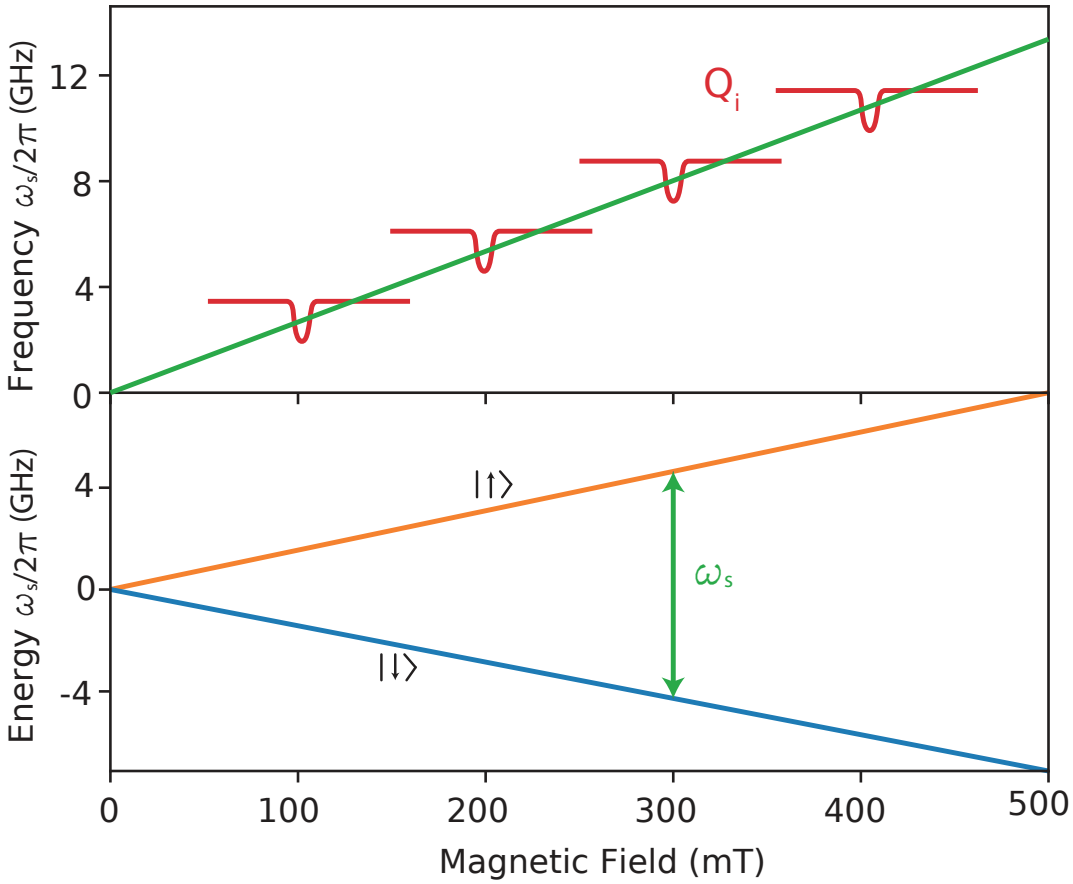

Figure 2.9: Example for a cwEPR measurement on a spin 1/2 with an isotropic $g = 2$. In the lower panel, the two energy levels $|\downarrow\rangle$ and $|\uparrow\rangle$ being split by the static magnetic field are shown. The upper panel depicts the associated Larmor frequency. One can track this transition using resonators with different eigenfrequencies and measuring their internal quality factor (red).

and Γ_m is the measurement rate, i.e. the rate at which information can be gained on the system. Using quantum information theory, this rate can be expressed as [74]:

$$\Gamma_m = \kappa_c \frac{|\alpha_s - \alpha_0|^2}{2} = \frac{2\kappa_c^2\kappa_s^2}{\kappa_t^2(\kappa_t + \kappa_s)^2}|\alpha_{in}|^2. \tag{2.81}$$

If we make the assumption that we operate in the critical-coupling regime $\kappa_c = \kappa_t/2$, and that the spins' dissipation is negligible compared to the resonator decay $\kappa_s << \kappa_t$, we find that:

$$\mathrm{SNR} = \frac{4\sqrt{\eta}}{\kappa_t}\frac{\bar{g}_0^2}{\Gamma_t} pN|\alpha_{in}|. \tag{2.82}$$

This signal-to-noise-ratio is in fine limited by the input power that can be used to probe the resonator. Too large a power will saturate the spin ensemble and reduce the effective number of spins contributing to the signal. Using equation 2.72 we can evaluate the dependence of p and $|\alpha_{in}|$ on the resonator photon number, and we find

$$\mathrm{SNR} = \frac{2\sqrt{2\eta}}{\sqrt{\kappa_t}}\frac{\bar{g}_0^2}{\Gamma_t} p_0 N \frac{\sqrt{\bar{n}}}{1 + \frac{4\bar{g}_0^2}{\Gamma_2\Gamma_1}\bar{n}} \tag{2.83}$$

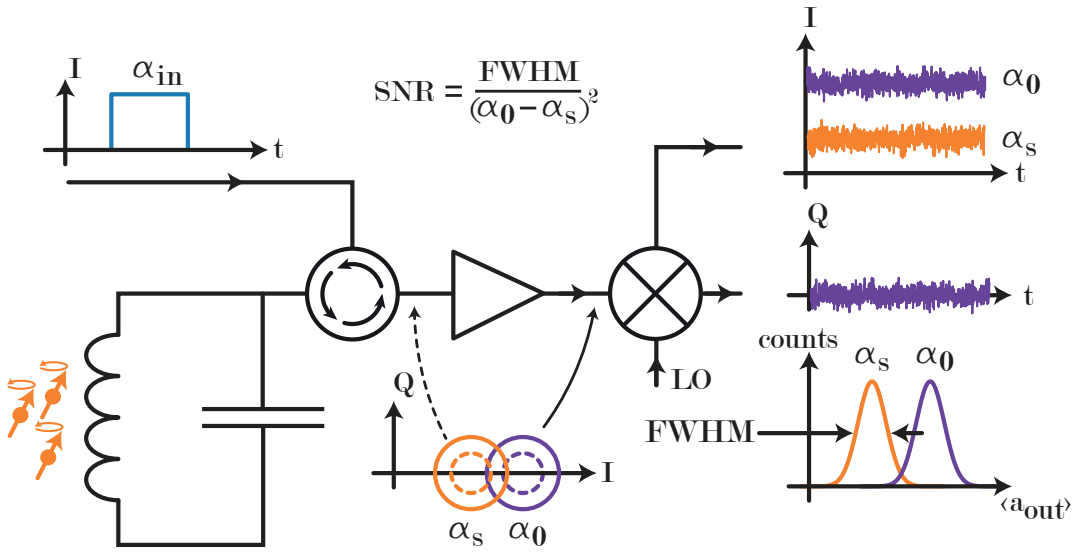

Figure 2.10: Schematic of a continuous wave EPR experiment. The drive of amplitude α_{in} is exciting the spin ensemble. The spin signal α_s leaving the cavity and is amplified together with the bare resonator signal α_0 via a phase-preserving amplifier. Subsequently, the signal is demodulated and detected.

where p_0 is the polarization in the absence of a drive. The SNR is maximum for

$$\bar{n} = \Gamma_2\Gamma_1/(4\bar{g}_0^2) \tag{2.84}$$

and reaches

$$\mathrm{SNR} = \frac{\sqrt{\eta}}{\sqrt{\kappa_t}} \frac{\sqrt{\Gamma_2\Gamma_1}}{2\Gamma_t} N p_0 \bar{g}_0 \tag{2.85}$$

If we define the sensitivity as the minimum number of spins N_{min} to have a signal-to-noise ratio of 1, we thus find that:

$$N_{\mathrm{min}} = \frac{\sqrt{\kappa_t}}{\sqrt{\eta} p_0 \bar{g}_0} \frac{2\Gamma_t}{\sqrt{\Gamma_2\Gamma_1}} \tag{2.86}$$

While part of the sensitivity is given by the properties of the spin ensemble, this formula makes clear that it is minimized for narrow line-width (small κ_t) small-mode volume (large g_0) resonators, homodyne detection setups operating close to the quantum limit ($\eta \to 1$), and well polarized spin ensemble.

2.5.2 *Pulsed EPR spectroscopy*

A big drawback of the cwEPR is that one cannot straightforwardly measure T_2. This is where time domain EPR comes into play [75]. Within this approach, one applies one or multiple microwave pulses and observes the response of the spin ensemble.

2.5.2.1 *Free inductive decay*

One of the simplest pulse measurements is a so-called Fourier transform EPR (FT-EPR) [75]. In this scheme, a $\pi/2$ pulse is applied, creating a transverse magnetization that fans

out due to inhomogeneous broadening. The transverse magnetization has nevertheless a back-action on the pulse, with a contribution uniquely due to the spins: this signal is called the free-induction decay. The Fourier transform of such a FT-EPR experiment in principle yields a peak at the frequency $\Omega = \omega_{\text{spin}} - \omega_{\text{drive}}$. It is therefore in principle possible to obtain the same as in a cwEPR experiment, but in a much shorter time. However, this is challenging as one needs a large bandwidth to observe the beating between the frequencies and a high enough microwave power to induce the rotation in a short time. This high microwave power can also pose a problem on the detection side, as the high-power pulse can create a dead time in the measurement apparatus, preventing the measurement of the FID. In the context of high-quality factor superconducting resonator, this technique is inapplicable since the FID signal duration is much shorter than the line-width of the resonator.

2.5.2.2 *Hahn-Echo pulse*

A way to circumvent the problem of the dead time of the FT-EPR is to use more elaborate pulse sequences. One of the more commonly used ones is an echo sequence. Here the spins are magnetized along the y-direction by the $\pi/2$ pulse and decay according to the FID. After a time τ, a π pulse is applied which is 180° rotation either around x-axis or the y-axis and leads to a refocussing of the spins and subsequently to the build-up of an echo after a time τ [75]. This sequence is known as Hahn-Echo sequence (although in the original publication by Hahn two π pulses are used [76]) and is shown in Figure 2.11 on the Bloch-sphere [75, 52].

2.5.2.3 *Sensitivity*

Let us now recall the sensitivity of a Hahn echo measurement using the formalism adopted for describing the coupling of an ensemble of spins to the resonator. Assuming the echo is emitted at the time $t = 0$, a perfect $\pi/2$ pulse creates a magnetization $S_-^{\text{m}}(t = -\tau) = -ipN_{\text{m}}/2$. After applying the π pulse, this magnetization evolves as $S_-^{\text{m}}(t = -\tau) = -ipN_{\text{m}}/2e^{i\Delta_{\text{m}}t}$. Integrating the contribution of all spins by assuming a Lorentzian distribution of width Γ_{inh} (eq 2.75), the overall transverse magnetization at the time of the echo is given by $M_{\text{t}} = -ipN_{\text{m}}/2e^{-\Gamma_{\text{inh}}|t|}$. Using Equation 2.68 and neglecting the filtering effect of the cavity, the intra-resonator field is thus $a(t) = \bar{g}_0 pNe^{-\Gamma_{\text{inh}}|t|}$, yielding an output signal $a_{\text{out}} = \sqrt{\kappa_{\text{c}}}a(t)$ which can be detected using homodyne detection.

We express the signal-to-noise ratio of this measurement using the integrated signal $\langle a_{\text{out}} \rangle$. To maximize the signal, we choose $u(t) = a_{\text{out}}(t)/\langle a_{\text{out}} \rangle$ so that $a_{\text{out}}(t) = p\bar{g}_0 N \frac{\sqrt{\kappa_{\text{c}}}}{\sqrt{\Gamma_{\text{inh}}\kappa_{\text{t}}}}$. Using Equation 2.41, we thus find

$$\text{SNR} = 2\sqrt{\eta}p\bar{g}_0 N \frac{\sqrt{\kappa_{\text{c}}}}{\sqrt{\Gamma_{\text{inh}}\kappa_{\text{t}}}} \tag{2.87}$$

This echo is generated at each sequence, with a repetition rate Γ_r governed by Γ_1. If we now define the sensitivity N_{min} as the number of spins detectable within an integration time of 1 s and a SNR of 1, we find in the critical coupling regime:

$$N_{min} = \sqrt{\frac{\kappa_t \Gamma_{inh}}{2\eta}} \frac{1}{\sqrt{\Gamma_r} p_0 \bar{g}_0}. \tag{2.88}$$

We find that the optimal sensitivity is reached for the same parameters as for cwEPR spectroscopy: narrow line-width (small κ_t) small-mode volume (large g_0), homodyne detection setups operating close to the quantum limit ($\eta \to 1$), and well polarized spin ensemble. It also makes obvious that for spin ensembles with ratio $\Gamma_{inh}/\Gamma_2 >> 1$, pulsed EPR detection has better sensitivity than cwEPR.

2.5.3 *State of the art of inductively detected EPR spectroscopy*

As we have discussed above, a highly-sensitive EPR spectrometer is achieved by using small-mode volume resonators with high-quality factors, working at low temperatures (or at high-frequency to reach higher polarization [75]) and use low-noise amplifiers. At room-temperature, one can obtain high-quality factors by using dielectric resonators [31], or by engineering small-mode-volume using micro-resonators [13], or bow-like structures [32], loop-gap [33, 34], or anapole resonators [35]. All planar geometries face two challenges: the resistance of the film, and potentially dielectric losses due to the substrate, limiting their quality factors, and the inhomogeneity of AC magnetic field which can severely reduce the signal-to-noise-ratio.

Lowering the temperature to 4 K improves the spin polarization, and enables the use of better amplifiers such as HEMT [77].

Quantum-circuit EPR implementations [12, 43, 28, 29, 30] played on these four factors and reached sensitivities in the range 1 spins/$\sqrt{\text{Hz}}$ to 1×10^4 spins/$\sqrt{\text{Hz}}$. The experiments were performed at millikelvin temperature to achieve full spin polarization ($p = 100\,\%$) and complete thermal noise suppression. In addition, quantum-limited amplifiers were used so that the noise in the spectrometer detection chain corresponds to quantum fluctuations. These demonstrations also made use of the micron-scale confinement offered by planar resonators and of the high-quality factors achieved by quantum circuits ($Q > 10^5$). An important component of these experiments was the use of a high-quality factor, combined with a small-mode volume, which enabled the use of the Purcell effect as a resetting mechanism and bring the relaxation time to a very convenient sub-second range. This allows to have a fast repetition rate and therefore a better sensitivity. Let us note that lately, a single spin could be detected using its fluorescence (Purcell relaxation) signal [21]. This achievement required a quantum circuit able to detect single photons [78]. This detection scheme allows for even better SNR than homodyne detection in the context of spins whose relaxation can become Purcell-limited. An overview of the mentioned experiments comparing the sample volume and the absolute sensitivity and setting this in relation to the associated spin-concentration is given in Figure 2.12.

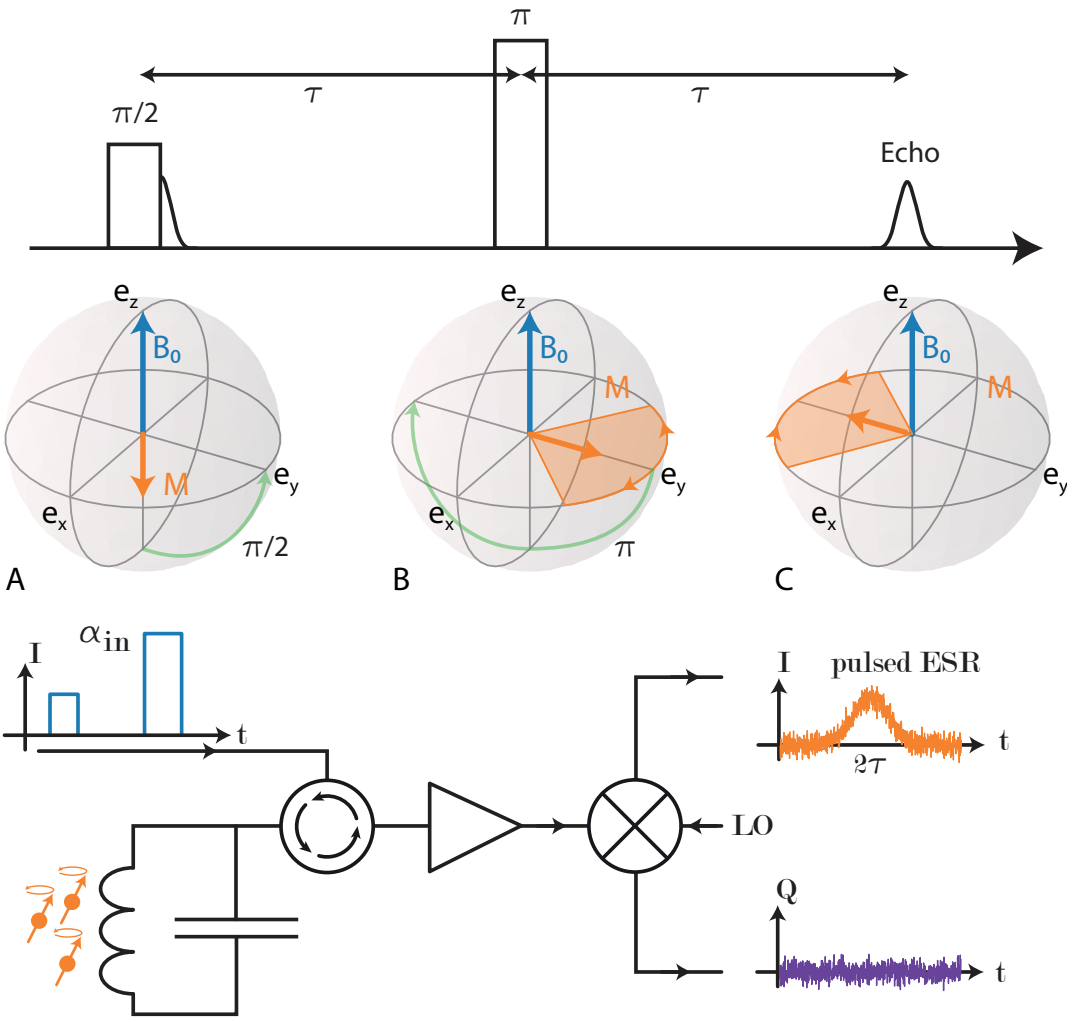

Figure 2.11: The Hahn-Echo sequence starting with a $\pi/2$ pulse bringing the magnetization vector along the e_y direction (A). The spin ensemble is showing the FID directly after the pulse and starts to de-phase. After a time τ the π pulse is applied (B), rotating the magnetization around the e_x axis leading to the refocussing (C) and the emission of the spin echo after the time 2τ. The schematic shows a typical pulsed EPR setup. The pulse is applied on one quadrature, stimulating the echo which is amplified (in our case with a phase-preserving amplifier), demodulated and detected.

2.5.4 *Quantum circuits EPR for pL samples*

Since unpaired electrons occur in many species, such as free radical molecules, molecules containing a transition metal, defects in semiconductors or oxide compounds, EPR spectroscopy has multiple fields of applications: in biology and medicine – for understanding the molecular structures of proteins and enzymes and their roles in biological processes [79, 80, 81]; in chemistry – to understand the structures of redox catalysts and their roles in chemical reactions [82]; in solid-state physics, to understand the structures of defects or formation of compounds at interfaces [83, 36, 84]. In many of these applications, however, samples are limited in volume. For example, proteins, enzymes and catalyst molecules are often crystallized to perform X-ray crystallography and obtain structural information. EPR spectroscopy would enable to obtain key complementary information, in particular in-situ distance measurement on the nanometre scale. However, these crystals have sizes ranging from 0.2 µm to 300 µm [10], putting the vast majority of them out of the detection range of all EPR spectrometers so far developed.

The quantum-circuit spectrometers demonstrated so far have only been used to measure well-known spin systems, such as donors and defects in semiconductors. To be able to measure other samples and apply this gain in sensitivity to other research fields, a quantum-limited EPR spectrometer has to fulfil a number of additional requirements that are not met yet:

- Maintain *High quality factors* despite the use of materials lossy at microwave frequencies and the application of large magnetic fields. For instance, a very common problem when probing biological samples is their aqueous composition. Dielectric losses of water usually limit the quality factor of conventional EPR resonators to 10^3. Another challenge for the quality factor is the application of magnetic fields in the range of 0.25 T to 0.5 T. The application of such large magnetic fields requires the resonator to be made of a superconducting material with a sufficiently high critical field.

- *Compatibility with micron-scale samples*, either crystalline or in solution. It should be possible to insert the spins into the resonator 'active' area.

- *High cycling rate*: In a conventional EPR spectrometer, it is possible to change samples quite rapidly, which is important in studies where a parameter, for instance concentration, is varied. With a dilution cryostat, cycling time is difficult to reduce below 10 h. However. for quantum-limited EPR spectroscopy to be practical, it is thus essential to find a way to measure several samples in a single-cool-down to compensate for these long cycling times.

- Operation with *unknown/short coherence times*. Whereas proof-of-principle experiments were performed with spin systems having long coherence times > 100 µs, EPR spectroscopy also aims at detecting species that may have short coherence times. This necessitates the use of short microwave pulses [20], or using moderate quality factors. However, a high sensitivity requires a high-quality factor. We have focused in this thesis on using short microwave pulses to alleviate this effect.

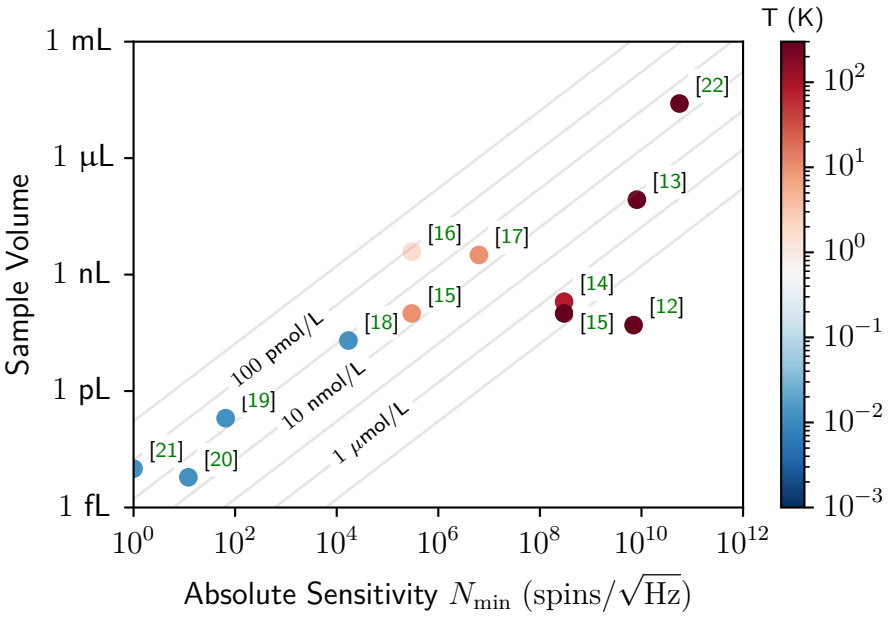

Figure 2.12: Sample volume defined by the magnetic-field active volume versus the minimal number of spins for various values found in literature. All cited experiments work in the frequency range of 7 GHz to 9 GHz except for [17] at 36 GHz and [15] at 16 GHz. [22] is a commercial EPR spectrometer.

The goal of this PhD work is thus to develop a quantum circuit able to detect pL samples, possibly with short coherence times.

3

EXPERIMENTAL SETUP

As outlined in the previous chapter, the project of this thesis aims at developing a spectrometer benefiting from the sensitivity increase brought by quantum circuits, yet able to probe samples from a wide range of origins and shapes, and in particular samples which are volume-limited. Previous quantum-circuit experiments targeted spins embedded in low-loss dielectric lattices, on which the resonator probing the spins could be patterned. In addition, the probe volume of the resonator was directly given by the width of its inductive wire, given that spins were located on the entire surface of the resonator.

We choose to design our experiment with a different mindset: We start with a hypothetical given sample of a typical volume ranging from 1 fL to 1 pL (equivalent to a cube with lateral size of 1 µm to 10 µm), for example a protein crystal or a single biological cell, where the matrix can be lossy (which is particularly true if the spins are embedded within a solvent or aqueous matrix). Given such a sample, in which way should the resonator to be designed? In particular, what adaptations are needed such that the prerequisites for increased sensitivity - a resonator with a high-quality factor and small-mode-volume - are met? Once this first challenge is overcome, the subsequent question arises: how can the sample be effectively deposited into the small-mode volume of the resonators?

In this chapter, we will first describe the resonator design with which we address the first question. This is followed by a broad overview of the layout of the experiment which we built in a dilution cryostat to reach quantum-limited sensitivity, as well as the 3D coil setup we have designed for the experiment. We will finish by reviewing different options for placing the samples, as well as describe the deposition platform we built for this purpose. Finally, we will discuss the spin sample we have decided to use to benchmark the spectrometer.

3.1 RESONATOR DESIGN

To probe spins in a micron-sized sample, with possibly large dielectric losses, we choose to implement the design shown in Fig. 3.1. It consists of an inductive loop in parallel with a large circular-shaped interdigitated-capacitance and creates an out-of-plane AC magnetic field B_1 at the centre of the inductive loop. This is also the region with no electric field and corresponds to the region where the spins are to be placed. This resonator shape is similar to the so-called Packman or loop-gap resonators developed for EPR [17, 85]. As the AC magnetic field is perpendicular to the plane of the superconductor, we can freely choose the orientation of the magnetic field within this plane. This can be of interest for probing anisotropic spin systems.

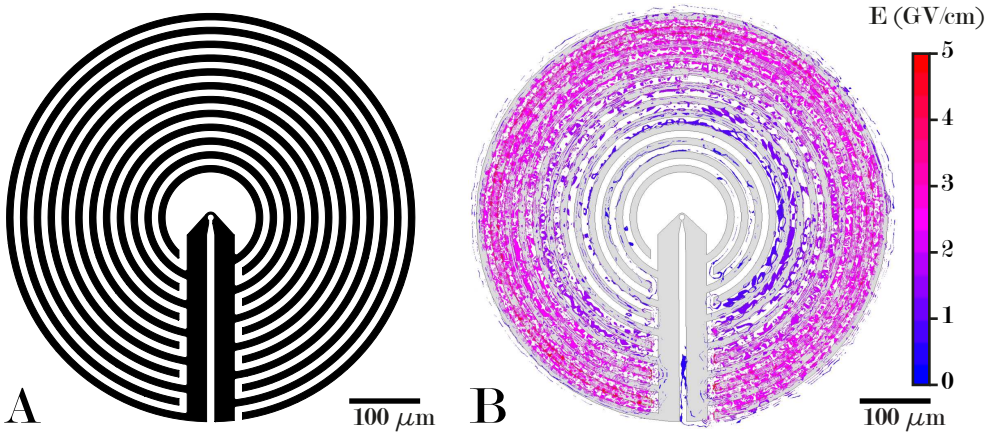

Figure 3.1: A: Example of one resonator using the final design. the sample space is in the centre loop, which in this case has an inner radius of 5 µm.B: Magnitude of the electric field when the resonator is driven on resonance, obtained using a HFSS simulation with 1 W of input power. In the centre of the loop, the electric field is averaged out.

3.1.1 *High-quality factor for lossy samples*

The circular shape of the capacitor minimizes the resonator electrical field in the sample region, and thus the contribution of the dielectric losses to the resonator damping is minimized. Numerical simulations indicate that a quality factor $Q > 5 \times 10^5$ can be maintained for samples with dielectric losses as large as $\tan\delta = 10^{-2}$, see Figure 3.2, given a sample radius $< 25\,\mu m$.

The resonator should also maintain its high-quality factor in the presence of a possibly large B_0 magnetic field (up to 0.5 T). There are different superconductors which have been tested in recent years in magnetic field to evaluate their use for high-quality factor resonators, among those are Nb, NbN, NbTiN, and granular aluminium. For NbN on high resistivity silicon, internal quality factors in the range of $10^4 - 10^5$ up to 6 T for an in-plane magnetic field have been demonstrated [86]. The overall situation for NbTiN is similar with observed internal quality factors $> 10^5$ on silicon and sapphire substrates with an applied in-plane magnetic field up to 6 T [87, 88, 89]. Granular aluminium (GrAl) on sapphire has also been shown to sustain internal quality factors $> 10^5$ for high in-plane magnetic fields up to 1 T [90]. Within all of these studies, a reduction in the intrinsic quality factor is observed when a magnetic field, corresponding to a spin 1/2, $g = 2$ impurity, is applied. This is a major concern for EPR spectroscopy as it has the potential to obscure the anticipated signal, we therefore discuss this effect in Chapter 5. In terms of sustaining the quality factor in magnetic field, all of the above materials are well suited. A second criterion is motivated by the choice of minimizing the impedance of the resonator to boost the sensitivity (discussed below). Comparing the typical kinetic inductance for thin films of the three materials with NbN (13 nm): ≈35 pH/□ to 170 pH/□ [86, 91], GrAl (20 nm): 1.5 nH/□ [90], and NbTiN (20 nm): ≈10.5 pH/□ [92, 93, 94], we choose NbTiN for our device.

One dominant source of losses expected at high magnetic fields is losses created by magnetic vortices. To improve further our quality factors, we will use a 3D magnet able to align the magnetic field onto the superconducting plane to achieve optimal

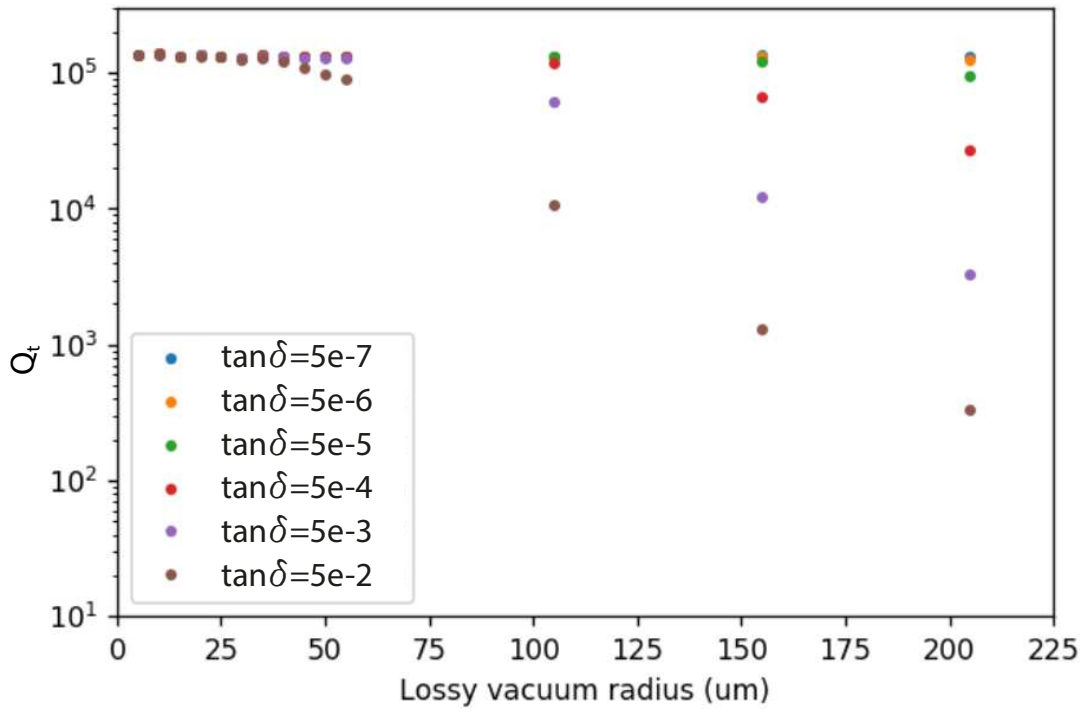

Figure 3.2: Total quality factor versus the radius of a lossy vacuum with height 5 µm with different tanδ, indicating a resilience of the design for samples with $\tan\delta < 5 \cdot 10^{-2}$.

parallelism. We will also reduce the size of the ground plane surrounding the resonator, and use a small width for the electrodes of the capacitor to both reduce the nucleation of vortices [95, 96] and their impact on the resonator[88, 89].

3.1.2 *Small-mode volume*

As discussed in Chapter 2.0.2, the coupling of a resonator to a spin is given by the strength of the root-mean-square vacuum fluctuation of the magnetic field at the position of this spin. To maximize the coupling to the spins, one thus needs to maximize the current flowing through the inductor, we thus adopt a low-impedance design and opt for an inductor design providing the best AC magnetic field coverage for the spin ensemble.

During the design process, we need to keep in mind that the total inductance L_{tot} of the resonator consists of the geometrical inductance L_{geom} and the kinetic inductance L_{kin} of the NbTiN: $L_{tot} = L_{geom} + L_{kin}$. In the initial tests, we found that the kinetic inductance of our 50 nm NbTiN film is 1.5 pH. This leads to two contrary requirements, on the one hand, a small wire width to increase the AC magnetic field to couple more efficiently to the spins and on the other hand, larger wire width to decrease the overall inductance. We finally opt to have the leads connecting the fingers of the capacitor to the loop with a large width, while the loop in the centre has a small width. Using different loop diameters and widths, we can tune the inductance of the resonator and therefore target different sensitivities. The capacitance is then varied to tune the resonator frequency into the target range of 7 GHz to 8 GHz. The bandwidth of the

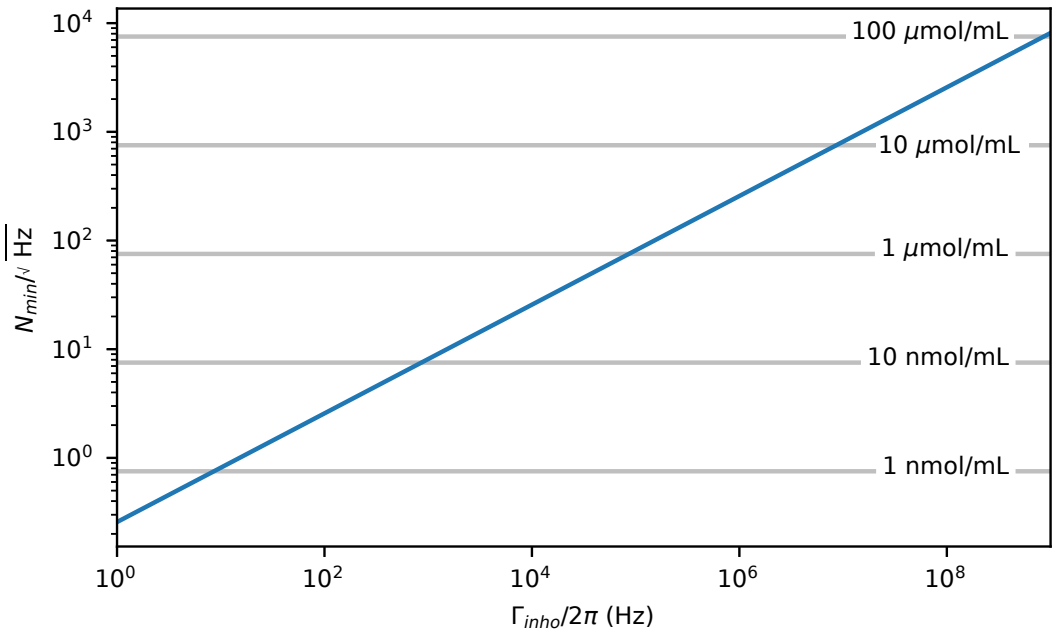

Figure 3.3: Using the simulated impedance (here $Z = 40\,\Omega$, loop radius: 5 µm) we can calculate the vacuum fluctuation of the magnetic field in the centre of the inductive loop. The sensitivity for a pulsed setup can then be calculated for different echo durations or inhomogeneous broadened lines.

used JTWPA allows for frequencies between 4 GHz to 5.8 GHz and 6.2 GHz to 8 GHz. Our choice of frequency is on the edge of the bandwidth of the used JTWPA and allows us to have the best sensitivity as $N_{\min} \propto \omega_0$. A typical EPR frequency is the X-Band (9 GHz) as this frequency is high enough to resolve features with only small differences in their g-value while using moderate magnetic fields. At this frequency and at 321.5 mT, the field position of a spin 1/2, $g = 2.0$, a change of 1 mT equates to a change of $1.5 \cdot 10^{-2}$ in g. A resonator with an impedance of $Z \approx 40\,\Omega$ (see Table 3.2) and a frequency of 7.5 GHz leads to $\delta I = 54$ nA.

The coupling to the spin's sample should ideally be the same for all spins within the sample space. However, this is difficult to achieve in a planar geometry. The next best coupling distribution which is achievable in a planar geometry is one which is sharp and well confined. We simulated our target design using the 3D-MSLI software package developed by Khapaev et al. [97] using a loop radius of 5 µm and a 4 µm by 4 µm cube as a sample (see Figure 3.4) and find that the thinner the wire the narrower is the coupling distribution. In the centre we find $g/2\pi = 60$ Hz and the FWHM of the coupling distribution is 45 Hz. These numerical simulations indicate that a coupling constant greater than $g/2\pi \approx 30$ Hz can be achieved over a volume of ≈ 100 fL. Assuming that $Q_{\text{i}} = Q_{\text{c}} = 5 \cdot 10^5$ and using the simulated impedance of 40 Ω we show in 3.3 an estimate for the expected pulsed EPR sensitivity as a function of the inhomogeneous broadening. For an inhomogeneous broadening of $\Gamma_{\text{inh}}/2\pi \approx 10$ MHz we thus expect a sensitivity of 250 spins/$\sqrt{\text{Hz}}$, assuming a sample of 125 fL (a cube with side lengths of 5 µm) results in a concentration sensitivity of 400 µmol mL^{-1}.

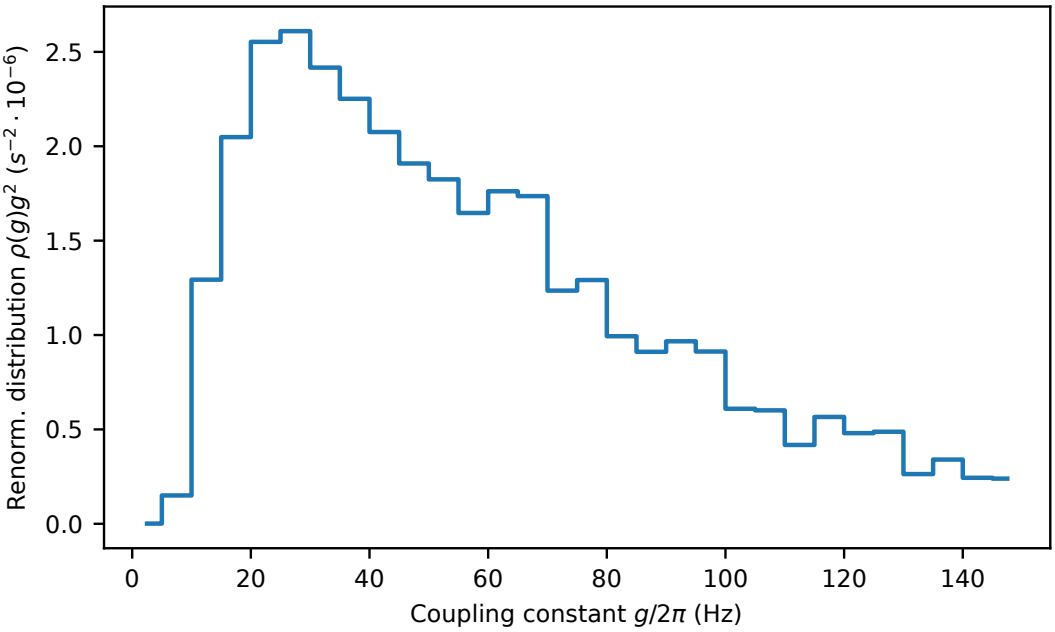

Figure 3.4: Simulated coupling distribution using a cube with a side length of 4 µm as a sample.

3.1.3 *Towards a Helmholtz configuration.*

The just discussed planar design does generate the necessary out of plane AC magnetic field. However, the field distribution has two main problems, starting with the exponential decrease in the field away from the 3D device and the resulting inhomogeneity. Secondly, the areas with the strongest field are also the areas closest to the surface and the NbTiN, causing the spectrometer to be potentially strongly influenced by surface impurities or impurities in the NbTiN. Progressing from a planar design towards a 3D structure could solve these issues. For this, we are envisioning using two resonators overlaid via a non-galvanic flip-chip technique. Each structure comprises an inductive loop in parallel with a large circular-shape interdigitated-capacitance and creates an out-of-plane B_1 field at the centre of the loops, corresponding to the region where the spins are to be placed. This Helmholtz configuration delimits a volume fixed by the loop radius and enables the B_1 field to be homogeneous over the spin sample ($< 10\%$ inhomogeneity).

3.1.4 *Chip layout*

Over the course of my PhD, I have designed three layouts: the first (Initial device) intended to benchmark the resonator design versus known designs, as well as check the performances of our experimental setup. The second device (BDPA device) aimed to benchmark the spin sensitivity of the circle resonator for test species. The last design (”Hunting Impurities” device) was aimed at better understanding the origins of the spurious species contributing to the signal we obtained when performing our first cwEPR characterizations.

3.1.4.1 *Initial Device*

For benchmarking purposes, we placed our resonator design next to an interdigitated capacitor (IDC) shorted by a wire, a $\lambda/4$ resonator and a long inductive wire with a short capacitor on the same device. The shorted IDC is a design used in hybrid systems to couple to spins ([18, 20, 21]). The long inductive wire style resonator was used in the experiments carried out in Delft [94, 89, 88] to demonstrate the resilience of resonators made from NbTiN against the loss of their quality factor in magnetic fields - their comparatively low cross-section makes them extremely resilient to vortices-induced losses. The $\lambda/4$ resonator is a standard design used in superconducting circuits and is therefore included. The design and key parameters of the individual resonators are shown in Figure 3.5 and Table 3.1. The resonators are probed in hanger geometry to estimate for the intrinsic losses. We realized this design in 50 nm NbTiN on high resistivity Silicon and on Sapphire using a CHF3 and an SF6 dry etch. The observed etch quality was visibly better when using the CHF3 etch, as we observed less roughness and fewer residues. While there was no difference in the microwave performances of the two chips at zero magnetic field, we later used only CHF3 etch for its better finish.

Table 3.1: Simulated resonance frequency and coupling quality factor of the four resonators on the initial device.

Resonator	f_{res} (GHz)	$Q_{sim}/1 \times 10^5$
Nano Wire	6.0135	3.0
Lambda/4	6.5156	2.2
IDR	7.1842	2.3
Circle Reso	7.4418	3.4

3.1.4.2 *BDPA Design*

The idea of this design is to allow for a benchmarking of the spectroscopy by varying the spin sensitivity of the resonators and by varying the spin concentration of the spin samples used. In order to do this, we collect eight resonators on one device (the key parameters of these resonators can be found in Table 3.2) coupled to a coplanar waveguide which terminates in an open on chip (see Figure 3.6). The device is measured in reflection to make sure to collect all emitted spin signal towards the output detection line. The distance between the resonator and the central coplanar waveguide is chosen such that the coupling quality factor is approximately 1×10^5. From the results obtained with the initial chip (detailed in the next chapter), we can reasonably expect intrinsic quality factor Q_i in the range 10^5 to 10^6, so that we expect to be in the critical coupling regime. This regime optimizes the spectrometer sensitivity since it maximises the Purcell rate. In Figure 3.6, the schematic of the device is shown.

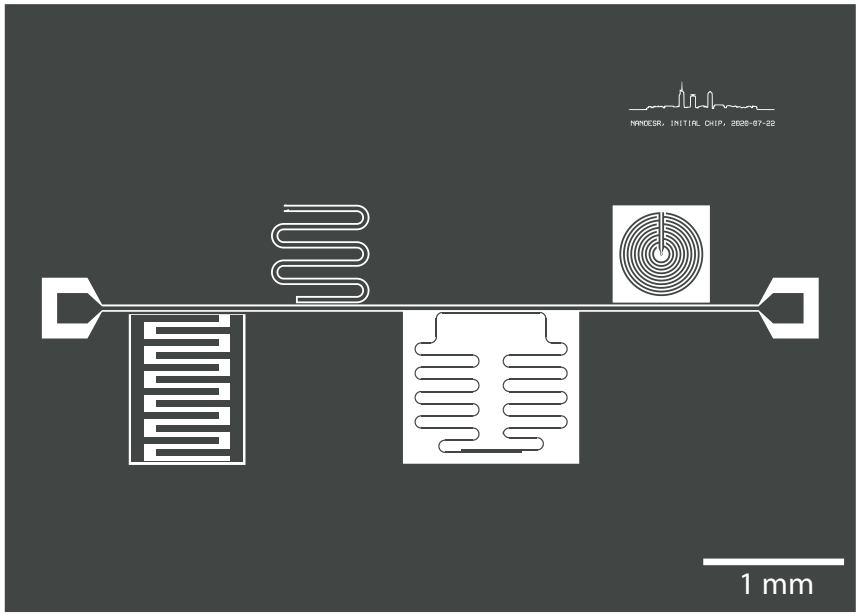

Figure 3.5: Layout of the initial device (grey: NbTiN, white: Sapphire/Si), with the four resonators (left to right): IDR, Lambda/4, Nano Wire, Circle. They are all capacitively coupled to the transmission line.

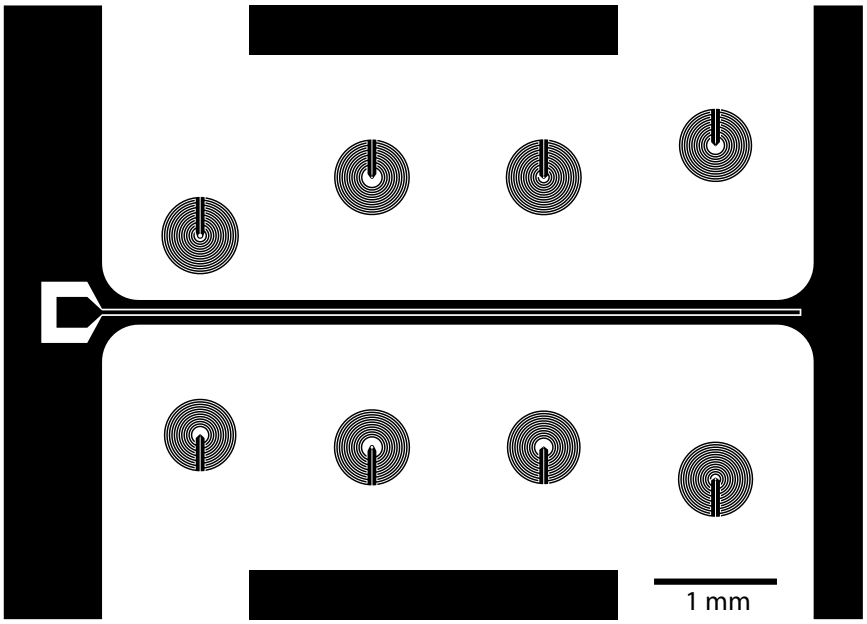

Figure 3.6: Overview of the BDPA design (grey: NbTiN, white: Sapphire). The resonators are labelled $1-8$ anti-clockwise starting from the lower left.

The device simulation was carried out using Ansys HFSS software. To infer the resonator impedance, we first integrate the magnetic field on a closed path surrounding the inductive loop of the resonator. From this, we calculate the current flowing through the wire. Knowing that HFSS is using an input power of 1 W we can infer the number of photons in the resonator and use the current fluctuations to calculate the impedance

Table 3.2: Summary of the resonator parameters for all resonators on the device. The resonator labelling corresponds to the labels introduced in Figure 3.6. The inductive loop radius r_{il} is the mean radius. We calculated three figures for the sensitivity: N_{min} as defined in Chapter 2.5, assuming the Purcell effect dominates and fixing $\Gamma_{\mathrm{r}} = \Gamma_{\mathrm{P}}/5$; the sensitivity per echo sequence, independent of the repetition rate $N_{\mathrm{min}}^{\mathrm{echo}}$; and the concentration sensitivity, defined as $C_{\mathrm{min}}^{\mathrm{V}} = N_{\mathrm{min}}/V$ which we express in units of $\mathrm{nM}/\sqrt{\mathrm{Hz}}$ where M = mol/L. These calculations assume an echo time of $1\Gamma_{\mathrm{inh}} = 1\,\mu\mathrm{s}$. The volume is estimated by a half sphere with radius r_{il}.

Resonator	1	2	3	4	5	6	7	8
r_{il} (µm)	5	15	5	10	5	10	10	21
w_{il} (µm)	2	6	2	4	2	4	4	8
V (pL)	0.26	7.06	0.26	2.09	0.26	2.09	2.09	19.40
$g/2\pi$ (Hz)	103	30	93	47	97	48	48	21
Z (Ω)	37	41	43	39	40	37	38	40
N_{min} (spins/$\sqrt{\mathrm{Hz}}$)	304	1231	432	940	376	677	756	1810
$N_{\mathrm{min}}^{\mathrm{echo}}$ (spins)	293	4788	590	2792	447	1447	1808	10364
C_{min} (nM/$\sqrt{\mathrm{Hz}}$)	1.94	0.29	0.28	0.75	2.39	0.53	0.60	0.15
Q_{sim} ($\times 10^5$)	7.5	2.2	1.7	1.2	2.6	4.3	2.5	1.8
f_{sim} (GHz)	7.8127	7.1659	7.6228	7.2944	7.6813	7.2601	7.3979	7.0713

using Equation 2.8. The kinetic inductance was considered by assigning a reactance to the sheets defining the NbTiN layers of $Z_{\Sigma} = jL_{\mathrm{kin}}\omega_{\mathrm{R}}$. We use for the kinetic inductance an estimate of 1.5 pH determined by measurements of the initial device (see Chapter 4.4).

A total of four devices with this design were fabricated. They are abbreviated as "BDPA-1" to "BDPA-4".

3.1.4.3 *Hunting Impurities Design*

During the measurements of the BDPA devices it became clear that we were dealing with different losses due to different origin which are discussed in detail in Chapter 5. After understanding the origin of all but one contribution, we wanted to track down whether this was due to magnetic or electric coupling, or on a specific region. This was to be done by comparing resonator geometries with different participation ratios of the capacitative and inductive part. With this in mind, the 'Hunting Impurities' device was designed. The transmission geometry was chosen to for better determination of the intrinsic losses. The simulated frequencies and quality factors are summarized in Table 3.3 and the device layout is shown in Figure 3.7. The four circular resonators are unaltered from the BDPA design and have different inner loop radii from 5 µm to 15 µm.

3.1.5 *Fabrication*

In total, four different fabrication runs were done, each with slightly different recipes. Changes to the fabrication recipe were done to minimize the impurities signals we were

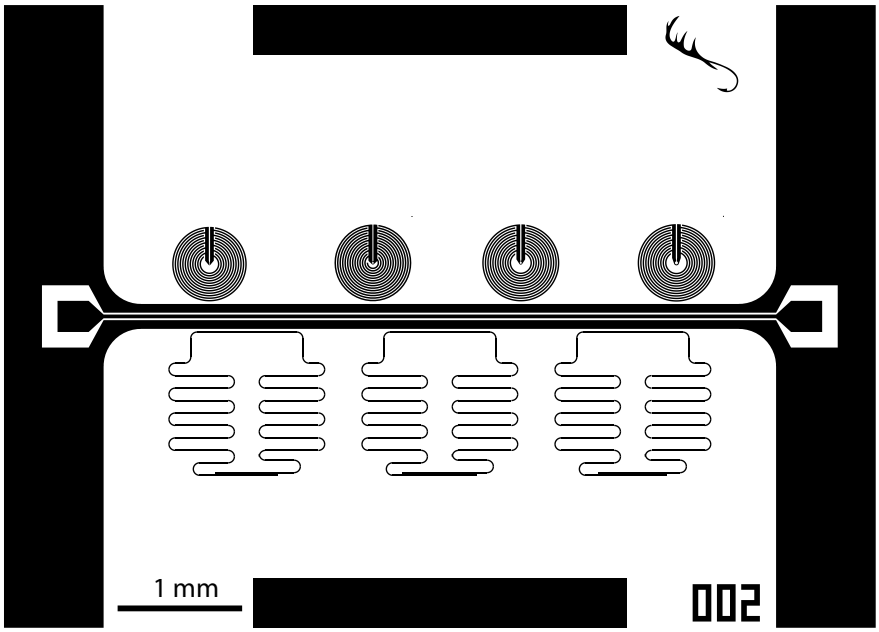

Figure 3.7: Overview of the Hunting Impurities design (grey: NbTiN, white: Sapphire). The nanowire resonators are labelled (left to right) $2, 1, 38$ and the circle resonators are (left to right) $5, 6, 7, 2$.

Table 3.3: Summary of the simulated quality factors and frequencies for the Hunting Impurities design. The resonators circle resonators correspond to the ones on the BDPA device.

Resonator	NWR 1	NWR 2	NWR 3	Circle 5	Circle 6	Circle 7	Circle 2
f_{sim}(GHz)	6.06	5.83	5.91	7.68	7.26	7.40	7.17
Q_{sim}	$2.9 \cdot 10^4$	$5.7 \cdot 10^4$	$3.3 \cdot 10^4$	$1.6 \cdot 10^5$	$0.9 \cdot 10^5$	$2.4 \cdot 10^5$	$5.6 \cdot 10^5$

seeing in the cwEPR scans of our resonators. These results are detailed in Chapter 5. In Figure 3.8 the exact recipe for each run is given. For all runs, we have realized an etch type of process, where the substrate was first cleaned and send to the SPEC laboratory (CEA-Saclay) for sputtering a 50-nm-thick film of NbTiN. We have used two types of wafer: Edge defined, film-fed growth (EFG) grown wafers procured through university wafers, and wafers grown using the heat exchanger method (HEM) bought from Crystek. We then diced the NbTiN wafer in 5X7 mm chip to fit in our sample holder (see next paragraph) using a DISCO tool from Université Lyon 1L. Prior to dicing, the chips were protected using either a layer of resist or a layer of Aluminium, covered by resist. The chips are then cleaned thoroughly, and we then pattern a resist mask using optical lithography (SmartPrint system of Microlight3D). We then use an ICP-RIE tool (SENTECH, located at Centrale Lyon) using a CHF3 chemistry. We then remove all resist residues with a solvent clean, possibly followed by an annealing step to remove hydrogen absorbed on the surface. The major change we later worked in the recipe was to move from a resist mask to a mask made out of Aluminium during both dicing and patterning to prevent contaminating the NbTiN with resist residues.

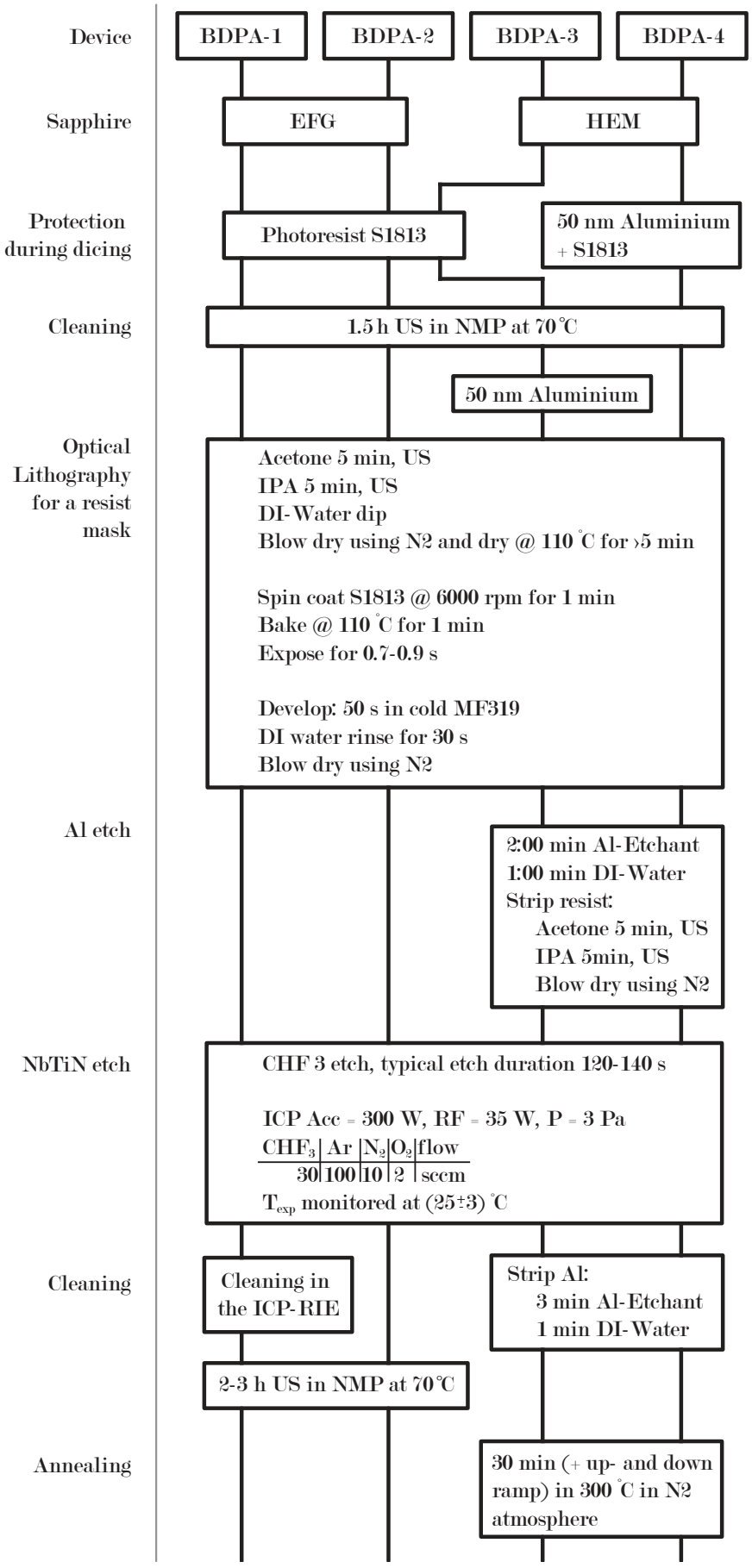

Figure 3.8: Overview of the fabrication for all devices. Also, the two first devices were realized on a Si-substrate, one of them using an SF_6 etch, other than that they follow the same fabrication as outlined for the "BDPA-2" device. We used the aluminium etchant type A from Transene. (Ultrasonic bath is abbreviated as US.)

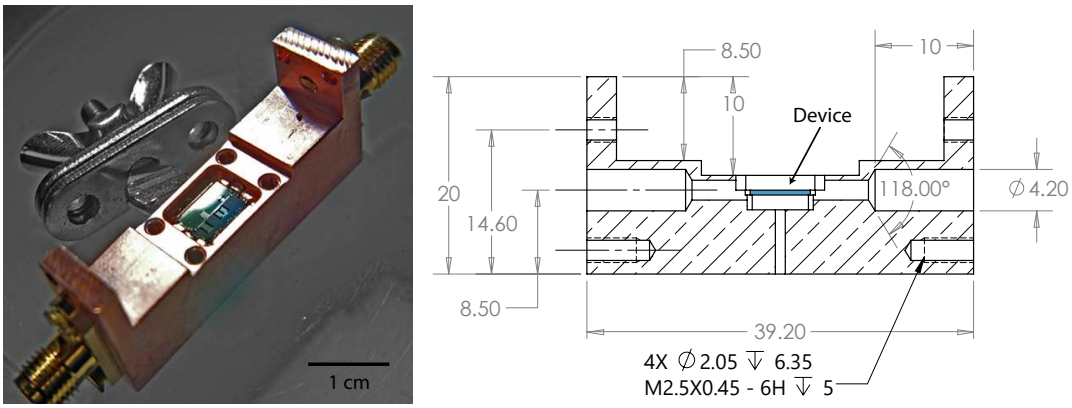

Figure 3.9: Sample holder with the initial device (left) and technical drawing of a longitudinal cut through the sample holder.

Table 3.4: Box modes of the sample holder, simulated in HFSS using the "Hunting Impurities" device without any resonator to connect the two ports.

Mode	Frequency (GHz)	Q
1	10.43	3
2	13.80	107
3	16.04	6
4	22.19	12

3.2 SAMPLE HOLDER

The design of the sample holder was mainly constrained due to the limited space inside to the coil setup. It is machined out of pure copper (CuC2 /OFHC) and hosts the devices suspended on a small ledge. The device is held in place by wire-bonds from a second ledge level with the device surface, connecting the device to the ground. There are two ports available made from female SMA flanges which are screwed to the outside of the box. The solder pads of the device are then wire-bonded to the pins of the SMA connectors. With the two ports available, the sample holder can host both, one port devices for reflection- and two port devices for transmission measurements. The holding box has the dimensions of 7.1 mm x 5.1 mm x 3.6 mm, a picture and a technical drawing of the longitudinal cut are shown in Figure 3.9. We have simulated the box modes of the sample holder using HFSS showing the first modes above 10 GHz with low-quality factors (see Table 3.4), providing a clean microwave environment for the device.

3.3 CRYOSTAT SETUP

In order to minimize the technical noise and get a high spin polarization, all experiments were carried out at 20 mK in a LD BlueFors dry dilution cryostat. The cryostat has several stages (50 K, 4 K, 800 mK, 50 mK and 20 mK) at which the signal lines are thermalized. To shield the following stages from radiation, there are in total 4 radiation shields anchored at the 50 K, 4 K, 1 K, and 20 mK stage. To reduce the thermal noise

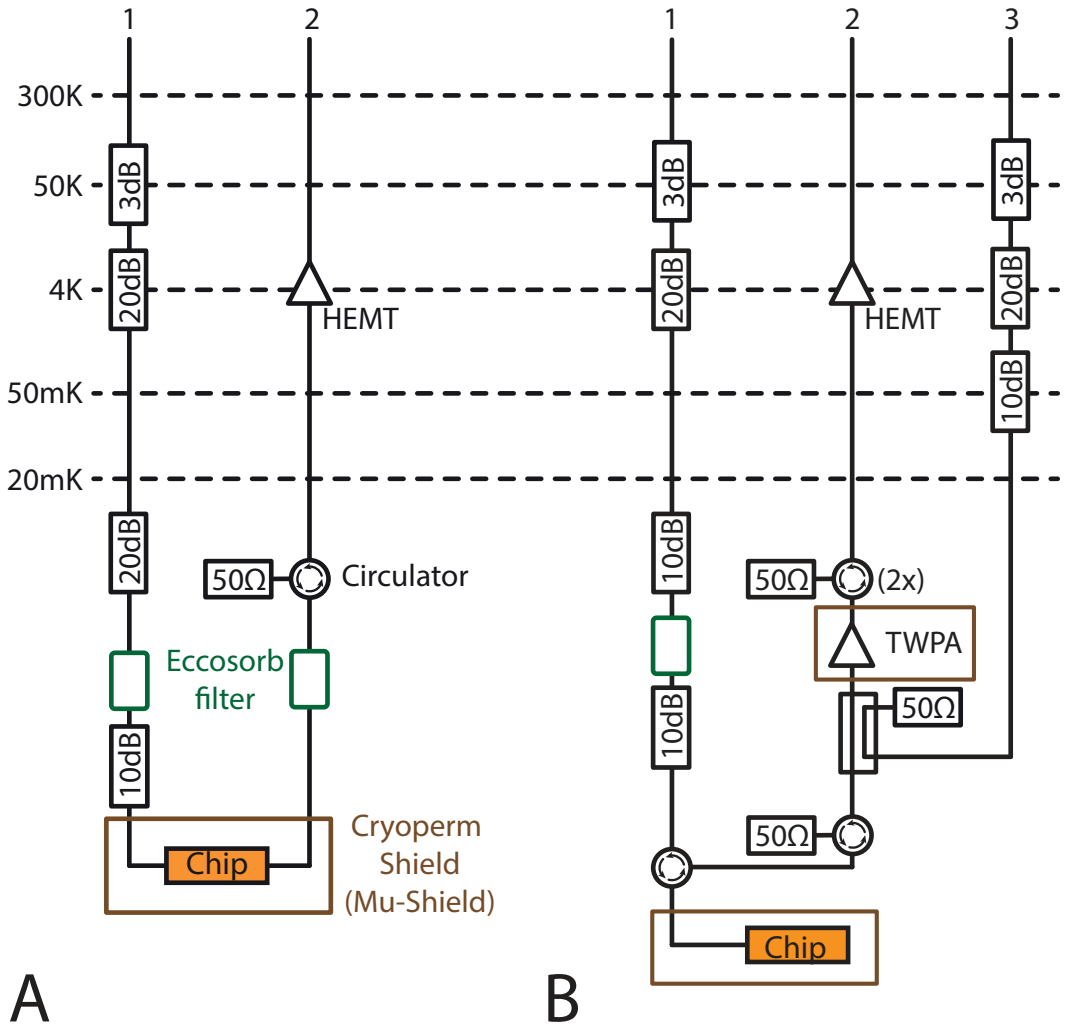

Figure 3.10: A: Initial setup for the first transmission tests without a JTWPA. B: Latest setup for a reflection measurement using the JTWPA within the amplification chain. For a transmission measurement, the device is placed in between the two circulators.

coming from room temperature, the signal is attenuated at each stage with thermally anchored attenuators (purchased from XMA) with a total of 43 dB. Considering an 7 GHz input signal at room temperature with $n_{\mathrm{th}} = k_{\mathrm{B}}T/(\hbar\omega) = 900$ photons, this leads to an expected thermal population of $n_{\mathrm{th}} = 0.1$ photons at 20 mK. Each attenuation step reduces the thermal noise by the attenuation A while adding its thermal noise $n_{\mathrm{th}}(T)$. An overview of the cabling for measurements in reflection and transmission is given in Figure 3.10.

To reduce the generation of quasi-particles into our superconducting devices, we shield the lines from infrared radiation by inserting Eccosorb filters. These filters are designed to attenuate linearly with frequency, and thus should absorb radiation about or above the superconducting gap. The output line comprises a JTWPA amplifier at 20 mK followed by a HEMT amplifier at 4 K. Circulators (Low Noise Factory) are inserted in between the JTWPA amplifier and the HEMT (Low Noise Factory) and

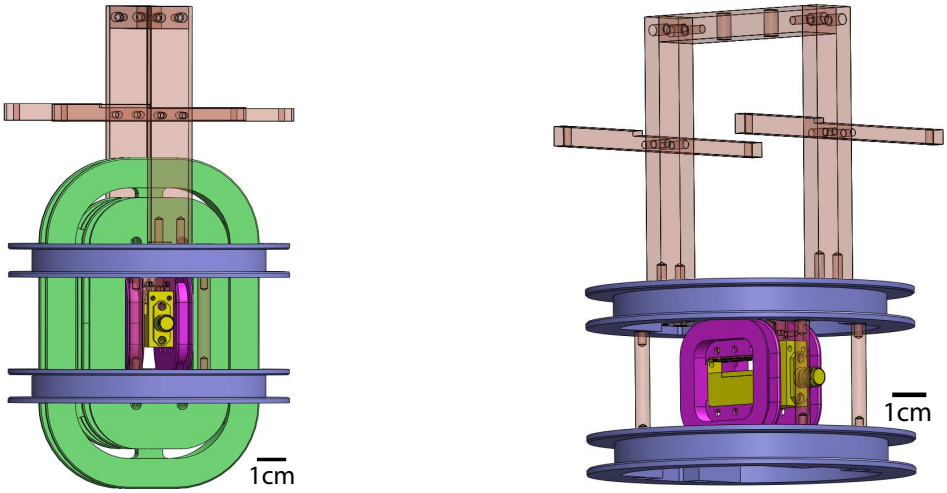

(a) All three coils, including the sample holder.

(b) Y-and x-coil, the z-coil is not shown for clarity.

Figure 3.11: False coloured CAD model of the coils. Colour code: z-coil = green, y-coil = blue, x-coil = red, sample holder = yellow. The copper frame is shown transparent.

between the sample and the JTWPA to shield the experiment from thermal noise and from back-scattered noise emitted by the amplifiers.

3.4 COILS DESIGN, WINDING AND CALIBRATION, TRAINING

To generate the magnetic field necessary to perform EPR measurements, a home built coil is installed on the 20 mK plate. The experiment is aiming to work in the frequency range from 5 GHz to 8 GHz. Assuming a spin 1/2 with a g-factor of 2, this translates to a magnetic field range from 200 mT to 300 mT. Higher magnetic fields would enable us to measure different spins, but being able to reach 300 mT is in principle sufficient for a first proof of concept and a spectrometer characterization using BDPA. The magnetic field has to be in plane with the NbTiN to minimize the generation of vortices, which lower the quality factor of the resonators. To ensure the best possible alignment between the magnetic field and the superconducting film, we include two compensating coils along the other two axes. To make sure to meet the required fields we aim for a magnetic field of 800 mT as we expect that effects like wire tension, kinks in the wire will occur and lower the in practice the achievable field. In the same cryostat as the coil, there will also be a qubit experiment. Therefore, the available space for the coils is relatively small, and a compact geometry is needed, which at the same time minimizes the stray field to not disturb the qubit experiment.

The final design consists of two Helmholtz coil pairs in x and y direction for the compensation of any misalignment between the main z-field and the device and one Helmholtz coil pair in the z-direction (see Figure 3.11). The z-coil pair also includes a coil in the middle in an anti-Helmholtz configuration to lower the stray magnetic field to about 10 mT at 5 cm. This does not significantly impact the homogeneity of the magnetic field but reduces the maximal achievable field by about 10 % to 20 %. It, however, allows the stray field to be low enough to be shielded using a single cryoperm

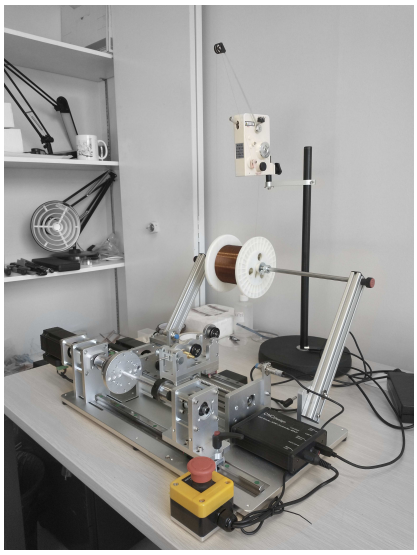

Figure 3.12: CNC design winding machine with the variable wire tensioner.

(cryogenic equivalent of μ-metal with $\mu_B = 10^4$) layer without reaching its saturation point ($B_{sat} \approx 200\,\mathrm{mT}$). To be as space efficient as possible, we opted for rectangular bobbins for the z-coil and the x-coil, and only for the y-coil we used a radial coil (see Figure 3.11), resulting in a 10 cm diameter footprint.

The coils are wound using 0.15 mm diameter NbTi isolated wire on a CNC Design coil winding machine (see Figure 3.12). The main challenge during the winding process arose due to the rectangular shape of the z and x-coils. In particular, the alternants between flat parts and small turn radius leads to a non-uniform tension during one wind. Reducing the tension turns out to be difficult if at the same time a neat nesting of the wire is to be achieved along the flat part of the coil. In an effort to keep the tension low, we used a variable wire tensioner. This is essentially a spring attempting to keep the tension on the wire constant by compensating for large radius changes.

After winding, the coils need to be ramped up and quenched repeatedly for the winds to settle. During this training process, the cryostat was operated at 4 K to not damage the dilution unit during the coil quenches. After a number of quenches, a plateau of a maximal current is reached. In Table 3.5 the maximally achieved current as well as the expected magnetic field is listed for each set of coils. In Figure 3.13 the training for the z-coil pair is shown. It turned out that we can achieve a field of 300 mT reliably, even after several warm and cool-down cycles. The exact magnetic field at the sample site was later calibrated using the $S = 1/2$ spin line.

We have forgone casting the coils after the winding and training due to the effort and risk involved. The final number of winds can be found in Table 3.5.

Each coil assembly is fed by one current source. As all coils are wound separately, we need to solder the coil pairs together. The coil is anchored at the 20 mK stage, with a cooling power of 20 μW. A solder joint at 20 mK would thus need to have a resistance of less than 0.2 μΩ to not warm up the fridge. While this is achievable, we preferred to place the joints at the 4 K stage, whose cooling power is 1.5 W. To protect the wires from kinks and accidental damage, the wire pair of each coil is sleeved with a PTFE

Table 3.5: Number of winds, expected maximal magnetic centre field for the maximally available current of 10 A. In the later experiment, the two compensating coils have a maximum available current of 0.5 A. Each set of coils was tested while the others were at zero field.

Coil set		Winds	$B_{max,theo}$	$I_{max,exp}$	$B_{max,exp}$
Bz	Helmholtz	3150	800 mT	6.0 A	540 mT
	Anti-Helmholtz	2310			
Bx		1530	165 mT	7.5 A	125 mT
By		312	300 mT	10 A	300 mT

tubing before routing it to the 4 K stage. The solder joints are done within small copper blocks, which are thermally anchored to the 4 K stage via a big copper L-bracket. They are electrically isolated using Kapton tape and plastic washers. From this solder block up into the connection to the high-current leads, the NbTi wires are protected by a copper tubing. The fit through 4 K stage is leak tight, with the copper tubing fixed in place with Stycast. The leak tight shielding of the NbTi wires protects them against the radiation from the 50 K stage. Due to practical reasons, all wires from the coils end at said L-bracket, where they are either soldered to wires going to the high T_C connectors or soldered together to form the coil pairs.

At room temperature, we use a current source with high precision (BE from iTest) for the z-coil and two current sources with lower precision (BK9171 from BK Precision) for the x-and the y-coils. We use the power supplies in current mode and monitor if they are current or voltage limited.

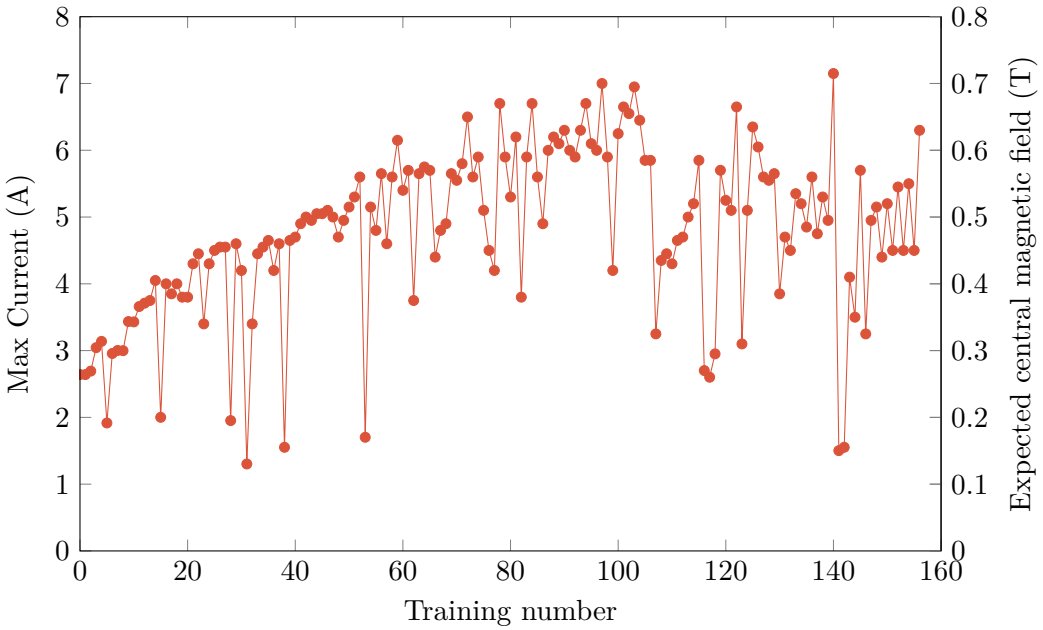

Figure 3.13: Coil training of the main coil pair. We see an overall increase of the quench current with the number of repeated quenches (Training number) and a saturation around 5 A, and a maximal achieved current of 7 A. The magnetic field is calculated from the coil dimension.

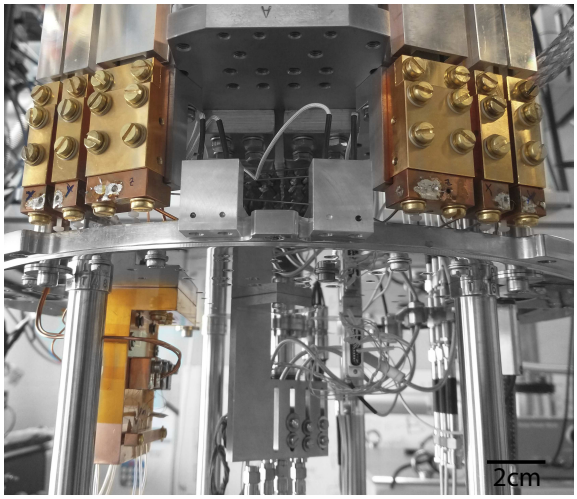

Figure 3.14: Image of the 4 K stage, where the NbTi wires of the magnet are connected with the high T_c wires in the cryostat. The NbTi wires guided through the stage plate within a copper tube leading to the solder connector.

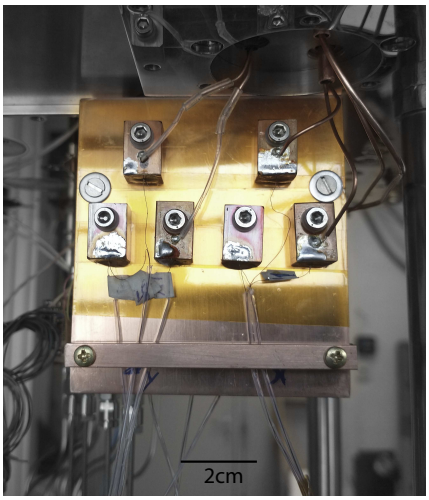

Figure 3.15: Thermalization L-bracket for the NbTi solder joints connecting the individual coils to form the Helmholtz-coil pairs (also seen in Figure 3.14 in the lower left). This bracket is also where the wires soldered to short connecting NbTi wires leading to the high T_c wires.

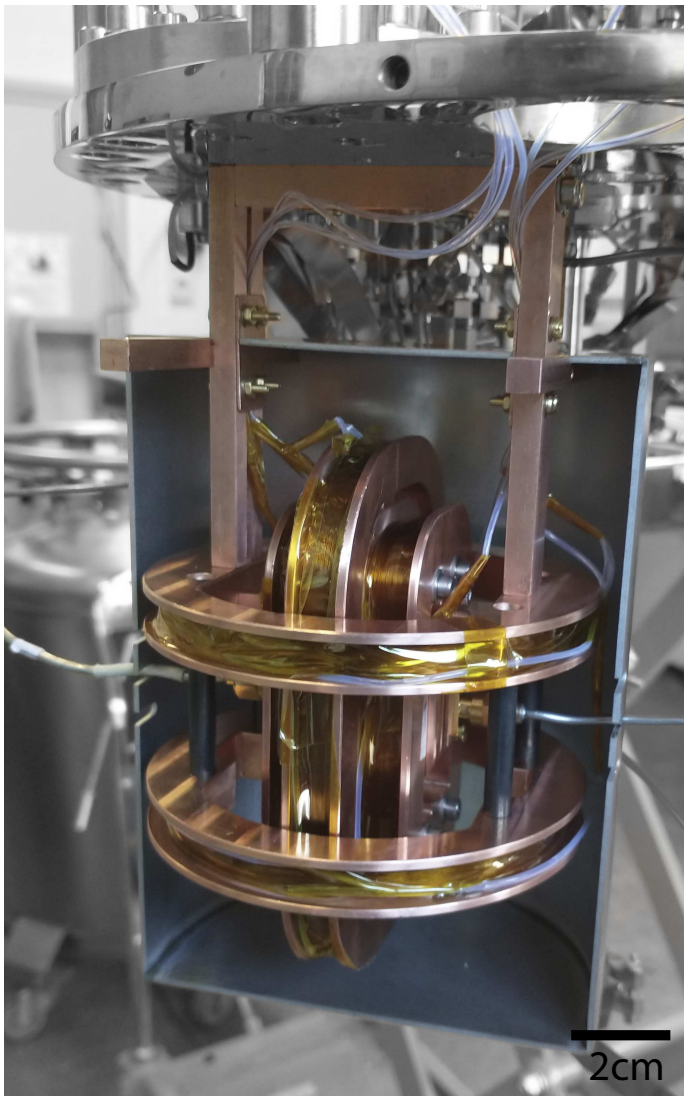

Figure 3.16: The fully assembled magnet including the sample holder is mounted to the 20 mK stage.

3.5 SAMPLE DEPOSITION

We aim to probe species which are not implemented in low-loss crystals. In the following, we will have a look at general sample deposition techniques and the possibility to employ them in the context of this project. We keep in mind that the maximally available sample volume is on the order of 0.3 pL to 20 pL (see Table 3.2) and that we are targeting a possibly wide variety of samples. Subsequently, we have a closer look at the drop casting sample deposition platform we have developed.

3.5.1 *Techniques Overview*

3.5.1.1 *Thermal Evaporation*

An established way of depositing thin films of metals and organic radicals is thermal evaporation. This is usually done under high vacuum. The material to be deposited is heated up and condenses on the target surface. Using this technique, layer thickness ranging from monolayers to nanometres can be achieved. However, this method requires the evaporation temperature of the sample to be high enough for precise evaporation and low enough for evaporation to take place. For example, [98] deposited BDPA on graphite with monolayer precision. The same is not possible with similar compounds such as TEMPO as the evaporation temperature is too low for precise control [98]. For our purpose, this method comes with a few drawbacks. The process requires a fine-tuning for each type of sample and requires the sample to be compatible. For example, with this technique, it would not be possible to place crystals such as diamonds with NV centres. It also requires the use of a mask to prevent the whole surface from being coated. [98]

3.5.1.2 *Solvent Deposition*

Another way of getting the sample into place could be solvent deposition. The sample molecules or crystals would be suspended in a solvent and spin coated on top of the whole chip. This is typically done in Biology to coat surfaces with protein structures such as DNA. Although alleviating the necessity to evaporate the sample, this technique comes with the same drawbacks as thermal evaporation, as the whole surface is coated. Nonetheless, this technique has been used by [98] to deposit BDPA. One could envision mixing the sample with a photo or e-beam resist and performing a lithography so that the sample is only present in the sample volume. This would, however, require that the resist used is EPR silent and that the sample is compatible with the lithography process.

In Chapter5 we will see that the background in the internal quality factors can be increased significantly when protecting the NbTiN during the fabrication with a layer of aluminium. Both processes, the thermal evaporation and the solvent coat, would require a coating of the surface after the removing of this protective aluminium layer.

3.5.1.3 *Inkjet Printing*

Inkjet printing is a technique routinely employed in the fabrication of organic electronics [99]. In drop on demand inkjet printing, a continuous stream of drops is dispensed from a gun either by a piezo electric or thermally. These drops are then electrically charged and guided by an electric field to be placed either on the substrate or into a waste container. The resolution for this is typically limited to 20 µm to 50 µm. This can be improved by engineering the surface energies of the substrate as well as the ink. However, although this inkjet printing allows placing individual drops, the resolution is too large for our specifications. [99]

3.5.1.4 *Micro Contact Printing*

Micro contact printing has been explored in the context of organic electronics or protein placements [100], [101]. This technique relies on manufacturing a stamp which is wetted with the ink and then pressed onto the surface. It is not limited by diffraction and can therefore be used for sub 100 nm structures [101]. In principle, the process always begins by fabricating a negative structure, on which the final stamp is made. This stamp is typically made out of an elastomer, such as Polydimethylsiloxane (PDMS). After lifting the stamp from the negative form, it is inked. Excess ink is washed off, and finally the stamp is pressed onto the target using two conformal surfaces. Having the slightly flexible stamp pressed onto the surface makes it possible for the stamp to compensate for some surface unevenness. Pong et al. has demonstrated the printing of BDPA circles with a diameter around 1 µm in a lattice. To be suitable for our project, this technique has to however be combined with precise alignment of the stamp, and accomplish it in a time short enough for the ink to remain liquid. Provided this challenge could be tackled, and that the sample is liquid, this technique could be used for the project.

3.5.1.5 *Micropipettes*

The last way of depositing samples that we will examine is micropipettes. These are pipettes of typically small volume of around 1 µL to 100 µL [102, 103]. They are also part of the fabrication repertoire of organic semiconductors [104]. Here, plastic pipettes are used in a last step to drop cast the organic compounds on the electric pads. In biology, micropipettes are used to perform aspiration measurements on single cells or to inject proteins into cells [105]. For this, a pipette, typically out of borosilicate, with diameters of around 5 µm to 50 µm is brought close to the cell. Using a negative pressure, the cell is then partially sucked into the needle and its deformation can then be analysed [106]. Depending on the particular application, the used pipettes can either have a flat or angled tip. One of the significant differences between the biology and the organic semiconductor application is that the first usually takes place in a liquid and the latter is an actual drop cast. If we were to use small borosilicate pipettes in a similar fashion as in biology setups together with a solution against the wetting of our surface, as seen in the micro pipetting of organics materials, this could be a way to drop cast our samples.

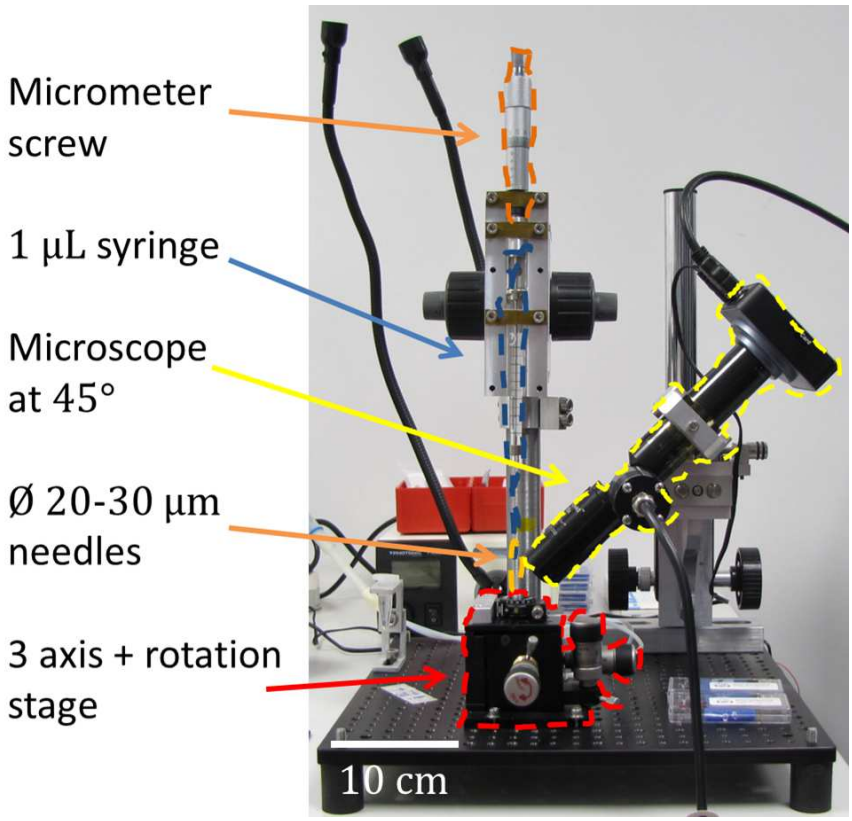

Figure 3.17: Picture of the drop casting setup.

3.5.2 *Drop Casting Setup*

We build the drop casting setup around a stainless-steel microlitre syringe (World Precision Instruments: SGE001RN). Together with the syringe, we use borosilicate tips with varying diameter (TIP30TW1 and TIP20TW1 from World Precision Instruments and MGM-1A-20-30 from Holzel). The seal between the tips and the syringe is done by slightly pressing the conical taper of the syringe into the tips, which are then taped in place. The needle is fixed onto a z-stage, which enables a rough approach to the sample. To control the plunger of the syringe, a micrometer screw is used. It is fixed to the plunger using two magnets, such that the rotation of the micrometer screw is still possible. To prohibit a rotation of the needle tip, the plunger is guided by a rail. The chip itself is placed on a 3 axis and rotation stage (MBT616D/M and PRM05/M from Thorlabs) and is held in place by applying negative pressure. To observe and control the setup, a microscope (Infinitube from Edmund optics outfitted with an Achrovid x10 objective) is mounted at an angle of 45°. It can be moved in all 3 axis using a set of translation stages.

During our tests, we tried out different needle diameters as well as different solvents. It became clear that the system is dominated by the interplay of surface energies. For pure water, anisole, and ethanol, every test resulted in an immediate wetting of either the sapphire surface or the needle tip. When trying to form a drop at the tip of the needle, there was no continuous forming of a drop with increasing pressure (plunger push). The liquid forms a convex surface, which then breaks for the liquid to spill out

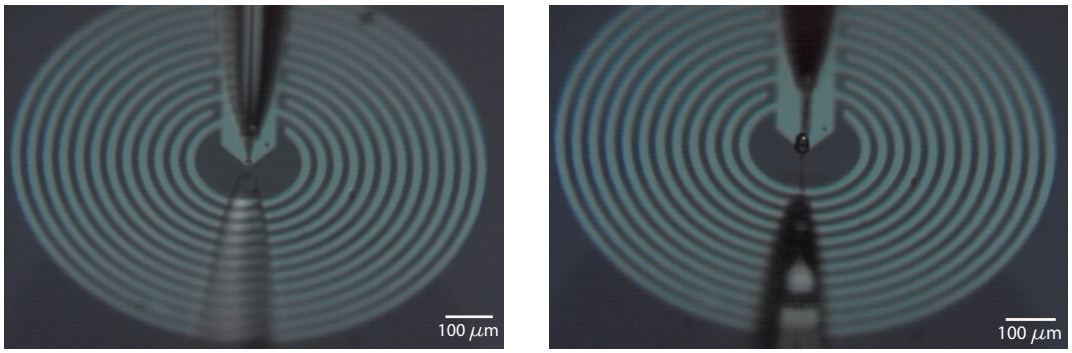

(a) Approaching the surface with the tip.

(b) The placed drop on the resonator.

Figure 3.18: Before and after the drop casting with a 20 µm diameter tip using A2 PMMA. The outer diameter of the drop is ≈10 µm.

and wet the needle surface. If one brings the convex liquid surface in contact with the sapphire, it results in a wetting of the sapphire surface. The covered area depends on the previously applied pressure. This behaviour was seen across all used needle diameters. Increasing the viscosity of the liquid resolves this issue. This goes hand in hand with the host matrix for the spin system. What we found works best is A2 PMMA (A4 PMMA: Anisole; 1:1) in combination with 30 µm diameter tips.

The final working procedure consists of:

- Load the syringe with A2 PMMA.
- Mount the tip with tape.
- Place the tip over the targeted spot.
- Push the plunger with the micrometer screw to fill the dead volume between the needle and tip until the liquid is at the tip opening.
- Move the tip down until it touches the surface and push the plunger a bit further. This presses the liquid onto the surface and forces a wetting.
- Move the tip upwards (or the sample down) until the drop has the desired height.
- Retract the plunger to break the connection of the liquid in the tip with the drop. If this is not done, this leads to a long pillar thinning out at the top.
- Move the tip up.

Using the pictures taken at an angle, one can estimate the drop's height and volume. To achieve this, the angle at which the picture was taken can be calculated from the distortion of the circles of the capacitor. With a being the long axis, which is the undistorted length and b the distorted axis, the angle of the camera is $\gamma = \cos^{-1}(b/a)$. An estimate for the height is then $h_{\text{est}} = \sin(\gamma) \cdot h_{\text{pic}}$. This is not necessarily the true value, but gives an upper bound, as shown in Figure 3.19b. The drop shown in 3.19b has a height of ≈32 µm and thus a volume of approximately $70 \times 10^3\,\mu\text{m}^3 = 70\,\text{pL}$.

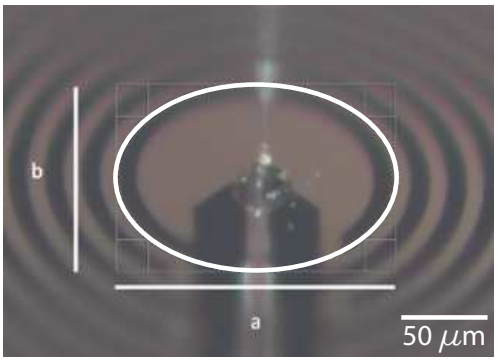

(a) Close-up on a drop on the resonator together with an ellipse matching a finger of the capacitor.

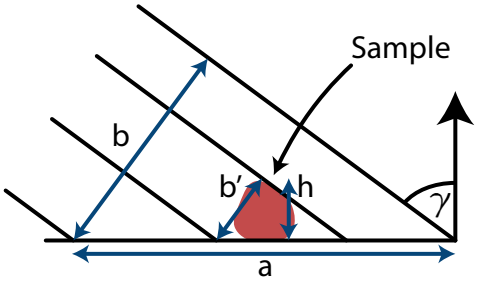

(b) Schematic to estimate the height and the volume of the placed drop.

Figure 3.19: Estimation of the drop height. As illustrated, this estimate is an upper bound, as it is possible that the highest point of the drop and the highest point in the picture do not coincide.

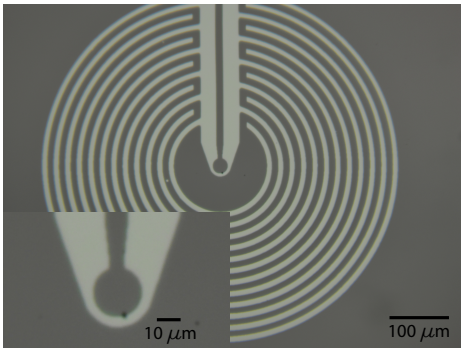

(a) The small black point on the inner loop is a diamond pushed in place.

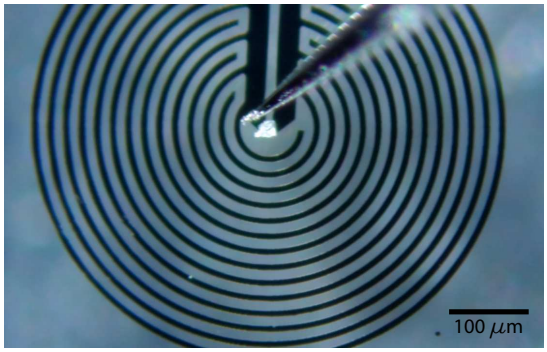

(b) Polypropylene piece being pushed into place using a tungsten tip.

Figure 3.20: Examples of crystalline samples placed on the resonators.

3.5.3 *Pushing*

Crystalline samples (e.g. NV Centres) which cannot be placed with the drop casting setup can be pushed into place by using a small enough tip of some sort. After placing some crystals on the side of the chip, they can be selected by size and pushed into place. To push a crystal, we fix the tip and move the chip, either already wire-bonded or on its own, with the 3 axis and rotation platform.

Another way of preparing a spin sample with PMMA/PS as host matrix is to cast a thin film. For this, the desired concentration is prepared and then poured onto a flat surface, if desired, one can spin coat the surface as well. A properly sized piece is then cut off and transferred to the sample space. We did this with moderate success by pouring a PS matrix and attempting to cut off a piece to finally push it in place. Cutting off a piece small enough was difficult and resulted in more of a 'ripped' than 'cut' piece (see Figure 3.22b). Due to the film being flexible, it folded back onto itself, and it was not clear where it touched the surface. This method of sample preparation seems unreliable and difficult to control.

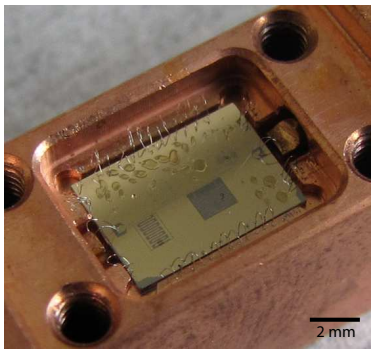

(a) Manual BDPA placements on the initial device.

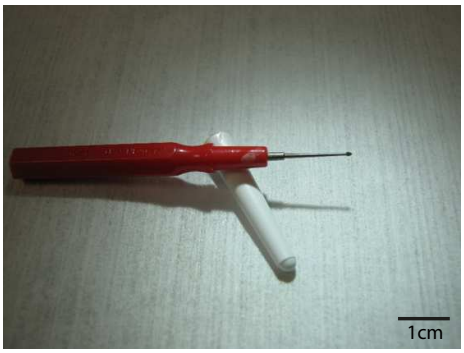

(b) Spatula used for the BDPA placements in Figure 3.21a.

Figure 3.21: The initial device with BDPA sample and the used spatula.

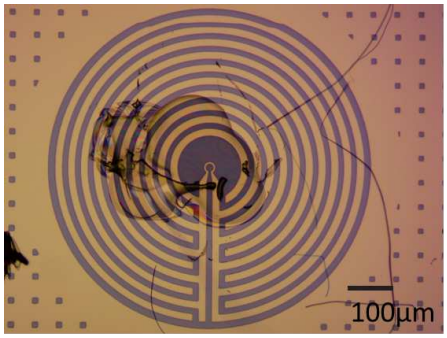

(a) BDPA in PMMA placed manually with a spatula on the circle resonator of the initial device, the capacitate region of the resonator is partially covered.

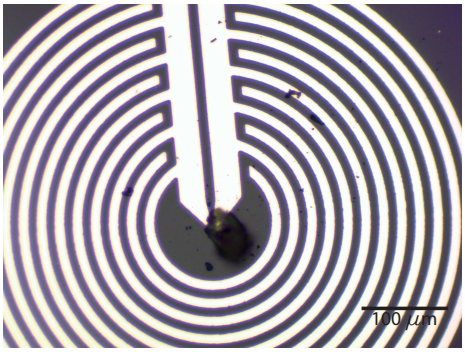

(b) BDPA in a PS thin film matrix pushed into place on resonator one of the "BDPA-A" device.

Figure 3.22: Comparison between a PS flake pushed into place and the BDPA sample, which was deposited using a spatula.

3.5.4 *Manual Placement*

The very first measurements we performed were done on BDPA in PMMA placed using a spatula (see Figure 3.21). This is a challenging to control process which requires a steady hand. We placed a big drop on the side and successively moved away from it while tapping the surface and thus placing drops of decreasing size until the drop size matched the desired size. The next tap should then be at the target place, depositing a drop of the correct size. This whole process is made difficult not only by the precision required but also by the time pressure, as the solvent evaporates quickly and one only has a couple of seconds until the final drop has to be in place.

3.6 SPIN SAMPLES AND HOSTS

As mentioned in section 1 the EPR community uses various techniques ranging from continuous wave high-frequency and high field studies [107] to pulsed experiments using quantum circuits [40]. Depending on the application of the spectrometer, there is a

need for a precise calibration of different experimental parameters as well as for a figure of merit for the spectrometer performance [108]. Common calibrations against a known sample are the signal-to-noise ratio or "weak pitch" which calibrates derivative signal amplitude, a g-value calibration and the spectrometer spin sensitivity (see Chapter 6).

The g-value calibration effectively probes the constant magnetic field and sets its value via the known g-factor of the calibration sample. At moderately low fields this is most commonly done using 2,2-diphenyl-1-picrylhydrazyl (DPPH) [109][108]. It is a free radical organic compound and as such has a g-factor $g_x = 2.00435$, $g_y = 2.00367$, and $g_z = 2.00245$ [110] close to two due to a free electron. In high field EPR, atomic hydrogen or rubies can be used [111] [108]. The reason for why DPPH cannot be used at high fields lies in its small g-factor anisotropy, which depends on its growth and preparation conditions [112]. This highlights that the reference sample is to be as closely related in chemistry and preparation to the actual sample as possible. As we would like to probe in the future crystalline organics, it would be a natural choice to do our spin sensitivity characterization on DPPH. However, DPPH-Bz, similar to other closely related compounds, undergoes a phase transition from paramagnetic to antiferromagnetic ordering below approximately 500 mK [113]. At low frequencies this leads to a drastic decrease in the intensity of the $g = 2$ line with a broadening of the line going up to 150 MHz [113, 114, 115] and a $g = 4$ dipolar transition takes over. Voesch et al. measured DPPH powder using a superconducting coplanar resonator out of niobium in the temperature range from to 30 mK to 800 mK at frequencies 1.5 GHz to 4.5 GHz. They found the g-factor to be dependent on magnetic field and temperature. This discourages the use of DPPH as a calibration sample for low temperature EPR in the X-Band regime.

Another compound which can be used for spectrum characterization is α,γ-Bisdiphenylene-β-phenylallyl (BDPA) (see Figure 3.23a for the chemical structure) [117] [118]. As DPPH, it is also a stable organic radical with a g-factor of 2.0026 ± 0.0002 at room temperature, which increases by 0.3 % when going to liquid helium temperature [119]. The crystal structure is well studied [120],[121], and it undergoes a phase transition from paramagnetic to a three-dimensional Heisenberg antiferromagnetic at 1.7 K (for BDPA crystallized from a benzine solution) [122] [123] [110]. Yamauchi shows that the EPR spectrum associated with the antiferromagnetic resonances vanishes with low concentration while strengthening the resonance with $g \approx 2$ (see Figure 3.23b) [124]. For the T1 and T2 relaxation times, one finds $T1 \approx T2 = 100$ ns at 77 K to [125], [126] and $T1 = 7$ µs, $T2 = 650$ ns at 7 K [127]. Recently Bonizzoni et al. reported $T_1 = 1.9$ µs to 2.3 µs measurements on BDPA using inverse anapole resonators at 4 K measured at frequencies from 7 GHz to 14 GHz [42]. We will mostly use BDPA as the spin sample throughout the thesis.

For the characterisation of the spin sensitivity and a proof of concept measurement, we dilute the BDPA to be able to place a precise and known number of spins in the resonator sample space. BDPA is solvable in toluene and anisole. To provide a homogeneous distribution of the BDPA within the drop and avoid any accumulation of BDPA at the edge of the drop, we chose to integrate BDPA into a host matrix. We tried Poly (methyl methacrylate) (PMMA) and Polystyrene (PS) as two different host matrices (see Figure 3.24 for the chemical structures). PMMA is one of the oldest

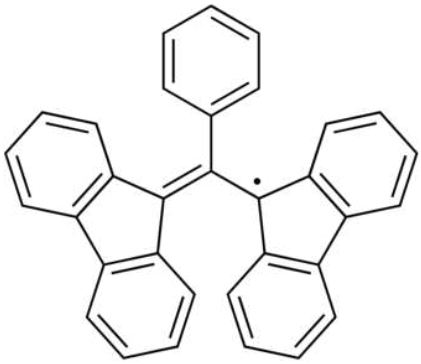

(a) Chemical structure of BDPA, the benzine is not shown. · is the free electron.

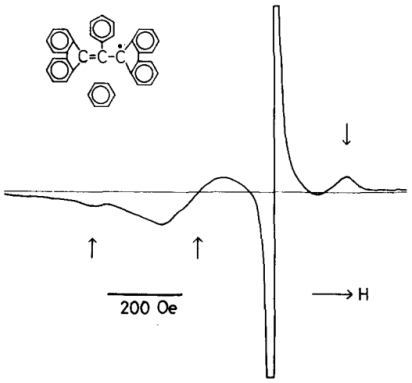

(b) EPR spectrum of BDPA at 339 mT measured at 1.528 K. The arrows show the antiferromagnetic resonances. The cut-off resonance is the paramagnetic g=2 line. [122]

Figure 3.23: Chemical structure of BDPA and its X-band EPR spectrum.

polymers used because of its biological compatibility [128] and is nowadays used as a resist in the fabrication of superconducting circuits [130, 131]. PS is a standard polymer used for Petri dishes and lab ware [129]. PMMA, as part of the fabrication processes, is readily available in an anisole solution and PS can be bought as a polymer. Both polymers are EPR silent, making them a sensible choice for a host matrix (PS: [132, 133],PMMA: [134, 135, 136]).

3.6.1 *Spin Sample Preparation*

We essentially have used four different BDPA concentrations, of 9.71×10^{12} spins mL^{-1}, 1.14×10^{12} spins mL^{-1}, 6×10^{15} spins mL^{-1} and 6.07×10^{17} spins mL^{-1}. The choice of these concentrations arises from the need to avoid the strong collective regime, but still have a high enough spin concentration to be detected. These conditions applied to the resonator designs of the BDPA device (see paragraph 3.1.4.2) result in an average minimum concentration of 2.4×10^{11} spins mL^{-1} and a maximum concentration of 2.4×10^{14} spins mL^{-1} (see tab. 3.6). The BDPA is from Sigma-Aldrich and comes in a glass flask with 100 mg of BDPA inside. To realize the dilutions, we have used a 10 µL fixed volume pipette and a 1 mL pipette. Between each dilution, the resulting solution is mixed using a vortexer.

PREPARATION FOR INITIAL DEVICE An initial attempt was done using a high concentration of 6.07×10^{17} spins mL^{-1} to observe a signal using the Initial device to provide a reference for the home-built coil (see Chapter 4) The solution measured on the initial device was prepared using PMMA A6:

- 100 mg of BDPA (1 flask)
- First dilution D0: Mixed flask content with two times 1 mL of PMMA A6

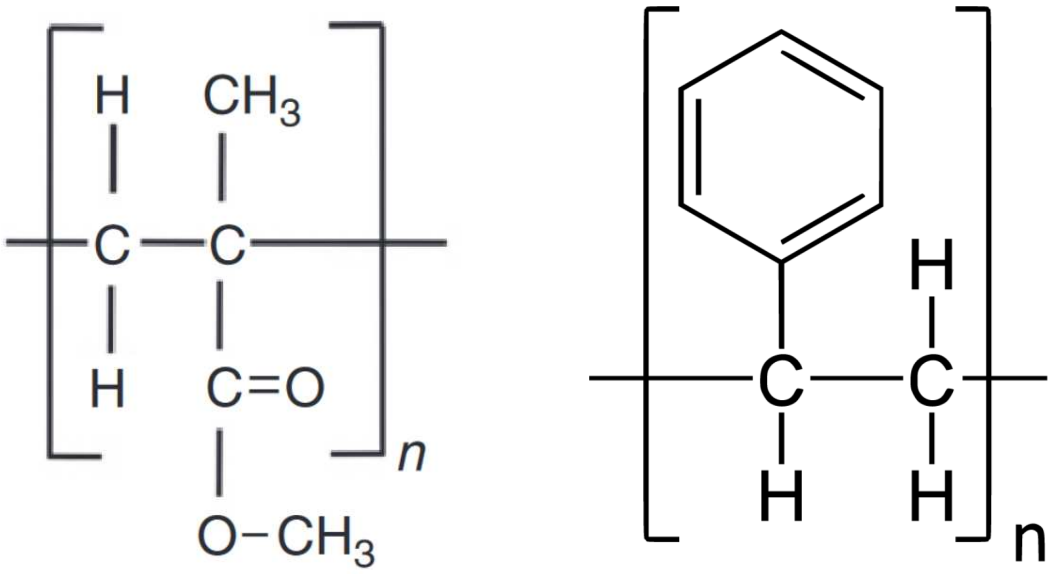

(a) Chemical structure of PMMA [128] (b) Chemical structure of PS [129]

Figure 3.24: Chemical structures of the host matrices used.

Table 3.6: Minimum and maximum spin concentration assuming a cooperativity of 0.5

Resonator	Min. conc. (spins/mL)	Max. conc. (spins/mL)
1	3.9×10^{11}	2.4×10^{14}
2	5.8×10^{10}	1.4×10^{14}
3	5.5×10^{11}	4.8×10^{14}
4	1.5×10^{11}	2.8×10^{14}
5	4.9×10^{11}	3.6×10^{14}
6	1.1×10^{11}	1.5×10^{14}
7	1.2×10^{11}	1.8×10^{14}
8	3.1×10^{10}	1.1×10^{14}

- Second dilution D1: 100 µL of D0 + 900 µL of PMMA A6
- Third dilution D2: 100 µL of D1 + 900 µL of PMMA A6

Using PMMA A6 has the advantage of a higher viscosity, which makes this initial solution better suited for a deposition using the spatula. The final spin concentration is 6.07×10^{17} spins mL^{-1}.

PREPARATION FOR BDPA DEVICE For measurements using the BDPA devices, we wanted to use the drop casting setup, and thus used a PMMA preparation with lower viscosity - A2 (Anisole with 2 % PMMA) as a solvent. We have worked with several spin concentrations using PMMA as a host matrix. The recipes for these samples are summarized in Table 3.7. The solutions C1, C3, C4A, and C4B have been measured. The BDPA samples in PS are prepared similarly as the PMMA ones (see tab. 3.8), with the main difference that the solvent is not anisole but toluene.

Table 3.7: Recipe and summary of BDPA solutions in anisole with PMMA as hostmatrix.

Solution	Preparation	Concentration (spins/mL)
C0	100 mg of BDPA mixed in 2 mL of A2	6×10^{19}
C1	10 µL of C0 mixed in 1 mL of A2	6×10^{17}
C2	10 µL of C1 mixed in 1 mL of A2	6×10^{15}
C3	10 µL of C2 mixed in 1 mL of A2	9×10^{13}
C4A	0.2 mL of C3 mixed in 1 mL of A2	1×10^{13}
C4B	20 µL of C3 mixed in 1 mL of A2	1×10^{12}

Table 3.8: Following this recipe, we end up with a solution containing a spin concentration of 6×10^{16} spins mL^{-1} with respect to the PS, once the toluene has evaporated.

Solution	Preparation	Concentration (spins/mL)
T0	100 mg of BDPA mixed in 2 mL of toluene	6×10^{19}
T1	100 µL of T0 mixed in 1 mL of toluene	6×10^{17}
T2	10 µL of T1 mixed in 1 mL of toluene	6×10^{16}
T3	109 mg of PS mixed into T2 (the whole solution)	

4

RESONATORS IN MAGNETIC FIELDS

In this chapter, we will discuss the characterization of the superconducting resonators in magnetic field. We will first explain our fitting protocol to extract the resonance frequency and coupling rates. We will then summarize the behaviour we have observed in magnetic fields.

4.1 FITTING EXPERIMENTAL RESPONSE OF RESONATORS TO EXTRACT INTRINSIC LOSSES

Fitting the microwave response of planar resonators to extract their resonance frequency as well as their coupling and intrinsic losses rates is a basic task in many superconducting circuits experiments. The literature on how to best conduct this task is extensive (see [137, 138, 139, 140, 141]), and we only aim here to summarize what are its hurdles, and how we proceeded to provide the best estimate of the resonator characteristics. In this thesis, we have used two configurations for measuring the superconducting resonators: Samples with the "Initial" and "hunting impurities" design were measured in hanger geometry (see Figure 4.1) whereas samples dedicated to measurements of BDPA spins were probed in reflection thanks to the use of a circulator (see 4.1). Both types of measurements are done by measuring the transmission of a microwave probe signal from port 1 to 2 using a vector network analyser (VNA) to obtain the corresponding S parameter. Typically, the acquired measurement will not show the theoretical S_{21}^{th} response derived in Equations 2.14 and 2.15, but a distorted, rotated, and scaled version S_{21}^{m}. In Figure 4.4, one such measurement is shown.

Two main effects can explain the distortion. First, the acquired signal is routed throughout the cryostat, using at least 20 m of cabling, several attenuators, circulators and amplifiers. It is thus acquired with a global scaling prefactor $A\mathrm{e}^{i\alpha}$, as well as an electrical delay τ:

$$S_{21}^{\text{m}}(\omega) = S_{21}^{\text{th}}(\omega) \cdot A\mathrm{e}^{i\alpha}\mathrm{e}^{-i\omega\tau}. \tag{4.1}$$

As the theoretical transmission $S_{21}^{\text{th}} = 1$ away from resonance in both geometries, these factors can be easily removed by taking a broad scan and flattening the phase response outside the resonance and rescaling by the transmission measured at large detuning z_∞. This is a somewhat easy task as in our case the resonators have a narrow bandwidth, we only need the baseline transmission to be flat on a range of ≈ 1 MHz, which is easily verified (see Figure 4.3) despite for example the ripples coming from the TWPA gain. Performing this correction allows the post-processed data $\tilde{S}_{21}$ to lie on a circle passing through the coordinates (1,0) in the complex plane. Diametrically opposed to this (1,0) point lies data captured close to the resonance frequency. Explicitly drawing the diameter linking these two points as in Figure 4.2 evidences the second distortion effect: even after this global correction, the expected circle is tilted from its

expected position by an angle ϕ. It also results in a visible asymmetry in the shape of the dip occurring when plotting $|\tilde{S}_{21}|$.

This second effect comes from impedance mismatches between the coaxial lines probing directly the resonator and their immediate environment (illustrated for example by Z1, Z2, Z3 in Figure 4.1). A Fano interference effect can also arise due to either the circulator leakage or direct coupling between the ports. The consequences of these impedance mismatches have been analysed in [139, 137] and directly impact the expected theoretical responses from the resonator. These effects are difficult to model accurately since we can not directly measure the leakage, but on the frequency range covered by our resonator, they can be captured using only 2 variables for the hanger geometry:

$$S_{21}^{\text{hang}}(f) = 1/(1+l) \cdot \left(1 - \frac{Q_\text{l}/Q_\text{c} \cdot \mathrm{e}^{i\phi}}{1 + 2iQ_\text{l}(f-f_0)/f_0}\right) + l/(1+l) \tag{4.2}$$

with ϕ accounting for a phase shift induced by the impedance mismatch, and l expresses the leakage between ports [139]. In addition to contributing to the tilting of the circle by an undetermined phase ϕ, the leakage between ports shrink the overall shape of the resonator, thus effectively setting a minimum bound for the contribution of the intrinsic losses. Indeed, at resonance $S_{21}(f = f_0) = (\kappa_\text{i}/\kappa_\text{c} + l)/(1+l)$ in the limit of $\kappa_\text{i} << \kappa_\text{c}$, such that only ratio larger than the leakage magnitude can be resolved. Experimentally, that means only κ_i smaller than κ_c by about a factor 100 can be resolved, since we have about $-20\,\text{dB}$ coupling between ports. The data can interestingly be plotted in the inverse complex plane. In this case, the circle diameter is equal to Q_i/Q_c when $Q_\text{i} >> Q_\text{c}$.

For a reflection measurement, the situation is similar [139], yet there is no known form accounting for the impedance mismatch [141]. For small mismatches, it leads to similarly tilted circles. In analogy to the hanger geometry, the phase shift can be included as a contribution to κ_c. We can also include the effect of interference due to the circulator leakage, which similarly limits the determination of Q_i:

$$S_{21}^{\text{refl}}(f) = 1/(1+l) \cdot \left(1 - \frac{2Q_\text{l}/Q_\text{c} \cdot \mathrm{e}^{i\phi}}{1 + 2iQ_\text{l}(f-f_0)/f_0}\right) + l/(1+l). \tag{4.3}$$

4.2 PROTOCOL FOR FITTING

The fitting for both cases, reflection and hanger, can be separated into two parts. First, we correct for the electric delay and the overall scaling factor. In a second step, we perform the actual fit, taking into account the impedance mismatch ϕ while assuming that there is no leakage.

4.2.0.1 *Optimal electric delay and overall scaling factor correction*

As outlined above, we perform a rough correction of the prefactor $\alpha e^{i\omega\tau}$ by flattening the baseline over a broad frequency range. To optimally correct the electrical delay τ

we then estimate the deviation of the data to its best circle fit. For a given electrical delay, this circle is found by performing the least square minimization of:

$$\epsilon(z_c, R, \tau) = \sum_{\omega_i} |S_{21}^{m} e^{-i\tau\omega} - z_c|^2 - R^2, \tag{4.4}$$

where z_c and R are respectively the centre and radius of the circle. The optimal electric delay τ_{opt} is then found by minimizing the normalized residual $\epsilon_n(\tau) = \epsilon(z_c, R, \tau)/R$. The data is then normalized by the off-resonant point z_∞ and becomes

$$\tilde{S}_{21} = S_{21}^{m} e^{-\tau_{opt}\omega}/z_\infty. \tag{4.5}$$

As seen in Figure 4.4, $\tilde{S}_{21}$ now lies on a circle crossing (1,0), with the radius R of the circle being related to Q_i and Q_c for the hanger geometry as $R_{hang} = \frac{Q_i/Q_c}{2Q_i/Q_c+1}$ and by $R_{refl} = \frac{Q_i/Q_c}{Q_i/Q_c+1}$ in reflection [139]. Finally, to determine the circle rotation arising from the impedance matching, and f_0, Q_i and Q_c, we perform the least square minimization using $|(\tilde{S}_{21})^{-1} - (S_{21}^{th})^{-1}|$.

Later on, we adapted our fitting approach following Probst et al. [137] and the paper of Ioan Pop's group [139]. The determination of the circle is identical, but then only the phase $\Theta[\tilde{S}_{21}]$ is fitted using

$$\theta^{hang}(f) = \theta_0 + 2\arctan\left(2Q_l\left[1 - \frac{f}{f_0}\right]\right), \quad \theta^{refl}(f) = \theta_0 + 4\arctan\left(2Q_l\left[1 - \frac{f}{f_0}\right]\right). \tag{4.6}$$

Since the model function only depends on Q_l, f_0, this procedure is more robust. Q_c and Q_i can then be determined using

$$Q_c = \frac{Q_l}{2R \cdot e^{i\arcsin(y_c/R)}} \tag{4.7}$$

and $Q_i^{-1} = Q_l^{-1} - \mathrm{Re}(Q_c^{-1})$ in hanger geometry. For magnetic field and power scans, we assume that Q_c is constant. For a power scan, we determine Q_c from simultaneous fitting of all the scans with a common value. For a magnetic field scan, this is not possible due to the high number of scans. Therefore, we simultaneously fit the scans at a field $B_0 < 10\,\mathrm{mT}$ to obtain the value of Q_c and keep it as a constant for the individual fits of the S-parameter measurements of the magnetic field scan.

4.3 BENCHMARKING THE FABRICATION PROCESS AND THE RESONATOR DESIGN

We perform these measurements using the initial device described in Chapter 3.1.4.1 containing 4 different resonator geometries. The design served as a first calibration point of our fabrication process. Using high resistivity silicon as a substrate, we tested the SF6 and CHF3 dry etch and later on fabricated the same design using a sapphire substrate. The zero field data of the resonators on these three devices are presented in Table 4.1 below.

Table 4.1: Summary of the zero field fit results of the three initial device samples. The devices on silicon are labelled by the etch and the device on sapphire by "Sp". All data has been taken using an input power of −30 dBm at the cryostat input, resulting in $\bar{n} \approx (1 \text{ to } 10) \cdot 10^4$photons in all three cases. The resonator identification is done by comparison with simulation.

	μWire		$\lambda/4$		IDR		Circle		
Device	SF6	CHF3	SF6	CHF3	SF6	CHF3	SF6	CHF3	Sp
f_0 (GHz)	5.27	5.45	6.07	6.0	4.95	6.11	6.77	6.64	7.89
Q_i (10^6)	1.20	1.02	1.01	3.50	1.62	1.57	1.20	6.00	0.18
Q_c (10^4)	1.35	1.61	0.85	0.67	5.06	3.95	5.44	5.46	3.99

We first compare a SF6 and a CHF3 reactive ion etch using two devices on a silicon substrate. As shown in Table 4.1 there is no significant difference in the quality factors across the four resonators between the two devices. Visibly, however, the device etched using SF6 displays black spots, while the device etched with CHF3 is visibly clean (see Figure 4.5).

To understand the limitation of the internal quality factors, we performed a power scan for both devices (see Figure 4.6). We calculate the number of photons in the resonators based on an estimated total attenuation of $\alpha = -69.3\,\text{dB}$ and the input power P (dBm) at the VNA using Equations 2.17 and 2.16. For both devices and across all resonator designs we find $Q_\text{i} \approx 10^5$ in the low-photon regime as well as a saturation of Q_i at high photon numbers. The Q_i of both devices are thus limited by power-dependent losses. Those are believed to be of microscopic origins (by the so-called TLS, two-level systems), and are discussed at length in the next chapter. Despite the absence of a clear difference in the Q_i of both devices even at low power, we chose CHF3 for later fabrication as it gave cleaner results. Furthermore, we later on switched to a sapphire substrate using the CHF3 dry etch. Figure 4.6 includes zero field power dependence of a later version of the circle resonator design (resonator two on the "Hunting Impurities" device. It is also showing it being limited by TLS losses, with internal losses a factor ten larger.

Furthermore, we find no significant difference between designs, despite the IDR and the circle resonator having a larger footprint of the capacitive area, and thus expected to suffer more from dielectric/TLS induced losses. Therefore, we can validate the circle resonator design.

4.4 CHARACTERIZATION OF THE NBTIN FILM

In the following, we will compare our measured values for the critical temperature and the kinetic inductance of our NbTiN films with values found in literature. To determine the critical temperature of the NbTiN films, we measured the S_{21} parameter of the initial devices on the silicon substrate during the cool down and the warm-up of the cryostat. Below Tc, the transmission through the CPW is high, as NbTiN is superconducting. As soon as the temperature is higher than the critical temperature T_c, the film resistivity induces a high amount of insertion losses, and we observe a severely

reduced transmission. We performed these measurements without the TWPA since its T_c is less than 1 K. We find a critical temperature of 12.1 K during the cool-down and 13.6 K for the warm-up of the cryostat (see Figure 4.7). The two temperatures differ because the thermometer is located on the mixing chamber plate, 20 cm away from the sample, which therefore implies $T_c(warm-up) > T_c > T_c(cool-down)$. In addition, we expect $T_c(cool-down)$ to be more reliable as the temperature evolves more smoothly during the cool-down. This value is comparable to what found in the literature [142, 93, 143, 94, 89, 87] for similar thin films.

The kinetic inductance of the NbTiN film is an important parameter to include in the design of the devices, as it has a possibly large effect on the resonance frequencies. Furthermore, the kinetic inductance is connected to the penetration depth, which in turn is interesting for the calculation of the distribution of the coupling factor g as shown in Chapter 3.1. To estimate the kinetic inductance, we have compared the measured frequencies on the initial design to simulations performed with HFSS. The NbTiN is treated as a zero-thickness film with a surface impedance given as $Z_\Sigma = iL_{kin}\omega$. The inductance which is needed to match simulation and experiment is then concluded to be the kinetic inductance (see Table 4.2). We find a sheet kinetic inductance of approximately 1.5 pH/□ to 2 pH/□ for our 50 nm NbTiN films with a variation we attribute to a lack of control over the size if the resonators' features. We can compare this to the literature values collected in Figure 4.8 and find that this is comparably low but of the right order of magnitude.

Table 4.2: Resonance frequencies f_0 of the four resonators on the initial CHF3 device and the additional kinetic inductance necessary to match the measured resonance frequencies and the simulation.

	Circle	IDR	$\lambda/4$	μWire
f_0 (GHz)	6.63	6.11	6	5.45
L_{kin} (pH/□)	2.0	2.3	1.6	1.5

4.5 RESPONSE IN MAGNETIC FIELD

In the following, we will have a closer look at the response of the resonator to an external magnetic field. We will see that we need to suppress vortices in the vicinity of the resonator to ensure a proper functioning spectrometer.

4.5.1 *Frequency jumps and vortices*

Using the CHF3 initial device, we apply a magnetic field which is approximately parallel to the plane of the device. According to the London equations, the resonators' frequency at $T = 0K$ can be described by

$$f(B) = f(0)\left(1 - \beta\frac{L_{kin}}{L_{tot}}\frac{B^2}{B_c^2}\right), \tag{4.8}$$

with the applied magnetic field B and the critical field B_c and a scaling factor β [56, 55, 144]. The scaling factor β is generally different for the in-and the out of plane magnetic field. We can observe this quadratic dependency of the resonator frequency across all resonators on the device. In addition to this expected quadratic behaviour, the resonator frequency exhibits random jumps (see Figure 4.9).

We attribute these jumps to vortices next or on the resonators, changing locally the magnetic field and thus shifting the resonance frequency according to equation 4.8. The effect of the vortices on the different resonators differs from each other. The $\lambda/4$ resonator and the IDR are seemingly much more affected than the μWire or the circle resonator. The frequency jumps per se are not detrimental to the spectrometer function. However, vortices existing near the sample space of the resonator limits our knowledge of the precise magnetic field at the sample.

There are several options to limit the nucleation of vortices in superconducting films. Prohibiting the emergence of vortices by transforming the ground plane into a thin grid too small for vortices to be induced [96, 145]. The other option we pursued is the reduction of the ground plane, as described in Chapter 3.1.1, and therefore simply reducing the area in which vortices can be induced and increasing its distance to the resonator. The effect of the reduction of the ground plane of the frequency stability is shown in Figure 4.9. Apart from these design solutions, we can also minimize the out of plane magnetic field by performing a careful alignment procedure.

4.5.2 *Alignment procedure*

To align the magnetic field to the plane of the device, we use the kinetic inductance response as a tool. The scaling factor β in equation 4.8 is generally different for the in-and out of plane magnetic field. This enables the determination of the angle θ of the magnetic field with respect to the plane of the device, and therefore allows us to compensate for this misalignment by applying an appropriately tilted field.

To determine θ we sweep the in plane field B_z to different set points in positive and negative field direction at which we sweep the out of plane field B_y from negative to positive fields. For each By-sweep, we fit the change of the resonance frequency with a parabola. The location of the maximum of this parabola gives the needed compensation $B_y(B_z) = -B_z \tan\theta$ to keep the field in-plane at this specific B_z field. Repeating the procedure at several B_z allows to accurately extract the angle of misalignment θ by fitting $B_y^{\text{offset}}(B_z)$. We typically find θ to be around $\approx 1°$. In Figure 4.10 the process is illustrated. The effect on the frequency stability before and after correcting the alignment is shown in Figure 4.12.

4.5.3 Q_i *versus* B

In the following, we compare the sapphire and silicon substrate in terms of magnetic impurities over the whole magnetic field range to motivate our decision to later on work with sapphire substrate. The spin signal which we are interested in later on in a continuous wave EPR experiment will manifest itself as a loss channel. As discussed in Chapter 2 we require a minimal internal quality factor of 10^5. Moreover, we need

to be able to differentiate a possible spin signal from the overall background. This is especially true for the field region around a $g = 2$ line, where we expect most of the possible biological spin samples to be. In order to do this, we want to characterize the background signal by measuring the resonators without any spin sample.

In Figure 4.11 such a measurement of $Q_\mathrm{i}(B)$ is shown for the circle resonator on the initial sapphire and silicon CHF3 device. For the silicon substrate, we find three distinct features. One broad feature with an effective g-value smaller than two and a less pronounced but, similarly broad line with an effective g-value larger than two. The third feature is a sharp line with $g_\mathrm{eff} = 2$. The region in which the internal quality factor is reduced by almost one order of magnitude is right around the relevant field range. The device having sapphire as a substrate displays a multitude of features, starting with a very narrow and deep line around 90 mT. At higher field there are several other features of which we will discuss their mitigation and origin in detail in Chapter 5 as well as in the next chapter. It is however noteworthy that the Q_i decrease due to those features is less pronounced compared to the silicon case. This is especially true for the feature at $g_\mathrm{eff} = 2$. We thus decided preferentially to use sapphire substrate, but we nevertheless need to understand this background and how to minimize it.

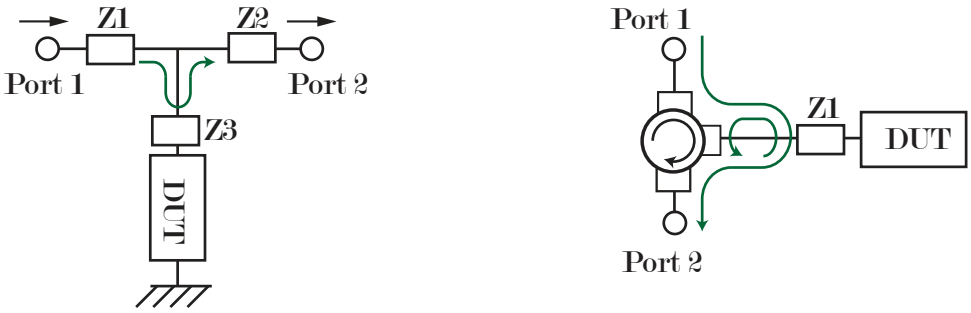

Figure 4.1: Left: Hanger geometry measurement, right: reflection measurement. In both cases, we perform a S_{21} measurement from port 1 to 2 to measure the device under test (DUT) [139]. The green arrow indicates the possible signal path. In principle, the impedances Z1 and Z2 are not equal to Z3. This impedance mismatch leads to a rotation around the z_∞ point [139].

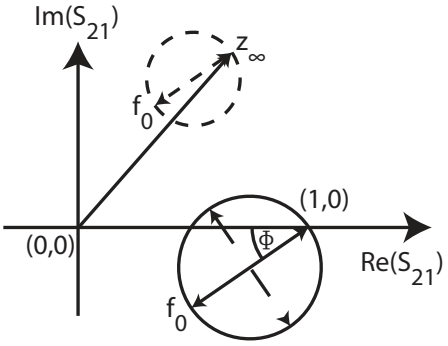

Figure 4.2: Representation of a measured S_{21}^{m} (dashed circle) after the correction for the electric delay in the complex plane. Normalizing with the off-resonant point z_∞ gives $\tilde{S}_{21}$ (solid circle), with the z_∞ at $(1, 0)$. $\tilde{S}_{21}$ is rotated away from the real axis by a phase ϕ. [139, 137]

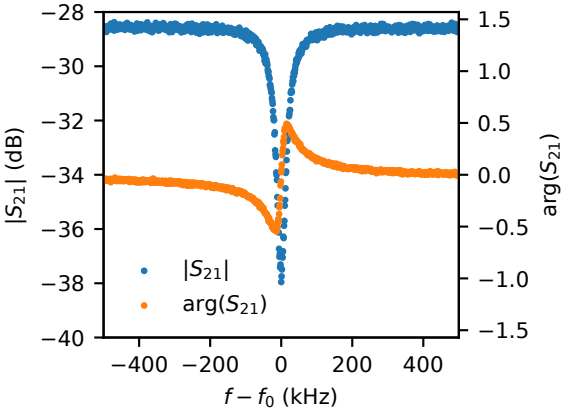

Figure 4.3: A typical broad scan of the S_{21} parameter. The shown resonance is resonance 7 of the "BDPA-3" device, measured with the JTWPA turned on. f_0 =7.808 847 GHz.

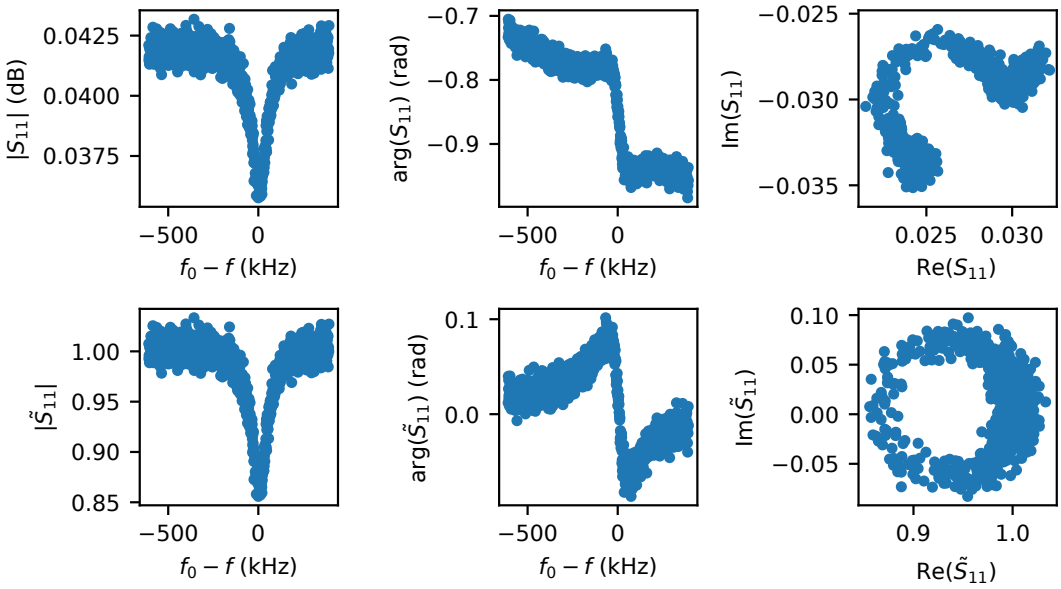

Figure 4.4: Reflection measurement on the BDPA resonator design (resonator 8 on "Sanity TED 90" device). The resonance frequency is $f_0 = 7.023\,842\,\mathrm{GHz}$. The upper row shows data without correction of the electric delay. The lower row shows the data after correcting for the electric delay and rescaling by z_∞.

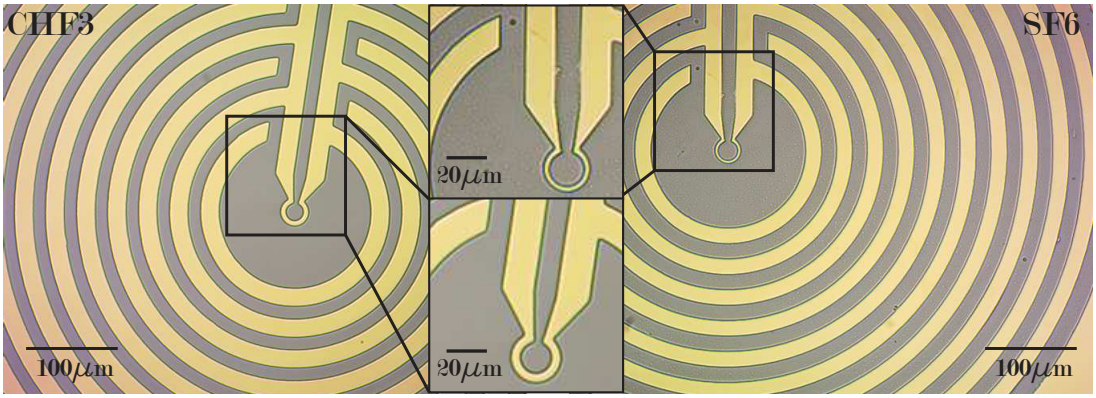

Figure 4.5: Compassion between CHF3 and SF6 Si devices. The two devices fabricated in NbTiN on silicon. The device fabricated using a CHF3 dry etch (left) is visibly cleaner compared to the device fabricated with SF6 dry etch, which displays black dots.

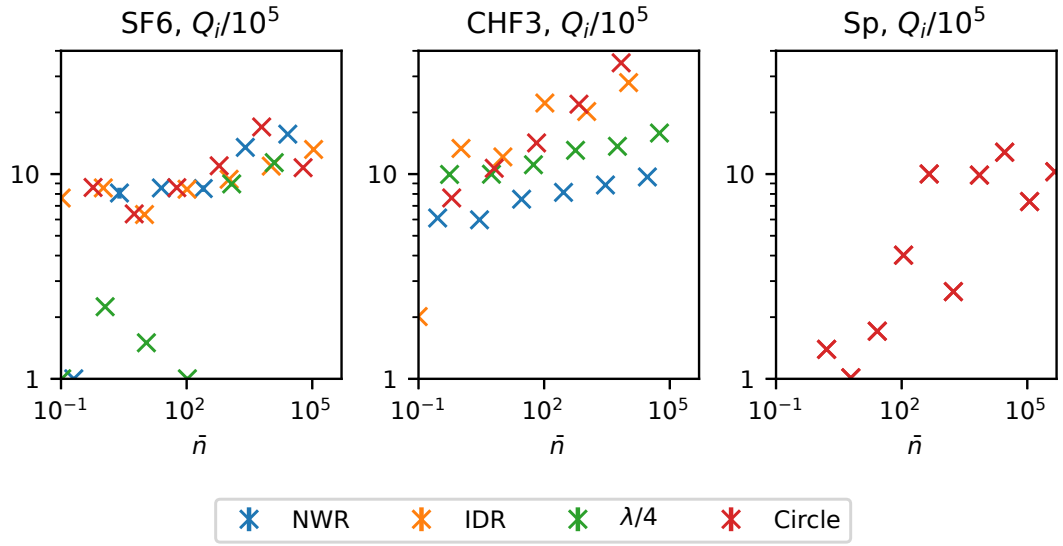

Figure 4.6: Power dependence of Q_i for the different resonators on the silicon substrate, initial chips at zero field. The error of the fits is likely to underestimate the real error, as there are visible problems with the fits of the SF6 device in the single photon limit. The plot labelled "Sp" is showing the measurement on resonator 2 of the "Hunting Impurities" device, fabricated on sapphire using a CHF3 etch. The legend is true for all three plots.

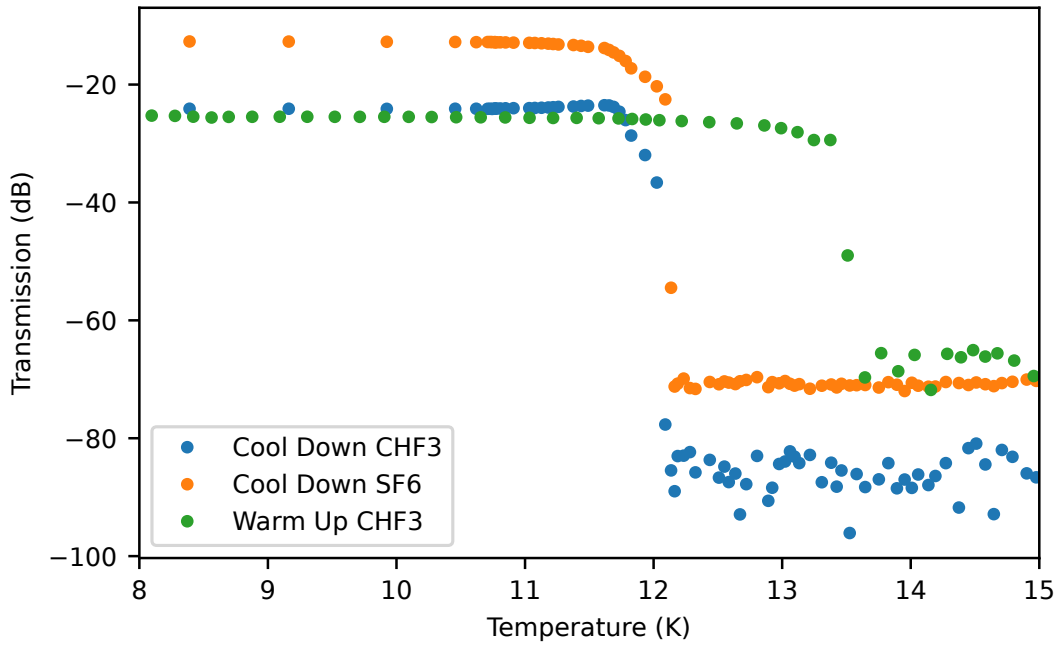

Figure 4.7: Transmission versus the mixing chamber plate temperature during the cool down and the warm-up of the cryostat.

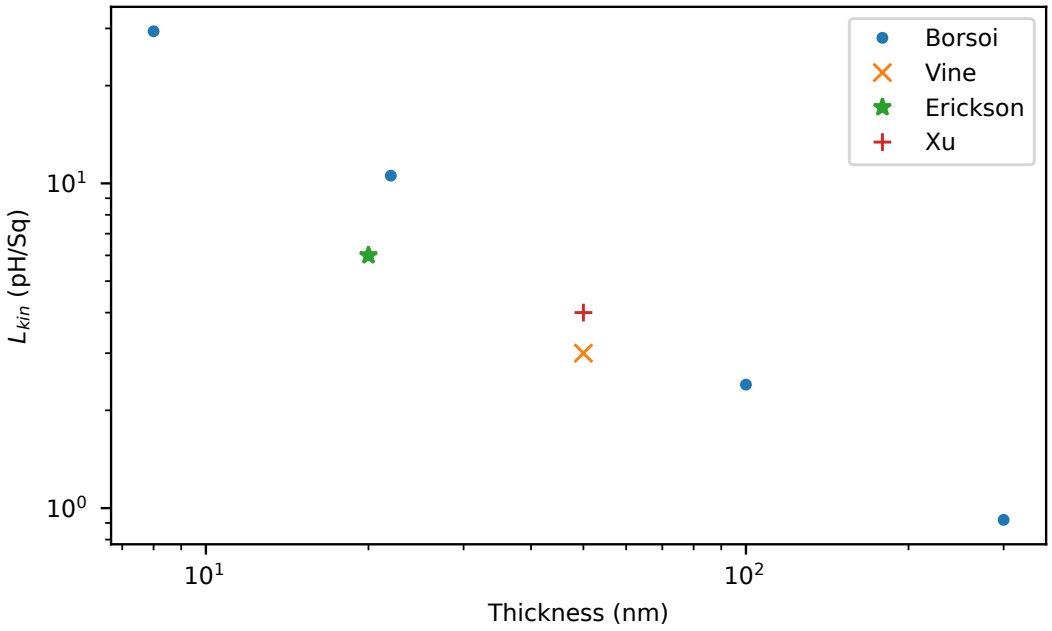

Figure 4.8: Incomplete summary of the kinetic inductance versus film thickness found in literature for NbTiN. (Borsoi: [94], Vine: [41], Erickson: [143], Xu: [142])

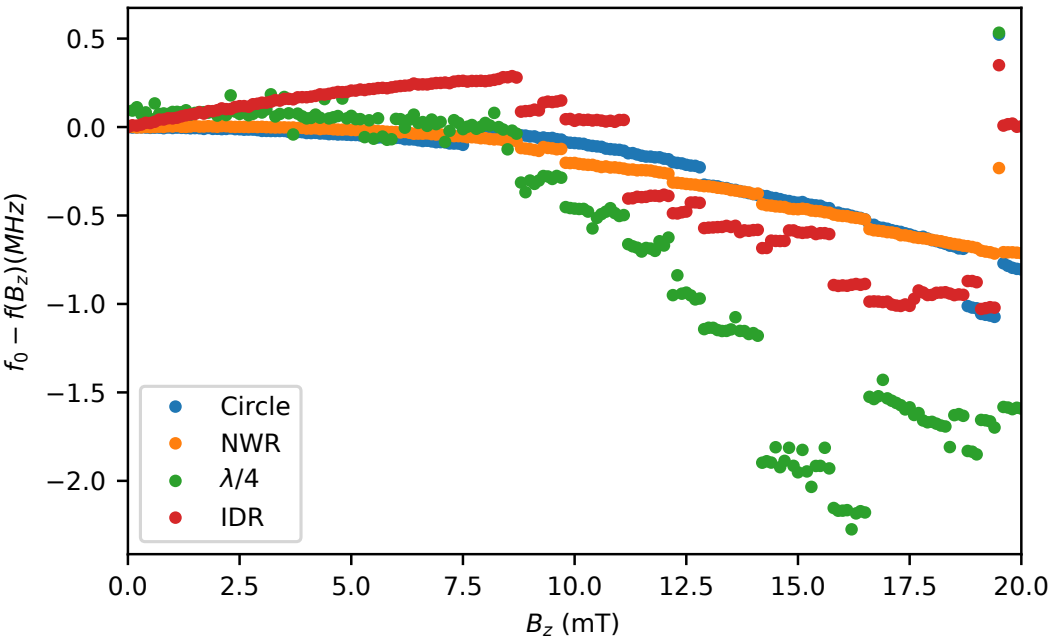

Figure 4.9: Change of the resonance frequency for the different resonators on the CHF3 initial device under an approximate in-plane magnetic field. The IDR and the $\lambda/4$ resonator experience the most jumps.

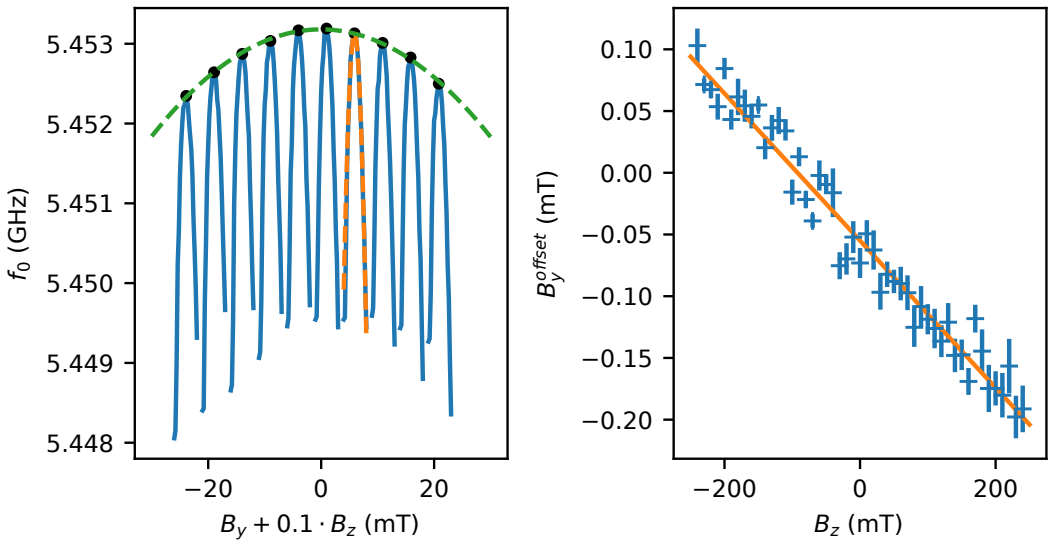

Figure 4.10: Extracting the B_y offsets at each B_z set point using a parabolic fit. The overall quadratic dependence of the resonance frequency due to the B_z field is shown in green.

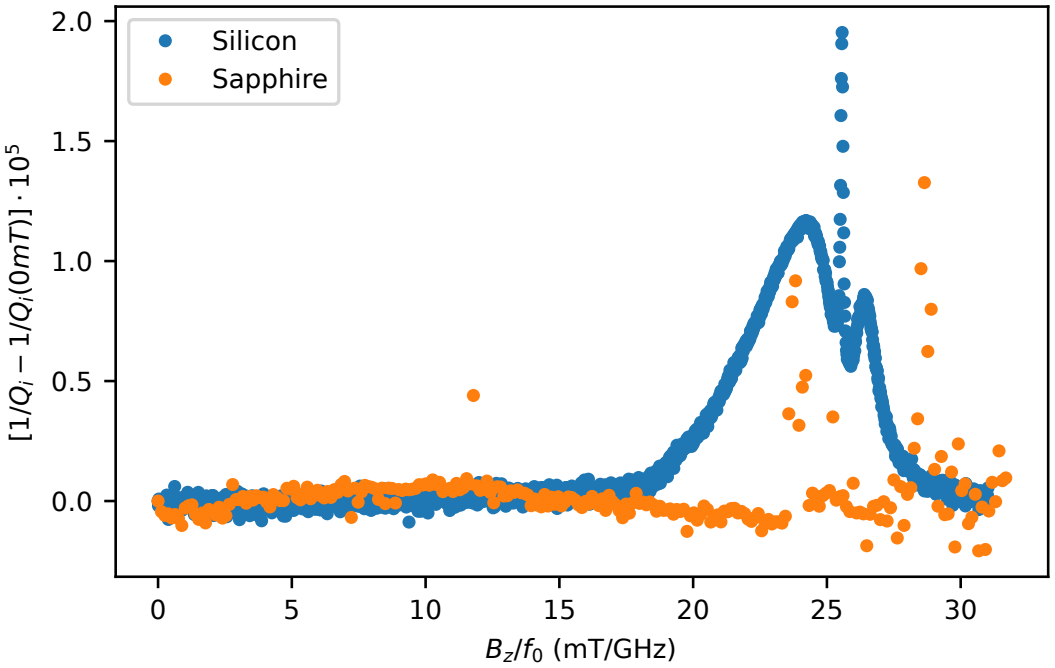

Figure 4.11: Comparison of $1/Q_\mathrm{i} - 1/Q_\mathrm{i}(0\,\mathrm{mT})$ for the circle resonator of the initial design on sapphire (CHF3 etch, $f_0 = 7.89\,\mathrm{GHz}$) and silicon (CHF3 etch, $f_0 = 6.77\,\mathrm{GHz}$). The resonator made on top of silicon displays two broad and one narrow decreases in Q_i, while the losses of the resonator on sapphire are narrow.

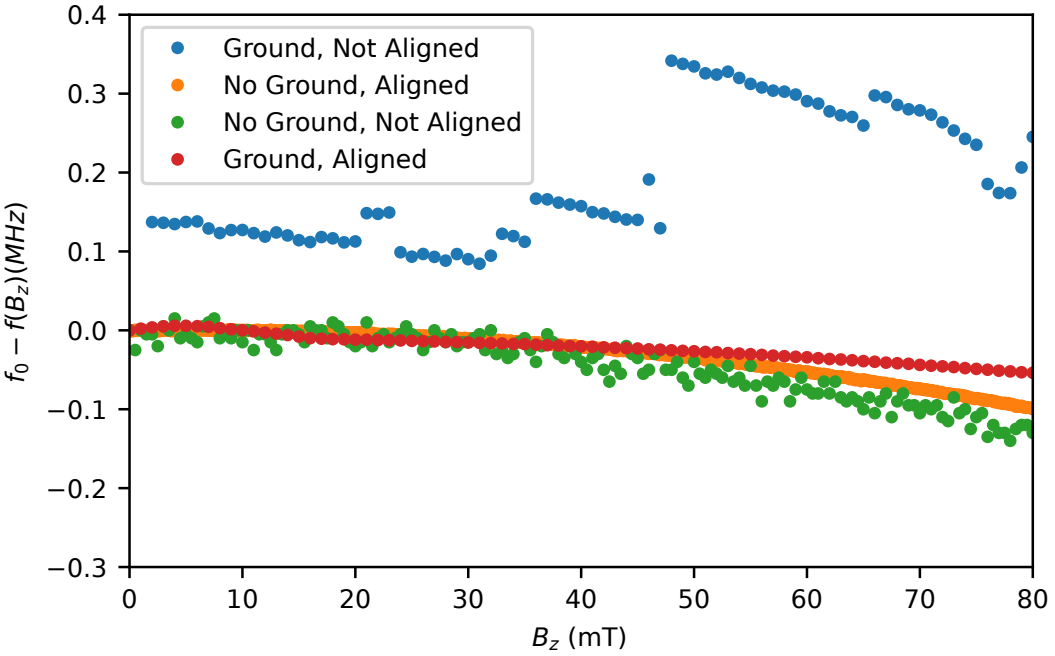

Figure 4.12: Tracking of the resonance frequency f_0 for the circle resonator on the initial device on sapphire and silicon (CHF3 etch) as well as the BDPA design with a minimal ground plane. We cover both cases of an aligned and not aligned magnetic field. In both cases, with and without a minimized ground, we find that the resonance frequency is jittering less if the magnetic field is aligned. For the case of a full ground plane and a not aligned field, the frequency jumps wildly.

5

MITIGATING MICROWAVE LOSSES INDUCED BY SPIN SYSTEMS

As seen in the previous chapter, our resonators suffer from losses occurring at specific magnetic fields, as reported in literature. In the following, we detail the origins of these spin systems, and which fabrication technique we use to mitigate them.

5.1 TWO-LEVEL-SYSTEMS: MICROSCOPIC LOSSY SYSTEMS

Detrimental effects for superconducting resonators have been largely studied [146], with evidence that obtaining high-quality factors requires shielding from quasi-particles [147], preventing vortex nucleation [148, 88, 149, 150], using low-loss dielectric substrates, and mitigating microscopic defects [151, 152, 153]. This last effect arises from so-called two-level-systems (TLS) whose contribution can be removed by saturating them, leading to higher quality factors observed at higher power. They can have multiple origins: adsorbates, fabrication residues, uncontrolled oxides, substrate contaminants, including spurious spin systems. An intense research effort in the superconducting circuits community is ongoing to mitigate these TLS as they are currently limiting performances of superconducting quantum bits [154, 155, 151, 156]. This research relies on studies measuring the various contribution of substrates, cleaning protocols, choice of superconductor, design layouts, fabrication processes, correlation with material characterization, etc. In addition, there is a specific interest in characterizing spin systems lying at interfaces, since they have long been suspected of being responsible for flux noise [157, 158, 159]. The current state-of-the-art values for flux noise are thought to be limited by these microscopic systems, and is limiting the performance of SQUID magnetometers [160] as well as flux-based superconducting quantum bits such as a fluxonium or flux qubits [161].

In this section, we will only focus on TLS and studies pertinent to magnetic-field induced losses, as they could lead to a decrease in sensitivity for our designed spectrometer.

5.1.1 *TLS modelling and identification*

These TLS can be modelled as an artificial spin coupled either to the electrical field or the magnetic field of the resonator. If coupled to the electrical fields, its nature is rather akin to an electrical dipole (such as a charge state) or if coupled to the magnetic field, it will rather be an effective nuclear or electronic spin (such as a hydrogen dangling bond). Similarly to the description introduced for a spin coupled to a resonator in Chapter 2.4, we can introduce for each TLS a coupling constant g_0, as well as T_2 and T_1 coherence and relaxation times. TLS has been observed to have a large coupling to qubits [154, 162], and can lead to a coherent interaction.

For a TLS bath in the weak coupling regime, containing N spins and of polarisation p, its contribution to the resonator behaviour will be similar to that of a weakly coupled spin ensemble: when resonant, they provide an additional decay channel, which scales at $\kappa_b = 4pN\bar{g_0}^2/\Gamma_t$, and an additional frequency shift if weakly detuned. In addition, the TLS bath can be saturated under a microwave drive, effectively suppressing their associated decay channel. Let us now derive the power law associated to this saturation using the formalism developed in chapter 1. We consider again that the spin ensemble has some distribution in frequency $\rho(\omega)$ but for the sake of simplicity, we assume all spins have a similar coupling constant $\bar{g_0}$. At each spin frequency, the spin saturation can be expressed so that its effective polarisation is given by:

$$p_{\text{eff}} = p_0 \frac{\Gamma_2^2 + \Delta^2}{\Gamma_2^2 + \Delta^2 + 4\bar{g_0}^2 \frac{\Gamma_2}{\Gamma_1}\bar{n}}, \tag{5.1}$$

where Δ is the detuning between the spin and the resonator. Following the same method as for Equation 2.77, we can express the spin decay channel as:

$$\kappa_{\text{b}} = N \int \rho(\Delta) p_{\text{eff}} \frac{2\bar{g_0}^2 \Gamma_2}{\Gamma_2^2 + \Delta^2}. \tag{5.2}$$

Assuming the spin frequency distribution is a Lorentzian of width Γ_{inh} centred on the resonator frequency, we find:

$$\kappa_{\text{b}} = p_0 \frac{2N\bar{g_0}^2}{\sqrt{1 + \frac{4\bar{g_0}^2}{\Gamma_2\Gamma_1}\bar{n}}} \frac{1}{\Gamma_{\text{inh}} + \sqrt{1 + \frac{4\bar{g_0}^2}{\Gamma_2\Gamma_1}\bar{n}}} \tag{5.3}$$

which can be further simplified by considering the spin line-width to be much broader than the resonator:

$$\kappa_{\text{b}} = p_0 \frac{2N\bar{g_0}^2/\Gamma_{\text{inh}}}{\sqrt{1 + \frac{4\bar{g_0}^2}{\Gamma_2\Gamma_1}\bar{n}}} \tag{5.4}$$

Introducing $n_{\text{c}} = \Gamma_2\Gamma_1 \frac{4}{\bar{g_0}^2}$, we find the typical TLS saturation law:

$$\kappa_{\text{b}}(\bar{n})/\kappa_{\text{b}}(\bar{n} = 0) = \frac{p_0}{\sqrt{1 + (\bar{n}/n_{\text{c}})}^{\alpha}} \tag{5.5}$$

evaluated for $\alpha = 1$. This derivation is valid if one assumes the T_1 and T_2 processes are Markovian. If spin-spin interaction is introduced in the model [163], α can become lower than 1: this behaviour matches the often made observation that TLS saturation fits well with $\alpha < 1$, with values ranging in $0.2 - 1$, [164, 165, 166, 167, 154].

Several distinct TLS baths can be interacting with the resonator at the same time: one can distinguish between their individual contributions and summing them into a total TLS-induced loss rate: $\kappa_{\text{b}} = \sum_i \kappa_{\text{b},i}$. In particular, this is useful when attempting to distinguish between different contributions. For example, TLS located within the substrate, or at the interfaces substrate-vacuum, metal-vacuum, or metal-substrate may have different origins, and thus different pre-factors. A useful quantity in this case is the participation ratio p_i of each volume/surface to the global electrical (magnetic) field, so that one may write the contribution explicitly:

$$\kappa_{\text{b}} = \sum_i p_i \kappa_{\text{b},i}. \tag{5.6}$$

This quantity is key to comparing losses between resonators (or 3D cavities) geometries, and this type of analysis can even allow isolating the specific contribution of each interface and bulk layer.

5.1.2 *Magnetic field losses*

As we mentioned before, increased losses appearing at specific magnetic fields have already been observed for superconducting resonators, as well as increased flux noise for flux-sensitive qubits. For resonators, these increased losses are localized at magnetic fields corresponding to spin systems with a gyromagnetic ratio close to a spin 1/2. Indeed, using resonators fabricated using NbTiN on Si, NbN on SiO2, and granular Al on sapphire, [88, 86, 90] observed a dip corresponding to g=2.0 +/- 0.3. Besides, [89] observed a dip for NbTiN on sapphire, but at a value slightly lower than 2 (about g = 1.9). [168, 36, 37] used NbN on sapphire and observed a line precisely at g=2.0, and also satellite peaks corresponding to hydrogen absorbed on the surface and creating a spin system comprising the trademark hydrogen hyperfine splitting of $A/(2\pi)$ =1.42 GHz. These hydrogen atoms absorbed on the surface are also thought to contribute significantly to flux noise, as observed by [159]. Additionally, this work reports contribution from O_2 absorbates and superoxides systems embedded into the sapphire lattice, further confirmed by high-field EPR studies [38] and by DFT calculations [37]. These identified spin systems also contribute to the frequency noise observed in superconducting resonators [157, 158]. In the following, we encounter these loss channels as well and find ways to mitigate them.

5.2 MAGNETIC-FIELD LOSSES FOR NBTIN RESONATORS FABRICATED ON SAPPHIRE

The section focuses on the presentation of the different devices and their field dependent associated losses. This is followed up with an identification of all features but one and a proposition for their mitigation. Finally, we present the results of the implementation of these proposed solutions.

5.2.1 *Observed intrinsic losses $Q_i(B_0)$*

The devices "Initial Device", "BDPA-1 to 3" have all been fabricated using an optical resist mask and the devices "BDPA-4" and "Hunting-Impurities" use an aluminium mask (see Chapter 3). We have measured the "BDPA-1" and "BDPA-2" devices twice, once quickly after their fabrication (in the following labelled "BDPA-1/2f") and once after several weeks of ageing in ambient atmosphere (labelled "BDPA-1/2a"). The measurements on all four devices were carried out using a power resulting in 1 photons to 100 photons intra-resonator photons. In Figure 5.1 the intrinsic quality factors and resonance frequencies at zero magnetic field for all measured resonators on the BDPA-devices and the Hunting-Impurities device are collected. All resonators lie in a 5 GHz to

8 GHz range, with $Q_\mathrm{i}(B = 0\,\mathrm{mT})$ above $2 \cdot 10^4$. On two devices (BDPA 3 and Hunting Imp), the intrinsic quality factors are systematically above $2 \cdot 10^5$.

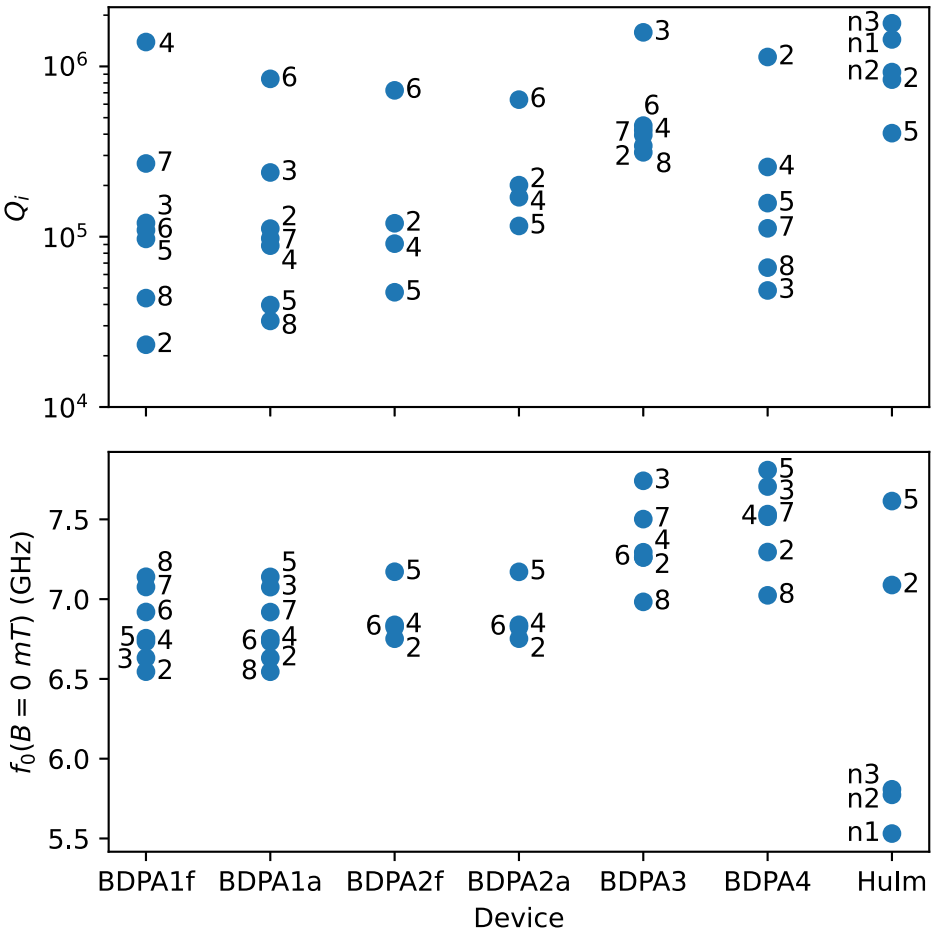

Figure 5.1: Resonance frequency and intrinsic quality factor at zero magnetic field for all devices. The devices "BDPA-1 to 3" were fabricated using an optical resist mask, while for the devices "BDPA-4" and "HuIm" ("Hunting Impurities") an aluminium mask was used. The resonators "n1", "n2", and "n3" are the nanowire resonators similar to the one used on the initial device. The "BDPA-4" device was exposed to resist once during dicing. The devices BDPA-1 and BDPA-2 have been measured straight after fabrication (fresh) and aged after a few weeks. We note that the variance of Q_i over the resonators on the "Hunting-Impurities" device is comparably smaller and that $Q_\mathrm{i}(HunIm) \gtrsim 10^5$.

We now turn to the magnetic-field dependent losses. To allow for a better comparison between the resonators, we will re-scale the magnetic field by the resonator frequency at zero field. To focus on these losses, we subtract the contribution from the zero-field losses by using $1/\Delta Q_\mathrm{i} = 1/Q_\mathrm{i}(B) - 1/Q_\mathrm{i}(B_\mathrm{z} = 0\,\mathrm{mT})$. Figure 5.2 shows a comparison of the fresh BDPA-1, 2 and the BDPA-3 devices. We can identify a total of six different absorption peaks. In the following we refer to these features numbered by their order in field as indicated in Figure 5.2. In addition to these six features, we find a jump at 10 mT and a plateau slowly rising at $B_\mathrm{z} \approx 50\,\mathrm{mT}$. The jump is occurring across all measured devices, consistently at the same magnetic field. A comparison between the BDPA-1 just after fabrication (fresh, f) and after ageing (a) is shown in Figure 5.3. In

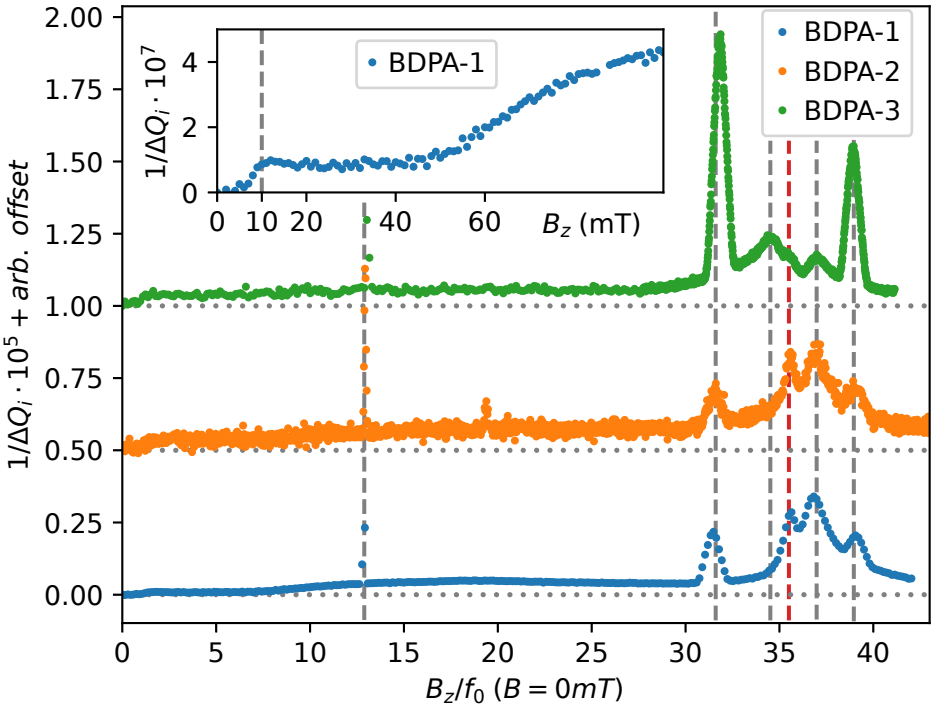

Figure 5.2: $1/\Delta Q_\mathrm{i}$ for resonator 4 of the devices "BDPA-1-3" with an arbitrary offset indicated by the dotted line. We renormalized the magnetic field by the zero field resonator frequency. In doing so, the losses introduced by a spin 1/2 with $g = 2$ will appear at the same position of $B_\mathrm{z}/f_0 = 35.72\,\mathrm{mT\,GHz^{-1}}$ (red dashed line). The dashed lines correspond to the identified features 1-6 (from left to right). The inset shows a jump of $1/\Delta Q_\mathrm{i}$ at 10 mT on the "BDPA-1" device.

the aged sample, we observe an intensity increase in feature 3 (not visible on the fresh BDPA-1,2 but BDPA-3).

Since the resonators cover a large frequency range as shown in Figure 5.1, we can track the position of the features as a function of frequency and magnetic field, giving the frequency-diagram shown in Figure 5.4. In the reduced range where we have investigated the losses, each feature appears to depend linearly on the magnetic field. In a first rough analysis, we thus treat each line as an independent spin transition with effective g-value g_eff and a zero-field-splitting Δ_0 giving $f_\mathrm{res} = \frac{\mu_\mathrm{B}}{h} g_\mathrm{eff} B_\mathrm{z} + \Delta_0$. We summarize the fit results in Table 5.1. We note that all but one effective g-values are close to two, and that one of the zero-field splitting is negative.

Table 5.1: Zero field splitting (Δ_0) and effective g-factor obtained by fitting the data presented in Figure 5.4.

Feature	1	2	3	4	5	6
$g_\mathrm{eff} \pm 1\%$	4.59	2	1.95	1.99	1.84	1.93
$(\Delta_0 \pm 0.1)$GHz	1.2	0.8	0.5	0.1	0.3	-0.4

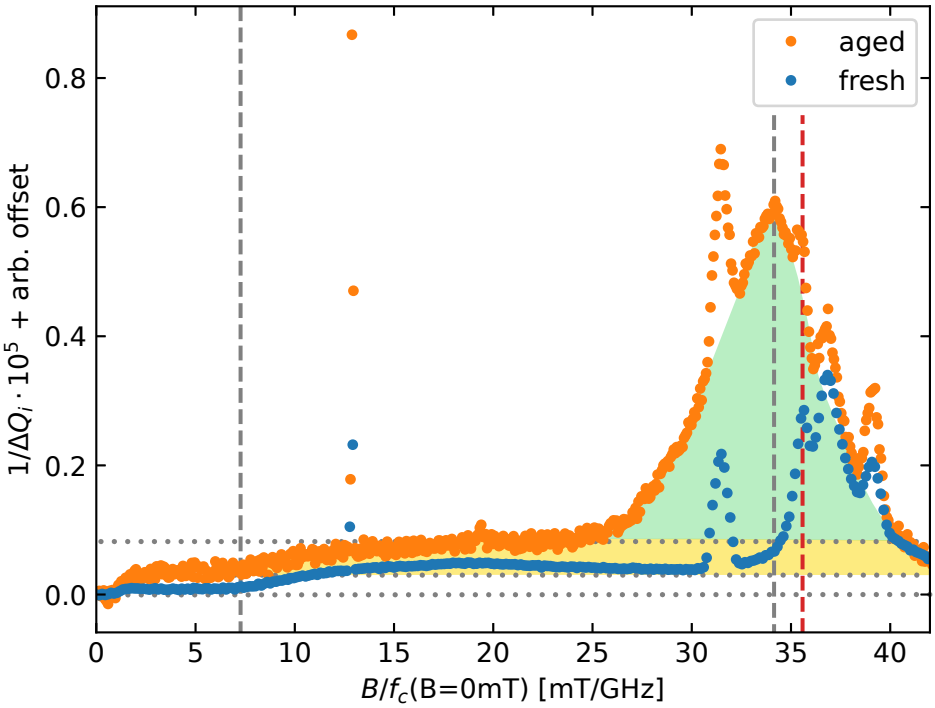

Figure 5.3: $1/\Delta Q_\mathrm{i}$ for resonator 4 of the "BDPA-1" device, once fresh and one aged. We see a broad peak emerging (green) and highlight the offset (also visible in Figure 5.2 on other devices) in green. The firs dashed line indicates the onset of this offset and the second and third of the feature positions 3 and 4, with the red line at the position of a spin 1/2, $g = 2$.

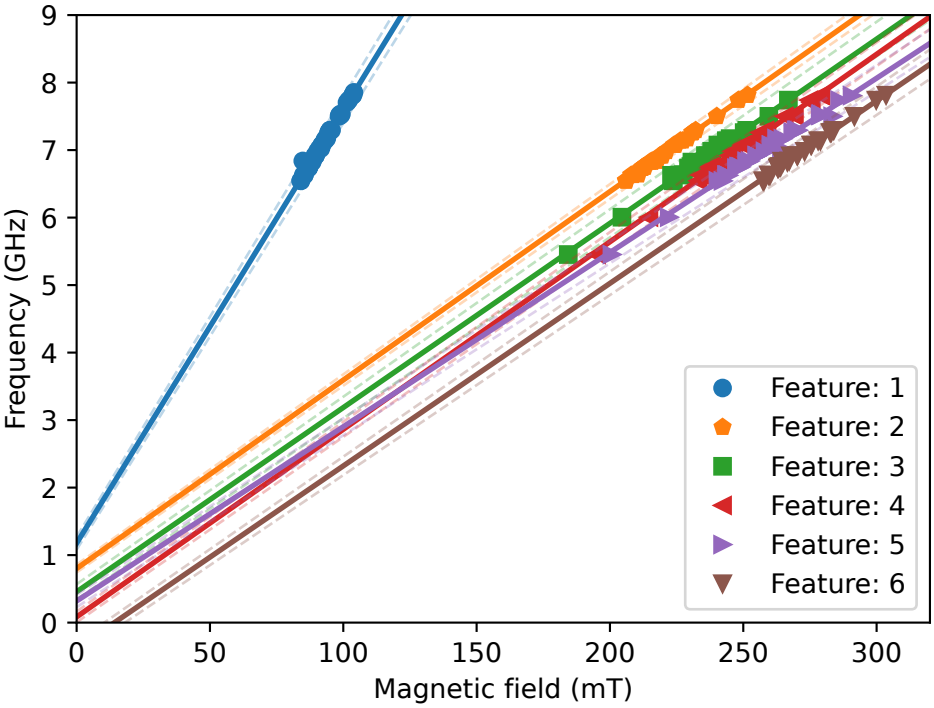

Figure 5.4: The constructed frequency-field plot of all six features and their fit. The data also includes data from the devices "BDPA-4" and "Hunting Impurities". The dashed lines show the error on the fit, most likely underestimating the error at low fields.

5.2.1.1 *Saturation analysis*

We have also investigated the power saturation of the features. The change of the internal quality factor for an increasing intra resonator photon number is fitted using Equation 5.5, while keeping the effective polarization fixed at 1. The data and fits for the "BDPA-3" device are shown in Figure 5.5, while the fit parameters are collected in Table 5.2. We have not been able to measure precisely the resonator response at high-field due to non-linear behaviour of the resonator and saturation of the amplification chain, so we are unable to assert what exponent α would fit better to our data - we thus take $\alpha = 1$ for the fit, and find n_c values reported in Table 5.2.

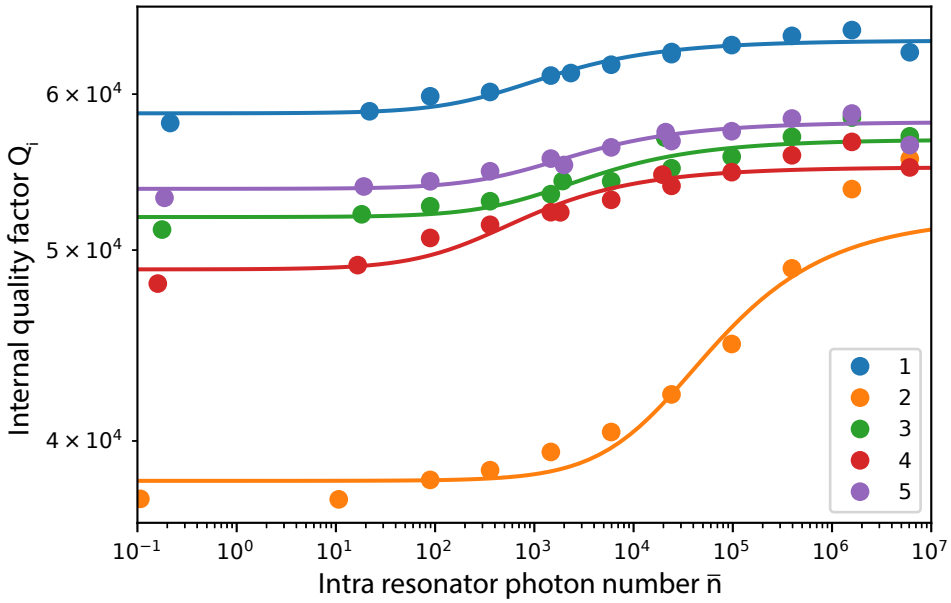

Figure 5.5: $Q_{\mathrm{i}}(\bar{n})$ measured on resonator 8 of the "BDPA-3" device. The intra resonator photon number is calculated with the resonance frequency of 6.983 GHz and $Q_{\mathrm{c}} = 1.75 \times 10^5$ measured at zero field and the corresponding $Q_i(\bar{n})$.

Table 5.2: Parameters of the fits shown in Figure 5.5. Q_{s} are the intrinsic losses at $\bar{n} \to 0$, n_{c} the critical photon number, and $Q_{\mathrm{i,hp}}$ the quality factor at high powers. The fits are ill-defined as we are lacking the saturation at high power, as measurements at these powers were affected by non-linear behaviour of the JTWPA.

Feature	1	2	3	4	5
$Q_{\mathrm{i,hp}}$ $(\times 10^4)$	6.39 ± 0.03	5.2 ± 0.17	5.69 ± 0.06	5.51 ± 0.04	5.81 ± 0.03
Q_{s} $(\times 10^4)$	71.97 ± 5.21	14.39 ± 1.3	60.03 ± 7.82	43.45 ± 4.4	71.54 ± 5.69
n_{c} $(\times 10^2)$	4.0 ± 2.0	165.0 ± 70.0	11.0 ± 7.0	2.0 ± 1.0	8.0 ± 3.0

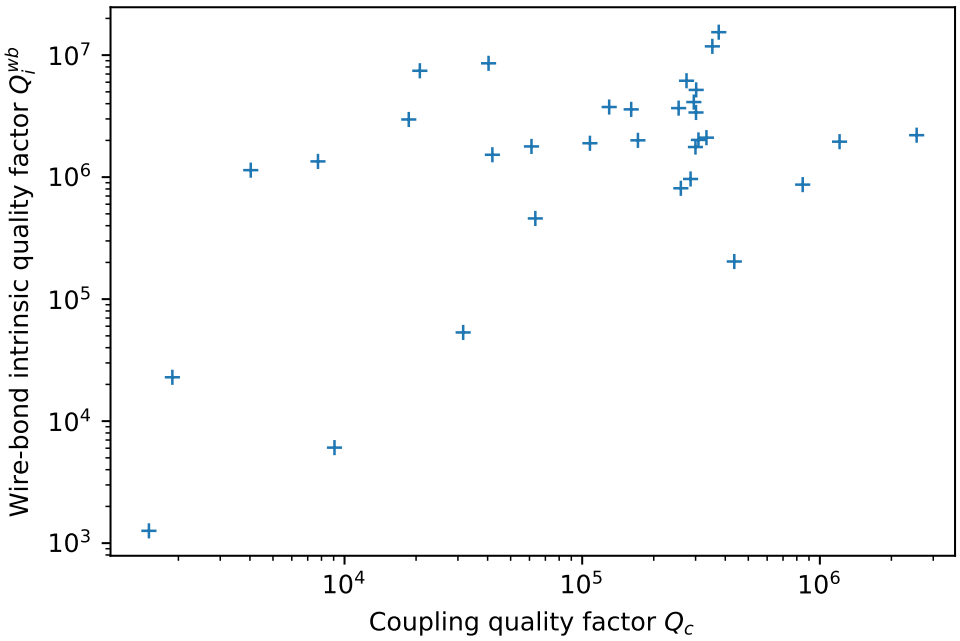

Figure 5.6: Intrinsic quality factor after wire bonds switch to normal state.

5.2.2 *Identification and mitigation solutions*

Building on this collected data-set, we now go through each of these features and attempt to identify the origin of these losses. We then discuss possible mitigation strategies.

JUMP AT 10 mT: ALSI WIRE-BONDS The jump at 10 mT is appearing faithfully across all devices. As it happens, we are using aluminium wire-bonds and the critical field of aluminium is $\approx 10\,\mathrm{mT}$ [169, 170]. We determine the loss contribution by evaluating $1/Q_i^{wb} = 1/Q_i(B < 10mT) - 1/Q_i(B > 15mT)$. We find values for Q_i^{wb} lying in the range $5 - 100 \times 10^5$. This is large enough to not impact our experiment significantly, yet on about 4 resonators, Q_i^{wb} drops below an acceptable level of $Q = 5 \times 10^5$. We naively expect this contribution of the wire bonds to depend on the external quality factor. Indeed, the wire bond turning normal having an incidence on the resonator quality factor is a measure that the resonator field extends to some measure into the central coupling coplanar waveguide. This leakage towards the outside is also directly given by the coupling quality factor. We observe only broad correlations between the two (see Fig. 5.6 probably due to the fact that depending on the sample, the chip is connected to the input ports with 1, 2, or 3 wire bonds. To remove the contribution from wire bonds, one could engineer an electrical-field node at the wire bond location [171].

FEATURE 1: SAPPHIRE IMPURITIES The first feature has a, compared to the other features, very narrow line-width and a high effective g-value (see Table 5.1). The narrow line-width is typical for crystalline spins, and a high g-factor is typical for the

lanthanides in sapphire [172, 173]. Based on these observations, we unfortunately could not identify the spin species. A matching resonance line has been reported by Farr et al. [38] in sapphire. They use a dielectric resonator made of EFG grown sapphire, and run cwEPR measurement at 115 mK from 9 GHz to 30 GHz. Although their extracted values $\Delta_0 = -0.065\,\mathrm{GHz}$ and $g_{\mathrm{eff}} = 5.3972$ are slightly larger than the ones presented here, we find the agreement is reasonable. The narrow line-width in combination with this reported data suggests that a change of sapphire might remove this impurity. We thus switched from an EFG (edge-defined film growth) grown sapphire to a HEM (heat exchanger method) grown sapphire. EFG-grown sapphire generally has a higher dislocation and bubble density than HEM-grown sapphire due to higher temperature gradients in the process [174, 175]. Although HEM-grown sapphire tends to have fewer impurities, it does not necessarily translate into less spin systems. We note this recent work [176] has identified that HEM wafers gave better quality factors for 3D superconducting cavities.

FEATURE 2, 4 AND 6: HYDROGEN ABSORBATES AND OXYGEN : The three features, line 2, 4 and line 6 can be described by a spin 1/2 with $g = 2$ and a nuclear spin $I = 1/2$ with $A/2\pi = 1.45\,\mathrm{GHz}$. In Figure 5.7 the energy-level structure for such a nuclear spin is shown together with the expected EPR transitions. The hyperfine splitting of $A/2\pi = 1.45\,\mathrm{GHz}$ is that of a hydrogen atom, and the model fits the data convincingly without any free parameters. De Graaf et al. have observed similar features and could show that these originate from atomic hydrogen physiosorbed on the sapphire surface.[36, 168]. The necessary spin 1/2 could be, adopting again the reasoning of [36], adsorbed oxygen in the O_2^- state.

Knowing that the feature 2 and 6 belong to the same spin system, we can calculate their spin temperature.

Indeed, we observe that the height of the second feature $\Delta Q_{\mathrm{i},2}$ is larger than on the sixth feature. From the modelling of a TLS bath, we expect the spin decay channel to be proportional to the polarization of the spin ensemble and the number of contributing spins, as well as to the coupling of the spin system to the resonator. As we study lines at $\approx 7\,\mathrm{GHz}$, we expect all the spins to be in their electronic ground state. Identically, we are far enough from the zero-field splitting that both transitions couple analogously to a spin 1/2. The height difference between the peaks can thus be explained by a different number of spins: we are seeing the finite polarization between nuclear levels. Approximately, the energy level splitting between the ground state is given by $\Delta f = g\mu_{\mathrm{B}}(B_6 - B_2)$, where B_i is the magnetic field at which the peaks are observed. We can thus relate the nuclear polarization to the peak height:

$$p_{\mathrm{eff}} = \delta Q_{\mathrm{i},2}/(\delta Q_{\mathrm{i},2} + \delta Q_{\mathrm{i},6}) = \tanh\left(\frac{g\mu_{\mathrm{B}}\Delta B}{k_{\mathrm{B}}T}\right). \tag{5.7}$$

We extract a spin temperature averaged over the resonators of the "BDAP-3" device is $(93 \pm 2)\mathrm{mK}$. This is the same order of magnitude compared to Lucas et al. [177]who have found $T_{\mathrm{s}} \approx 100\,\mathrm{mK}$ with an operating temperature at $T \approx 45\,\mathrm{mK}$.

To mitigate the losses due to the hydrogen atoms, De Graaf et al. annealed their devices at 300 °C out-gassing the adsorbed hydrogen by the reaction $2\mathrm{H} \rightarrow \mathrm{H}_2$ [178, 36]. We could not anneal in a vacuum, but used a nitrogen atmosphere and annealed as

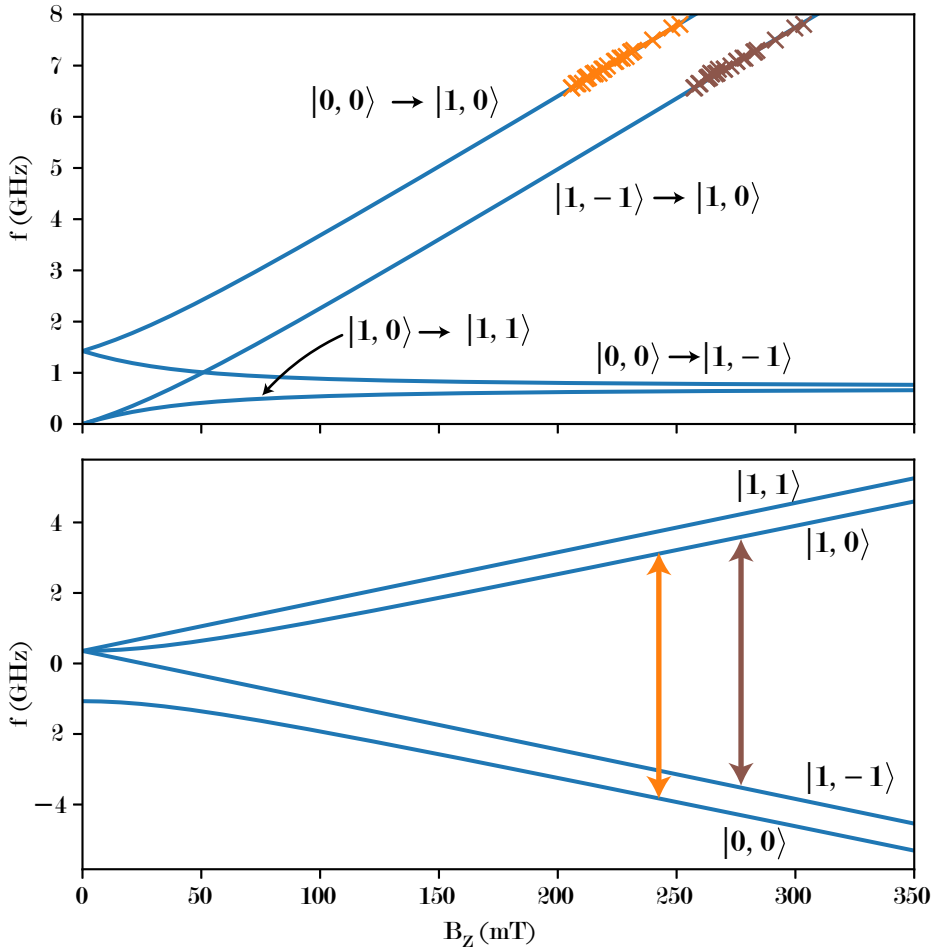

Figure 5.7: The energy - field - and resulting frequency-field diagram for a hydrogen atom coupled to a spin 1/2, $g = 2$. The states are labelled $|J, m_J\rangle$ and transitions with $\Delta J = \pm 1$, $\Delta m_J = 0$ and $\Delta J = 0$, $\Delta m_J = \pm 1$ are allowed [63]. The field positions of the features 2 and 6 are overlaid and match the predicted resonance positions.

well at 300 °C. The devices "BDPA-4" and "Hunting Impurities" have included this as the last fabrication step. Figure 5.8 shows the resulting disappearance of the features associated to hydrogen.

LINE 4 : This is a up to now unidentified feature, called USO for Unknown Spin Object. The extracted $g_{\text{eff}} = 1.84 \pm 1$ % and $\Delta_0 = (0.3 \pm 0.1)$ GHz do not fit to known impurities of sapphire [38]. Looking further other metal impurities such as cobalt or nickel, no convincing identification can be made [179]. We have investigated this feature further by looking at its participation ration and the effect annealing has on it. This is discussed in 5.2.4.

PLATEAU AND FEATURE 3 : The plateau and the feature 3 have been reported in [36] and discussed in great detail by Un et al. using high field EPR and density functional theory (DFT) calculations in [37]. They relate feature 3 to the superoxides $O_2^{\cdot -}$ and $HO_2^{\cdot -}$ and explain the offset by triplet O_2. Both contributions could be enhanced by

treatment with an O_2 plasma and an exposure to water [37]. These findings prompted us to protect the NbTiN with an aluminium layer to avoid any contact between the NbTiN and photo resist.

5.2.3 *Mitigating losses using an Aluminium mask*

Following the above presented experiments and literature, we included an aluminium, protecting the NbTiN, as well as an annealing step in the fabrication process. The aluminium mask was removed after before the annealing. Figure 5.8 shows the internal losses of the "BDPA-4" and the "Hunting Impurities" devices. The "BDPA-4" device was exposed to the photoresist during dicing. The "Hunting Impurities" device, however, was covered with aluminium throughout the part of the fabrication using optical resist. We find that the "Hunting Impurities" device shows no sign of the superoxides and the triplet O_2. Furthermore, the hydrogen lines are absent and no feature at the spin 1/2, $g = 2$ position is observed. The two last remaining features visible are the jump due to the wire bonds and the USO.

5.2.4 *Discussion on the USO line*

We now try to identify the origin of the USO line. This section also includes two samples not discussed so far:

- 'NV sample': Sample containing a simplified version of the circle resonators, where the loop is replaced by a micron-sized wire. The fabrication technique is analogous to the Hunting Imp, yet these chips have not been annealed.
- 'Kin sample': Sample containing thinner microwires to precisely calibrate the kinetic inductance. This sample was annealed at 600 °C.

These samples were fabricated and measured by Matteo Boselli.

5.2.4.1 *Identified dependencies*

We note a dependence of the contribution of the USO line on the annealing temperature, shown in Figure 5.9. We have tested annealing at 300 °C, 600 °C, 800 °C, and we find the USO losses increases with the annealing temperature. The annealing at 800 °C yielded at thicker and transparent NbTiN film, which has not been measured. We thus think we are incorporating extra nitrogen atoms in the films. Interestingly, the NbTiN films are organized in a NaCl lattice, and despite using a $50\% - 50\%$ target of NbTi, the films typically form a 50% N - 15% Ti and 35% Nb [180]. It would thus be interesting to analyse the stoichiometry and lattice structure of the films to understand how these extra N atoms incorporated into the film.

We have also used an annealing at 300 °C in argon atmosphere without noticing any difference compared to the annealing in nitrogen. To make a comparison, we plot the integral of the feature versus the annealing temperature in Figure 5.9. A first hypothesis for the origin of the USO peak would thus be oxides or nitrides formed at the surface of the NbTiN, whose concentrations would be increased when annealing in Nitrogen.

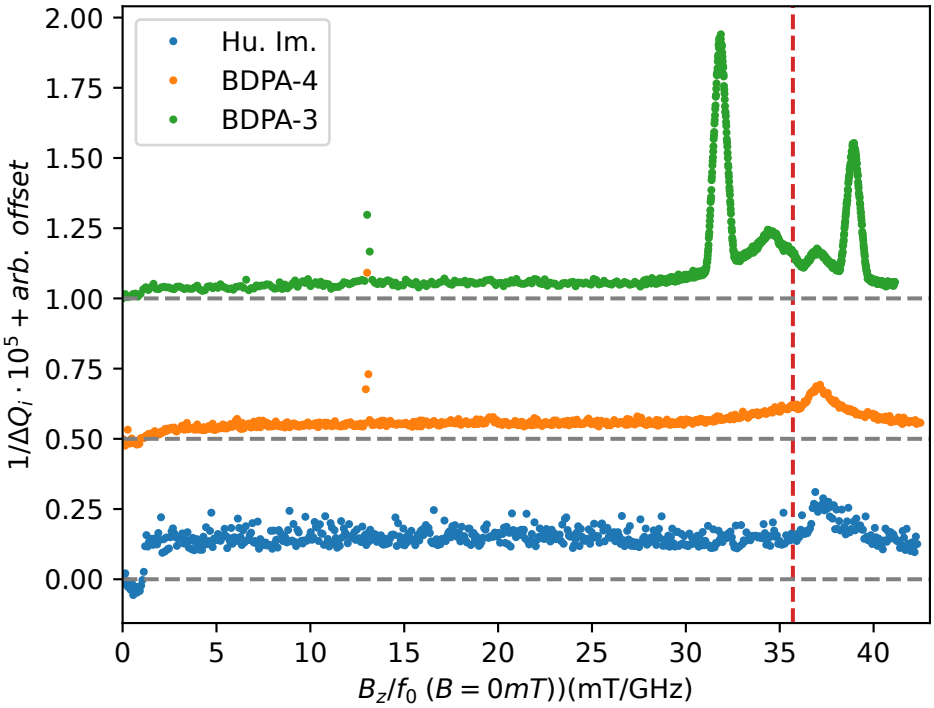

Figure 5.8: $1/\Delta Q_\mathrm{i}$ comparison between the two devices using an aluminium mask "BDPA-4" and "Hunting Impurities" with the "BDPA-3" device as reference. The "BDPA-4" device was exposed to the photoresist during dicing. The "Hunting Impurities" device shows no trace of any feature except the USO and the jump due to the wire bonds. The last contribution may vary compared to the "BDPA-x" devices as the device layout is different (transmission measurement, see Chapter 3.1.4).

However, another explanation could be that the etch is leaving residues, that get stabilized into some unknown spin system on the sapphire surface, and that this process is facilitated at higher annealing temperature.

5.2.4.2 *Participation ratio analysis*

To determine which interface contributed the most to the USO features, we have calculated the participation ratios for all resonator design. In particular, we expect the nanowire and the circle resonator to have vastly different contributions. We distinguish between the parts covered in NbTiN and the blank surface areas. To understand whether the coupling is electric or magnetic in nature, this analysis is done for the electric as well as for the magnetic participation ratios.

CALCULATING THE PARTICIPATION RATIOS In order to compute the electric p_E and magnetic participation ratio p_H we run a simulation (using Ansys HFSS) to obtain the electric/magnetic field $E_\mathrm{E}/E_\mathrm{H}$ energy in the selected area [181]. Setting

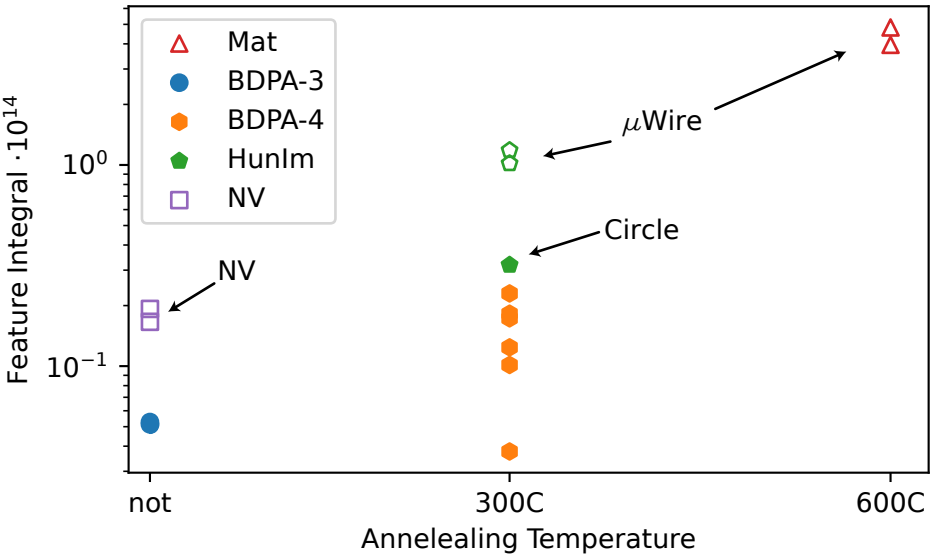

Figure 5.9: Integral of the USO line versus the annealing temperature. It was annealed in a nitrogen atmosphere. The data points labelled "NV" were obtained using an adapted design close to the circle resonator design.

this in relation to the total energy in the system U_{tot} we obtain the participation ratios as follows

$$p_{\text{E}} = 2\epsilon_0 t \frac{E_{\text{E}}}{U_{\text{tot}}}, \qquad \int_A |E|^2 \, \mathrm{d}A \tag{5.8}$$

$$p_{\text{M}} = \mu_0 \frac{t}{2} \frac{E_{\text{H}}}{U_{\text{tot}}}, \qquad \int_A |M|^2 \, \mathrm{d}A. \tag{5.9}$$

The thickness $t = 3\,\text{nm}$ is the material thickness in which we expect the interaction to happen and A the considered area. [181] carefully treats the edge areas, we, however, find no difference in our case. The individual electric and magnetic participation ratios for the NbTiN surface, the free sapphire surface as well as the two surfaces combined are then plotted versus the integral of the considered feature $I = \int_B 1/\Delta Q_{\text{i}}(ftr)\mathrm{d}B$. The integral takes only the contribution of the feature into account and subtracts the other contributions discussed earlier. Figure 5.10 collects these plots for the USO and the first hydrogen feature as a known reference using the fabrication without annealing. We do the same analysis for the USO on the two annealed devices, shown in Figure 5.11.

Assuming that the plotted features' origin is well captured by the selected participation ratio, we expect a linear relation going through the origin. Focusing first on the not annealed devices and restricting us to the USO the plots in Figure 5.10 suggest that the origin lies within the metal as the electric and the participation ratio restricted to the NbTiN area fit well, while the surface participation ratios do not. However, this evidence is fairly weak, as the deviation of the expected behaviour for the magnetic sapphire surface participation ratio is not strong. This is further emphasized when considering the first hydrogen line (feature 2). Here we clearly cannot see a linear behaviour between the integral over the feature and any of the considered surfaces. To obtain a definite conclusion, more resonators with different resonator geometries with different participation ratios would need to be included. Turning towards the

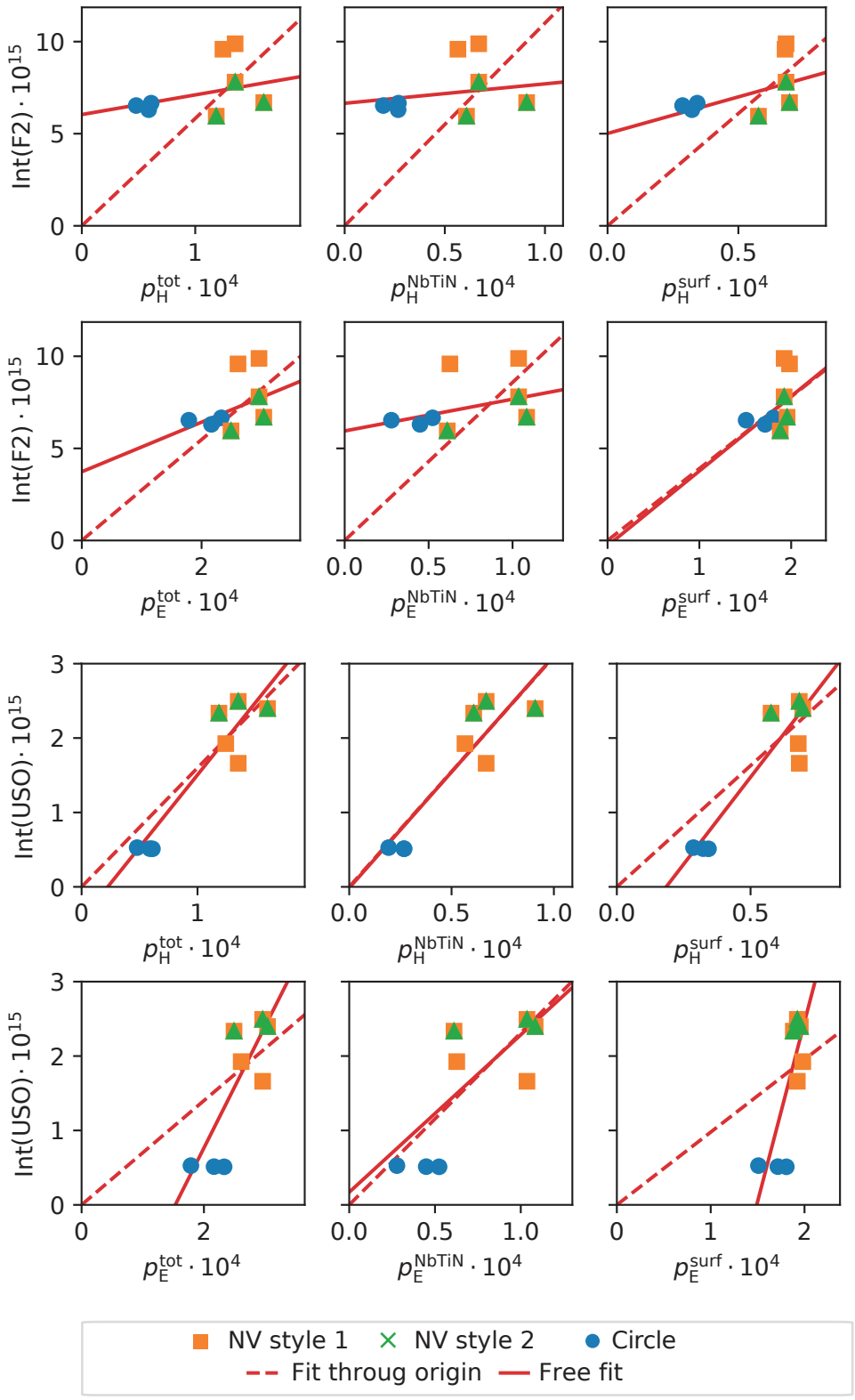

Figure 5.10: Integral over the feature contribution versus the magnetic and electric participation ratio of the area with NbTiN, the blank sapphire surface, and the total area. The devices included in this analysis are: ”BDPA-3”, ”Kin sample”, ”NV sample”. 5.9. ”F2” refers to the low field hydrogen feature.

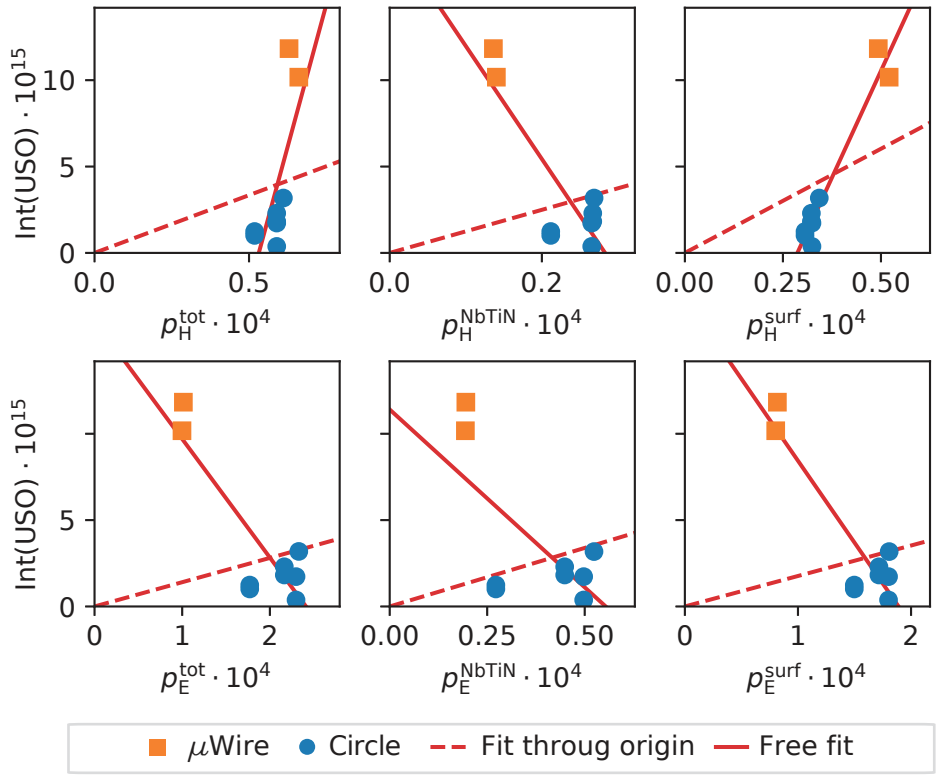

Figure 5.11: Integral over the feature contribution versus the magnetic and electric participation ratio of the area with NbTiN, the blank sapphire surface, and the total area. The devices included in this analysis have been annealed are: "BDPA-4", "Hunting Impurities". 5.11.

annealed devices, which cover a larger participation ratio range as they include two μWire resonators, we see that none of the considered areas produce a slope going through the zero point. According to the previous interpretation, this would mean that neither the magnetic nor the electric contributions to the surfaces are sufficient to explain the USO. This behaviour contributes to the puzzling nature of the USO and highlights that the conclusions drawn from Figure 5.10 have to be taken with care.

5.2.4.3 *Outlook*

To summarize the presented investigation, we can conclude that the internal losses of resonators fabricated with an aluminium mask are low enough for EPR experiments and that the observed spin systems are not the limiting factor at zero-field. Including the annealing at 300 °C in the fabrication removes the physisorbed hydrogen atoms and together with the aluminium mask yields an internal quality factor almost independent of the applied magnetic field. Using the annealing step, we note that the observed intrinsic quality factor at zero-field shows little variation across the different fabrication techniques, except that the number of "bad" outliers with $Q_i < 1 \times 10^5$ diminishes. The two field dependent contributions are due to the wire bonds and the USO. The effects of the wire bond can be minimized by ensuring they lie at an electrical node for the mode of the resonators. The origin and how to mitigate the USO remains to be

understood. This can be done by varying the annealing conditions, the resonators design, preparing different NbTiN films on different substrates and lastly searching for unknown impurities using quantitative methods such as X-ray photoelectron spectroscopy.

6

CWEPR AND PULSED EPR DETECTION OF BDPA

This chapter will outline the measurements and steps taken to characterize the sensitivity of the setup using BDPA. We start by explaining the microwave setup we have used, and then move on to cwEPR measurements before describing our attempts to measure a Hahn-Echo. We have deposited BDPA on four different devices: the Initial Device and four BDPA devices. The initial device was used for field characterisation with a very high BDPA concentration. Motivated by these measurements, we placed lower concentrations of BDPA on the BDPA devices, although the first two devices showed many extra peaks as discussed in the previous chapter, including a $g = 2$ line which could not be attributed to BDPA. After implementing the previously outlined improvements to the fabrication, we could observe a signal in cwEPR measurements and measure a relaxation time using the pulsed setup on the "BDPA-4" device.

6.1 PULSE GENERATION AND HOMODYNE DETECTION

To study the response of the resonators containing BDPA, we have used a mixture of simple VNA measurements, and then switched to a pulsed setup for observing spin saturation, relaxation, and for attempting to observe spin echoes. This setup can be roughly separated into three parts and is shown in Figure 6.1.

PULSE GENERATION To send pulses at resonance on the spins, we use an IQ-mixer (Analogue Devices HMC525ALC4) to modulate the output of a LO oscillator (Anapico APUASYN20-4) using low-frequency signals generated by an arbitrary wave form generator (Tektronics 5014C). After the IQ-mixer, a switch with 90 dB isolation (RFLambda RFSPSTA0218G) is placed and only opened during the time in which a pulse is applied. This way, the spin ensemble is protected from any microwave leakage that would lead to their saturation.

HOMODYNE DETECTION The signal outgoing of the cryostat is demodulated using another IQ-mixer, after which the I and Q signal are amplified (Femto HVA-200M-40-B) with 20 dB of gain and then digitised by an Alazar card (ATS9353).

INTERFEROMETRIC CANCELLING We also generate pulses sent onto the JTWPA's pump line in order to cancel the pulses used to probe the spin ensemble prior to entering the JTWPA. The pulses are generated analogue to the probe pulses. The JTWPA itself was in the beginning pumped using a Windfreak Tech frequency generator, and later on by the Anapico source on a different channel.

All long scale timings are scheduled by the square pulse generator (TTi TGF4042) triggering the AWG.

6.2 CONTINUOUS WAVE SPECTROSCOPY

We start by discussing our efforts at performing cwEPR spectroscopy on our devices. This is done in chronological order, starting from the Initial Device with a high spin concentration sample. For the following devices, we have used the BDPA design that we tested with various, iteratively increased concentrations.

6.2.1 *Spectroscopy at large concentration: Initial device*

After measuring the empty Initial chip (fabricated on Si using the CHF3 etch), BDPA mixed with PMMA was placed with a spatula on all three working resonators, see Figure 3.22a. We used a concentration of 6×10^{17} spins/ml and the estimated probe volume for the circle resonator is 3 pl. From this, we expect about 2×10^9 spins to couple to the resonator. Taking into account the resonator geometry, we expect an ensemble coupling constant of about $\bar{g}/(2\pi) = 1.4\,\mathrm{MHz}$ which far exceeds the resonator line width ($\kappa_t/2\pi = 242\,\mathrm{kHz}$). We thus expect to be in the strong coupling regime and to observe an avoided level crossing when the spins are brought to resonance. Our intention for this test was to provide a calibration of the magnetic field generated by our home-made magnet and to get a first characterization of BDPA at room-temperature.

Figure 6.2 shows the observed avoided level-crossing (ALC) on the circular resonator when tuning the spins at resonance. The calibration of the coil gave us a ratio $B/I = 90.03\,\mathrm{mT\,A^{-1}}$, which was 10 % off from our ab-initio calculation and is mostly due to the uncertainty of the re-normalization brought by the cryoperm shield.

Adjusting the model given in Equation 2.77 for the ensemble coupling constant and for the spin line width, we find an ensemble coupling of $g_{\mathrm{ens}}/(2\pi) = 8\,\mathrm{MHz}$, a line-width of $\Gamma_t/(2\pi) = 2\,\mathrm{MHz}$. We find that the resonator is coupled to $N_{\mathrm{spins}} = 6 \times 10^{10}$ spins. This matches roughly the first estimate of the number of placed spins, and we attribute the discrepancy to an uncontrolled dilution due to the difficulty of pipetting BDPA mixed with PMMA A6 due to the high viscosity of PMMA A6. This first successful attempt of measuring the BDPA spins motivated us to immediately try smaller spin concentrations, which should place us in the low-cooperativity regime in the following attempts.

Using this sample, we have tried unsuccessfully to saturate the spins by sending a long strong microwave pump tone before probing the transmission, or by increasing the power of the probe. We have also run pulsed EPR measurements (which we will describe later), but we were unable to observe an echo.

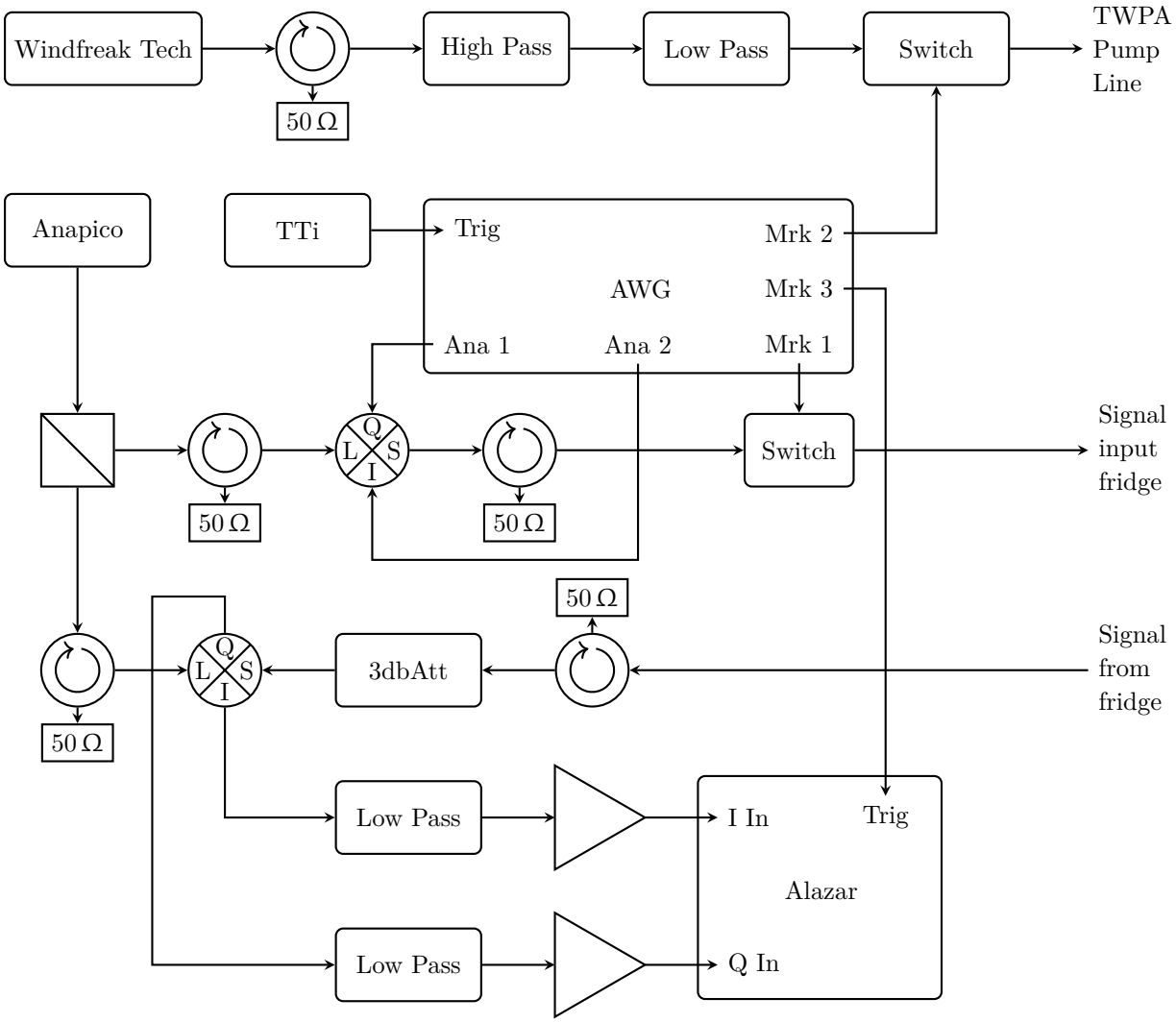

Figure 6.1: Schematic of the pulsed setup at room temperature, the cabling in the cryostat is the same as for the cwEPR setup shown in Figure 3.10. The setup related to the JTWPA cancellation pulses is not shown, but analogue to the pulse generation of the input signal. The 3 dB attenuation before the demodulation mixer to decrease spurious reflections.

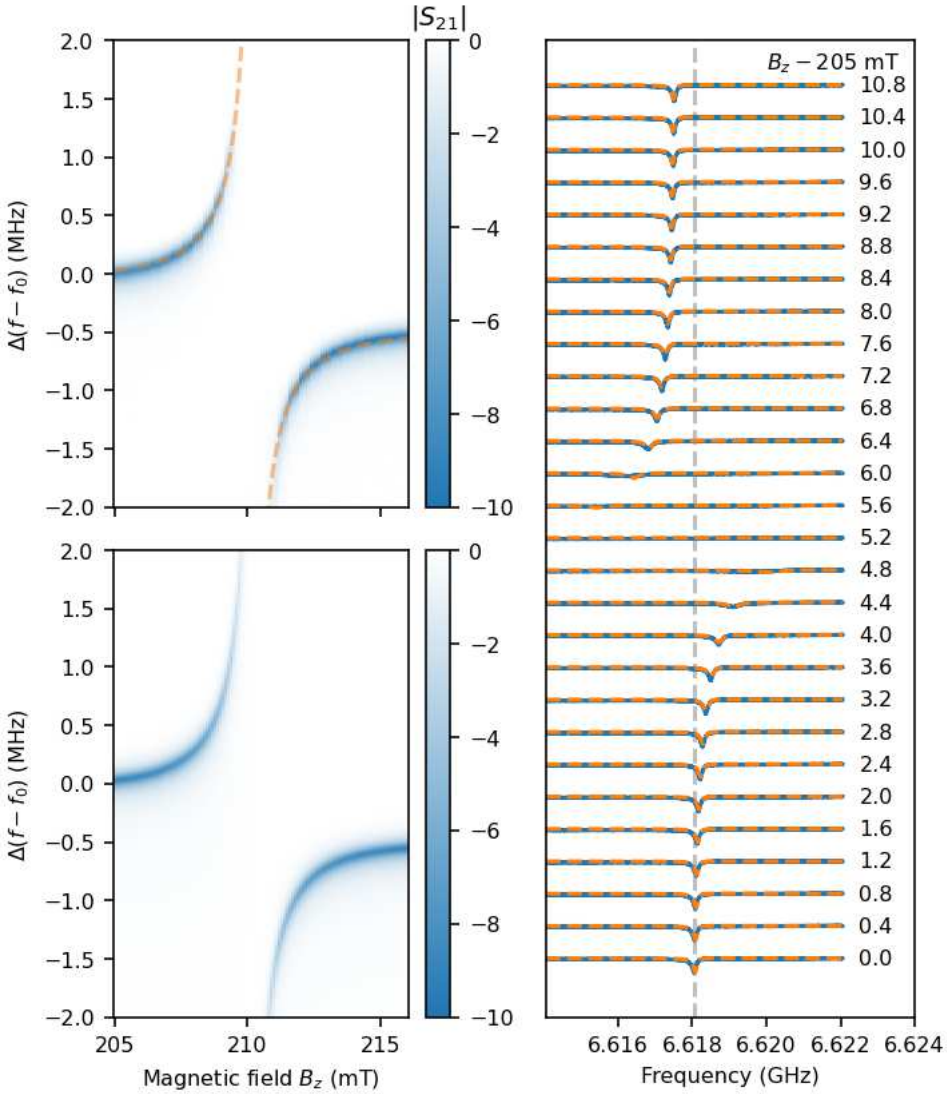

Figure 6.2: Top left: Transmission through the initial device near the circle resonator frequency while tuning the dc magnetic field, re-normalized by its off-resonance value. The orange dashed lines correspond to the resonance frequency extracted from a simple calculation of expected frequency modes using Equation 2.77 and on the bottom left. The model is adjusted to $g_{\mathrm{ens}}/(2\pi) = 8\,\mathrm{MHz}$ and a line-width of $\Gamma_t/(2\pi) = 2\,\mathrm{MHz}$ (right). Right: Example of individual $|S_{21}|$ measurements (blue) and predicted $|S_{21}|$ with arbitrary offset. The dashed line indicates the resonance frequency of the resonator $f_0 = 6.618\,\mathrm{GHz}$ at $B_z = 205\,\mathrm{mT}$. The shift of the resonance to lower frequencies at higher fields is due to the kinetic inductance.

6.2.2 *Spectroscopy at low concentration: BDPA devices*

We have run a total of three experiments using the BDPA device containing 8 resonators that were loaded with BDPA-PMMA drops. The optimized resonator geometry is shown in Chapter 3.1 and each device is probed in reflection. The configuration of the samples inserted in the resonators for the three devices is summarized in Table 6.1, and pictures of a few achieved drops are shown in Figures 3.18, 3.19a. We initially started with low concentrations ranging from 10^{12} to 10^{13} spins mL^{-1} on "BDPA-1", and then increased to 10^{15} spins mL^{-1} for "BDPA-2", and then to 10^{16} to 10^{17} spins mL^{-1} for "BDPA-4", recovering the concentration used in the Initial device. The dilutions and placements techniques are detailed in Chapter 3.5. The devices "BDPA-1" and "BDPA-2" were part of the second fabrication batch, and thus suffered from resist contamination, and we therefore expect the BDPA signal to overlap with the observed $g = 2$ line. Device "BDPA-4" was fabricated using an Al mask and a HEM wafer so that no contaminants are affecting the intrinsic losses (see Chapter 5.2.3).

We single out three resonators out of the three runs (resonator 4 on the "BDPA-1" and "BDPA-2" device and resonator 6 on the "BDPA-4" device, who have a similar targeted sensitivity and are thus geometrically close. Their design parameters are discussed in detail in Chapter 3.1.4.2). In Figure 6.3, we show the cwEPR spectroscopy acquired in the three runs, with BDPA for the first two samples, as well as the response expected taking the parameters extracted from the initial device and our numerical estimate for the coupling constant distribution and the sample volume. We note that using the values obtained from the initial device, we should have seen a signature of the BDPA on the "BDPA-2" and a larger signal on the "BDPA-4" device.

After the unsuccessful attempts of measuring BDPA on the two first devices, we decided to further increase the spin concentration using BDPA and to try different host matrices in order to recover the behaviour seen on the initial device as well as in the literature (especially the experiments carried out by [42] using YBCO anapole resonators with which a $T_2 = 2\,\mu\mathrm{s}$ of BDPA at 4K and 6.91 GHz was obtained). This was done to understand and exclude the sample deposition as a possible reason for the missing detection on previous devices. The different concentrations, host matrices and deposition methods for each resonator are summarized in table 6.1. The resonance frequencies and quality factors of the resonators at zero field are indicated in the same table. In general, the identification turns out to be difficult due to a somewhat random frequency shift of the resonators.

All 4 resonators with BDPA placed on them were showing a faint signature of spins crossing the resonators about the expected field for $g = 2$, see Figure 6.4. We again use Equation 2.77 to model the datasets for each resonator. The parameters showing the best adjustments are given in Table 6.2. A very unforeseen result is that the spin line width increased by a factor 5 compared to the initial device. We stress that the BDPA samples for both runs were prepared using the same protocol, and started both with a sealed BDPA flask purchased from Sigma-Aldrich. The main difference between the two runs is the use of PMMA A2 resist compared to PMMA A6. However, resonators 1, 3, and 6 contained BDPA mixed with toluene and polystyrene, which shows similar line width. Comparing the measured ensemble coupling with the $g_{\mathrm{ens}}/(2\pi) = 8\,\mathrm{MHz}$ on the initial

Table 6.1: Spin concentrations for the 3 measured BDPA devices. The volume is estimated as a half ellipsoid, with the height and radius extracted from the pictures taken at 45°. For the samples places with a toothpick or spatula, as well as in case of spillage during the drop deposition, only the estimated side length is given.

Device	Reso.	f_r (GHz)	Q_c ($\times 10^5$)	Q_i ($\times 10^5$)	Deposition	Sample size	Concentration (spins / mL)
BDPA-1	r2	6.630	2.82	0.86	Drop	1.8 pL	$1 \cdot 10^{12}$
	r3	7.075	2.72	1.91	Drop	3.5 pL	$1 \cdot 10^{12}$
	r4*	6.754	1.33	0.73	Drop	2.3 pL	$1 \cdot 10^{12}$
	r5*	7.139	3.38	0.38	Drop	7.6 pL	$1 \cdot 10^{13}$
	r6*	6.732	3.68	2.84	Drop	3.7 pL	$1 \cdot 10^{13}$
	r7	6.919	2.70	0.83	Drop	9.8 pL	$1 \cdot 10^{13}$
	r8	6.545	4.85	0.32	Drop	10.2 pL	$1 \cdot 10^{13}$
BDPA-2	r2	6.753	1.86	0.85	Drop	6.6 pL	$6 \cdot 10^{15}$
	r3	7.172	3.03	1.09	Drop	5.2 pL	$6 \cdot 10^{15}$
	r4	6.839	1.31	1.05	Drop	> 50µm	$6 \cdot 10^{15}$
	r6	6.825	1.30	1.51	Drop	6.2 pL	$6 \cdot 10^{15}$
BDPA-4	r1	7.809	4.38	2.13	W tip (PS)	≈ 20µm	6×10^{16}
	r3	7.516	2.73	2.48	Spatula (PS)	> 50µm	$6 \cdot 10^{16}$
	r4	7.532	2.64	1.12	Spatula (PMMA A6)	> 50µm	$6 \cdot 10^{17}$
	r6	7.706	5.87	0.49	Drop (PS)	5 pL	$6 \cdot 10^{16}$
	r7	7.516	2.73	2.48	Spatula (PMMA A2)	> 50µm	$6 \cdot 10^{17}$

device to what is measured on the BDPA device shows a factor 4 to 10 discrepancy, despite very similar single-spin coupling distributions and spin concentrations. This might be a further hint towards a degradation of the BDPA.

Using the pictures of the deposited spin samples together with the spin concentration, we again calculate the ensemble coupling g_{ens} (see Table 6.2) using the spin-resonator coupling distribution. For all the drops we assume a cylinder with the measured drop width and height and for the spillage/spatula placement we found that a film thickness of ≈ 1 µm leads to an agreement between the calculated and experimental ensemble coupling. With this, we tentatively identify resonator 4 and 7 to the resonances 4 and 5 as they both show similar ensemble coupling and have a sample placed with the spatula. This film thickness seems reasonable from the pictures, but has not been confirmed by a thickness measurement. The large ensemble coupling of resonance 6 hints towards a large loop radius and a higher spin concentration. This does match well with resonators 7 and 4 who both carry samples with the higher spin concentration and have a loop radius of 10 µm, with resonator 4 being unlikely due to the large required frequency shift. This leaves resonance 7 to be either resonator 3 or 1.

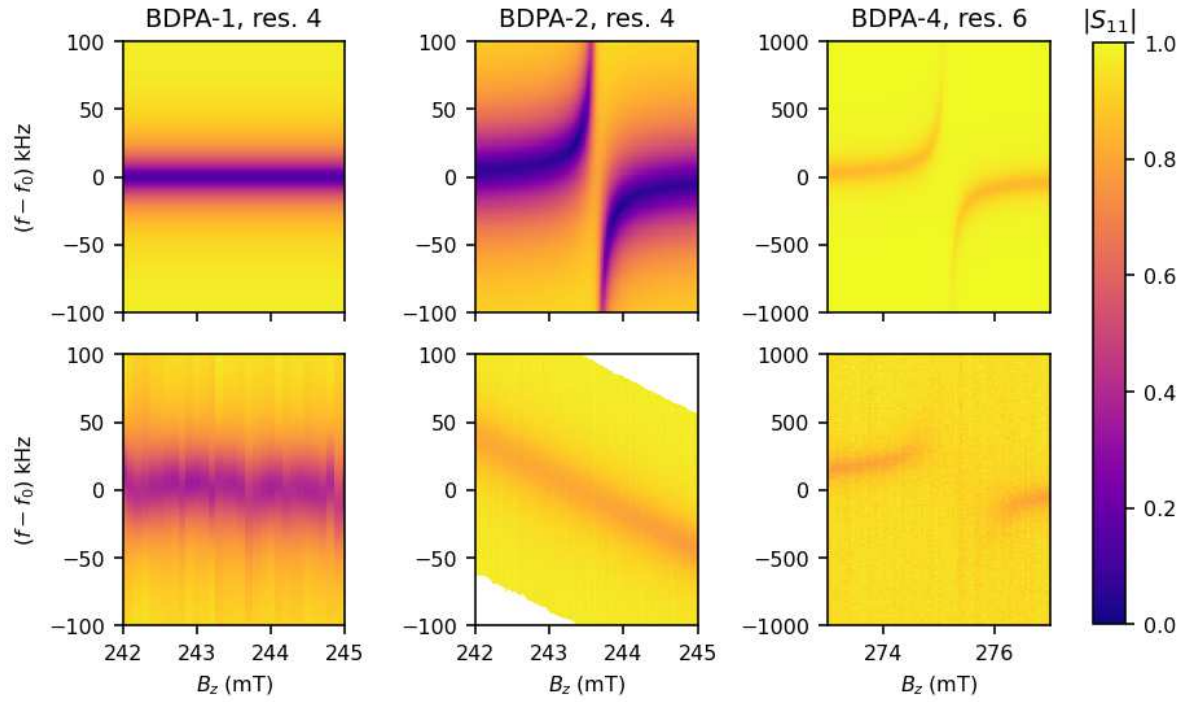

Figure 6.3: Expected (top row) and experimental (bottom row) reflection measurements at the expected field value for the BDPA spins. The expected S-parameter is calculated with the BDPA-parameters obtained from the initial measurement, the estimated number of spins calculated from the drop size, and the numerical estimated of the spin-resonator coupling of $g/(2\pi) \approx 40\,\mathrm{Hz}$. The resonance frequencies f_0 are: $f_0^{\mathrm{BDPA-1}} = 6.732\,47\,\mathrm{GHz}$, $f_0^{\mathrm{BDPA-2}} = 6.821\,87\,\mathrm{GHz}$, $f_0^{\mathrm{BDPA-4}} = 7.704\,25\,\mathrm{GHz}$. The data shown for the "BDPA-4" device is from resonance 6.

Table 6.2: Fit results of the avoided level crossings shown in figure 6.4. The theoretical ensemble coupling was calculated assuming a film thickness of 1 µm for the samples on resonator 3 and 7.

Resonance	possible resonator	$\gamma_{\mathrm{exp}}/\gamma_{\mathrm{theo}}$	$\Gamma_{\mathrm{t}}/(2\pi)$ (MHz)	$g_{\mathrm{ens}}^{\mathrm{exp}}/(2\pi)$ (MHz)	C	$g_{\mathrm{ens}}^{\mathrm{theo}}/(2\pi)$ (MHz)
4	7,4	0.9984	10	0.6	2.13	1.4
5	4,6	0.9984	10	0.6	1.16	1.4
6	3,7	0.9986	5	2.3	28.05	4.47
7	3,1	0.9967	12.5	0.3	0.33	0.5

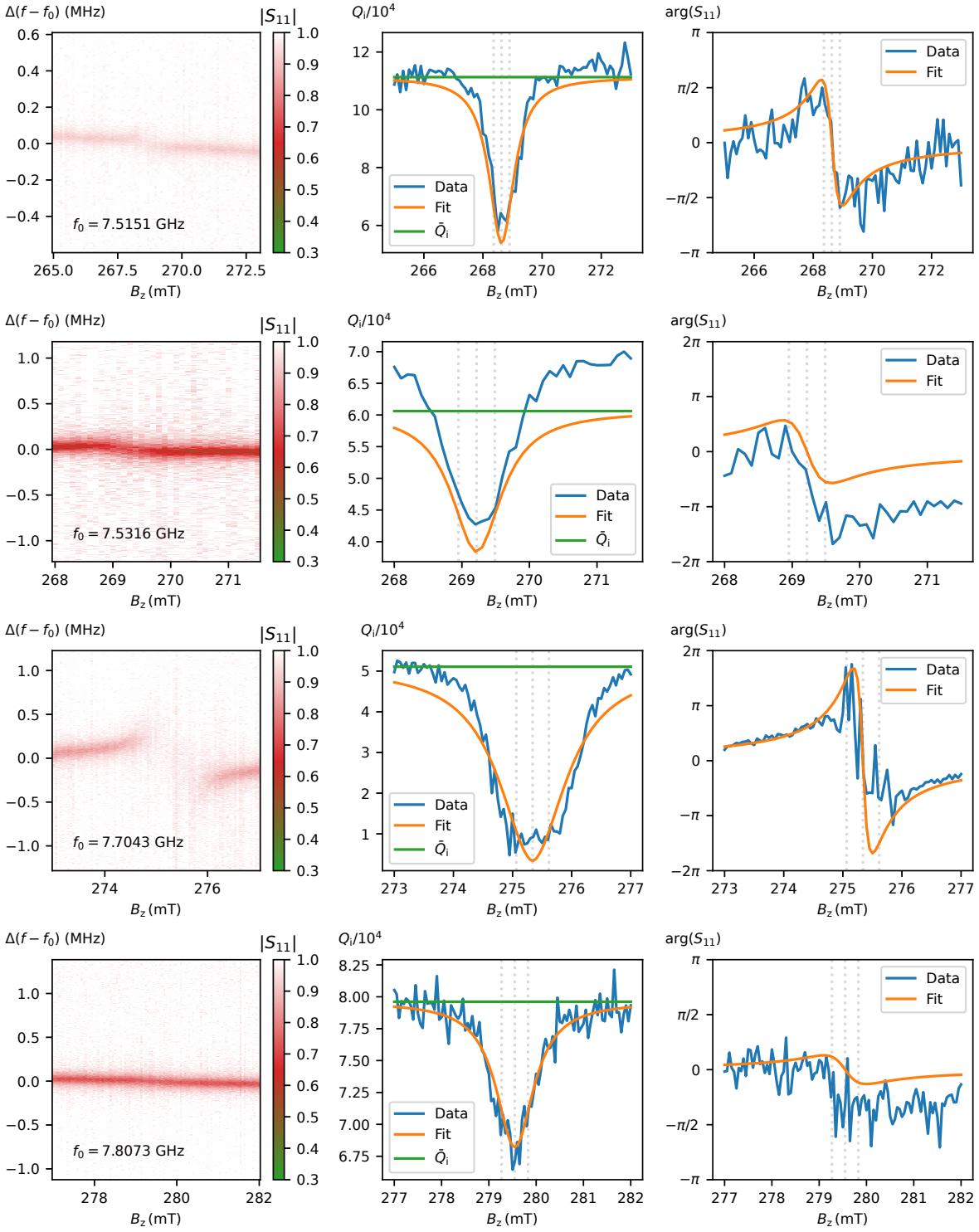

Figure 6.4: Avoided level crossings measured on the resonances (from top to bottom) four to seven. The dotted grey lines indicate the 99.9 % percentiles of magnetic field position. $\bar{Q}_\mathrm{i}$ is the average internal quality factor.

6.2.3 *Sensitivity of cwEPR measurements*

The successfully cwEPR measurements on BDPA prompt the question of the sensitivity of the cwEPR setup. To evaluate it, we need to calibrate the quantum efficiency, measure the T_1 and T_2 times of the BDPA spins. The T_1 time could be measured using the saturation recovery method. Combined with power saturation measurements, we determine a value for T_2 with which we then calculate the cwEPR sensitivity.

6.2.3.1 *Calibration of the quantum efficiency when using the JTWPA*

We first wish to calibrate the quantum efficiency of our near quantum-limited amplification. We thus need to characterize the number of noise photons added by the JTWPA. However, we can only detect signals at the output, and thus we can only detect the amplified noise from the combination of the JTWPA and the HEMT, as well as from the room-temperature amplifier (whose contribution we neglect): $P_\mathrm{n} = G_\mathrm{H}(G(N_\mathrm{a} + N_\mathrm{in}) + N_\mathrm{H})$. In our experiment, we have not installed any setup allowing to calibrate precisely the power incident either on the sample or on the JTWPA, so that we cannot relate directly this noise power to the input of the JTWPA and thus simply express N_a.

An alternate poor-man method consists in comparing the SNR with and without the JTWPA. The corresponding noise figure F is given by:

$$F = \frac{\mathrm{SNR_{on}}}{\mathrm{SNR_{off}}} = \frac{GS}{Gn_\mathrm{in} + (G-1)n_\mathrm{a} + n_\mathrm{H}} \frac{n_\mathrm{in} + n_\mathrm{H}}{S} = \frac{G}{1 + (G-1)\frac{n_\mathrm{in}+n_\mathrm{a}}{n_\mathrm{in}+n_\mathrm{H}}}. \tag{6.1}$$

In figure 6.5, we show the noise figure versus the JTWPA gain. The noise figure is calculated using a measurement of the I and Q quadratures with and without applying the JTWPA pump tone. At a gain of G =15 dB, we obtain a noise figure of $F = 11dB$. Using Equation 6.1 to fit the noise figure dependence on gain, we can extract that $\frac{n_\mathrm{in}+n_\mathrm{a}}{n_\mathrm{in}+n_\mathrm{H}} = 0.0583$.

Our HEMT is specified with a noise temperature 2 K: $n_\mathrm{H} = k_\mathrm{B}T/(\hbar\omega) = 6.1$ photons, with $\omega/2\pi = 7$ GHz. However, this figure does not consider losses between the HEMT and the JTWPA, which degrades the effective noise temperature of the JTWPA. Many solutions using a situ-calibration apparatus allow measuring this figure precisely; however, we have not used them. By comparing our setup to similar ones in the literature [182, 62], we can find a typical value of $n_\mathrm{H} = 25$ ($T_H \approx 8.5K$). We also make the approximation that the input microwave field of the JTWPA is well thermalized, so that $n_\mathrm{in} = 1/2$. We can then estimate the noise temperature of the JTWPA is

$$n_\mathrm{a} = 0.96 \,\text{photons}, \tag{6.2}$$

twice higher than what found in the original JTWPA publication [62]. We can then also calculate the quantum efficiency, taking into account the noise contribution (see Chapter 2.2.2)

$$\eta = \frac{1/2}{1/2 + n_\mathrm{a} + n_\mathrm{H}/G} = 0.25 \tag{6.3}$$

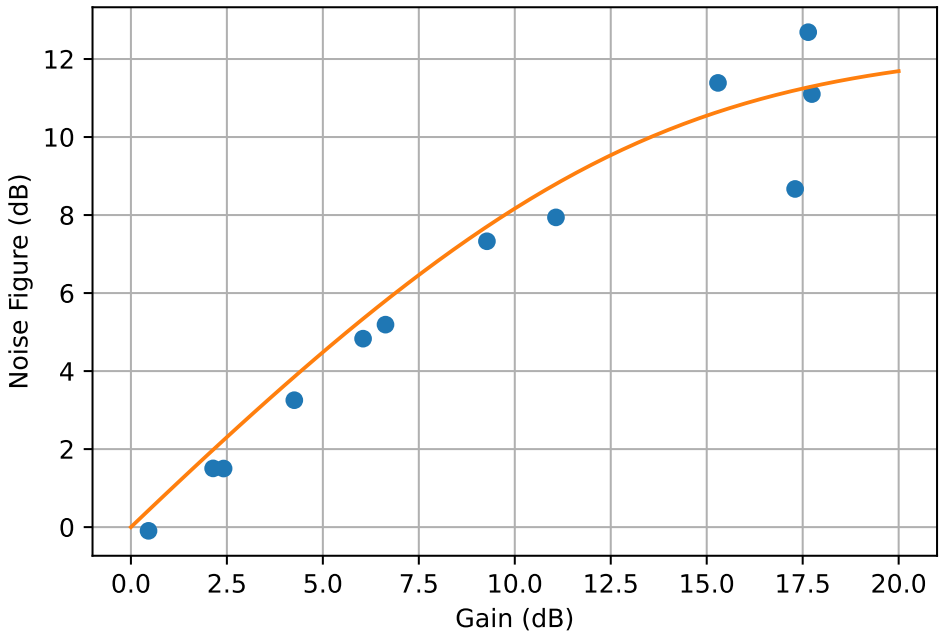

Figure 6.5: Noise Fig vs TWPA Gain with fit using Equation 6.1.

6.2.3.2 *Extracting relaxation time T_1 and single-spin coupling constant*

One direct way to measure the T_1 relaxation time, is by saturating the transition. This is done by a long, high-power pulse depleting the magnetization along the z-axis as all spins are on the x-y plane. Subsequently one can monitor the recovery from the saturation to obtain T_1. This can either be done by using an echo sequence or by the using cwEPR measurements [183][75]. When using a cwEPR measurement one expects right after the pulse when all spins are in the x-y plane that $\tilde{\kappa_{\text{int}}} = \kappa_{\text{i}}$ and afterwards a recovery following

$$\tilde{\kappa}_{\text{i}} = \kappa_{\text{i}} + \kappa_{\text{s}} \left(1 - \mathrm{e}^{-t/T_1}\right), \tag{6.4}$$

where κ_{s} are the losses introduced by the spin ensemble at resonance.

We have used this saturation recovery method to measure the T_1 time of the BDPA sample on resonance 5 (likely to be resonator 7). We applied a magnetic field of 269.40 mT and worked at 7.531 20 GHz to be at resonance with the spin transition. We are using pulses with our maximal available input power of 10 dBm before entering the cryostat with a pulse length of 100 µs. After a varying delay, we measure the transmission at resonance. Right after the pulse, the measured amplitude is proportional to

$$A_0 \propto \frac{\kappa_{\text{c}} - \kappa_{\text{i}}}{\kappa_{\text{c}} + \kappa_{\text{i}}}, \tag{6.5}$$

as spins are saturated and therefore do not contribute to the losses. Every field dependent loss (e.g. through the wire bonds) still contributes and is thus still included in κ_{i}. After

a sufficiently long time, the spin system has relaxed back to the thermal state and therefore contributes again fully to the resonator losses:

$$A_\infty \propto \frac{\kappa_c - \kappa_i - \kappa_s}{\kappa_c + \kappa_i + \kappa_s}. \tag{6.6}$$

The results are shown in figure 6.6. We can follow the recovery of the spin induced losses of the resonator and fit an exponential to extract T_1. With this, we find $T_1 = 15\,\mathrm{s}$.

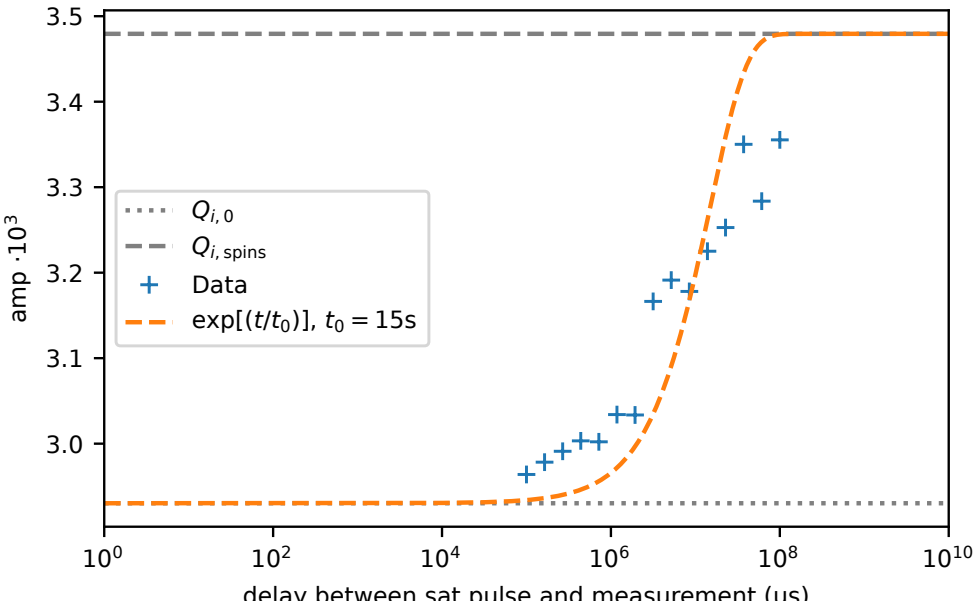

Figure 6.6: Measurement of the T_1 time using the saturation recovery method.

Assuming the Purcell effect comes into play and sets this T_1 time, we find $\bar{g}_0/(2\pi) = 19.5\,\mathrm{Hz}$. This value is compatible with the median value we expect from our numerical simulation. Given the ensemble coupling constant, we find that the number of spins within the resonator volume is about $N = 9.8 \cdot 10^8$, which is coherent with the spin concentration we have used.

6.2.3.3 *Determining the spin coherence time from saturation data*

We now turn to the power saturation of the resonator to extract the coherence time. Indeed, if the BDPA spin ensemble can be considered as weakly coupled, then its main effect is to add an effective decay channel to the resonator. Similarly to TLS baths, this decay channel can be suppressed by probing the resonator at high power, with a decay law given by Equation 5.5. Extracted quality factor at $0mT$ and at the centre of the avoided level crossing for various intra-resonator photon numbers is shown in Figure 6.7. This dataset was taken with resonance 5. Similarly to the previous chapter, we see a more pronounced saturation at higher fields than at zero field, due to more TLS being present: here these are the BDPA. Using Equation 5.5 to fit directly the BDPA resonator saturation, we find $n_c = 6$ photons. In all fairness, this number is an overestimate as we are neglecting the fact that we also saturate the other TLS baths,

such as the ones responsible for losses at zero field. However, taking into account both contributions is difficult since the dataset is relatively poor, we thus take this value as an upper bound. Also, there are not enough points in power to assess whether we are in the situation of a purely Markovian spin bath with a justified use of the exponent $\alpha = 1$.

Using the relation $n_C = 4g^2/(\Gamma_2\Gamma_1)$, we find $\Gamma_2/2\pi = 0.9$ MHz, corresponding to a T_2 of 180 ns. As we overestimate n_c, we are also overestimating T_2.

Despite the low quality of this determination, we can nevertheless say we are far from the µs timescale for T_2 observed by [42].

Multiple explanations are possible: the BDPA molecules could have aged despite being kept in sealed flasks (there is however no decay time reported for BDPA in the literature). The mixing with anisole could degrade the BDPA molecule. Similarly to DPPH, a broadening mechanism could be happening at lower temperatures.

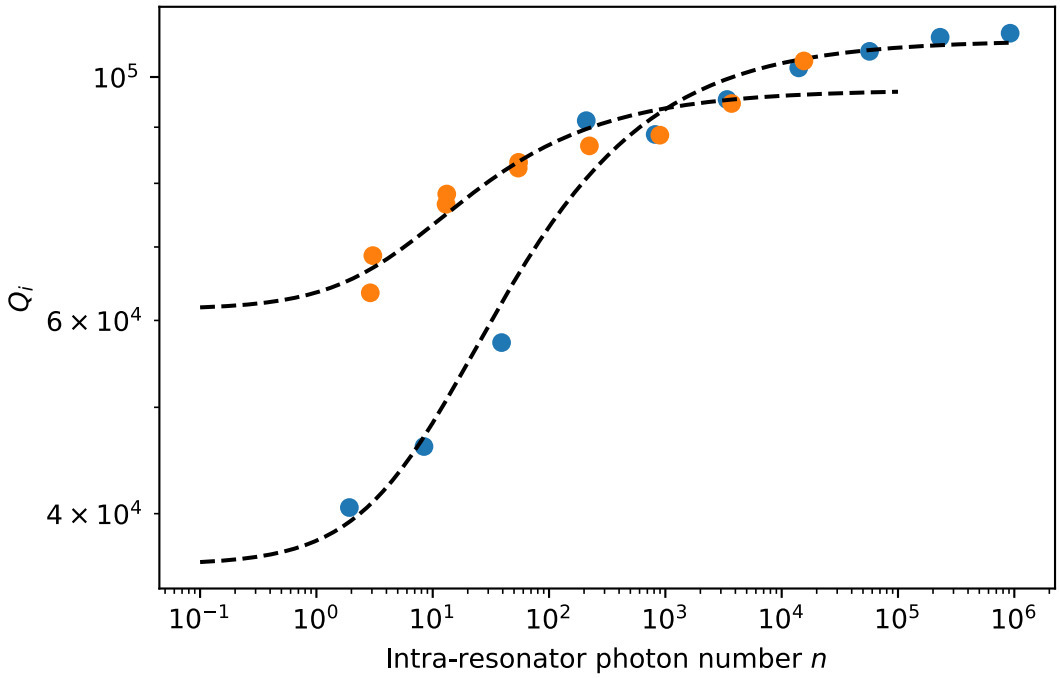

Figure 6.7: Intrinsic quality factors depending on the intra-resonator photon number. Orange dots are for data taken at zero magnetic field, blue dots for data taken at the anti-crossing with BDPA. Black dashed lines are fits using Equation 5.5.

6.2.3.4 *Determining the sensitivity*

Having fully characterized the spin ensemble, its coupling to the resonator, as well as the quantum-limited amplification chain, we can use Equation 2.86 to evaluate the sensitivity of our setup. We find $N_{min} = 2.3 \times 10^5 spins/\sqrt{Hz}$. To put this sensitivity into context, we would like to quote the sensitivity of some other experiments using superconducting planar resonators used to detect spins. Sears [115] has measured DPPH (temporarily

solved using toluene) with a coplanar waveguide resonator at 10 mK, quoting a sensitivity for their spectrometer of $N_{\min} = 1 \times 10^4\,\text{spins}/\sqrt{\text{Hz}}$. De Graaf et al.[36] has measured a surface spins with a minimal concentration of $N_{\min} = 1 \times 10^{13}\,\text{spins}\,\text{m}^{-2}$ (with a spin linewidth of 90 MHz and an approximately probed surface of 60 µm × 2 µm this is approximate $N_{\min} = 1.3 \times 10^3\,\text{spins}/\sqrt{\text{Hz}}$). We conclude that our cwEPR sensitivity lies in the range of the typically reported literature values.

6.3 TOWARDS PULSED EPR SPECTROSCOPY

We now want to outline the efforts undertaken in order to detect a spin echo using the pulsed EPR setup.

6.3.1 *Probing a spin ensemble with short pulsing sequences*

Detecting an echo for short-coherence samples such as BDPA requires using short $\pi/2$ and π pulses, so that the full sequence can be run within the decoherence time T_2. We thus need to apply pulses considerably shorter than the long decay time of our resonators ($\sim 5\,\mu\text{s}$). This is possible using fast-loading pulses, which enables to cancel the exponential decay. One of the simplest implementations is to have two consecutive squares pulses, with the second pulse of the opposite sign and of reduced duration or amplitude compared to the first. The first pulse, eventually followed by a waiting time, allows loading the resonator with photons. The second pulse acts as an unloading pulse and cancels the exponential decay that would otherwise be visible. As can be seen in Figure6.8, using a compensation pulse is power-consuming: to achieve a Rabi drive in 200 ns realizing the same tipping angle on the spins, about 1600 times (30 dB) more power is required. To perform a $\pi/2$ pulse on a spin ensemble whose mean coupling constant is $\bar{g_0}/(2\pi) = 30\text{Hz}$ in 200 ns, this is equivalent to sending a pulse on the resonator of power −22 dBm, which is close to the limit of what is currently possible in our room-temperature setup considering the attenuation on the line. Of course, another power amplifier can be added, but eventually, it is the non-linearity of the NbTiN resonator which will set the upper bound on the power which can be used to drive the spins.

We now wish to know whether use of these short loading pulses is sufficient to observe an echo in the experimental conditions we have observed for BDPA probed in cwEPR. We consider a spin ensemble similar to what is studied above: $N_{\text{spins}} = 10^9$ (or alternatively a concentration of 6×10^{17} spins/mL), $\Gamma_{\text{inh}}/2\pi = 10$ MHz, and the coupling constant distribution derived for resonator 4. The resonator has frequency $f_r = 7$ GHz, no losses, and a coupling quality factor of $Q_c = 2 \times 10^5$. We start by assuming a coherence time of 5 µs. We simulate using Equation 2.69 the response of the spin ensemble to a $\pi/2$ pulsed followed by a π pulse a time $\tau = 600\,\text{ns}$ later. The corresponding Hahn echo sequence is shown in Figure 6.9. The $\pi/2$ and π pulses are compensation pulses with 200-ns on-time and whose powers are calibrated to maximize the strength of the echo. We see the appearance of an echo at a time 2τ. We now consider the effect of shorter T_2. Simulations for $T_2 = 0.15$, 0.5, and $1, 5\,\mu\text{s}$ are shown. We see an echo appearing for $T_2 = 1\,\mu\text{s}$ and $5\,\mu\text{s}$, with respectively emission power

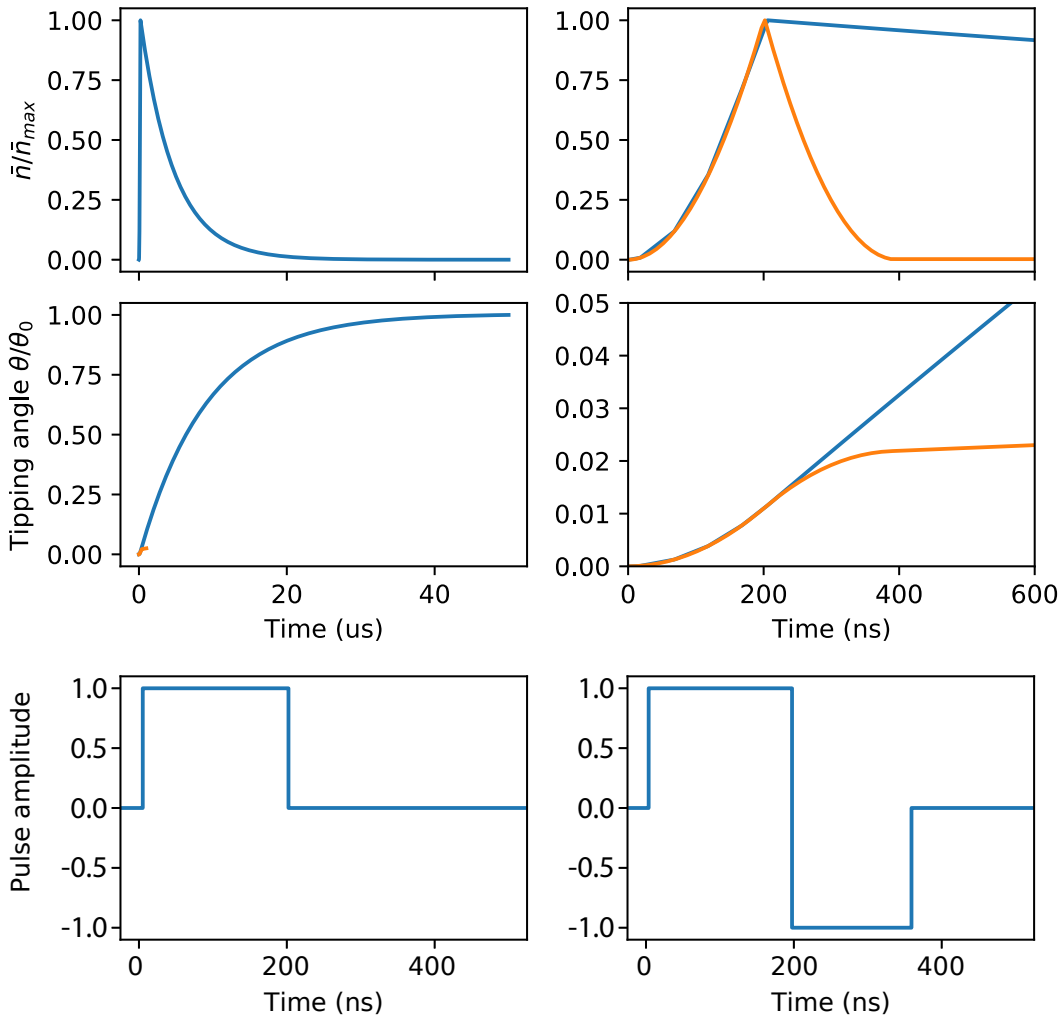

Figure 6.8: Numerical modelling of the response of a resonator of frequency 7 GHz and quality factor $Q = Q_c = 2 \times 10^5$ to fast-loading pulses. (Left column) Response for a simple square pulse of width 200 ns. (Right column) Response to a square of width 200 ns, immediately followed by a cancelling square pulse of length 188ns and of identical power

$P_{out} = -71\,\text{dBm}$ and $-75\,\text{dBm}$. For $T_2 = 500\,\text{ns}$ and $T_2 = 150\,\text{ns}$, unsurprisingly, no signal can be observed.

From these simulations, we can conclude that if our characterization of T_2 using cwEPR is of the right order of magnitude, no echo can be seen using 200 ns pulses. We could have attempted using shorter pulses, but it would have meant increasing the amount of power deliverable by the room-temperature setup considerably (+24 dB to go to 50 ns pulses). While physically possible, we ran into issues linked to the JTWPA saturation (described below) which prevented us from considering this option. We can also conclude that if the BDPA has a T_2 longer than 1 µs, the emitted echo is powerful enough that it should be visible even for concentration as low as 10^{15} spins/mL.

To distinguish the echo from the pulses, we use phase cycling. Each sequence is repeated twice, with the second iteration using a $\pi/2$ pulse of opposite phase compared to the first, leading to echoes being emitted in opposition of phase.

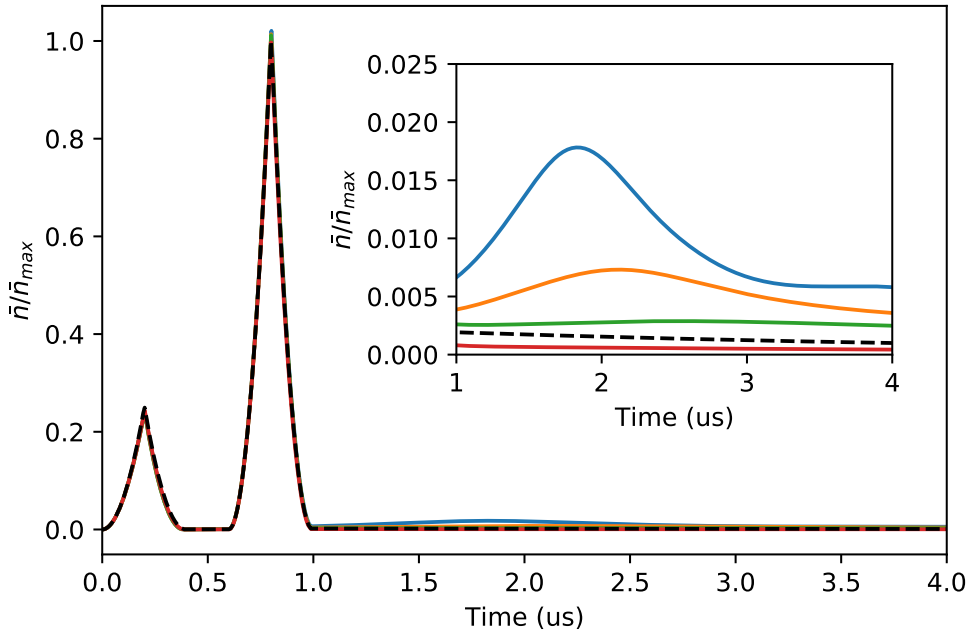

Figure 6.9: Simulation of a Hahn echo sequence with compensation pulses, yielding the intra-resonator photon number $\bar{n}$(t) during the sequence. The resonator and spin system parameters are given in the text. The simulations are performed for $T_2 = 5us$(blue), $T_2 = 1$us (orange), 500 ns (green) and 150 ns (red). The black dashed line represents a simulation with no spins included. For clarity, the graph is rescaled at its maximum point $n_{\max} = 4.6 \times 10^9$ photons, which corresponds to an output power of -54 dBm.

6.3.2 *Combining high-power pulses and JTWPA operation*

When attempting to use shorter and more powerful pulses in the Hahn-Echo sequence, the JTWPA started to show non-linear behaviour. In particular, the applied pulses lead to an ”echo” within the first couple hundred nanoseconds, prohibiting the detection of an actual spin echo. This echo remains present outside of resonance, detuned from any magnetic field feature, even when probing directly the JTWPA through its pump line. It is a result from ring-down oscillations occurring after each high-power pulse. When using phase cycling averaging, the oscillations are invisible as they perfectly cancel, except at the time of the echo. The origin of these ring-down oscillations and this echo is a bit obscure, but we suspect that the JTWPA chain is forming a standing wave oscillator due to unwanted impedance mismatch at each end. We have observed that a sharp high-power square pulse is distorted so that its edges have a rising/falling time of 2 µs. This time is similar to the ”coherence time” of this spinless echo. The ring-down oscillations could be due to entering an auto-oscillation regime for this standing mode.

A way to prevent this problem is to not apply the pulses to the JTWPA, but only to the resonator. We can do this by sending a pulse on the same input line as the JTWPA pump. This pulse should be shaped and have a phase such that we can by interference cancel the applied high-power pulses, keeping the JTWPA in its linear regime. In figure 6.10 a high-power Hahn-Echo sequence is shown, once with and once without the cancellation pulse.

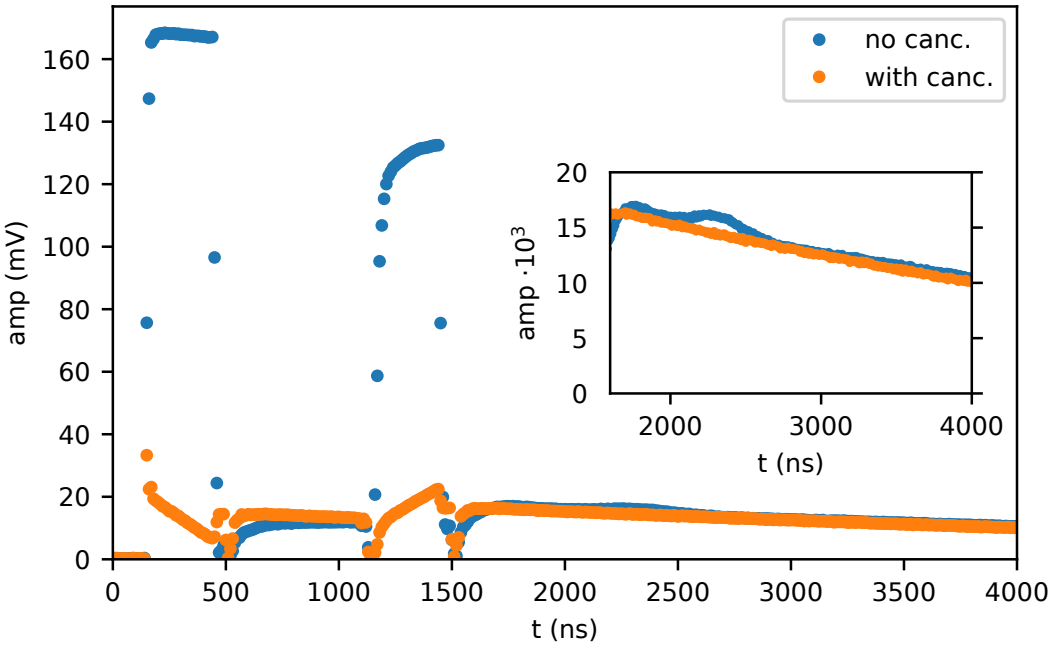

Figure 6.10: Hahn-Echo sequence applied on resonator four of the "BDPA-3" device with and without a cancellation pulse. The inset shows the exponential energy leakage out of the resonator with the JTWPA "echo".

Unfortunately, these efforts have not yet been rewarded with the detection of a spin-echo.

6.3.3 *Outlook*

In this chapter, we have shown first cwEPR measurements on BDPA at mK temperatures. We were able to extract a $T_2 = 180\,\text{ns}$ with cwEPR power saturation measurements and a saturation recovery measurement of $T_1 = 15\,\text{s}$. The coherence time is smaller than reported values at higher temperature measurements. An interesting reason could be due to the phase transition of BDPA, similar to the one in DPPH. It would be interesting to follow the EPR transition through this phase transition, connecting high temperatures of $\approx 2\,\text{K}$ down to 20 mK. A different direction would be the improvement of the pulsed setup, aiming for shorter pulses. Here the cancellation technique could be further improved, or an amplifier better suited for high-power measurements could be implemented.

7

CONCLUSION

This thesis focused on the development of a specialized resonator for high-sensitivity EPR spectroscopy using superconducting circuits. The resonator's circular geometry ensures its resilience to dielectric losses that may be introduced by the spin sample. Through our investigation of these resonators in magnetic field, we identified various contributions to the field-dependent intrinsic losses. By employing an aluminium mask and incorporating an annealing step, we successfully mitigated these losses, but for one unidentified (USO) contribution. The resonators consistently achieve quality factors $Q_\mathrm{i} > 10^5$ that remain nearly constant under the applied in plane magnetic field. These high-quality factors are essential for achieving high sensitivity in EPR experiments.

To validate the effectiveness of our approach, we conducted measurements using a BDPA, a well-known spin sample for EPR spectrometer characterization. We first developed a drop casting technique to place the spin samples within the active volume. In order to set a specific concentration, we dilute the BDPA in PMMA (an EPR-silent polymer) and drop cast through a borosilicate needle using a microlitre syringe.

After successfully placing BDPA at various concentrations, we performed cwEPR measurements. By analysing these measurements along with saturation recovery experiments showing a relaxation time of $T_1 = 15\,\mathrm{s}$, we extracted a coherence time (T_2) of 180 ns, which is shorter than values reported in literature at higher temperatures. We hypothesize that this discrepancy may be due to a phase transition in BDPA similar to the one observed in DPPH. Nevertheless, these values allowed us to characterize our cwEPR spectrometer with a minimum detectable number of spins of $N_{min} = 2.3 \times 10^5 spins/\sqrt{Hz}$.

Several open questions still remain. Understanding the origin of the USO and finding ways to mitigate it would be interesting. To address this, one could further expand on the participation ratio analysis by using different resonator structures. Changing the substrate would allow determining for certain whether the impurity is originating from the sapphire of the NbTiN. Additionally, employing quantitative methods like X-ray photoelectron spectroscopy could help to identify any unknown impurities within the NbTiN and sapphire materials. We could also investigate other superconductors, such as granular aluminium, to evaluate if they are better suited for the use in an EPR spectrometer as NbTiN.

Looking ahead, several possibilities for advancing the project can be considered. To tackle the problem of probing spins with large line-widths in a limited volume, a solution could be to modulate the resonator quality factor. It would enable a broad band excitation of the spin ensemble and allow preserving the quality factor required for high sensitivity. This tunability could be realized by controlling the kinetic inductance through the flow of a DC current [184]. Second, we have observed that BDPA, similarly to DPPH has lower coherence at 20 mK than at 4 K. It thus seems crucial to be able to probe the spin behaviour as a function of temperature. Implementing a temperature

control at the sample would allow us to study these effects and provide further insights into the behaviour of these samples. Such a setup would require to heat locally the sample, while ensuring the resonator microwave field and the quantum limited amplifier modes remain in their quantum ground state.

BIBLIOGRAPHY

[1] David E Lewis. "Yevgenii Konstantinovich Zavoiskii and the Battle for Electron Paramagnetic Resonance Spectroscopy." In: *Pioneers of Magnetic Resonance*. ACS Publications, 2020, pp. 113–122 (Cited on pages 1, 7).

[2] Isidor Isaac Rabi et al. "A new method of measuring nuclear magnetic moment." In: *Physical review* 53.4 (1938), p. 318 (Cited on pages 1, 7).

[3] Felix Bloch. "Nuclear induction." In: *Physical review* 70.7-8 (1946), p. 460 (Cited on pages 1, 7, 29).

[4] Edward M Purcell, Henry Cutler Torrey, and Robert V Pound. "Resonance absorption by nuclear magnetic moments in a solid." In: *Physical review* 69.1-2 (1946), p. 37 (Cited on pages 1, 7, 27).

[5] Maxie M Roessler and Enrico Salvadori. "Principles and applications of EPR spectroscopy in the chemical sciences." In: *Chemical Society Reviews* 47.8 (2018), pp. 2534–2553 (Cited on pages 1, 7).

[6] Gunnar Jeschke. "The contribution of modern EPR to structural biology." In: *Emerging Topics in Life Sciences* 2.1 (2018), pp. 9–18 (Cited on pages 1, 7).

[7] Sabine Kempe, Hendrik Metz, and Karsten Mäder. "Application of electron paramagnetic resonance (EPR) spectroscopy and imaging in drug delivery research–chances and challenges." In: *European Journal of Pharmaceutics and Biopharmaceutics* 74.1 (2010), pp. 55–66 (Cited on pages 1, 7).

[8] Johann P Klare and Heinz-Jürgen Steinhoff. "Spin labeling studies of transmembrane signaling and transport: applications to phototaxis, ABC transporters and symporters." In: *Methods in Enzymology*. Vol. 564. Elsevier, 2015, pp. 315–347 (Cited on pages 1, 7).

[9] Alasdair C Steven and Wolfgang Baumeister. "The future is hybrid." In: *Journal of structural biology* 163.3 (2008), pp. 186–195 (Cited on pages 1, 7).

[10] Lawrence J DeLucas et al. "Protein crystal growth in space, past and future." In: *Journal of crystal growth* 237 (2002), pp. 1646–1650 (Cited on pages 1, 7, 40).

[11] Aharon Blank, Ygal Twig, and Yakir Ishay. "Recent trends in high spin sensitivity magnetic resonance." In: *Journal of Magnetic Resonance* 280 (2017), pp. 20–29 (Cited on pages 1, 7).

[12] Nandita Abhyankar et al. "Scalable microresonators for room-temperature detection of electron spin resonance from dilute, sub-nanoliter volume solids." In: *Science advances* 6.44 (2020), eabb0620 (Cited on pages 2, 7, 38, 41).

[13] Jason W Sidabras et al. "Extending electron paramagnetic resonance to nanoliter volume protein single crystals using a self-resonant microhelix." In: *Science Advances* 5.10 (2019), eaay1394 (Cited on pages 2, 3, 7, 8, 38, 41).

[14] Enrica Montinaro. *Methods and microfabrication techniques for subnanoliter magnetic resonance spectroscopy*. Tech. rep. EPFL, 2017 (Cited on pages 2, 7, 41).

[15] Aharon Blank et al. "Induction-detection electron spin resonance with sensitivity of 1000 spins: En route to scalable quantum computations." In: *Physics Letters A* 377.31-33 (2013), pp. 1937–1942 (Cited on pages 2, 7, 41).

[16] Anthony J Sigillito et al. "Fast, low-power manipulation of spin ensembles in superconducting microresonators." In: *Applied Physics Letters* 104.22 (2014) (Cited on pages 2, 7, 41).

[17] Nir Dayan et al. "Advanced surface resonators for electron spin resonance of single microcrystals." In: *Review of Scientific Instruments* 89.12 (2018), p. 124707 (Cited on pages 2, 7, 41, 43).

[18] A Bienfait et al. "Reaching the quantum limit of sensitivity in electron spin resonance." In: *Nature nanotechnology* 11.3 (2016), pp. 253–257 (Cited on pages 2, 7, 8, 41, 48).

[19] S Probst et al. "Inductive-detection electron-spin resonance spectroscopy with 65 spins/Hz sensitivity." In: *Applied Physics Letters* 111.20 (2017), p. 202604 (Cited on pages 2, 7, 15, 41).

[20] Vishal Ranjan et al. "Electron spin resonance spectroscopy with femtoliter detection volume." In: *Applied Physics Letters* 116.18 (2020), p. 184002 (Cited on pages 2, 3, 7–9, 40, 41, 48).

[21] Zhiren Wang et al. "Single electron-spin-resonance detection by microwave photon counting." In: *arXiv preprint arXiv:2301.02653* (2023) (Cited on pages 2, 7, 8, 38, 41, 48).

[22] D Schmalbein et al. "The Bruker high-frequency-EPR system." In: *Applied Magnetic Resonance* 16.2 (1999), pp. 185–205 (Cited on pages 2, 7, 41).

[23] J Wrachtrup et al. "Optical detection of magnetic resonance in a single molecule." In: *Nature* 363.6426 (1993), pp. 244–245 (Cited on pages 1, 8).

[24] A Gruber et al. "Scanning confocal optical microscopy and magnetic resonance on single defect centers." In: *Science* 276.5321 (1997), pp. 2012–2014 (Cited on pages 1, 8).

[25] Felix Hoehne. "Electrical detection of hyperfine interactions in silicon." In: (2012) (Cited on pages 1, 8).

[26] M Xiao et al. "Electrical detection of the spin resonance of a single electron in a silicon field-effect transistor." In: *Nature* 430.6998 (2004), pp. 435–439 (Cited on pages 1, 8).

[27] Y Manassen et al. "Direct observation of the precession of individual paramagnetic spins on oxidized silicon surfaces." In: *Physical review letters* 62.21 (1989), p. 2531 (Cited on pages 1, 8).

[28] Daniel Rugar, CS Yannoni, and JA Sidles. "Mechanical detection of magnetic resonance." In: *Nature* 360.6404 (1992), pp. 563–566 (Cited on pages 1, 8, 38).

[29] Daniel Rugar et al. “Single spin detection by magnetic resonance force microscopy.” In: *Nature* 430.6997 (2004), pp. 329–332 (Cited on pages 1, 8, 38).

[30] MS Grinolds et al. “Subnanometre resolution in three-dimensional magnetic resonance imaging of individual dark spins.” In: *Nature nanotechnology* 9.4 (2014), pp. 279–284 (Cited on pages 1, 8, 38).

[31] Haakon Tassilo Adam Wiedemann et al. “Towards High Performance Microwave Resonators for EPR Spectroscopy.” In: *Available at SSRN 4334856* () (Cited on pages 3, 8, 38).

[32] Marcus Frederick Charles Ladd, Rex Alfred Palmer, and Rex Alfred Palmer. *Structure determination by X-ray crystallography*. Vol. 233. Springer, 1977 (Cited on pages 3, 9, 38).

[33] Kazuyoshi Murata and Matthias Wolf. “Cryo-electron microscopy for structural analysis of dynamic biological macromolecules.” In: *Biochimica et Biophysica Acta (BBA)-General Subjects* 1862.2 (2018), pp. 324–334 (Cited on pages 3, 9, 38).

[34] Rüdiger-A Eichel. “Structural and dynamic properties of oxygen vacancies in perovskite oxides—analysis of defect chemistry by modern multi-frequency and pulsed EPR techniques.” In: *Physical Chemistry Chemical Physics* 13.2 (2011), pp. 368–384 (Cited on pages 3, 9, 38).

[35] KJ Satzinger et al. “Simple non-galvanic flip-chip integration method for hybrid quantum systems.” In: *Applied Physics Letters* 114.17 (2019), p. 173501 (Cited on pages 3, 9, 38).

[36] SE De Graaf et al. “Direct identification of dilute surface spins on Al 2 O 3: Origin of flux noise in quantum circuits.” In: *Physical Review Letters* 118.5 (2017), p. 057703 (Cited on pages 5, 10, 40, 85, 91, 92, 111).

[37] Sun Un et al. “On the nature of decoherence in quantum circuits: Revealing the structural motif of the surface radicals in α-Al2O3.” In: *Science Advances* 8.14 (2022), eabm6169 (Cited on pages 5, 10, 85, 92, 93).

[38] Warrick G Farr et al. “Ultrasensitive microwave spectroscopy of paramagnetic impurities in sapphire crystals at millikelvin temperatures.” In: *Physical Review B* 88.22 (2013), p. 224426 (Cited on pages 5, 10, 85, 91, 92).

[39] R.O.C. Norman and B.C. Gilbert. “Electron-Spin Resonance Studies of Short-Lived Organic Radicals.” In: ed. by V. Gold. Vol. 5. Advances in Physical Organic Chemistry. Academic Press, 1967, pp. 53–119 (Cited on page 13).

[40] Yaron Artzi et al. “Superconducting micro-resonators for electron spin resonance-the good, the bad, and the future.” In: *Journal of Magnetic Resonance* 334 (2022), p. 107102 (Cited on pages 13, 64).

[41] Wyatt Vine et al. “In situ amplification of spin echoes within a kinetic inductance parametric amplifier.” In: *Science Advances* 9.10 (2023), eadg1593 (Cited on pages 13, 79).

[42] Claudio Bonizzoni et al. “Coupling sub-nanoliter BDPA organic radical spin ensembles with YBCO inverse anapole resonators.” In: *Applied Magnetic Resonance* 54.1 (2023), pp. 143–164 (Cited on pages 13, 65, 103, 110).

[43] Nandita Abhyankar et al. “Recent advances in microresonators and supporting instrumentation for electron paramagnetic resonance spectroscopy.” In: *Review of Scientific Instruments* 93.10 (2022), p. 101101 (Cited on pages 13, 38).

[44] David M Pozar. “Microwave engineering.” In: *Third Editions, University of Massachusetts at Amherst, John Wiley & Sons, Inc* (2005) (Cited on pages 13, 15, 16).

[45] Michel H Devoret et al. “Quantum fluctuations in electrical circuits.” In: *Les Houches, Session LXIII* 7.8 (1995), pp. 133–135 (Cited on page 13).

[46] Qi-Ming Chen et al. “Scattering coefficients of superconducting microwave resonators. I. Transfer matrix approach.” In: *Physical Review B* 106.21 (2022), p. 214505 (Cited on pages 13, 15, 16, 18).

[47] Qi-Ming Chen et al. “Scattering coefficients of superconducting microwave resonators. II. System-bath approach.” In: *Physical Review B* 106.21 (2022), p. 214506 (Cited on pages 13, 15).

[48] Audrey Bienfait. “Magnetic resonance with quantum microwaves.” PhD thesis. Université Paris Saclay (COmUE), 2016 (Cited on pages 14–16, 27, 28).

[49] Bernard Yurke and John S Denker. “Quantum network theory.” In: *Physical Review A* 29.3 (1984), p. 1419 (Cited on pages 14, 28).

[50] Marianne Le Dantec. “Electron spin dynamics of erbium ions in scheelite crystals, probed with superconducting resonators at millikelvin temperatures.” PhD thesis. Université Paris-Saclay, 2022 (Cited on pages 16, 18, 32).

[51] B Julsgaard and K Mølmer. “Reflectivity and transmissivity of a cavity coupled to two-level systems: Coherence properties and the influence of phase decay.” In: *Physical Review A* 85.1 (2012), p. 013844 (Cited on pages 16, 28, 32).

[52] Audrey Bienfait et al. “Controlling spin relaxation with a cavity.” In: *Nature* 531.7592 (2016), pp. 74–77 (Cited on pages 16, 27, 37).

[53] Siegfried Hunklinger. “Festkörperphysik.” In: *Festkörperphysik*. De Gruyter Oldenbourg, 2017 (Cited on page 19).

[54] Anthony J Annunziata et al. “Tunable superconducting nanoinductors.” In: *Nanotechnology* 21.44 (2010), p. 445202 (Cited on page 19).

[55] SK Yip and JA Sauls. “Nonlinear Meissner effect in CuO superconductors.” In: *Physical review letters* 69.15 (1992), p. 2264 (Cited on pages 20, 74).

[56] AB Pippard. “Field variation of the superconducting penetration depth.” In: *Proceedings of the Royal Society of London. Series A. Mathematical and Physical Sciences* 203.1073 (1950), pp. 210–223 (Cited on pages 20, 74).

[57] M Tinkham. *Introduction to Superconductivity 2nd ed (Mineola, New York*. 1996 (Cited on page 20).

[58] Michel H Devoret et al. *Quantum machines: measurement and control of engineered quantum systems*. Vol. 96. Oxford University Press, USA, 2014 (Cited on pages 20–22).

[59] Hermann A Haus and JA Mullen. "Quantum noise in linear amplifiers." In: *Physical Review* 128.5 (1962), p. 2407 (Cited on page 22).

[60] Carlton M Caves. "Quantum limits on noise in linear amplifiers." In: *Physical Review D* 26.8 (1982), p. 1817 (Cited on page 22).

[61] Kevin O'Brien et al. "Resonant phase matching of Josephson junction traveling wave parametric amplifiers." In: *Physical review letters* 113.15 (2014), p. 157001 (Cited on page 23).

[62] Chris Macklin et al. "A near–quantum-limited Josephson traveling-wave parametric amplifier." In: *Science* 350.6258 (2015), pp. 307–310 (Cited on pages 23, 24, 107).

[63] Hermann Haken and Hans C Wolf. *Atomic and quantum physics: an introduction to the fundamentals of experiment and theory*. Springer Science & Business Media, 2012 (Cited on pages 24, 92).

[64] Anatole Abragam and Brebis Bleaney. *Electron paramagnetic resonance of transition ions*. Clarendon P., 1970 (Cited on pages 24, 30).

[65] Graham Palmer. *The electron paramagnetic resonance of metalloproteins*. 1985 (Cited on pages 24, 25).

[66] Serge Haroche and J-M Raimond. *Exploring the quantum: atoms, cavities, and photons*. Oxford university press, 2006 (Cited on pages 25–27).

[67] Edwin T Jaynes and Frederick W Cummings. "Comparison of quantum and semiclassical radiation theories with application to the beam maser." In: *Proceedings of the IEEE* 51.1 (1963), pp. 89–109 (Cited on page 26).

[68] Jin Wang, Howard M Wiseman, and Gerard J Milburn. "Dynamical creation of entanglement by homodyne-mediated feedback." In: *Physical Review A* 71.4 (2005), p. 042309 (Cited on page 28).

[69] Michael Tavis and Frederick W Cummings. "Exact solution for an N-molecule—radiation-field Hamiltonian." In: *Physical Review* 170.2 (1968), p. 379 (Cited on page 30).

[70] I Diniz et al. "Strongly coupling a cavity to inhomogeneous ensembles of emitters: Potential for long-lived solid-state quantum memories." In: *Physical Review A* 84.6 (2011), p. 063810 (Cited on pages 30, 32).

[71] T Holstein and Hl Primakoff. "Field dependence of the intrinsic domain magnetization of a ferromagnet." In: *Physical Review* 58.12 (1940), p. 1098 (Cited on page 30).

[72] Z Kurucz, JH Wesenberg, and K Mølmer. "Spectroscopic properties of inhomogeneously broadened spin ensembles in a cavity." In: *Physical Review A* 83.5 (2011), p. 053852 (Cited on page 30).

[73] Mark C Butler and Daniel P Weitekamp. "Polarization of nuclear spins by a cold nanoscale resonator." In: *Physical Review A* 84.6 (2011), p. 063407 (Cited on page 32).

[74] Aashish A Clerk et al. “Introduction to quantum noise, measurement, and amplification.” In: *Reviews of Modern Physics* 82.2 (2010), p. 1155 (Cited on page 35).

[75] Arthur Schweiger. “Pulsed Electron Spin Resonance Spectroscopy: Basic Principles, Techniques, and Examples of Applications [New Analytical Methods (43)].” In: *Angewandte Chemie International Edition in English* 30.3 (1991), pp. 265–292 (Cited on pages 36–38, 108).

[76] Erwin L Hahn. “Spin echoes.” In: *Physical review* 80.4 (1950), p. 580 (Cited on page 37).

[77] Mantas Šimėnas et al. “A sensitivity leap for X-band EPR using a probehead with a cryogenic preamplifier.” In: *Journal of Magnetic Resonance* 322 (2021), p. 106876 (Cited on page 38).

[78] Raphaël Lescanne et al. “Irreversible qubit-photon coupling for the detection of itinerant microwave photons.” In: *Physical Review X* 10.2 (2020), p. 021038 (Cited on page 38).

[79] Malte Drescher. *EPR spectroscopy: applications in chemistry and biology*. Springer, 2012 (Cited on page 40).

[80] Arnold J Hoff. *Advanced EPR: applications in biology and biochemistry*. Elsevier, 2012 (Cited on page 40).

[81] Graeme Hanson and Lawrence Berliner. *Metals in biology: Applications of high-resolution EPR to metalloenzymes*. Vol. 29. Springer, 2010 (Cited on page 40).

[82] Elena Morra, Elio Giamello, and Mario Chiesa. “EPR approaches to heterogeneous catalysis. The chemistry of titanium in heterogeneous catalysts and photocatalysts.” In: *Journal of Magnetic Resonance* 280 (2017), pp. 89–102 (Cited on page 40).

[83] Marc Warner et al. “Spin-based diagnostic of nanostructure in copper phthalocyanine–C60 solar cell blends.” In: *ACS nano* 6.12 (2012), pp. 10808–10815 (Cited on page 40).

[84] WL Warren et al. “Electron paramagnetic resonance investigation of charge trapping centers in amorphous silicon nitride films.” In: *Journal of applied physics* 74.6 (1993), pp. 4034–4046 (Cited on page 40).

[85] R Narkowicz et al. “A cryogenic receiver for EPR.” In: *Journal of Magnetic Resonance* 237 (2013), pp. 79–84 (Cited on page 43).

[86] Cécile Xinqing Yu et al. “Magnetic field resilient high kinetic inductance superconducting niobium nitride coplanar waveguide resonators.” In: *Applied Physics Letters* 118.5 (2021), p. 054001 (Cited on pages 44, 85).

[87] Manuel Müller et al. “Magnetic field robust high quality factor NbTiN superconducting microwave resonators.” In: *Materials for Quantum Technology* 2.1 (2022), p. 015002 (Cited on pages 44, 73).

[88] Nodar Samkharadze et al. “High-kinetic-inductance superconducting nanowire resonators for circuit QED in a magnetic field.” In: *Physical Review Applied* 5.4 (2016), p. 044004 (Cited on pages 44, 45, 48, 83, 85).

[89] James G Kroll et al. "Magnetic-field-resilient superconducting coplanar-waveguide resonators for hybrid circuit quantum electrodynamics experiments." In: *Physical Review Applied* 11.6 (2019), p. 064053 (Cited on pages 44, 45, 48, 73, 85).

[90] K Borisov et al. "Superconducting granular aluminum resonators resilient to magnetic fields up to 1 Tesla." In: *Applied Physics Letters* 117.12 (2020), p. 120502 (Cited on pages 44, 85).

[91] Simone Frasca et al. "High-kinetic inductance NbN films for high-quality compact superconducting resonators." In: *arXiv preprint arXiv:2302.13930* (2023) (Cited on page 44).

[92] A Giachero et al. "Characterization of NbTiN Films With Thicknesses Below 20 nm for Low Power Kinetic Inductance Amplifiers." In: *IEEE Transactions on Applied Superconductivity* 33.5 (2023), pp. 1–5 (Cited on page 44).

[93] Shigehito Miki et al. "Superconducting NbTiN nanowire single photon detectors with low kinetic inductance." In: *Applied physics express* 2.7 (2009), p. 075002 (Cited on pages 44, 73).

[94] FRANCESCO Borsoi. "Magnetic field resilient superconducting circuit elements for Majorana parity detection." In: (2015) (Cited on pages 44, 48, 73, 79).

[95] I Nsanzineza and BLT Plourde. "Trapping a single vortex and reducing quasiparticles in a superconducting resonator." In: *Physical review letters* 113.11 (2014), p. 117002 (Cited on page 45).

[96] Gheorghe Stan, Stuart B Field, and John M Martinis. "Critical field for complete vortex expulsion from narrow superconducting strips." In: *Physical review letters* 92.9 (2004), p. 097003 (Cited on pages 45, 74).

[97] MM Khapaev et al. "Current distribution simulation for superconducting multilayered structures." In: *Superconductor Science and Technology* 16.1 (2002), p. 24 (Cited on page 46).

[98] Wing-Tat Pong et al. "Strategies for the deposition of free radical organic molecules for scanning-probe microscopy experiments." In: *Journal of Scanning Probe Microscopy* 1.2 (2006), pp. 55–62 (Cited on pages 59, 60).

[99] H. Sirringhaus et al. "High-Resolution Inkjet Printing of All-Polymer Transistor Circuits." In: *Science* 290.5499 (2000), pp. 2123–2126. eprint: https://www.science.org/doi/pdf/10.1126/science.290.5499.2123 (Cited on page 60).

[100] Bruno Michel et al. "Printing meets lithography: Soft approaches to high-resolution patterning." In: *IBM Journal of Research and Development* 45.5 (2001), pp. 697–719 (Cited on page 60).

[101] Hongwei Li et al. "High-resolution contact printing with dendrimers." In: *Nano Letters* 2.4 (2002), pp. 347–349 (Cited on page 60).

[102] Robert M Hochmuth. "Micropipette aspiration of living cells." In: *Journal of biomechanics* 33.1 (2000), pp. 15–22 (Cited on page 60).

[103] A Yeung et al. "Micropipette: a new technique in emulsion research." In: *Colloids and Surfaces A: Physicochemical and Engineering Aspects* 174.1-2 (2000), pp. 169–181 (Cited on page 60).

[104] Hee Taek Yi et al. “Ultra-flexible solution-processed organic field-effect transistors.” In: *Nature communications* 3.1 (2012), p. 1259 (Cited on page 60).

[105] Kenichiro Hiraoka and Seiji Kitamura. “Clinical efficiency of Piezo-ICSI using micropipettes with a wall thickness of 0.625 μm.” In: *Journal of assisted reproduction and genetics* 32 (2015), pp. 1827–1833 (Cited on page 60).

[106] K. Guevorkian and J.-L. Maître. “Chapter 10 - Micropipette aspiration: A unique tool for exploring cell and tissue mechanics in vivo.” In: *Cell Polarity and Morphogenesis*. Ed. by Thomas Lecuit. Vol. 139. Methods in Cell Biology. Academic Press, 2017, pp. 187–201 (Cited on page 60).

[107] Anton Savitsky and Klaus Möbius. “High-field EPR.” In: *Photosynthesis research* 102 (2009), pp. 311–333 (Cited on page 64).

[108] Sandra S Eaton and Gareth R Eaton. “Quality assurance in EPR.” In: *Bull. Magn. Reson* 13.3-4 (1992), pp. 83–89 (Cited on page 65).

[109] ND Yordanov. “Is our knowledge about the chemical and physical properties of DPPH enough to consider it as a primary standard for quantitative EPR spectrometry.” In: *Applied Magnetic Resonance* 10.1-3 (1996), pp. 339–350 (Cited on page 65).

[110] William Duffy Jr et al. “Antiferromagnetic linear chains in the crystalline free radical BDPA.” In: *The Journal of Chemical Physics* 56.6 (1972), pp. 2555–2561 (Cited on page 65).

[111] Stefan Stoll et al. “Atomic hydrogen as high-precision field standard for high-field EPR.” In: *Journal of Magnetic Resonance* 207.1 (2010), pp. 158–163 (Cited on page 65).

[112] SV Kolaczkowski, JT Cardin, and DE Budil. “Some remarks on reported inconsistencies in the high-field EPR spectrum of DPPH.” In: *Applied Magnetic Resonance* 16 (1999), pp. 293–298 (Cited on page 65).

[113] Teruaki Fujito. “Magnetic interaction in solvent-free DPPH and DPPH–solvent complexes.” In: *Bulletin of the Chemical Society of Japan* 54.10 (1981), pp. 3110–3116 (Cited on page 65).

[114] AM Prokhorov and VB Fedorov. “Antiferromagnetism of free radicals.” In: *Soviet Physics JETP* 16.6 (1963) (Cited on page 65).

[115] Adam Patrick Sears. *Extending Coherence in Superconducting Qubits: from microseconds to milliseconds*. Yale University, 2013 (Cited on pages 65, 110).

[116] Wolfgang Voesch et al. “On-chip ESR measurements of DPPH at mK temperatures.” In: *Physics Procedia* 75 (2015), pp. 503–510 (Cited on page 65).

[117] CF Koelsch. “Syntheses with triarylvinylmagnesium bromides. α, γ-Bisdiphenylene-β-phenylallyl, a stable free radical.” In: *Journal of the American Chemical Society* 79.16 (1957), pp. 4439–4441 (Cited on page 65).

[118] M Bennati et al. “Pulsed electron-nuclear double resonance (ENDOR) at 140 GHz.” In: *Journal of Magnetic Resonance* 138.2 (1999), pp. 232–243 (Cited on page 65).

[119] WO Hamilton and GE Pake. "Linear antiferromagnetism in the organic free radical 1, 3-bisdiphenylene-2-phenyl allyl." In: *The Journal of Chemical Physics* 39.10 (1963), pp. 2694–2697 (Cited on page 65).

[120] V Weis et al. *High-field DNP and ENDOR with a novel multiple-frequency resonance structure*. 1999 (Cited on page 65).

[121] Nagao Azuma, Takehiro Ozawa, and Jun Yamauchi. "Molecular and crystal structures of complexes of stable free radical BDPA with benzene and acetone." In: *Bulletin of the Chemical Society of Japan* 67.1 (1994), pp. 31–38 (Cited on page 65).

[122] Jun Yamauchi. "Microscopic evidence of antiferromagnetic long range ordering in the organic free radical, 1,3-bisdiphenylene-2-phenyl allyl (BDPA) benzene complex." In: *Physics Letters A* 70.3 (1979), pp. 238–240 (Cited on pages 65, 66).

[123] Jun Yamauchi. "Magnetic Phase Transition of the 1, 3-Bis (2, 2 -biphenylene)-2-phenylallyl (BDPA) Complex with Acetone." In: *Bulletin of the Chemical Society of Japan* 67.3 (1994), pp. 633–636 (Cited on page 65).

[124] Jun Yamauchi. "Microscopic evidence of antiferromagnetic long range ordering in the organic free radical, 1, 3-bisdiphenylene-2-phenyl allyl (BDPA) benzene complex." In: *Physics Letters A* 70.3 (1979), pp. 238–240 (Cited on page 65).

[125] JP Goldsborough, M Mandel, and GE Pake. "Influence of exchange interaction on paramagnetic relaxation times." In: *Physical Review Letters* 4.1 (1960), p. 13 (Cited on page 65).

[126] Deborah G Mitchell et al. "Electron spin relaxation and heterogeneity of the 1: 1 α, γ-bisdiphenylene-β-phenylallyl (BDPA)/benzene complex." In: *The Journal of Physical Chemistry B* 115.24 (2011), pp. 7986–7990 (Cited on page 65).

[127] Samuel Lenz et al. "Measurement of quantum coherence in thin films of molecular quantum bits without post-processing." In: *Chemical Communications* 55.50 (2019), pp. 7163–7166 (Cited on page 65).

[128] B.D. Ratner. "9.21 - Polymeric Implants." In: *Polymer Science: A Comprehensive Reference*. Ed. by Krzysztof Matyjaszewski and Martin Möller. Amsterdam: Elsevier, 2012, pp. 397–411 (Cited on pages 66, 67).

[129] Erwin Berthier, Edmond WK Young, and David Beebe. "Engineers are from PDMS-land, Biologists are from Polystyrenia." In: *Lab on a Chip* 12.7 (2012), pp. 1224–1237 (Cited on pages 66, 67).

[130] Luigi Frunzio et al. "Fabrication and characterization of superconducting circuit QED devices for quantum computation." In: *IEEE transactions on applied superconductivity* 15.2 (2005), pp. 860–863 (Cited on page 66).

[131] Ampere A Tseng et al. "Electron beam lithography in nanoscale fabrication: recent development." In: *IEEE Transactions on electronics packaging manufacturing* 26.2 (2003), pp. 141–149 (Cited on page 66).

[132] Chiao-Chi Lin et al. “EPR kinetics in irradiated syndiotactic polystyrene at elevated temperatures.” In: *Polymer* 49.18 (2008), pp. 3987–3992 (Cited on page 66).

[133] Viktor P Balema et al. “Depolymerization of polystyrene under ambient conditions.” In: *New Journal of Chemistry* 45.6 (2021), pp. 2935–2938 (Cited on page 66).

[134] P Silva et al. “Study of the gamma irradiation effects on the PMMA/HA and PMMA/SW.” In: *Radiation Physics and Chemistry* 79.3 (2010), pp. 358–361 (Cited on page 66).

[135] JF Kircher et al. “On the Degradation and Electron Spin Resonance Spectra of Irradiated Methacrylate Polymers1.” In: *The Journal of Physical Chemistry* 69.1 (1965), pp. 189–193 (Cited on page 66).

[136] K Miklešová and F Szöcs. “Free-radical decay in a polymer blend PMMA/PEO studied by the EPR method.” In: *European Polymer Journal* 28.5 (1992), pp. 553–554 (Cited on page 66).

[137] Sebastian Probst et al. “Efficient and robust analysis of complex scattering data under noise in microwave resonators.” In: *Review of Scientific Instruments* 86.2 (2015), p. 024706 (Cited on pages 69–71, 76).

[138] Anthony Megrant et al. “Planar superconducting resonators with internal quality factors above one million.” In: *Applied Physics Letters* 100.11 (2012), p. 113510 (Cited on page 69).

[139] D Rieger et al. “Fano Interference in Microwave Resonator Measurements.” In: *arXiv preprint arXiv:2209.03036* (2022) (Cited on pages 69–71, 76).

[140] X Dai et al. “New method for fitting complex resonance curve to study nonlinear superconducting resonators.” In: *Superconductor Science and Technology* 36.1 (2022), p. 015003 (Cited on page 69).

[141] Chunqing Deng, Martin Otto, and Adrian Lupascu. “An analysis method for transmission measurements of superconducting resonators with applications to quantum-regime dielectric-loss measurements.” In: *Journal of Applied Physics* 114.5 (2013), p. 054504 (Cited on pages 69, 70).

[142] Mingrui Xu et al. “Frequency-tunable high-Q superconducting resonators via wireless control of nonlinear kinetic inductance.” In: *Applied Physics Letters* 114.19 (2019), p. 192601 (Cited on pages 73, 79).

[143] Robert P Erickson et al. “Frequency comb generation in superconducting resonators.” In: *Physical review letters* 113.18 (2014), p. 187002 (Cited on pages 73, 79).

[144] JE Healey et al. “Magnetic field tuning of coplanar waveguide resonators.” In: *Applied Physics Letters* 93.4 (2008), p. 043513 (Cited on page 74).

[145] Chunhua Song et al. “Microwave response of vortices in superconducting thin films of Re and Al.” In: *Physical Review B* 79.17 (2009), p. 174512 (Cited on page 74).

[146] Alexander V Gurevich. “Tuning microwave losses in superconducting resonators.” In: *Superconductor Science and Technology* (2023) (Cited on page 83).

[147] Rami Barends et al. “Minimizing quasiparticle generation from stray infrared light in superconducting quantum circuits.” In: *Applied Physics Letters* 99.11 (2011) (Cited on page 83).

[148] Daniel Flanigan et al. “Magnetic field dependence of the internal quality factor and noise performance of lumped-element kinetic inductance detectors.” In: *Applied Physics Letters* 109.14 (2016) (Cited on page 83).

[149] Chunhua Song et al. “Reducing microwave loss in superconducting resonators due to trapped vortices.” In: *Applied Physics Letters* 95.23 (2009) (Cited on page 83).

[150] Daniel Bothner et al. “Improving the performance of superconducting microwave resonators in magnetic fields.” In: *Applied Physics Letters* 98.10 (2011), p. 102504 (Cited on page 83).

[151] Conal E Murray. “Material matters in superconducting qubits.” In: *Materials Science and Engineering: R: Reports* 146 (2021), p. 100646 (Cited on page 83).

[152] William D Oliver and Paul B Welander. “Materials in superconducting quantum bits.” In: *MRS bulletin* 38.10 (2013), pp. 816–825 (Cited on page 83).

[153] Clemens Müller, Jared H Cole, and Jürgen Lisenfeld. “Towards understanding two-level-systems in amorphous solids: insights from quantum circuits.” In: *Reports on Progress in Physics* 82.12 (2019), p. 124501 (Cited on page 83).

[154] Jürgen Lisenfeld et al. “Electric field spectroscopy of material defects in transmon qubits.” In: *npj Quantum Information* 5.1 (2019), p. 105 (Cited on pages 83, 84).

[155] PV Klimov et al. “Fluctuations of energy-relaxation times in superconducting qubits.” In: *Physical review letters* 121.9 (2018), p. 090502 (Cited on page 83).

[156] Alex Krasnok et al. “Advancements in Superconducting Microwave Cavities and Qubits for Quantum Information Systems.” In: *arXiv preprint arXiv:2304.09345* (2023) (Cited on page 83).

[157] R Barends et al. “Noise in NbTiN, Al, and Ta superconducting resonators on silicon and sapphire substrates.” In: *IEEE transactions on applied superconductivity* 19.3 (2009), pp. 936–939 (Cited on pages 83, 85).

[158] SE De Graaf et al. “Suppression of low-frequency charge noise in superconducting resonators by surface spin desorption.” In: *Nature communications* 9.1 (2018), p. 1143 (Cited on pages 83, 85).

[159] CM Quintana et al. “Observation of classical-quantum crossover of 1/f flux noise and its paramagnetic temperature dependence.” In: *Physical review letters* 118.5 (2017), p. 057702 (Cited on pages 83, 85).

[160] Matthias Schmelz and Ronny Stolz. “Superconducting Quantum Interference Device (SQUID) Magnetometers.” In: *High Sensitivity Magnetometers* (2017), pp. 279–311 (Cited on page 83).

[161] Long B Nguyen et al. “High-coherence fluxonium qubit.” In: *Physical Review X* 9.4 (2019), p. 041041 (Cited on page 83).

[162] RW Simmonds et al. “Coherent interactions between phase qubits, cavities, and TLS defects.” In: *Quantum Information Processing* 8 (2009), pp. 117–131 (Cited on page 83).

[163] Lara Faoro and Lev B Ioffe. “Internal loss of superconducting resonators induced by interacting two-level systems.” In: *Physical review letters* 109.15 (2012), p. 157005 (Cited on page 84).

[164] H Wang et al. “Improving the coherence time of superconducting coplanar resonators.” In: *Applied Physics Letters* 95.23 (2009) (Cited on page 84).

[165] Jan Goetz et al. “Loss mechanisms in superconducting thin film microwave resonators.” In: *Journal of Applied Physics* 119.1 (2016) (Cited on page 84).

[166] Paul Heidler et al. “Non-Markovian effects of two-level systems in a niobium coaxial resonator with a single-photon lifetime of 10 milliseconds.” In: *Physical Review Applied* 16.3 (2021), p. 034024 (Cited on page 84).

[167] John M Martinis et al. “Decoherence in Josephson qubits from dielectric loss.” In: *Physical review letters* 95.21 (2005), p. 210503 (Cited on page 84).

[168] Sebastian Erik de Graaf et al. “Galvanically split superconducting microwave resonators for introducing internal voltage bias.” In: *Applied Physics Letters* 104.5 (2014), p. 052601 (Cited on pages 85, 91).

[169] Sandor Caplan and Gerald Chanin. “Critical-field study of superconducting aluminum.” In: *Physical Review* 138.5A (1965), A1428 (Cited on page 90).

[170] Erik Preston Harris and DE Mapother. “Critical field of superconducting aluminum as a function of pressure and temperature above 0.3 K.” In: *Physical Review* 165.2 (1968), p. 522 (Cited on page 90).

[171] Jingjing Niu et al. “Low-loss interconnects for modular superconducting quantum processors.” In: *Nature Electronics* 6.3 (2023), pp. 235–241 (Cited on page 90).

[172] JK Krebs and U Happek. “Yb3+ energy levels in α-Al2O3.” In: *Journal of luminescence* 94 (2001), pp. 65–68 (Cited on page 91).

[173] Gavin Dold et al. “High-cooperativity coupling of a rare-earth spin ensemble to a superconducting resonator using yttrium orthosilicate as a substrate.” In: *Physical Review Applied* 11.5 (2019), p. 054082 (Cited on page 91).

[174] Mark S Akselrod and Frank J Bruni. “Modern trends in crystal growth and new applications of sapphire.” In: *Journal of crystal growth* 360 (2012), pp. 134–145 (Cited on page 91).

[175] Daniel C Harris. “A century of sapphire crystal growth: origin of the EFG method.” In: *Optical Materials and Structures Technologies IV*. Vol. 7425. SPIE. 2009, pp. 215–226 (Cited on page 91).

[176] Oliver Dial et al. “Bulk and surface loss in superconducting transmon qubits.” In: *Superconductor Science and Technology* 29.4 (2016), p. 044001 (Cited on page 91).

[177] M Lucas et al. “Quantum bath suppression in a superconducting circuit by immersion cooling.” In: *Nature Communications* 14.1 (2023), p. 3522 (Cited on page 91).

[178] Yu-Huan Lu and Hsin-Tsung Chen. “Hydrogen generation by the reaction of H 2 O with Al 2 O 3-based materials: A computational analysis.” In: *Physical Chemistry Chemical Physics* 17.10 (2015), pp. 6834–6843 (Cited on page 91).

[179] Jurek Krzystek, Andrew Ozarowski, and Joshua Telser. “Multi-frequency, high-field EPR as a powerful tool to accurately determine zero-field splitting in high-spin transition metal coordination complexes.” In: *Coordination chemistry reviews* 250.17-18 (2006), pp. 2308–2324 (Cited on page 92).

[180] L Zhang et al. “Superconducting properties and chemical composition of NbTiN thin films with different thickness.” In: *Applied Physics Letters* 107.12 (2015) (Cited on page 93).

[181] Chen Wang et al. “Surface participation and dielectric loss in superconducting qubits.” In: *Applied Physics Letters* 107.16 (2015), p. 162601 (Cited on pages 94, 95).

[182] Anita Fadavi Roudsari et al. “Three-wave mixing traveling-wave parametric amplifier with periodic variation of the circuit parameters.” In: *Applied Physics Letters* 122.5 (2023) (Cited on page 107).

[183] Sandra S Eaton, Gareth R Eaton, and Lawrence J Berliner. *Biomedical EPR-Part B: methodology, instrumentation, and dynamics*. Vol. 24. Springer Science & Business Media, 2004 (Cited on page 108).

[184] Sumedh Mahashabde et al. “Fast tunable high-q-factor superconducting microwave resonators.” In: *Physical Review Applied* 14.4 (2020), p. 044040 (Cited on page 115).